DISSERTATION

# PROPERTIES OF $Th^{4+}$ AND $Th^{3+}$ FROM RF SPECTROSCOPY OF HIGH-L THORIUM RYDBERG IONS

Submitted by

Julie Adel Keele

Department of Physics

In partial fulfillment of the requirements

For the Degree of Doctor of Philosophy

Colorado State University

Fort Collins, Colorado

Summer 2013

Doctoral Committee:

Advisor: Stephen R. Lundeen

David A. Krueger
Nancy E. Levinger
Jacob L. Roberts

Copyright by Julie Adel Keele 2013

All Rights Reserved

# ABSTRACT

## PROPERTIES OF $Th^{4+}$ AND $Th^{3+}$ FROM RF SPECTROSCOPY OF HIGH-L THORIUM RYDBERG IONS

Several properties of radon-like $Th^{4+}$ and francium-like $Th^{3+}$ were determined from measurements of high-$L$ Rydberg fine structure in $Th^{3+}$ and $Th^{2+}$ ions. The measurements were carried out using the resonant excitation Stark ionization spectroscopy (RESIS) technique to detect rf transitions between levels in the same $n$. The measured Rydberg fine structures were then fit to an effective potential model, and the properties of the ions were extracted. Properties of the ${}^1S_0$ ground state of $Th^{4+}$ extracted from the measurements of the $n$=37 $Th^{3+}$ Rydberg fine structure were the scalar dipole polarizability, $\alpha_{D,0} = 7.702(6) a.u.$ and the scalar quadrupole polarizability, $\alpha_{Q,0} = 29.1(1.6) a.u.$. The $Th^{2+}$ Rydberg fine structure is much more complex since the ground state of $Th^{3+}$ is a ${}^2F_{5/2}$, and the presence of low-lying excited states cause non-adiabatic effects in the fine structure which are not well described by the effective potential. To extract the properties, non-adiabatic corrections had to be calculated. The properties of $Th^{3+}$ extracted were the permanent quadrupole moment, $Q = 0.5931(14) a.u.$, the scalar and tensor dipole polarizabilities, $\alpha_{D,0} = 15.224(33) a.u.$ and $\alpha_{D,2} = -5.30(11) a.u.$, the permanent hexadecapole moment, $\Pi = -0.69(28) a.u.$, and the reduced dipole and octupole matrix elements coupling the ground state to the $6d\ {}^2D_{3/2}$ state, $\left|\left\langle g^2F_{5/2}\left\|M^{[1]}\right\|6d^2D_{3/2}\right\rangle\right| = 1.436(2) a.u.$ and $\left|\left\langle g^2F_{5/2}\left\|M^{[3]}\right\|6d^2D_{3/2}\right\rangle\right| = 3.3(1.1) a.u.$.

TABLE OF CONTENTS

LIST OF TABLES

LIST OF FIGURES

## Chapter 1: Introduction

The spectroscopy of high-$L$ Rydberg states using the RESIS technique provides a way of measuring the properties of positive ions. This technique can be used on any positive ion without major changes to the experimental set-up and for that reason is very powerful. The study of the radon-like and francium-like thorium reported here was motivated by the importance of the chemistry of actinide elements in issues of high national priority, such as storage of waste from nuclear power. The biggest unknown in actinide chemistry is the actinide elements themselves which are usually found in ionization states near the Rn-like ion. Yet little is known about these isolated ions. This makes it difficult to understand how these elements will interact with other well-known elements. The modeling of these ions even in isolation is difficult given their high nuclear charge and large number of electrons. This makes any experimental measurement valuable as a test of these challenging calculations.

This dissertation reports measurements of high-$L$ Rydberg fine structures in $Th^{2+}$ and $Th^{3+}$ ions using rf spectroscopy. From these measurements many properties of the Fr-like $Th^{3+}$ ion and Rn-like $Th^{4+}$ ions, the core ions of these Rydberg systems, were extracted and compared with theoretical calculations. Section 1 of this Chapter will present background on high-$L$ Rydberg states. The second section will discuss the theoretical model used to describe these high-$L$ Rydberg states and additional effects that can contribute to the energies of high-$L$ Rydberg states. A brief overview of the experimental technique is then presented in the third section of this chapter. The fourth section of this chapter discusses the motivation for the Th measurements and gives a history on the previous work done in preparation for this study.

### 1.1 High-*L* Rydberg States

A high-*L* Rydberg state is made up of a highly excited electron orbiting around a positive ion, $X^{q+}$, as seen in Fig. 1.1 [1]. The Rydberg state has a core, $X^{q+}$, which can be any positive ion. The Rydberg electron is described by its principal quantum number, *n*, and its angular momentum, *L*.

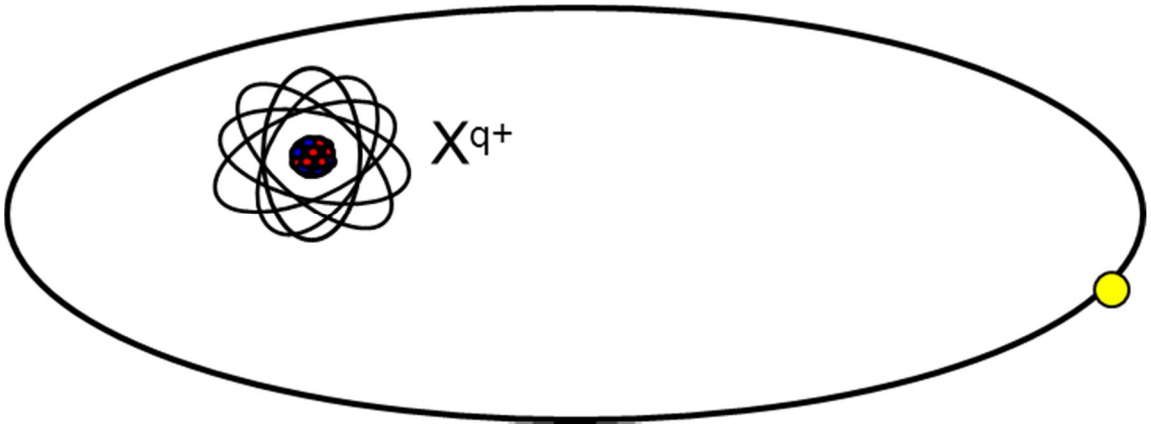


Figure 1.1: High-*L* Rydberg state with the core ion being $X^{q+}$. The Rydberg electron orbiting around it is in a high angular momentum state, *nL*.

If the Rydberg electron remains far away from the core, as in a high angular momentum state, then the Rydberg state is very similar to a hydrogen atom or a hydrogenic ion and the Rydberg electron's wave function is an almost purely hydrogenic wave function. The approximate classical inner turning point for the Rydberg electron is given by Eq. 1.1 [1].

$$r_{-} \geq \frac{L(L+1)}{2q} a_0 \tag{1.1}$$

Eq. 1.1 allows for the calculation of the distance of closest approach for the Rydberg electron to the core. If the inner turning point of the state of interest is near or outside the atomic radius of the core ion, it is considered a high-*L* state. For example, for $Th^{3+}$ the Rydberg states studied were $L \geq 7$, making the inner turning points $r_{-} \geq 9.3a_0$. The estimated atomic radius of $Th^{3+}$ is

$r_{rms} \sim 1.5a_0$ [2], thus the states studied are referred to a high-$L$ state since they are outside the atomic radius of the core of the Rydberg state. For the most part, the Rydberg states studied using the technique presented in this work are $L \geq 4\sqrt{q}$ , but this is just an approximate cut-off of the class of Rydberg states that can be described as "high-$L$".

The wave function of a single electron in the hydrogen atom or a hydrogen-like ion with principal quantum number $n$ is closely analogous to a family of classical orbits of a common major axis. These classical orbits vary in possible eccentricities, from linear when $L$=0 to an almost circular at maximum $L$, and all have the same energy since they are subject only to the $1/r$ Coulomb potential. The analogous hydrogenic quantum levels are degenerate, except for small relativistic corrections. With actual high-$L$ Rydberg states there also exists the possibility of additional long-range interactions between the more complex core and the Rydberg electron. These long-range interactions break the degeneracy of the hydrogenic energy levels and produce a fine structure pattern that is sensitive to the properties of the core, other than its total charge.

The scale and the shape of the energy levels in the fine structure pattern is determined by the properties of the core that control these long-range interactions. These properties fall into two categories. The first category is made up of the permanent electric moments of the core. The permanent electric moments create multipole fields that the Rydberg electron interacts with. These moments exist for the core ion with or without the presence of the Rydberg electron. The dominant permanent moment, the permanent electric quadrupole moment, $Q$, corresponds to a $2^{nd}$ rank tensor potential, but other even order moments are also possible as long as $\kappa \leq 2J_c$ , where κ is the rank of the tensor potential. For example, the ground state of $Th^{3+}$, studied here, with $J_c$=5/2, may have a permanent hexadecapole moment with $\kappa = 4$ . The second category of properties controlling the long-range interaction is made up of induced moments of the core,

characterized by polarizabilities. The dominant polarizability is the scalar dipole polarizability, $\alpha_{D,0}$, but there is a rich variety of other polarizabilities corresponding to various multipole orders and tensor orders.

The two dominant core properties, $\alpha_{D,0}$ and $Q$, determine the majority of the fine structure pattern, but each affects the fine structure in different way. The number of energy levels for each $L$ in the fine structure pattern will be determined by the number of different ways the angular momentum of the core can be aligned with the orbit with the Rydberg electron. Quantum mechanically the number of ways this can happen in high-$L$ Rydberg levels is $2J_c+1$ , where $J_c$ is the total angular momentum of the ground state of the core. For example a core with $J_c$=5/2 will have six energy levels for each $L$ in the fine structure. As the orbit of the Rydberg electron around the core becomes more circular, i.e. as $L$ increases, the splitting between the levels will become smaller; this is due to the interaction between the Rydberg electron and the quadrupole moment being proportional to $1/r^3$. The $\alpha_{D,0}$ affects the fine structure pattern in a different way than $Q$. It does not cause a splitting in the levels for each $L$, but instead causes a shift of the energy level or levels for each $L$ away from their hydrogenic zeroth order values. The interaction between the core and Rydberg electron due to $\alpha_{D,0}$ is proportional to $1/r^4$ therefore the shift away from hydrogenic will be larger when the orbit of the Rydberg electron is more eccentric (low $L$) and the shift will approach zero as the orbit becomes nearly circular (high $L$).

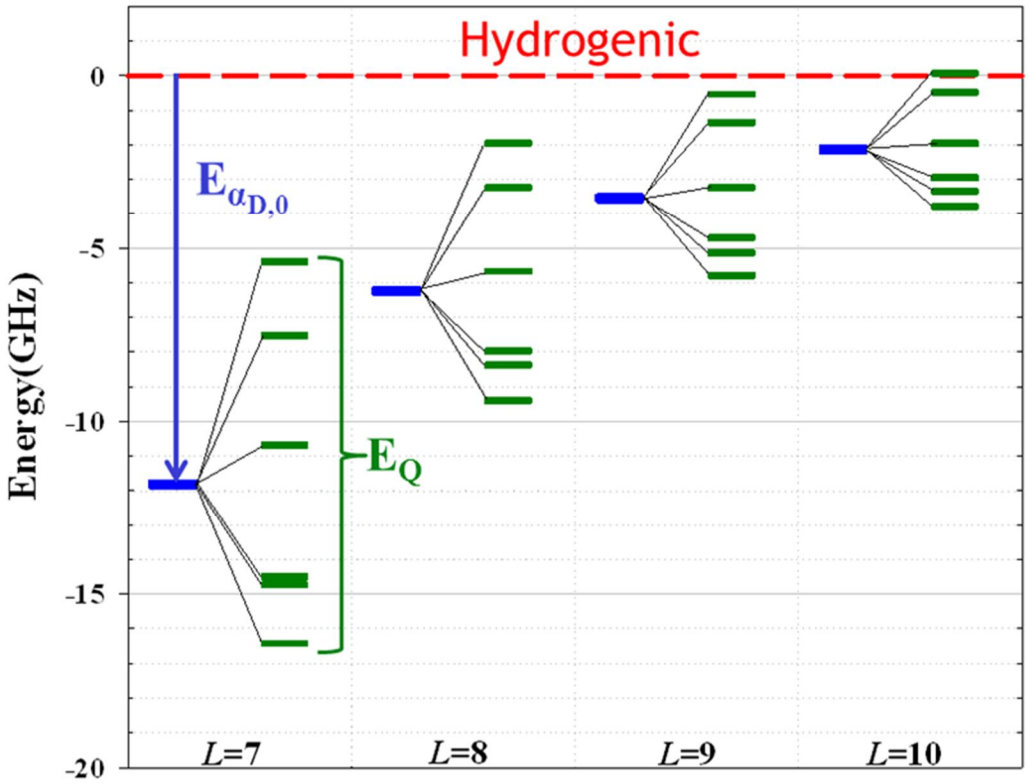


Figure 1.2: Simulated $n$=28 $Th^{2+}$ Rydberg fine structure, $L$=7 to 10, using the properties of the core, $Th^{3+}$, $J_c$=5/2, $Q$=0.54a.u. and $\alpha_{D,0}$=15.42a.u [3]. $E\alpha_{D,0}$ represent the energy shift away from hydrogenic for each $L$ due to the $\alpha_{D,0}$ and $E_Q$ represent the splitting of the energy levels for each $L$ due to $Q$.

Figure 1.2 illustrates the effect of these dominant properties on the fine structure pattern. The quadrupole moment causes the splitting of the levels for each $L$ and the scalar dipole polarizability shifts the center of gravity of the levels away from hydrogenic. In practice, the actual fine structure is also sensitive to additional permanent moments and polarizabilities of the core.

Each level in the Rydberg fine structure pattern is described by three quantum numbers: $n$, $L$ and $K$. The $n$ is the principal quantum number, and $L$ is the angular momentum of the

Rydberg electron. $K$ is the total angular momentum of the system, exclusive of the Rydberg electron spin, representing the vector addition of the $L$ and $J_c$,

$$\vec{K} = \vec{L} + \vec{J}_c \tag{1.2}$$

and it ranges in value in integer steps from $L+J_c$ to $L-J_c$. Each of the energy levels in the fine structure will be labeled by its $n$, $L$, and $K$ values when $J_c>0$. When $J_c=0$ the level for each $L$ will be labeled by their $n$ and $L$ values alone, since there will only be one level per $L$. The contribution of the spin of the Rydberg electron is nearly negligible to the fine structure energy.

A vast majority of excited states in atoms and ions are high angular momentum states, $L \geq 4\sqrt{q}$ , but observations of these states are rare with traditional spectroscopy methods. Tables of atomic energy levels, as seen on the NIST website [4], illustrate this. The use of absorption spectroscopy to observe these high-$L$ states is limited because it is impossible to reach high angular momentum states with this technique. Absorption spectroscopy starts with a ground state atom or ion normally a relatively low $L$ state, and excites that state to a higher angular momentum state. That excitation is limited by the dipole selection rule $\Delta L=\pm 1$, making it impossible to reach the high-$L$ states. Emission spectroscopy is also limited in its ability to observe these higher $L$ states. The first limitation on emission spectroscopy is the weakness of these emissions. The high-$L$ states are much longer lived then the lower $L$ states making radiative decay less probable compared to collisional loss. The second limitation is that the high resolution needed to see the deviation of the fine structure from hydrogenic is difficult to obtain. These two limitations on emission spectroscopy make it difficult but not impossible to observe the high-$L$ Rydberg states. Some recent studies of high-$L$ Rydberg states using high resolution emission spectroscopy have been reported [5]. Since high-$L$ Rydberg states are difficult to

access with traditional spectroscopy methods the measurement of the fine structure of these high-*L* states is most efficient with the use of special techniques.

The work reported here uses the resonant excitation Stark ionization spectroscopy (RESIS) technique to measure the fine structure of the high-*L* Rydberg state, Fig. 1.3. The RESIS technique allows for the creation of the population in a broad range of high-*L* Rydberg states. The Rydberg states are created by charge exchange. A beam of the ion of interest, $X^{q+}$, intercepts a Rydberg target and captures a highly excited electron to become a beam of Rydberg states, $X^{+(q-1)}$. The capture process forms states of all *L*s. Those high-*L* Rydberg states are then excited upward from one *n* state, $n_{lower}$, to a much higher *n* state, $n_{upper}$ for detection. Since the excitation is upward, all high-*L* states can be detected without being limited by selection rules. The excitation is carried out using a laser and this allows for the fine structure of the high-*L* Rydberg state to be resolved. The central aspects of the RESIS technique are illustrated in Fig. 1.3. The RESIS technique is discussed more fully in Section 1.3 and details of the apparatus used are discussed in Chapter 2.

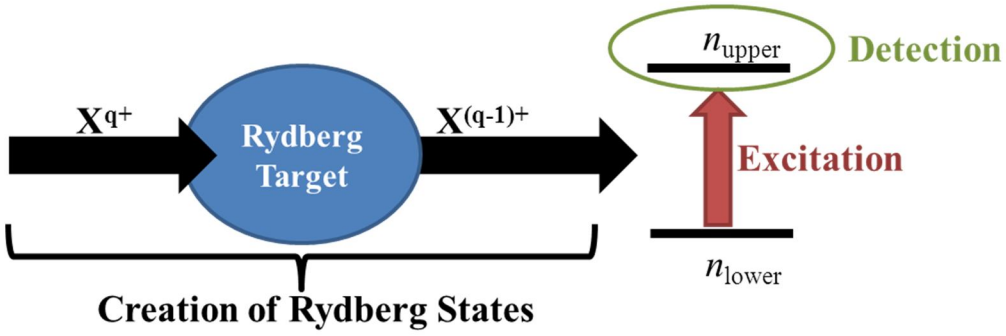


Figure 1.3: Basic Steps of the RESIS technique. The creation of the Rydberg states through charge exchange with a Rydberg target, the Rydberg state is excited between *n* levels using a laser. The upper *n* state is then detected by Stark ionization.

## 1.2 The Effective Potential

The Rydberg states studied consist of two nearly separate systems, a free core ion and a hydrogenic electron. The fine structure for high-$L$ Rydberg states produced by the long-range interaction between the core and the Rydberg electron can be modeled by an effective potential. The work in this dissertation does not derive the effective potential, but an understanding of where the effective potential comes from and the assumptions made in its derivations is necessary to understand how properties are extracted from fine structure measurements. The approach of using an effective potential to describe the long-range interaction between the core and the Rydberg electron was pioneered by Drachman [6] for the Rydberg levels of helium. Recently this approach was generalized by Woods [7], providing the theoretical framework necessary to study and extract properties from the fine structure of ions with higher $J_c$. The approach set forth by these works requires two initial assumptions.

(A1) The Rydberg electron is distinguishable from the electrons contained in the core.

(A2) The Rydberg electron is always further from the nucleus than any of the core electrons.

If these two assumptions hold true then it is possible to use the approach presented in [6, 7] to derive an effective potential to describe the Rydberg state.

The first step in modeling the system is to come up with a Hamiltonian for the system. The first assumption allows for the full Hamiltonian, $H$, for the high-$L$ Rydberg states to be written as the sum of three parts. The first part, $H^0_{core}$ describes core, which is a just a free ion of charge $q$=$Z$-$N$+1. The second part, $H^0_{Ryd}$ describes the distinguishable $N^{th}$ electron which is the hydrogenic Rydberg electron. The third part is the potential, $V$, which describes the interactions between the core and the Rydberg electron.

$$H = H^0_{core} + H^0_{Ryd} + V \tag{1.3}$$

where

$$H^0_{core} = \sum_{i=1}^{N-1}\left[\frac{\left|\vec{p}_i\right|^2}{2} - \frac{Z}{r_i}\right] + \sum_{\substack{i,j=1 \\ j>i}}^{N-1}\frac{1}{\left|\vec{r}_i - \vec{r}_j\right|}\ , \tag{1.4}$$

$$H^0_{Ryd} = \frac{\left|\vec{p}_N\right|^2}{2} - \frac{q}{r_N}\ , \tag{1.5}$$

and

$$V = \sum_{i=1}^{N-1}\frac{1}{\left|\vec{r}_N - \vec{r}_i\right|} - \frac{N-1}{r_N}\ . \tag{1.6}$$

In the Hamiltonian, $N$ is the total number of electrons in the ion, Z is the nuclear charge, and the $q$ is the net charge of the core ion, $q$=Z-($N$-1). Since the Hamiltonian can be broken into parts, due to the first assumption, it is also possible to write the zeroth order wave function for the system as a product of wave functions for the core and Rydberg electron.

$$\left|\Psi^0\right\rangle = \left|\Psi^{[0]}_{core}\right\rangle\left|\Psi^{[0]}_{Ryd}\right\rangle \tag{1.7}$$

The zeroth order wave function for the Rydberg electron is just the wave function of a hydrogenic electron, represented by the quantum numbers $n$, $L$. The zeroth order wave function for the core is much more complicated and is known only abstractly, but it is described by the quantum numbers $\lambda$ and $J_c$, where $J_c$ is the core's total angular momentum and $\lambda$ is any additional quantum numbers necessary to describe the state of the core. When the core is in the ground

electronic state this is denoted as *g*. The notation used to represent the wave functions is seen in Eq. 1.8.

$$\left|\lambda J_c, nL\right\rangle = \left|\lambda J_c\right\rangle \left|nL\right\rangle . \tag{1.8}$$

Using the interaction potential $V$ and perturbation theory, the approach set forth by Drachman [6] and Woods [7] can now be applied to calculate the energy of Rydberg levels. In many cases the deviation from the zeroth energies can be written as an expectation value of an effective potential. This approach requires the use of three expansions.

(1) Static Perturbation Theory

(2) Multipole Expansion

(3) Adiabatic expansion

The first expansion used is static perturbation theory

$$E = E^{[0]} + E^{[1]} + E^{[2]} + \ldots \tag{1.9}$$

where the zeroth order energy is the sum of the energy core ion and the energy of the hydrogenic Rydberg electron,

$$E^{[0]} = E(gJ_c) - \frac{1}{2}\frac{m_{core}}{(m_{core} - m_{electron})}\frac{q^2}{n^2} . \tag{1.10}$$

The first order energy has the form

$$E^{[1]} = \left\langle \Psi^0 \left| V \right| \Psi^0 \right\rangle \tag{1.11}$$

and the second order energy has the form

$$E^{[2]} = \sum_{\Psi'^0 \neq \Psi^0} \frac{\left|\left\langle \Psi^0 \left| V \right| \Psi'^0 \right\rangle\right|^2}{E(\Psi^0) - E(\Psi'^0)} . \tag{1.12}$$

The denominator of the second order energy is the energy difference between the Rydberg state of interest and an intermediate state.

The second expansion used is the multipole expansion, which is just a rewriting of the potential that describes the interaction between the core the Rydberg electron. Using assumption A2, it is the possible to rewrite the potential as a multipole expansion in terms of spherical tensor operators of rank κ, and having the form

$$V = \sum_{\kappa=1}^{\infty} M^{[\kappa]} \frac{C^{[\kappa]}(\hat{r}_N)}{r_N^{\kappa+1}} \tag{1.13}$$

where

$$M^{[\kappa]} = \sum_{i=1}^{N-1} r_i^{\kappa} C^{[\kappa]}(\hat{r}_i) \tag{1.14}$$

.

$C^{[\kappa]}(\hat{r}_i)$ is a spherical tensor of rank κ in the space of electron i, and $\hat{r}_i$ represent the angular position of that electron. The $M^{[\kappa]}$ operator acts only on the wave function of the core. Because of the second assumption, A2, there cannot be any scalar terms, $\kappa$=0, since the Rydberg electron is farther from the core than any of the $N$-1 core electrons. The dipole term is when $\kappa$=1, the quadrupole term is when $\kappa$=2 term, and so on.

The third expansion is the adiabatic expansion and seen here are the first three terms

$$\frac{1}{[\Delta E(\lambda', J_c') + \Delta E_{Ryd}]} = \frac{1}{\Delta E(\lambda', J_c')} + \frac{\Delta E_{Ryd}}{[\Delta E(\lambda', J_c')]^2} + \frac{[\Delta E_{Ryd}]^2}{[\Delta E(\lambda', J_c')]^3} + \ldots \tag{1.15}$$

where $\Delta E(\lambda', J')$ represents the energy difference between the ground state of the core and some excited level

$$\Delta E(\lambda', J_c') = E(\lambda', J_c') - E(g, J_c) \tag{1.16}$$

and $\Delta E_{\mathrm{Ryd}}$ represents the energy difference between two different Rydberg states

$$\Delta E_{Ryd} = E(n') - E(n) \quad . \tag{1.17}$$

The first term of the adiabatic expansions is called the adiabatic term, the second term is the 1st non-adiabatic and third term is the 2nd non-adiabatic. The adiabatic expansion works best when the energy difference between the ground state of the core and some excited state is large. For this reason, the derivation of the effective potential from the second-order perturbation energy explicitly excludes any contributions from intermediate levels where the core is not electronically excited. These are considered separately and their effects are usually found to be small for high-$L$ states. These excluded intermediate states represent other Rydberg levels bound either to the true ground state of the core ion or possibly to an excited fine structure level of the ground electronic state.

The derivation of the effective potential requires the use of all three of these expansions. The contributions to the effective potential from the permanent moments of the core are found as a result of the first order perturbation theory. The first possible permanent moment is the quadrupole moment, when $\kappa$=2. The permanent moments are limited to be only even due to the restriction of parity, so they only occur when $\kappa$ is even. The majority of the effective potential comes as result of the application of the second order perturbation theory to the potential and the denominator of the second order perturbation energy expanded out by the adiabatic expansion. These second order energies result in the polarizabilities seen in the effective potential. Eq. 1.18 shows some of the leading terms of the effective potential, whose expectation value would describe energy of a specific level in the fine structure of a high-$L$ Rydberg state.

$$
\begin{aligned}
V_{eff} = & -\left[\frac{\alpha_{D,0}}{2r^4}+\frac{(\alpha_{Q,0}-6\beta_{D,0})}{2r^6}+\ldots\right] \\
& +\left[\frac{\beta_{D,1}}{r^6}+\ldots\right]\vec{L}\cdot\vec{J}_c \\
& -\left[\frac{Q}{r^3}+\frac{\alpha_{D,2}}{2r^4}+\ldots\right]\times\frac{X^{[2]}(J_c)\cdot C^{[2]}(\hat{r})}{\begin{pmatrix} J_c & 2 & J_c \\ -J_c & 0 & J_c \end{pmatrix}} \\
& +\left[\frac{(\beta_{Q,3}+\beta_{DO,3})}{r^8}+\ldots\right]\times X^{[3]}(J_c)\cdot T^{[3]}(\hat{r}) \\
& -\left[\frac{\Pi}{r^5}+\frac{(\alpha_{Q,,4}+\alpha_{DO,4})}{2r^6}+\ldots\right]\times\frac{X^{[4]}(J_c)\cdot C^{[4]}(\hat{r})}{\begin{pmatrix} J_c & 4 & J_c \\ -J_c & 0 & J_c \end{pmatrix}}+\ldots
\end{aligned}
\tag{1.18}
$$

where

$$
\vec{L}\cdot\vec{J}_c \equiv \frac{1}{2}[K(K+1)-J_c(J_c+1)-L(L+1)] \tag{1.19}
$$

$$
\frac{\left\langle X^{[2]}(J_c)\cdot C^{[2]}(\hat{r})\right\rangle}{\begin{pmatrix} J_c & 2 & J_c \\ -J_c & 0 & J_c \end{pmatrix}} = (-1)^{J_c+K}\begin{Bmatrix} K & L & J_c \\ 2 & J_c & L \end{Bmatrix}\frac{(2L+1)\begin{pmatrix} L & 2 & L \\ 0 & 0 & 0 \end{pmatrix}}{\begin{pmatrix} J_c & 2 & J_c \\ -J_c & 0 & J_c \end{pmatrix}} \tag{1.20}
$$

$$
\begin{aligned}
\left\langle X^{[3]}(J_c)\cdot T^{[3]}(\hat{r})\right\rangle \equiv & (-1)^{J_c+K+L}\begin{Bmatrix} K & L & J_c \\ 3 & J_c & L \end{Bmatrix} \\
& \times\left[-\frac{1}{4}\sqrt{\frac{3}{5}}\sqrt{\frac{(2L-2)2L(2L+1)(2L+2)(2L+4)}{(2L-1)(2L+3)}}\right]
\end{aligned}
\tag{1.21}
$$

and

$$\frac{\left\langle X^{[4]}(J_c)\cdot C^{[4]}(\hat{r})\right\rangle}{\begin{pmatrix} J_c & 4 & J_c \\ -J_c & 0 & J_c \end{pmatrix}} = (-1)^{J_c+K}\begin{Bmatrix} K & L & J_c \\ 4 & J_c & L \end{Bmatrix}\frac{(2L+1)\begin{pmatrix} L & 4 & L \\ 0 & 0 & 0 \end{pmatrix}}{\begin{pmatrix} J_c & 4 & J_c \\ -J_c & 0 & J_c \end{pmatrix}} \tag{1.22}$$

In the effective potential, $r$ is the radial coordinate of the Rydberg electron, the subscript $N$ has been dropped since the positions of the core electrons are not explicitly contained in the effective potential. The interactions in the effective potentials are described by the terms of increasing tensor rank and increasing inverse powers of $r$. $X^{[\kappa]}(J_c)$ is a unit $\kappa^{\text{th}}$ rank tensor in the space of the core and $C^{[\kappa]}(\hat{r})$ is a $\kappa^{\text{th}}$ rank spherical tensor in the space of the Rydberg electron. The specific third rank tensor is used in the Eq. 1.21 is defined by Eq. 1.23.

$$T^{[3]}(\hat{r}) \equiv \left(C^{[2]}(\hat{r})\otimes \vec{L}\right)^{[3]} \tag{1.23}$$

The first term in the effective potential is referred to as the scalar component and the dominant property contained in it is the scalar dipole polarizability, $\alpha_{D,0}$. The second term is referred to as the vector component, the dominant vector property is the 1st non-adiabatic vector dipole polarizability, $\beta_{D,1}$, sometimes called the vector hyperpolarizability [8]. The third term in the effective potential is the 2nd rank tensor component, the dominant properties contained in this term are the permanent quadrupole moment, $Q$, and the tensor dipole polarizability, $\alpha_{D,2}$. The 3rd rank tensor component, the fourth term in $V_{eff}$, is the dominated by 1st non-adiabatic 3rd rank tensor quadrupole polarizability, $\beta_{Q,3}$ and the 1st non-adiabatic 3rd rank tensor dipole- octupole polarizability, $\beta_{DO,3}$. The final term in the effective potential is the fourth rank tensor component, which is dominated by the permanent hexadecapole of the core, $\Pi$. The properties

contained in the effective potential are defined explicitly in terms of matrix elements of the core and the excitation energies, for example $\alpha_{D,0}$ is given by

$$\alpha_{D,0} = \frac{2}{3}\frac{1}{2J_c+1}\sum_{\lambda',J_c'}\frac{\left\langle gJ_c \left\| M^{[1]} \right\| \lambda' J_c' \right\rangle^2}{\Delta E(\lambda', J_c')} \tag{1.24}$$

The complete definition of all the properties in terms of matrix elements and excitation energies is contained in the work of Woods [7].

Just as the effective potential can be broken into components of increasing tensor rank, so can the observed fine structure. The observed fine structure can be fit to the different tensor components. The variation of the tensor components with $L$ can be used to find the permanent moments and polarizabilities. The number of tensor terms in the effective potential and the observed fine structure will depend on the total angular momentum, $J_c$, of the core ion. For example the effective potential for $Th^{3+}$ Rydberg states whose core ion is $Th^{4+}$ will have only a scalar component to the fine structure due to the fact $J_c$=0. As the angular momentum of the core increases additional tensor components in the effective potential contribute to the fine structure, increasing the number of properties that control the fine structure pattern.

**Additional effects**

While the a majority of the Rydberg fine structure pattern is a result of the expectation value of the effective potential,

$$E^{[1]}(V_{eff}) = \left\langle nL_K \left| V_{eff} \right| nL_K \right\rangle \tag{1.25}$$

there also exists additional effects that are not in the effective potential that contribute to the fine structure. The derivation of the effective potential from the second-order perturbation energy excluded intermediate states that are bound to ground electronic states of the core ion. All such

states can be considered "Rydberg states". For example, $Th^{3+}$ has two states in the ground electronic configuration, the $^2F_{5/2}$ is the ground state and the $^2F_{7/2}$ is an excited state, located approximately $4325cm^{-1}$ above the $^2F_{5/2}$ [9]. The contribution to the second order perturbation energy of the Rydberg state of interest, due to these intermediate states, was excluded in the effective potential model. The second order energies due to these states would have the form

$$E_{RS}^{[2]} = \sum_{J_c',n',L'} \frac{\left\langle (gJ_c)nL_K \left| V \right| (gJ_c')n'L_K' \right\rangle \left\langle (gJ_c')n'L_K' \left| V \right| (gJ_c)nL_K \right\rangle}{\Delta E(gJ_c') + E(n') - E(n)} \tag{1.26}$$

where $nL_K$ is the Rydberg state of interest bound to the ground state and $n'L_K'$ is the intermediate Rydberg state bound to one of states in the ground states electronic configuration. Of course, the sum over the intermediate Rydberg states does not include the Rydberg state of interest, $(gJ_c)nL_K$. The coupling potential, $V$, must be even given the fact that the parity is the same for all the states in the ground state electronic configuration. The lowest order even coupling is quadrupole coupling; the $\kappa = 2$ term of Eq. 1.13. Plugging the quadrupole potential, Eq. 1.13, into Eq. 1.26 results in Eq. 1.27

$$\begin{aligned} E_{RS}^{[2]}(QQ) = -\sum_{J_c'n'L'} & \begin{Bmatrix} K & L & J_c \\ 2 & J_c' & L' \end{Bmatrix}^2 \begin{pmatrix} L & 2 & L' \\ 0 & 0 & 0 \end{pmatrix}^2 (2L+1)(2L'+1) \left\langle gJ_c \left\| M^{[2]} \right\| gJ_c' \right\rangle^2 \\ & \times \left( \frac{\left\langle nL \left\| r^{-3} \right\| n'L' \right\rangle^2}{\Delta E(gJ_c') + E(n') - E(n)} \right) \end{aligned} \tag{1.27}$$

where this second order energy has been rewritten in terms of factors, such 6J and 3J symbols, matrix elements that describe the coupling between core states and a sum over intermediate Rydberg states [7]. The sum over the intermediate Rydberg state, $n'$, is completed using the Dalgarno and Lewis technique [10].

One might think because of the small energy denominators, this shift would be large and dominate the energy of the Rydberg state of interest, but in fact the energy shift due to this coupling is small. The small size of the coupling is due in part to the fact that the quadruple coupling, $V_{\kappa=2}$, decreases as $L$ increases and in part due to the selection rules governing the quadrupole coupling. The quadrupole coupling scales like $1/L^3$ thus would decrease as $L$ increases, as long as the Rydberg state of interest and the intermediate Rydberg state are not degenerate in energy. For quadrupole coupling two selection rules exist, the first limits the $L$ of the intermediate Rydberg state, $L' = L, L \pm 2$ and the second limits the core states that can couple, $J_c' = J_c, J_c \pm 1, J_c \pm 2$. The energy shift would be largest when the Rydberg state of interest is nearly degenerate with the intermediate Rydberg state. For the quadruple coupling this would occur when both the Rydberg state of interest and the intermediate Rydberg state are bound to the ground state, and have the same $n$. For $n' = n$, since $L' \neq L$ the intermediate state must be $L' = L \pm 2$. In this case, a special selection rule, valid for hydrogenic radial functions,

$$\left\langle n, L \left\| r^{-3} \right\| n, L \pm 2 \right\rangle = 0$$

makes this coupling exactly zero. Given the decreasing size of the coupling matrix element with $L$ and the zero for the degenerate case, the second order quadrupole energy, $E_{RS}^{[2]}(QQ)$, is a small correction in comparison to the energy calculated from the effective potential for the Rydberg state of interest [7]. This can be seen for example in the study of high-$L$ Rydberg states of nickel, where the energy shift due to the effective potential are on the order of 1 to 10GHz, while the corrections necessary due to Eq. 1.27 are on the order of 10MHz or less [11], and decrease rapidly with $L$.

The quadrupole coupling is the leading even coupling term of the potential, but additional higher order even terms in the potential can also couple the Rydberg state of interest and the intermediate Rydberg states in Eq. 1.26. These shifts to the energy of the Rydberg state of interest would be smaller than quadrupole-quadrupole coupling though since they are proportional to higher inverse powers of *r*. The Rydberg states could possibly also couple via higher order perturbation terms, such as those third or fourth order in *V*. These terms contain multiple intermediate states so these couplings would not be limited to just the even terms of the potential. The work of Drachman with helium [6] and the work of Woods [7] showed that as long as the adiabatic expansion is valid, the contribution from the higher order terms in perturbation can be accounted for by calculating the second order energy using the effective potential, $E^{[2]}(V_{eff})$, instead of the full potential

$$E^{[2]}(V_{eff}) = \sum_{J_c',n',L'} \frac{\left\langle (gJ_c)nL_K \left| V_{eff} \right| (gJ_c')n'L_K' \right\rangle \left\langle (gJ_c')n'L_K' \left| V_{eff} \right| (gJ_c)nL_K \right\rangle}{\Delta E(gJ_c') + E(n') - E(n)} \tag{1.28}$$

where the intermediate states are only "Rydberg states". For example, if just three of the dominant terms of the effective potential were considered, Eq. 1.29

$$V_{eff} = -\frac{\alpha_{D,0}}{2r^4} - \left[\frac{Q}{r^3} + \frac{\alpha_{D,2}}{2r^4}\right] \times \frac{X^{[2]}(J_c) \cdot C^{[2]}(\hat{r})}{\begin{pmatrix} J_c & 2 & J_c \\ -J_c & 0 & J_c \end{pmatrix}} \tag{1.29}$$

the second order energies in term of effective potential would have six terms.

$$\begin{aligned} E^{[2]}(V_{eff}) = {} & E_{Veff}^{[2]}(QQ) + E_{Veff}^{[2]}(Q\alpha_{D,0}) + E_{Veff}^{[2]}(Q\alpha_{D,2}) \\ & + E_{Veff}^{[2]}(\alpha_{D,0}\alpha_{D,0}) + E_{Veff}^{[2]}(\alpha_{D,2}\alpha_{D,0}) + E_{Veff}^{[2]}(\alpha_{D,2}\alpha_{D,2}) \end{aligned} \tag{1.30}$$

The first term, $E_{Veff}^{[2]}(QQ)$, is exactly the same result found using Eq. 1.27 to calculate the quadrupole coupling with the intermediate states. The second and third terms proportional to αQ

term, $E_{Veff}^{[2]}(Q\alpha_{D,0})$ and $E_{Veff}^{[2]}(Q\alpha_{D,2})$, would be the result of the quadruple-dipole-dipole coupling in the third order perturbation energy using the full potential. This term is shown below, where $D$ and $Q$ denote $M^{[1]}$ and $M^{[2]}$, the dipole and quadrupole moment operators I n the space of the core ion.

$$E_{QDD}^{[3]} = \sum_{\substack{n',n'',L',L'' \\ J_c',J_c''}} \frac{\langle (gJ_c)nL_K | Q | (gJ_c')n'L_K' \rangle}{\left[\Delta E(gJ_c') - E(n) + E(n')\right]} \underbrace{\frac{\langle (gJ_c')n'L_K' | D | (\lambda'' J_c'')n''L_K'' \rangle \langle (\lambda'' J_c'')n''L_K'' | D | (gJ_c)nL_K \rangle}{\left[\Delta E(\lambda'' J_c'') - E(n) + E(n'')\right]}}_{\alpha} \tag{1.31}$$

Careful inspection of this formula shows that part of Eq. 1.31 looks very similar to the definitions of either the scalar dipole polarizability or the tensor dipole polarizability. In fact, if the adiabatic approximation is applied to the bracketed energy denominator in Eq. 1.31, it reduces exactly to the $Q\alpha$ term in Eq. 1.30. The final terms of the Eq. 1.30 are proportional to αα and are the result of a dipole-dipole-dipole-dipole coupling in the fourth order perturbation energy. Thus by calculating the second order energies using the effective potential instead of the full potential, it is possible to account approximately for the contribution from the couplings with intermediate Rydberg states in the second, third and fourth order perturbation energies.

Additional corrections that need to be considered when modeling or interpreting Rydberg fine structure are the relativistic effect and magnetic interactions between the core and the Rydberg electron of the Rydberg states. The relativistic effect is due to the "$p^4$" contribution to the kinetic energy of the Rydberg electron. The relativistic correction is given by Eq. 1.32 where $\alpha_{FS}$ is the fine structure constant.

$$E_{\mathrm{Rel}}(n,L) = \frac{\alpha_{FS}^2 q^4}{2n^4}\left(\frac{3}{4} - \frac{n}{L+\frac{1}{2}}\right) \tag{1.32}$$

For each state measured in the Rydberg fine structure, the relativistic correction is calculated and applied to the measurements as a correction. The next class of the effects that contribute to the fine structure energies is due to the magnetic interactions between the magnetic moments of the core and the Rydberg electron. The first possible magnetic interaction is due to a possible magnetic dipole moment in the core and given by

$$E_{M1} = \left\langle -\frac{g_J \alpha_{FS}^2}{2r^3} \vec{L} \cdot \vec{J}_c \right\rangle \tag{1.33}$$

where the $g_J$ is the core's Landé $g$ factor. The $E_{M1}$ can only occur when $J_c$>0, and it will contribute to the vector component of the fine structure pattern. The second possible magnetic interaction is due to the magnetic octupole moment of the core; this effect would have the form

$$E_{M3} = \left\langle \frac{C_{M3}}{r^5} (X^{[3]}(J_c) \cdot T^{[3]}(\hat{r})) \right\rangle . \tag{1.34}$$

This magnetic octupole interaction would only occur if $J_c$>1 and it would be observed in the 3rd rank tensor component of the fine structure pattern. The fine structure observed will then be given by

$$E_{obs} = E^{[1]}(V_{eff}) + E^{[2]}(V_{eff}) + E_{\mathrm{Rel}} + E_{M1} + E_{M3} \tag{1.35}$$

For the work reported in this dissertation, the contribution of the spin of the Rydberg electron to the energy of the fine structure is neglected, since its effect was not observed. A complete discussion of the interaction involving the Rydberg spin and its contribution to the fine structure is discussed in the work of Woods [7].

### 1.3 The RESIS Technique

The fine structure produced by the interaction between the core ion and the Rydberg electron can be measured using the RESIS technique. The RESIS technique is very versatile

since it can be used on any positive ion without major changes to the experimental setup. The technique uses charge exchange to populate all $L$ states, so there is no limitation on what $L$s can be measured. The basic approach of the technique is to produce a beam of the ions of interest with a velocity ~0.001c. That beam then charge captures a highly excited Rydberg electron to become a beam of Rydberg states. Then transitions are excited from one discrete $n$ level to a much higher $n$ level. That higher $n$ level is then Stark ionized and detected. The advantage of this technique is since the excitation is upward, there are no selection rules that limit the high-$L$s that can be observed.

The resolution of the fine structure would only be possible if one could scan through a frequency range for a given transition between $n$ levels continuously. The $CO_2$ laser is a convenient choice of laser to use to resolve the fine structure. It offers a large selection of high power single frequency laser lines around 10μm. The $CO_2$ laser used in this experiment has approximately 65 laser lines, between ~924cm$^{-1}$ and ~1085cm$^{-1}$. Fig. 1.4 illustrates the available frequencies.

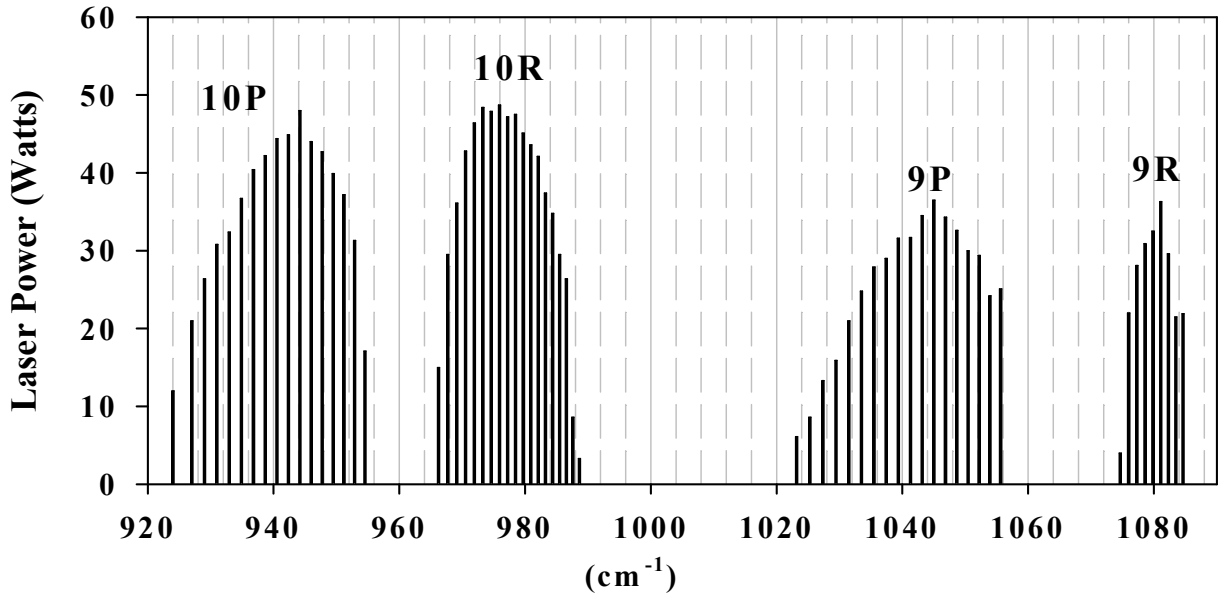


Figure 1.4: $CO_2$ laser lines available on the Coherent GemSelect50 $CO_2$ laser . The y-axis gives the measured power, and the x-axis gives the wavenumber of the laser line in $cm^{-1}$.

The $CO_2$ laser line used to excite transitions between $n$ levels is chosen to have a frequency similar to the difference in the hydrogenic energy of the two $n$ levels. The difference in hydrogenic energies in wavenumber is given by

$$E_{Hyd} = R_{mass} q^2 \left[ \frac{1}{n_{lower}^2} - \frac{1}{n_{upperr}^2} \right] \tag{1.36}$$

where $q$ is the charge and $R_{mass}$ is the mass corrected Rydberg and given by

$$R_{mass} = \frac{R_\infty}{1 + \frac{M_{electron}}{M_{Ion}}} \tag{1.37}$$

with $R_\infty$=109737.3157$cm^{-1}$. Some examples of thorium transition frequencies and the laser line that would be selected to observe a given transition can be seen in Table 1.1.

Table 1.1: Examples of thorium transitions observed with the RESIS technique. Column one gives the charge, column two gives the transition, and column three gives the hydrogenic energy of the transitions. The fourth column gives the laser line used to observe the transition. The final column gives the range that the laser line can be Doppler tuned.

| q | $n_{lower}$ to $n_{upper}$ | $E_{Hyd}$ ($cm^{-1}$) | Laser Frequency ($cm^{-1}$) | Tuning Range ($cm^{-1}$) |
|---|---|---|---|---|
| 3 | 28 to 66 | 1033.0072 | 9P(34) = 1033.4880 | 1032.5930 to 1034.3830 |
| 4 | 37 to 73 | 953.0579 | 10P(10) = 952.8809 | 952.0557 to 953.7061 |

The frequency seen by the ion beam is then tuned finely by Doppler tuning. Doppler tuning is done by altering the angle of intersection between the $CO_2$ laser and the ion beam, thus changing the frequency of the $CO_2$ laser the ion beam sees. Table 1.1 shows the frequency range a laser line can be tuned assuming a beam speed of $0.001c$. This allows for a large frequency range to be available to be used for laser excitation of the Rydberg states from one $n$ level to another. The fine tuning of the $CO_2$ laser frequency by Doppler tuning allows for the full frequency range of the fine structure pattern to be scanned in steps of approximately 50MHz steps. The result is an optical RESIS excitation spectrum; an example of this is seen in Fig. 1.5 for $Th^{3+}$ Rydberg levels. The optical spectrum allows for the resolution of some of the levels, $L$=8 to $L$=11. The fine structure levels for $L$>11 are not resolved in the optical excitation, these unresolved levels around hydrogenic are referred to as the high-$L$ peak.

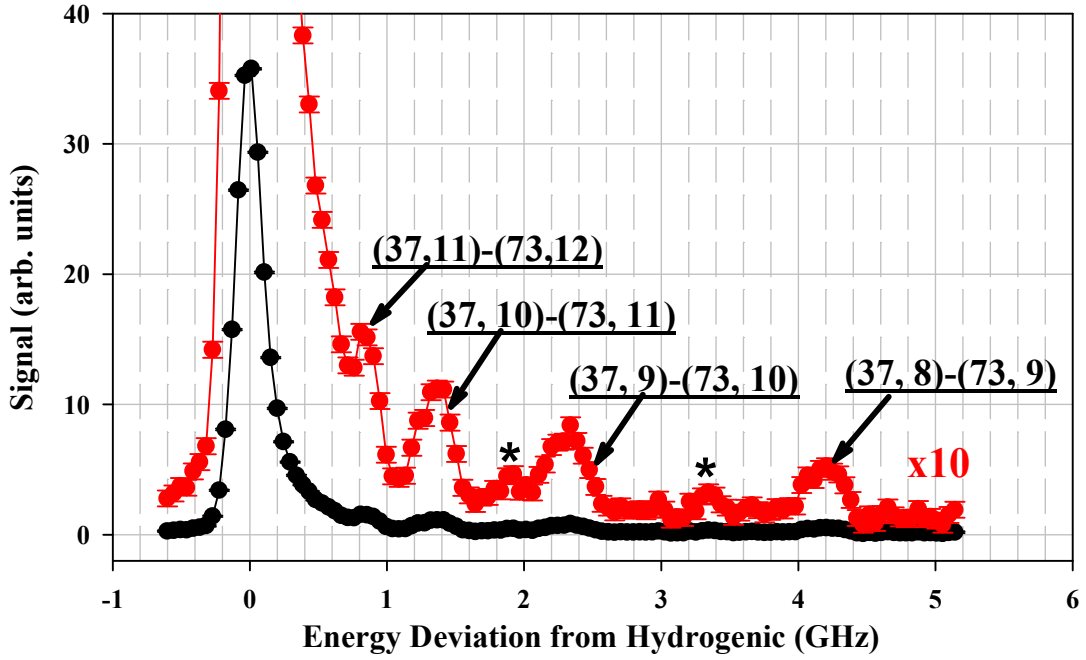


Figure 1.5: A RESIS optical spectrum of $Th^{3+}$ Rydberg levels $n$=37 to 73 . This fine structure is determined primarily by the $\alpha_{D,0}$ of $Th^{4+}$. The x-axis is the difference of the Doppler tuned laser frequency from hydrogenic transition frequency. The signal marked with asterisks represent weaker $\Delta L$=-1 transitions.

The RESIS technique is powerful because it allows observation of high-$L$ states, but this technique can be improved. Improvements to the precision of the RESIS measurements can be made by using the RESIS technique as a detector of rf transitions. The rf RESIS technique detects direct rf transitions between levels in the same $n$ with approximately two orders of magnitude improvement in the precision compared to the RESIS excitation spectrum. This rf RESIS technique also offers the opportunity to resolve levels with higher $L$ than possible with the optical RESIS technique. Illustrated in Fig. 1.6 is rf resonance for $n$=37 $L$=11 to $L$=12 in $Th^{3+}$ Rydberg levels. The energy difference between the $L$=11 and $L$=12 can be measured to sub-MHz precision. The rf RESIS technique also enabled the resolution of the $L$=12 position, not resolved in the optical excitation spectrum of Fig. 1.5.

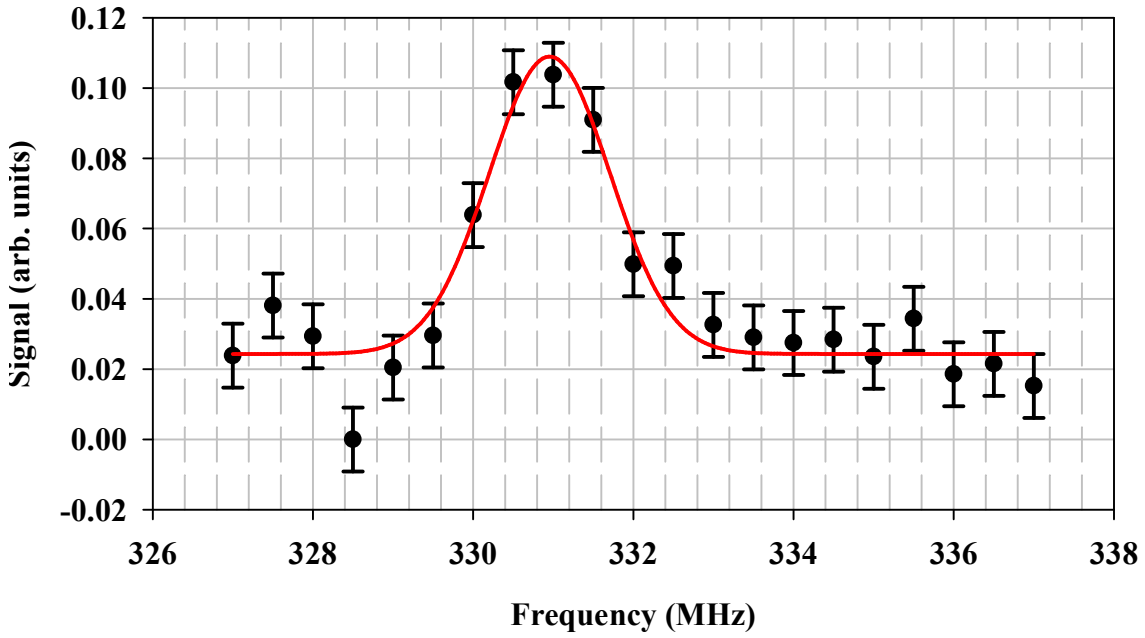


Figure 1.6: The $L$=11 to 12 transition in the $n$=37 $Th^{3+}$ Rydberg fine structure.

### 1.4 Motivation and Context

The two thorium ions studied in this work are the Rn-like $Th^{4+}$ and the Fr-like $Th^{3+}$. $Th^{4+}$ is the most common oxidation state of thorium in actinide chemistry [12], yet no spectroscopy data exists on it and no properties have ever been measured. The measurements of the properties of $Th^{4+}$ using the RESIS technique could provide a check on the theoretical models, and the properties themselves might be used to help predict the interaction of the $Th^{4+}$ ion with other ions. The ground state of $Th^{4+}$ is a $^1S_0$ , so the $Th^{3+}$ Rydberg fine structure would have one level for each $L$. For this reason the study of $Th^{4+}$ is a relatively simple project. By contrast, the study of $Th^{3+}$ is much more challenging. The francium-like ion, $Th^{3+}$ does not have the $^2S_{1/2}$ ground state as one would expect. Its ground state is actually a $^2F_{5/2}$. The ground state of the $Th^{3+}$ would make the $Th^{2+}$ Rydberg fine structure have six levels for each $L$, making the measurement of the fine structure one of the most complex measurements completed using the RESIS technique.

Unlike $Th^{4+}$, 24 energy levels of $Th^{3+}$ have been measured with optical spectroscopy [13], but no polarizabilities or permanent moment have been reported. While $Th^{3+}$ is not as common in actinide chemistry, it is present at times [14]. The $Th^{3+}$ ion has also been proposed to be used in a nuclear clock [15], so any information on the ion could prove to be important to that project. The theoretical models of ions such as $Th^{3+}$ are highly developed, since $Th^{3+}$ has a single valance electron outside a closed shell. Given the nuclear charge of the $Th^{3+}$, the measured properties would provide a test of these models for a highly relativistic single valence electron ion. Similar measurements of Rn-like $U^{6+}$ and Fr-like $U^{5+}$ would also be very valuable, but are not reported in this dissertation.

To give this work some context, one must understand that the study of the thorium ions was the culmination of years of work. This work started in 2005 when the first proposal to the Department of Energy (DOE) to study U and Th ions using the RESIS technique was made. As mentioned previously, the experiments with the actinides would be difficult due to the high charge of the ions being studied and the high angular momentum of the francium-like ions. Work towards the goal of these measurements took place on two fronts and with two apparatuses. The CSU beam line was used to study singly charged ions with high angular momentum, and the second beam line located at J. R. Macdonald Lab (JRML) at Kansas State University was used to study multiple charged ions. At the time of the first proposal a major improvement was needed to the JRML apparatus, a new ion source capable of producing ion beams of multiple charged uranium and thorium. The existing ion source at KSU could only produce beams from gases. Before the DOE would fund the new ion source, they wanted a proof of concept that the fine structure of a multiple charged ion could be measured. This proof was

provided in 2007 with the measurement of the fine structure of Rydberg levels of $Kr^{5+}$ using the old ion source, from which the properties of $Kr^{6+}$ were extracted and published [16].

With this proof the DOE then funded the purchase a new ion source which was delivered in January 2008 to JRML. For the next year the lab underwent remodeling and the new ion source was installed and the rest of the RESIS apparatus was reassembled. The previous graduate student, Mark Hanni, oversaw the assembling of the apparatus and the installation of the new ion source during his dissertation work [17]. The new ion source was turned on for the first time in January 2009. The ion source and the rest of the apparatus was then tested by measuring the fine structure of Rydberg levels of $Pb^{+}$ and $Pb^{3+}$ enabling the properties of $Pb^{2+}$ and $Pb^{4+}$ to be found and published in the spring of 2010 [18]. The work at KSU then turned to attempts to study Rn-like $U^{6+}$. Unfortunately, that work was not successful, and the reasons for its failure are still under study.

At the same time as the work at JRML, the work on the CSU beam line was pursuing the understanding of the high angular momentum Rydberg states with $J_c>1$. In December of 2008 a rf study of Rydberg states argon was completed and properties of $Ar^{+}$ were published [19]. This was training on the RESIS technique for both Mark Hanni and myself. The rf study of argon led to an increased understanding of the properties controlling the fine structure pattern of an ion with $J_c>1$, since the ground state of $Ar^{+}$ has $J_c=3/2$. Attention then turned to completing a study of Rydberg levels of Ni, providing a measurement of the properties of $Ni^{+}$ whose ground state has $J_c=5/2$. The nickel study represented the first time an ion with angular momentum of 5/2 was studied using the optical RESIS technique [20], the knowledge gained in the study would prove invaluable in the study of the Fr-like thorium.

Then on March 12, 2010, the first $Th^{4+}$ beam was produced at JRML using the new ion source, and work to find the properties of $Th^{4+}$ began using the RESIS technique. Despite the apparent similarity between the two Rn-like ions, $U^{6+}$ and $Th^{4+}$, this work was immediately successful. Preliminary properties of $Th^{4+}$ were published in August 2010 [21], less than six months after the first thorium beam was produced. The work then turned to finding the properties of $Th^{3+}$ from the measured $Th^{2+}$ Rydberg fine structure. The measurement of this fine structure did not take long, but the analysis of the fine structure pattern and the extraction of the properties proved challenging. Preliminary properties of $Th^{3+}$ were extracted from the data and published in June 2011 [3], this work is discussed in Chapter 5 of this dissertation.

The work reported in this dissertation is the culmination of years of work with high charge and high angular momentum Rydberg states, and it expands on the preliminary work done with $Th^{4+}$ and $Th^{3+}$ using the optical RESIS technique. In this work, the rf RESIS technique was used to measure their respective Rydberg fine structures with a higher precision and resolving more levels than reported in the preliminary studies. This increased precision and resolution allows for an increase in precision of the properties of the thorium ions, providing a much more rigorous test of the atomic theory used in their prediction. This chapter provided background on Rydberg states, the theoretical model, and a brief overview of the experimental approach. Chapter 2 will discuss the experimental apparatus used in both the optical RESIS studies and rf RESIS studies. The third chapter will present the results of the rf study of $n$=37 $Th^{3+}$ Rydberg fine structure and the $Th^{4+}$ properties extracted. Chapter 4 will discuss the results of the optical study of $Th^{2+}$ Rydberg fine structures and the properties of $Th^{3+}$ found. The fifth chapter will present the rf measurement made of $n$=28 $Th^{2+}$ Rydberg fine structure. Chapter 6 will then present the analysis of the rf measurements of the $n$=28 $Th^{2+}$ Rydberg fine structure.

## Chapter 2: Experimental Apparatus

The Resonant Excitation Stark Ionization (RESIS) technique offers the resolution and precision necessary to measure high-$L$ Rydberg fine structures for the purpose of extracting core ion properties. The experimental measurements reported in this work were completed on the RESIS apparatus located at J. R. MacDonald lab at Kansas State University, a DOE funded facility. This lab has played host to the experimental endeavors of this research program since the mid-1990s. Initially, the existing ECR ion source in Kansas was unable to produce ion beams from solids, but funding from the DOE allowed for the ion source to be replaced. The new electron cyclotron resonance source, ECR, is capable of producing beams from solids, thus enabling the study of the actinide ions. The specific beam line used in this work was assembled during the dissertation work of Mark Hanni, the previous graduate student heading up the work on the KSU apparatus. Mark Hanni's dissertation has detailed descriptions and pictures of all the components of the beam line used in the RESIS technique [17]. The work reported here required only slight modifications of that apparatus. The modification of the apparatus will be discussed in detail, but the remaining beam line will only be discussed in general, since this work did not deal with the design or assembly of the components that make up a majority the beam line.

The schematic of the RESIS apparatus is shown in Fig. 2.1; in the schematic the three key steps involved in the RESIS technique are identified and labeled. The first being the creation of the Rydberg states of interest; this is done through the use of the ion source and charge capture from the Rb Rydberg target. The second step involves the excitation of the Rydberg states population from one discreet $n$ state to a much higher $n$ state. This excitation is done with a $CO_2$ laser in the laser interaction region (LIR). The final step of the RESIS technique is the detection of the excited Rydberg states population through Stark ionization. The RESIS technique may

only involve three overall steps, but the experimental implementation of the RESIS technique is a bit more involved as can be seen by Fig. 2.1. Each of the three key states involves multiple experimental steps. Two forms of the RESIS technique also exist, the basic RESIS technique relies only on the $CO_2$ laser to excite transitions between different $n$ states, and this is called the optical RESIS technique, which is shown in Fig 2.1. The optical RESIS technique can be improved upon by using that technique as a way to detect rf transitions between levels of the same $n$. This improved technique is referred to as the rf RESIS technique. The two techniques differ only very slightly in their experimental set-up, therefore the experimental set-up for the optical RESIS technique will be discussed first, and then the additional steps needed for the rf RESIS technique will be discussed.

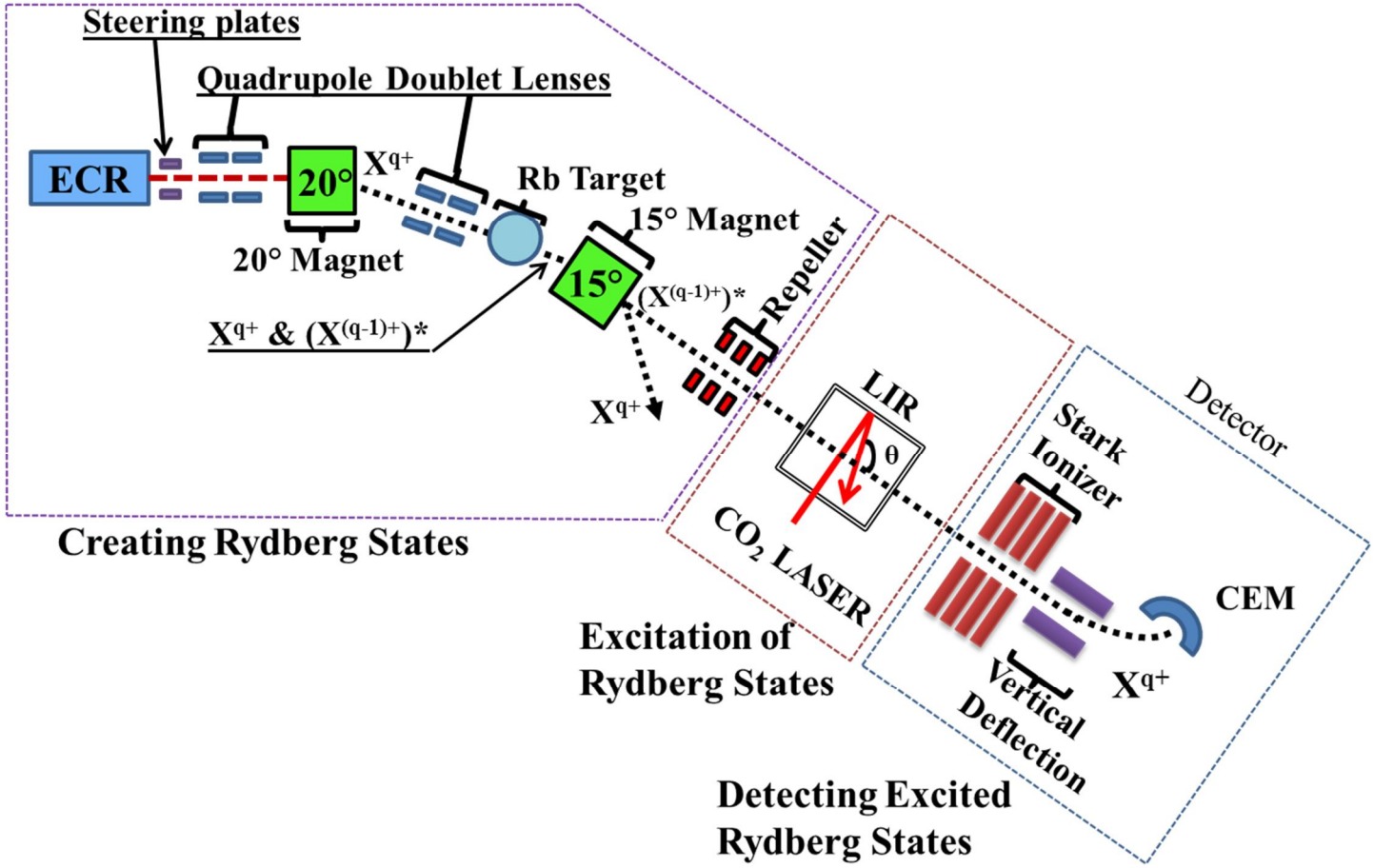


Figure 2.1: Schematic of the optical RESIS apparatus. The beam line is broken into three major areas. The first part creates the Rydberg states, the second part excites the Rydberg states, and the third part detects the excited Rydberg states.

## 2.1 The optical RESIS technique

The RESIS technique is a versatile technique since it can measure the Rydberg fine structure for any positive ion that can be produced from an ion source. The Kansas beam line was designed to study multiply charged ions, with charge greater than one. The major improvement to the Kansas beam line was the addition of the new ECR ion source. The ECR is made up of a plasma chamber surrounded by strong permanent magnets. Into that plasma chamber a seed gas and microwaves are sent, the seed gas in the case of the work reported here was xenon. The frequency of the microwaves sent into the plasma chamber is 14GHz, which matches the cyclotron frequency of the electrons confined by the magnetic field produced by the strong permanent magnets surrounding the plasma chamber. The microwaves heat up the electrons in the plasma chamber. The electrons then ionize the seed gas and produce a plasma of positive ions. Figure 2.2 shows an exterior picture of the ECR with seed gas and microwaves feed indicated, pictures of the interior of the ECR ion source are in Mark Hanni's dissertation.

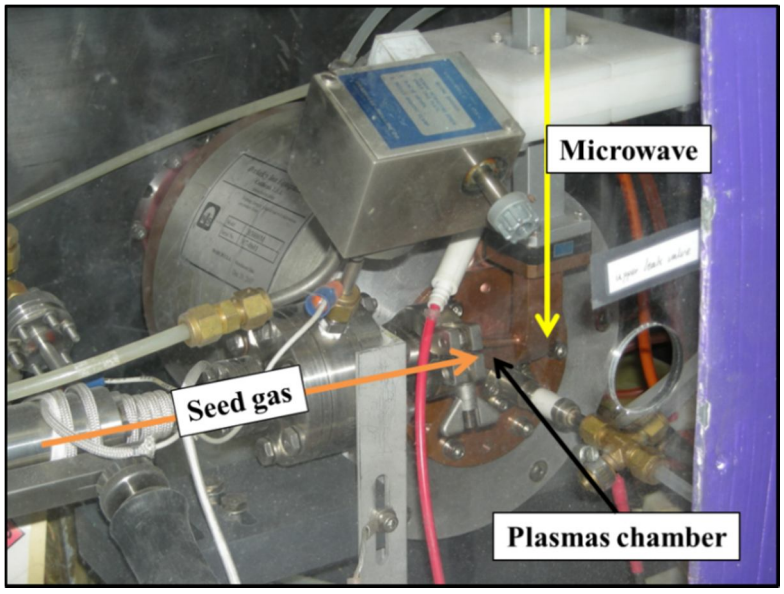


Figure 2.2: Picture of the ECR ion source during operations. The orange arrow indicates the seed gas feed and the yellow arrow indicates the microwave feed for the ECR. The entire ECR is contained behind plastic since entire ion source is held at high voltage.

The back of the plasma chamber is made of up of the sputter cathode. The sputter cathode has a piece of the material of interest bolted to; in the case studied here that material is thorium. A negative potential is placed on the thorium, and the thus the positive ions contained in the plasma are attracted. The positive ions in the plasma bombard the thorium and sputter ions of thorium into the plasmas. Figure 2.3 shows pictures of the sputter cathode with thorium bolted to it, before and after use in the ECR.

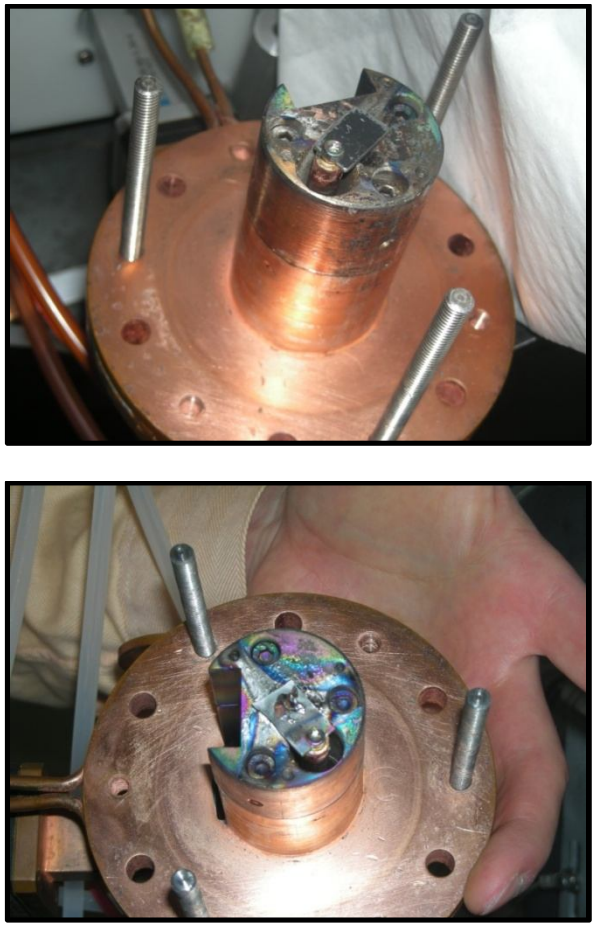

Figure 2.3: Pictures of the sputter cathode. The top picture shows the installation of a fresh piece of thorium on the sputter cathode, the bottom picture shows what the thorium looks like after use in the ECR.

The plasma in the ECR then contains thorium ions and ions from the seed gas xenon. The entire ECR ion source is held at high potential by the acceleration power supply. In this case that potential was approximately 25kV, therefore the ions produced in the plasma of the ECR are then accelerated down the beam line since the rest of the beam line is ground. The ions leaving the ion source are not distinguished by their mass or charge. There is just one beam that contains all the ions.

As the beam exits the ion source, it passes through some vertical and horizontal steering plates that allow fine tuning of the trajectory of the ion beam. The beam is also focused by the first quadrupole doublet lens. But neither of these components is capable of the resolving the beam in terms of the mass or charge, but the resolution of the beam is required in order to select the ion interest. The separation of the beam is accomplished by sending the beam into a 20° bending magnet with a 2mm aperture approximately~1m from its output. The combination of those two things allows for the separation of the different ions in the beam. While all of the ions exciting the ion source have been excited by the same potential, $V_{\text{terminal}}$, not all of the ions have the same velocity, $v$. The velocity of each ion, Eq. 2.1, is dependent on its mass, $M_{Ion}$ and charge, $q$.

$$v = \sqrt{\frac{2qV_{\text{terminal}}}{M_{Ion}}} \tag{2.1}$$

In the most of the work presented, the velocity of the beam is written as $\beta$, which is just the ratio of the beam speed to the speed of light, Eq. 2.2.

$$\beta = \frac{v}{c} \tag{2.2}$$

As the ions in the beam pass through the 20° bending magnet they encounter a force that is equal to charge times the velocity of the beam times the magnetic field in the 20° bending magnet.

$$F = qvB \tag{2.3}$$

This force alters the trajectory of the different ions in the beam. The different ions exciting the 20° bending magnet will be deflected differently. The amount of the angular deflection is proportional to the magnetic field in the 20° bending magnet times the square root of the ratio of the charge to the mass of the ion, Eq. 2.4

$$\Delta\theta \sim \frac{B \cdot l}{\sqrt{2V_{\text{terminal}}}} \sqrt{\frac{q}{M_{Ion}}} \tag{2.4}$$

where $l$ is the length of the magnet in meters, $B$ is the magnetic field in Tesla, $V_{\text{terminal}}$ is in volts, $q$ is in Coulombs and $M_{Ion}$ is in kilograms.

This angular deflection along with the small aperture about 1m from the exit of the 20° bending magnet allows for the separation of the singular beam leaving the ion source into beams for each ion since the small aperture limits the angular acceptance of the beam line. Therefore, by scanning through the range of magnetic field for 20° bending magnet, a spectrum of all the beams coming out of the ECR can be recorded, one such scan in shown in Fig 2.4.

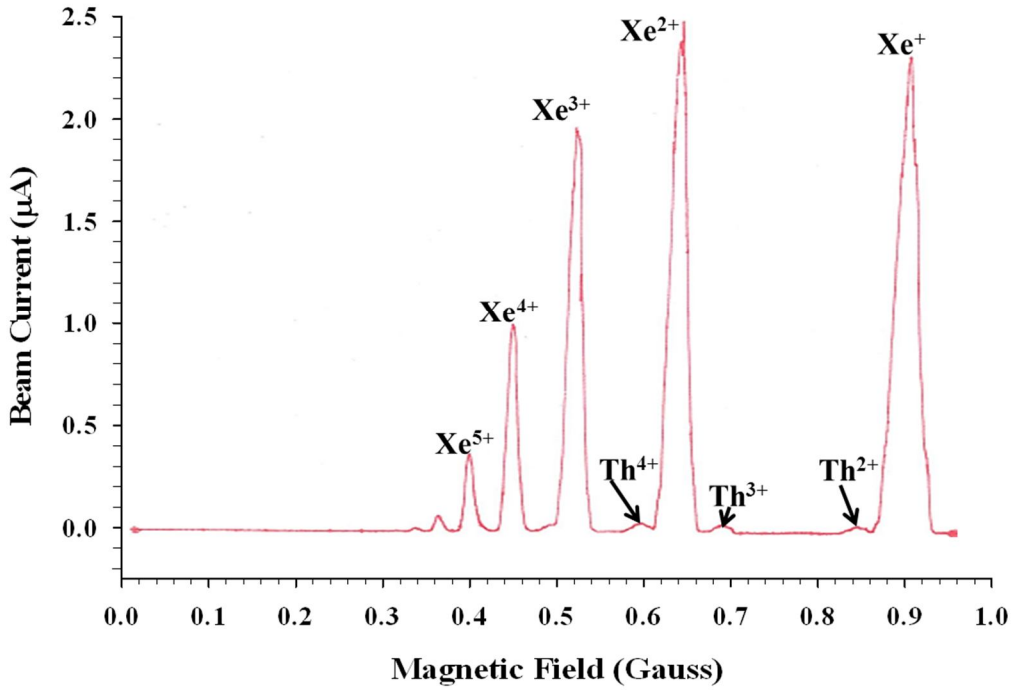


Figure 2.4: Scan of the beams coming from the ECR, on the x-axis is the magnetic field in Gauss, read from a probe inserted into the 20° bending magnet. On the y-axis is the beam current, read just after the 20° bending magnet, in micro-amps. Some of the peaks have been labeled with their identifications.

The x-axis of Fig. 2.4 is the magnetic field in Gauss, as read from a Hall probe inserted into the 20° bending magnet. The y-axis is the beam current, being read just after the aperture placed 1m from the exit of 20° bending magnet. As can be seen from Fig. 2.4, the 20° bending magnet and the aperture are capable of separating the different ions leaving the ECR into beams. The large beams are the xenon beams, produced from the seed gas being fed into the ECR; these beams are on the order of 1 to 3μA. The smaller beams are the thorium beams, these beams are less than 100nA.

After the 20° bending magnet, the beam of interest produced by the ECR, referred to as $X^{q+}$ in Fig. 2.1, has been selected. The beam is sent through the second doublet quadrupole lens to help focus it, this is just before the aperture that assists in the separating of the beams. At this

time the beam is not made up of Rydberg states necessary for the RESIS technique. The production of the Rydberg state is done through charge exchange; the beam of $X^{q+}$ intersects a Rb Rydberg target. The Rb Rydberg target is a cloud of highly excited Rb atoms. When the beam intersects this target a small fraction of the ions in the beam will capture a highly excited Rydberg electron, thus producing Rydberg states bound to the ion of interest. For the work here only a very basic understanding of the details of the Rb Rydberg target is necessary. The experimental development and previous work with the target is well documented [22, 23]. The Rb target is produced by intersecting a thermal beam of Rb with three CW lasers. The intersection of the three lasers with the beam excites the Rb atoms from the ground state to the 10*F* state, Fig. 2.5. The first two excitations from the ground state and to the *D* state are completed using two diode lasers, their respective frequency are given in the Figure 2.5. The first two lasers are combined and propagated together through a Rb vapor cell and then into Rb Rydberg target region. The fluorescence from the Rb vapor cell is used to lock the first two lasers to their resonance frequencies. The third excitation from the *D* state to the *F* state is completed with a Ti:Sapphire laser, tuned to the frequency given in Fig. 2.5, this laser is transported to the target region via an optical fiber. The third laser is set to intersect the Rb plume in the same place as the first two lasers. When the Ti:Sapphire is on resonance and all three lasers are aligned with the Rb beam, the Rb Rydberg target will be produced. When this occurs the Rb Rydberg target emits blue fluorescence. This florescence can be seen in Fig. 2.6. The blue florescence is due to a mirrorless maser transition between the 10*F* state and the 11*D* state [24]. A complete discussion of the construction of the target region and the optical set-up used to produce the target is completed in Mark Hanni's dissertation [17].

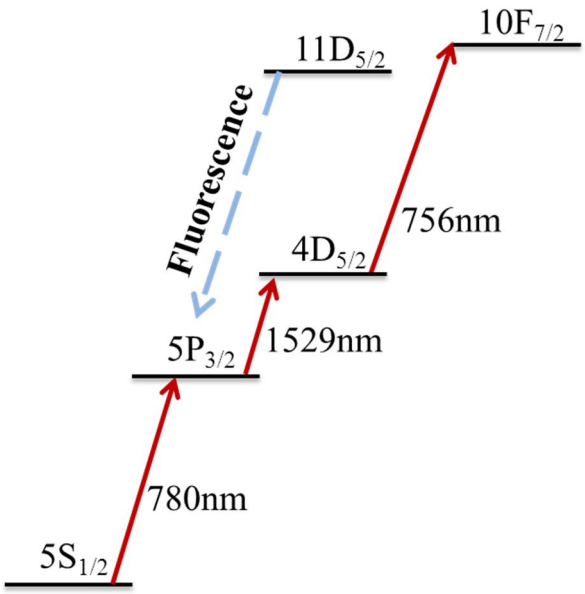


Figure 2.5: Excitation scheme for producing the Rb Rydberg target. Three CW lasers are used to excite the Rb to the 10F state. The wavelength for each of the lasers is given.

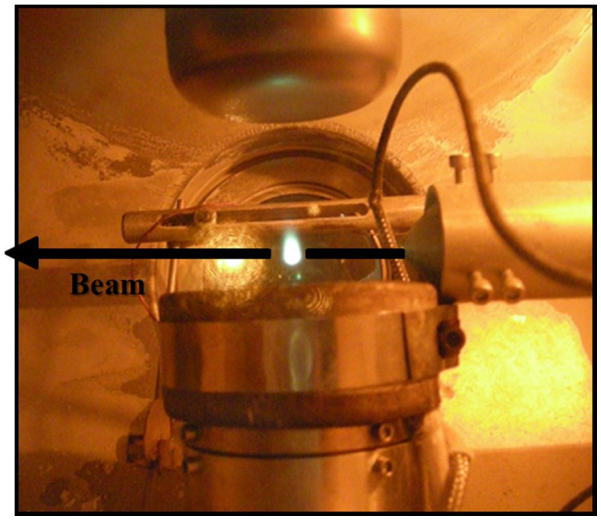


Figure 2.6: Picture of the blue florescence from the Rb Rydberg target. The trajectory of the beam of interest is placed through the Rb Rydberg target.

As the ion beam intersects the Rb Rydberg target as shown in Fig. 2.6, a few percent of the beam captures a highly excited Rydberg electron. The remaining beam does not capture, so two beams exist after the target. The original beam of interest, $X^{q+}$, referred to as primary beam and the Rydberg beam for the beam of interest, $(X^{(q-1)+})^*$, referred to as the charge transfer

beam. The primary beam that did not capture is no longer needed and its presence could result in additional background, so it is prevented from entering the remaining experimental apparatus. To accomplish this, both beams the pass through a 15° bending magnet. The beam of Rydberg states is selected and the remaining beam that did not capture is deflected from going down the rest of the beam line. The beam of Rydberg states is then prepared before undergoing the RESIS excitation between *n* states, by emptying out the population of the higher *n* states. This is done by passing the beam of Rydberg states through the repeller region of the beam line, which is made up of two Einzel lenses assemblies. The first Einzel lens is referred to as the pre-ionizer. Its purpose is to remove higher *n* states from the Rydberg beam. The potential of the pre-ionizer depends on what RESIS transition is being observed, for example Fig. 1.5 shows the RESIS optical spectrum for $Th^{3+}$ Rydberg states for the *n*=37 to 73 transition, in that case the repeller was set high enough to ionize and remove the population of the upper *n*, *n*=73, but not high enough to affect the population of the *n*=37 level. The field necessary to ionize the lowest Stark state of an *n* state is given by Eq. 2.5

$$F_{\min} = \frac{q^3}{9n^4}(5.14x10^9)V/cm \tag{2.5}$$

and the field necessary to ionize the highest stark state connected to an *n* is given approximately by Eq. 2.6

$$F_{\max} = \frac{2q^3}{9n^4}(5.14x10^9)V/cm \tag{2.6}$$

In practice it was determined that it is best to the set the pre-ionizer to double the field necessary to ionize the highest stark state connected to a *n* state [23]. For the case of the example, *n*=73, the field required in the pre-ionizer would be approximately 5.2kV/cm, the effective distance of the pre-ionizer is 2.4cm, thus the power supply for the pre-ionizer needs to be set to at least

12.5kV to remove the higher *n* Rydberg states of concern from the Rydberg beam. With the removal of the higher *n* states involved in the RESIS excitation from the Rydberg beam, it would be expected the detection of the RESIS excitation would be background free.

The second Einzel lens in the repeller region is referred to as the remixer; its purpose is to repopulate the lower-*L* states population by mixing the populations all the *L* states together. The lower-*L* states populations are more likely to decay between their creation in the target and their excitation by the $CO_2$ laser since their lifetimes are shorter. Therefore the remixer is used to mix the populations just before the RESIS excitation, increasing the likelihood of observing the lower-*L* states in the RESIS excitation spectrum. The second Einzel lens also helps to focus the beam through the apparatus. In the experiments reported in this work, the primary use of the remixer was to focus the ion beam, not to repopulate lower-*L* Rydberg states. The decay of the low-*L* states was not a problem in the studies in this work. A complete discussion of the use of the remixer and its design is discussed in the work of Mark Hanni [17], in that work the enhancement the remixer has on lower-*L* states population is explored.

With the completion of the creation and preparation of the Rydberg beam of interest the beam enters the second the part of the RESIS apparatus, the part responsible for the excitation of the Rydberg states from one *n* level to a much higher *n* level. Since the RESIS excitation is upward, all *L* states in the lower *n* level can be detected without facing the limitations of selection rules that other techniques face. This excitation is accomplished with the use of a Doppler tuned $CO_2$ laser in the laser interaction region (LIR). The $CO_2$ laser is a versatile choice of laser for the RESIS excitation, since it has a wide variety of the laser lines as is illustrated in Fig. 1.4. A particular $CO_2$ line is chosen that is near the transition frequency of one of the transitions, as defined in Eq. 1.36. Table 1.1 shows two examples. By Doppler tuning it is

possible to cover an energy range almost continuously, enabling the scanning and mapping out of the Rydberg fine structure for a given RESIS excitation transition. As the laser is Doppler tuned through the energy range, the excitation spectrum becomes almost a direct map of the fine structure of the lower *n* level.

The $CO_2$ laser is Doppler tuned by varying the angle of the intersection between the Rydberg ion beam and the $CO_2$ laser, in the laser interaction region, Fig. 2.7. The $CO_2$ laser enters the laser interaction region through a ZnSe window, and reflects off a mirror and intersects the ion beam. The ion beam intersects the $CO_2$ laser twice, the first time the ion beam and the $CO_2$ laser are perpendicular to each other, and the second time they intersect at the intersection angle, $\theta_{\text{int}}$. The mirror is mounted on a post that enables it to be rotated. This rotation of the mirror is controlled by the computer through a *Labview* program, that angle recorded by the computer is $\theta_{stage}$. The angle of intersection can be varied to allow the Doppler tuning $CO_2$ laser frequency through a full range of frequencies.

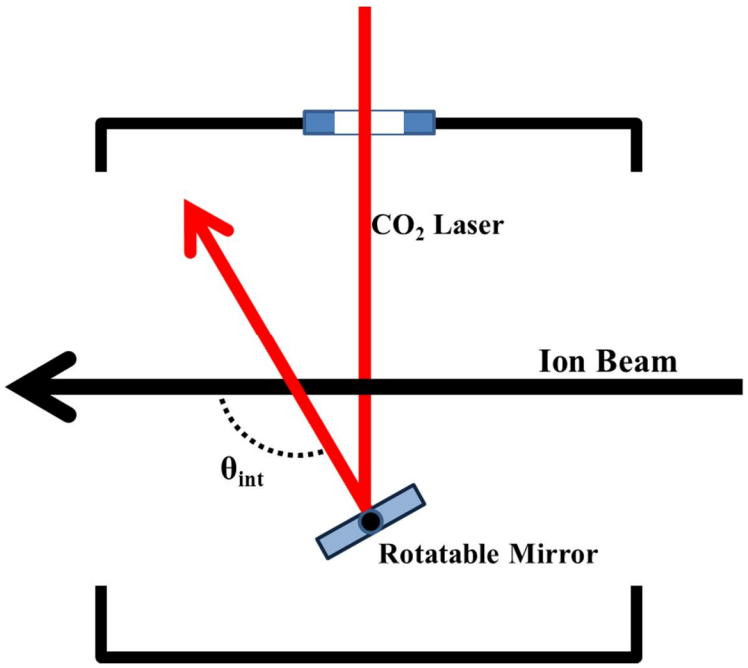


Figure 2.7: Schematic of the laser interaction region (LIR). The ion beam enters the LIR and the intercepts the $CO_2$ laser. The $CO_2$ laser enters the LIR through a ZnSe window, and reflects off a rotatable mirror and intersects the ion beam at the intersection angle, $\theta_{\text{int}}$.

The Doppler tuned frequency of the $CO_2$ laser is given by

$$v_L' = \frac{v_L}{\sqrt{1-\beta^2}}(1+\beta\cos(\theta_{\text{int}})) \tag{2.7}$$

where $v_L'$ is the Doppler tuned frequency of the $CO_2$ laser the ion bean sees. To calculate the Doppler tuned frequency three things are needed: the frequency of the $CO_2$ laser line, $v_L$, the speed of the ion beam, $\beta$, and the intersection angle, $\theta_{\text{int}}$. The intersection angle, $\theta_{\text{int}}$ is related to the angle recorded by the computer, $\theta_{stage}$, by Eq. 2.8. In Eq. 2.8, $\theta_{\perp}$, is the angle at which the $CO_2$ laser beam is perpendicular to the ion beam.

$$\theta_{\text{int}} = 90° - 2(\theta_{Stage} - \theta_{\perp}) \tag{2.8}$$

$\theta_{\perp}$ is determined from the calibration of the angle recorded by the computer with the intersection angle of a known Rydberg fine structure pattern. The speed of the beam is determined from Eq. 2.1, which requires knowledge of the mass, charge and acceleration voltage for the calculation. The determination of both $\theta_{\perp}$ and the beam speed will be discussed in more detail later in this section for the case of a specific example spectrum.

After the RESIS excitation the beam then passes into the detector region of the RESIS apparatus, where the upper state of the RESIS excitation transition is Stark ionized and deflected into a channel electron multiplier, CEM. The Stark ionizer in the detector has been set to ionize anything that has been excited to the upper *n* state in the RESIS transitions. The Stark ionizer used in the experiment is referred to as the long gap stripper. The Stark ionizer consists of a series of five plates, the first four plates, labeled P1 through P4, are spaced 2.5cm apart, and they make up the long gap stripper. The sixth and final plate, P5, is separated from the previous plate by 0.8cm, and is part of the unused short gap stripper. This plate is grounded externally. The other two plates labeled in Fig. 2.8 are the entrance plate to the Stark ionizer, which is held at ground and the plate that makes up the detector lens, used to focus the Stark ionized beam going into the CEM.

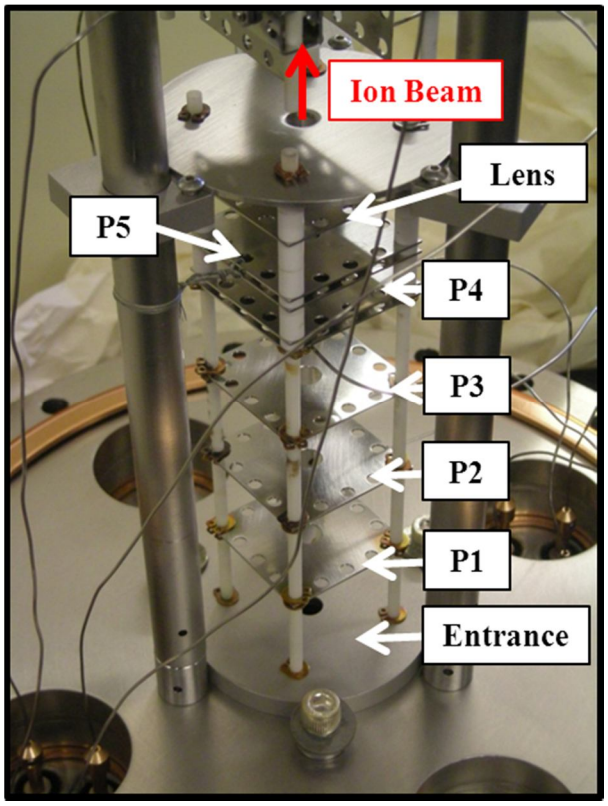


Figure 2.8: A picture of the Stark ionizer with the plates labeled. The center aperture on each of the plates is 0.25". The stark ionizer is mounted in between three support rods on and 10" conflat flange. Each of the plates receives it potential through MHV feedthroughs, also mounted on the 10" conflat flange.

The detection of the excitation begins with the beam entering the detector region through 10 inch conflat flange and the beam enters the Stark ionizer through the entrance plate, Fig 2.8, which is mounted on the 10 inch conflat flange. The field necessary to Stark ionize the upper *n* state for detection is calculated using Eq. 2.6, then knowing the gap in long gap stripper the potential necessary to produce that field is calculated, Eq. 2.9.

$$V_{Long}(Volts) = F_{\max}(Volts/cm)\cdot(2.5cm) \tag{2.9}$$

The long gap stripper is made up of four plates, labeled P1 through P4, each of the plates is placed at a fraction of the total long potential need for long gap stripper, $V_{Long}$,

$$V_{P1} = \frac{V_{Long}}{3} \qquad V_{P2} = \frac{2V_{Long}}{3} \qquad V_{P3} = V_{Long} \tag{2.10}$$

the final plate P4 is grounded. For the case of detections the $n$=37 to 73 $Th^{3+}$ Rydberg fine structure excitation, the total potential needed to ionize the $n$=73 was determined to be approximately -6000V. This means that the P1 plate would be placed at -2000V, the P2 plate at --4000V and the P3 plate at -6000V. Figure 2.9 gives a schematic of the plates, a plot of the voltage in the stripper versus position in the detector and a plot of the electric field versus the position in the detector. As the Rydberg beam enters the long gap stripper, the beam encounters a field that is a third of the field necessary to completely ionize the $n$=73 level. In this field, none of the $n$=73 levels should ionize. As it enters the region between the P3 and P4 plates, it encounters a field three times larger, a field large enough to ionize all Stark states in the $n$=73 level. The ions that are ionized experience a change in their kinetic energy that is proportional to the change in charge times the total voltage in the long gap stripper. Therefore, the ionization will either accelerate or decelerate the ions ionized depending on the polarity of the voltage in the long gap stripper. For the case of the $n$=37 to 73 transition for the$Th^{3+}$ Rydberg fine structure the potential was -6000V, thus the ion ionized in the long gap were slowed down by 6keV.

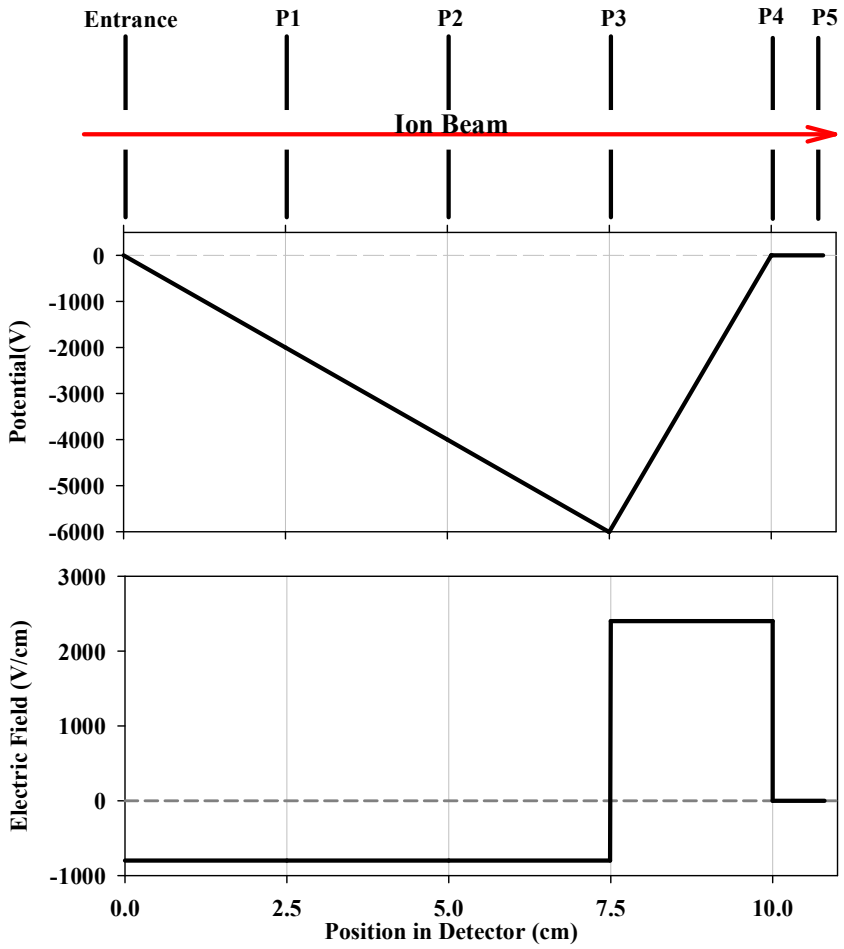


Figure 2.9: Schematic of the Stark ionizer, on the top is a drawing of the plates in the Stark ionizer. The middle plot shows the potential each plate is placed at to detect the excitation to the $n$=73 level for the case of the $Th^{3+}$ Rydberg states. The bottom plot shows the electric field. For both the plots the x-axis is the position in the detector.

After the Rydberg beam passes through the long gap stripper the beam then passes through a lens that helps to focus the beam for detection. The Rydberg beam is deflected into a channel electron multiplier, CEM, by horizontal and vertical defection plates. The CEM is horizontally centered on the output of the Stark ionizer, but vertically it is ~5.9 inches higher, therefore the ions leaving the Stark ionizer must be vertically deflected into the CEM. This vertical deflection can separate the different ions that exist in the beam after Stark ionization,

ions that may have different charges and different speeds. Fig. 2.10 gives a side view of the detector region, with some of the rough dimensions given.

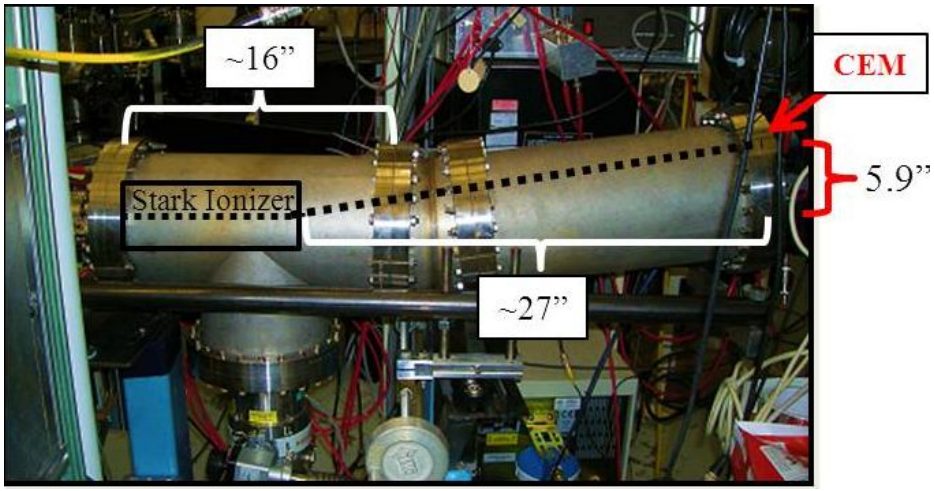


Figure 2.10: Side view of the detector region for the RESIS apparatus, all the measurements are in inches. The box shows the location of the Stark ionizer and defection plates inside the apparatus, and the arrow point out the location of the channel electron multiplier.

A scan versus the vertical deflection voltage of ions leaving the Stark ionizer and entering the CEM is shown in the Fig. 2.11. The top plot of Fig. 2.11 gives a scan of the voltage coming out of the CEM, CEM DC, as a function of vertical deflection voltage. The bottom plot gives RESIS excitation signal as a function of the vertical deflection voltage. In the case of the scan in Fig. 2.11 the $CO_2$ laser was sitting on the high-$L$ peak for the $n$=37 to 73 RESIS transition for the $Th^{3+}$ Rydberg states. The $Th^{3+}$ Rydberg states were produced from a 100keV $Th^{4+}$ beam from the ECR, thus the energy of the charge transfer beam will be 100keV. Both the charge transfer beam, $(Th^{3+})^*$ and the primary beam, $Th^{4+}$, are seen in the scan of the deflection voltage. The presence of the primary beam though is a surprise since that beam was deflected out of the apparatus before the RESIS excitation, this beam is therefore referred to as the regenerated primary. The presence of the regenerated primary depends on the presence of the Rb Rydberg target, indicating that the regenerated primary is somehow produced from Rydberg ions.

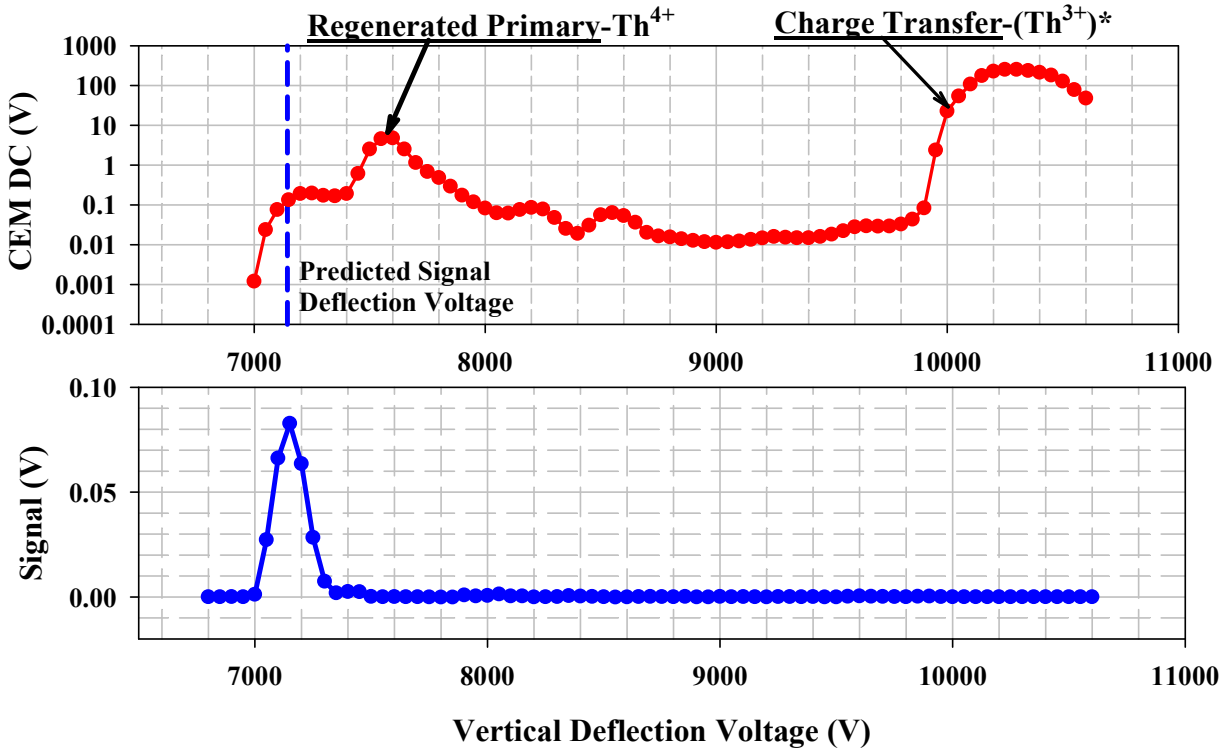


Figure 2.11: Profile of the 100keV $Th^{4+}$ and $Th^{3+}$ beams entering the CEM , the top plot is the output of the CEM voltage as a function of the deflection. The bottom plot gives the RESIS excitation as a function of the deflection voltage. This data is from JAK3-022, during the scan for this data the CEM high voltage was 1600V and the long gap stripper was set to -6000V.

The mechanism for the production of the regenerated primary is not known, but its presence produces a background in the area of the predicted signal deflection voltage, thus the RESIS technique is not background free as hoped. The location in the vertical deflection voltage of the RESIS excitation signal is predicted from the location of the regenerated primary. The signal ions and regenerated primary ions have the same charge; but the signal ions will be slowed down by the potential in the long gap. For the case seen in Fig. 2.11 the long gap stripper was set to -6000V, so therefore the beam was slowed down and the vertical deflection necessary to get the signal into the CEM was less since the signal ions spend a longer time in the vertical deflection field. The ratio of the kinetic energies for regenerated primary and signal ions will provide the

location of the signal on the vertical deflection scan. For the case seen in Fig. 2.11 this predicted location is indicated by the vertical dashed line, which lines up with the location of the observed RESIS excitation signal. The data from Fig. 2.11 showed that the signal on the high-$L$ peak for the $n$=37 to 73 RESIS transition was 83mV. The CEMDC at the same deflection as the signal corrected for the contribution from the signal, the background, is 133mV. The background is 1.6 times larger than the high-$L$ signal. This level of background greatly increase the difficulty of seeing the resolved signals in the RESIS excitation spectra, since the resolved signals are more than an order of magnitude smaller that the high-$L$ signal. This background is a limiting factor for the RESIS technique. Currently the source of the background is not understood. It is clear that the background and the regenerated primary beam are somehow due to Rydberg ions since both are absent when the Rydberg target is mistuned. However the mechanism is still a mystery.

The optical RESIS excitation from the $CO_2$ laser is detected by feeding the output of the CEM into a lock-in amplifier. The lock-in amplifier is referenced to the frequency of the chopper for the $CO_2$ laser. The computer program controlling the rotation of the mirror records the signal from the lock-in amplifier as a function of the angle being recorded by the computer, $\theta_{stage}$. As the intersection angle is varied, different states in the lower $n$ level are excited up to the upper $n$ level and detected, thus mapping out the Rydberg fine structure. Then by knowing the speed of the beam and the $\theta_{\perp}$, the recorded angle is converted into energy, thus measuring the Rydberg fine structure for the ion of interest. Fig. 2.12 shows the RESIS optical excitation spectrum for the $n$=37 to 73 $Th^{3+}$ Rydberg fine structure. The top figure shows spectrum as a function of the angle recorded by the computer, $\theta_{stage}$. The bottom spectrum gives it as a function of the Doppler tuned energy minus the hydrogenic energy for the $n$=37 to 73 transition calculated using Eq. 1.36, the energy deviation from hydrogenic. The $n$=37 to 73 transition was

observed using the 10P(10) $CO_2$ laser line since its frequency was near the hydrogenic frequency for the transition listed in Table 1.1.

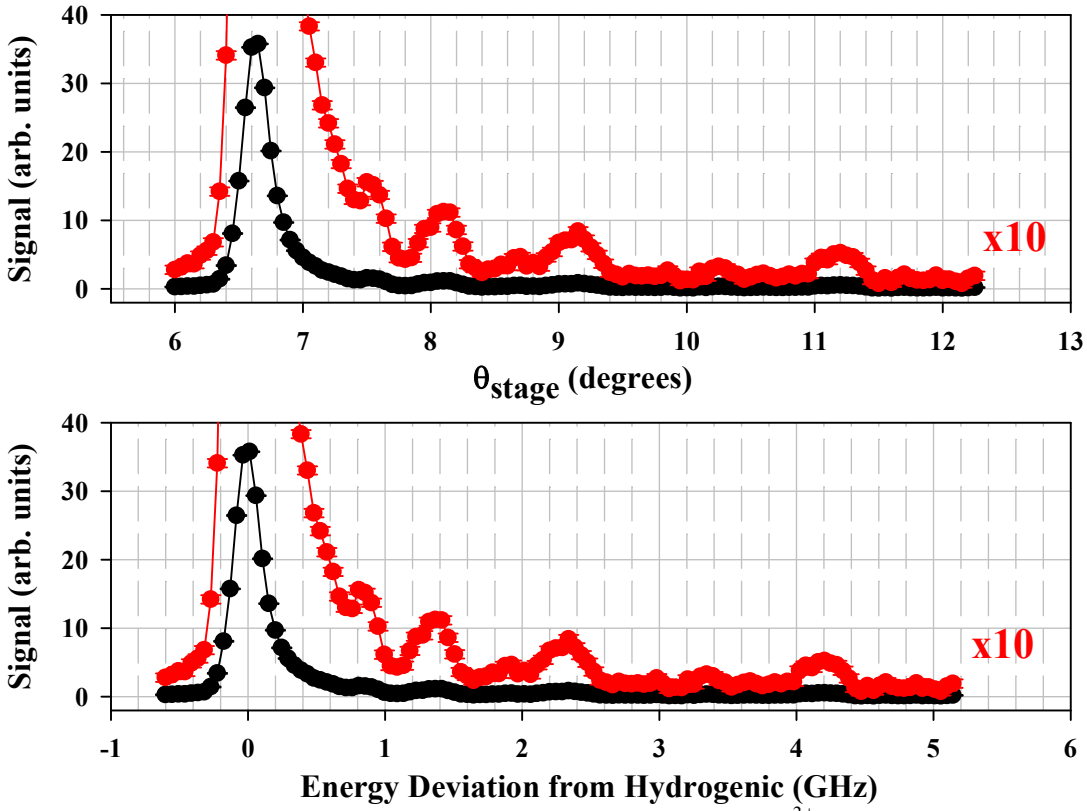


Figure 2.12: The optical RESIS spectrum for $n$=37 to 73 for $Th^{3+}$ Rydberg states. The top plot is the gives the RESIS excitation signal as a function of the angle recorded by the computer. The bottom plot gives the RESIS excitation signal as function of energy deviation from hydrogenic in GHz. The data on these plots is the average of four runs, MH12-120, 121, 122 and 123. On both of the plots the original signal is in black and signal time ten in red.

The optical RESIS excitation spectrum shown in the Fig. 2.12 shows a large peak around zero energy deviation, this peak is "high-$L$ peak" made up of all the $L$ states that are close to hydrogenic and are unresolvable from each other. The smaller peaks seen farther from hydrogenic represent individual $L$ states. The positions of these individual states in the $Th^{3+}$ Rydberg fine structure are used to determine properties of $Th^{4+}$. The exact location of these individual peaks is dependent on the conversion of the recorded angles into energies.

The conversion of the angle recorded by the computer into energy required the precise knowledge of the speed of the beam and the $\theta_{\perp}$ at the time of the scan. The beam speed is determined by the mass, charge and the potential the beam is accelerated by, $V_{\text{terminal}}$. The power supply that provides the acceleration to the ion source was been calibrated in the dissertation work of Mark Hanni's. The calibration determined the voltage for the terminal potential in terms of the dial reading on the high voltage power supply, $HVDial$ [17].

$$V_{\text{terminal}} = (2992(3)V) \cdot HVDial$$

Therefore, during all data taking the dial setting on the acceleration power supply is noted, so the beam speed can be precisely calculated for each of the optical RESIS spectra being measured.

The calibration of $\theta_{\perp}$ was also conducted during the work of Mark Hanni [17]. $\theta_{\perp}$ was determined by observing a known Rydberg fine structure, the $Si^{+}$ Rydberg fine structure. This fine structure has been previously studied using the rf RESIS technique and the properties controlling the structure are well known [25], therefore the energy of the fine structure levels can be calculated with a high level of precision. Measurements of the calculated $Si^{+}$ Rydberg fine structure with the optical RESIS technique allow for a determination of $\theta_{\perp}$, since the laser frequency, the beam speed and angle recorded by the computer are known. This calibration of $\theta_{\perp}$ took place during the time of optical measurements of the $Th^{3+}$ Rydberg fine structure [17, 21] and the measurements of the $Th^{2+}$ Rydberg fine structure reported in this work. The calibration of $\theta_{\perp}$ determined

$$\theta_{\perp} = 1.08(1)°$$

and the value of $\theta_{\perp}$ was used in the converting of all the recorded angles into energies for the optical RESIS spectra shown in this work. In the converting of the angles into energy the

uncertainties in both $\theta_{\perp}$ and the beam speed will result in uncertainties in the energies of the measured fine structure.

The optical RESIS technique is limited in its ability to resolve the fine structure pattern by the width of the individual transitions. There are two major sources of the width of the individual transition in the RESIS optical spectra. The first source of width is the due to the transit time through the $CO_2$ laser. The width of the transition, in MHz, due to the transit time through the Gaussian laser beam is given by Eq. 2.11 where $T_{Laser}$ is the transit time through the laser beam.

$$\Delta v_{Laser} = \frac{\sqrt{2\ln(2)}}{\pi\ T_{Laser}(\mu s)} MHz \tag{2.11}$$

Using time dependent perturbation theory it has been determined that the waist of the $TEM_{00}$ mode laser beam, not the actual width of the laser beam at the intersection point determines the effective transit time through the laser beam [26]. The transit time through the $CO_2$ laser is given by Eq. 2.12

$$T_{Laser} = \frac{w_0}{\beta c \sin(\theta_{\text{int}})} \tag{2.12}$$

where $w_0$ is the waist of the $CO_2$. The $CO_2$ laser used in this work had a waist of $w_0 = 0.9mm$. For one of the cases studied here, specifically for the transition in Fig. 2.12, where the $\beta \approx 0.000962$ and $\theta_{\text{int}} \approx 80°$ near the high-$L$, the width due to the transit time through the $CO_2$ laser was approximately $118MHz$. The second major source of the width for the transitions is due the possible angular spread of the ion beam as it travels through the apparatus, the contributions of this effect to the width of the RESIS transitions can be calculated using Eq. 2.13

$$\Delta v_{Beam} = v_L \cdot \beta \cdot \Delta\Theta \cdot \sin(\theta_{\text{int}}) \tag{2.13}$$

where $\Delta\Theta$ is the angular spread of the beam. For the Kansas beam line, experimental work showed $\Delta\Theta \leq 0.25°$ [17]. This means that for the case studied in Fig 2.12 the width due to the angular divergence of the beam would be approximately $118MHz$. The total width of a transition, $\Delta\nu_{Total}$, is estimated as the quadrature sum of the width due to the transit time through the laser and the width due to the divergence of the beam, Eq. 2.14.

$$\Delta\nu_{Total} = \sqrt{\Delta\nu_{Laser}^2 + \Delta\nu_{beam}^2} \approx 170MHz \tag{2.14}$$

Other effects contribute to the width of the observed transitions such as the velocity spread of the beam and the broadening to the transitions due to a stray electric field in the laser interaction region. The effect of the velocity spread of the beam is minimal and is therefore neglected. The effect of a stray electric field in the laser interaction region was minimized by minimizing the presence of the stray field during data taking. The additional effects that a stray electric field can have on a transition will be discussed in more detail later in this chapter. Previous work included a more detailed discussion of the width of the RESIS optical transitions and a comparison of the observed width with the calculated width [17].

The measurement of the fine structure with the optical RESIS technique provides the first step in the exploration of the Rydberg fine structure of the ions of interest. The optical measurements allow for the determination of the some of the properties for the ions that control the scale and features observed in the Rydberg fine structure patterns. The optical RESIS technique is limited in its ability to resolve the fine structure pattern for overlapping transitions and transitions near hydrogenic, given the width of the optical transitions. The precision of the determined locations of the transitions is also limited, in the case of the optical RESIS, measurements are limited to $\pm 20MHz$ on average. This is due to possible drifts in the $CO_2$ laser frequency. The limitations of the optical measurement limit the determination of the properties

of the ion of interest from the measured Rydberg fine structure and the precision of those determined properties. The precision and the resolution of the optical RESIS measurement of the Rydberg fine structure can be improved upon by measuring the Rydberg fine structure with the rf RESIS technique.

**2.2 The rf RESIS technique**

The rf RESIS technique is an extension of the optical RESIS technique since it relies on the optical RESIS technique to detect rf transitions between levels within the same $n$ state. The rf RESIS technique offers the opportunity to improve upon the optical technique since it will allow the resolution of the levels not resolvable in the optical RESIS excitation spectra, levels near the high-$L$ or the levels that are overlapping. The precision of the measured fine structure pattern can also be improved with the rf RESIS technique. The energy separation between levels can the determined within $0.1MHz$ at times. The rf RESIS technique only requires slight modification to the optical beam line set up, the addition of a second laser interaction region (LIR) and an rf region, Fig 2.13. Both of these components are added as additional components in the RESIS excitation part of the beam line before the RESIS excitation LIR, now referred to a LIR 2 in Fig. 2.13. Pictures of the rf RESIS apparatus are shown in Fig. 2.14 and 2.15, with Fig. 2.14 showing the apparatus from the ECR through the Rb Rydberg target region and Fig. 2.15 showing from the Rb Rydberg target region through the front flange of the detector region. In both of the pictures of the apparatus a scale has been given so the relative size of the beam line can be understood.

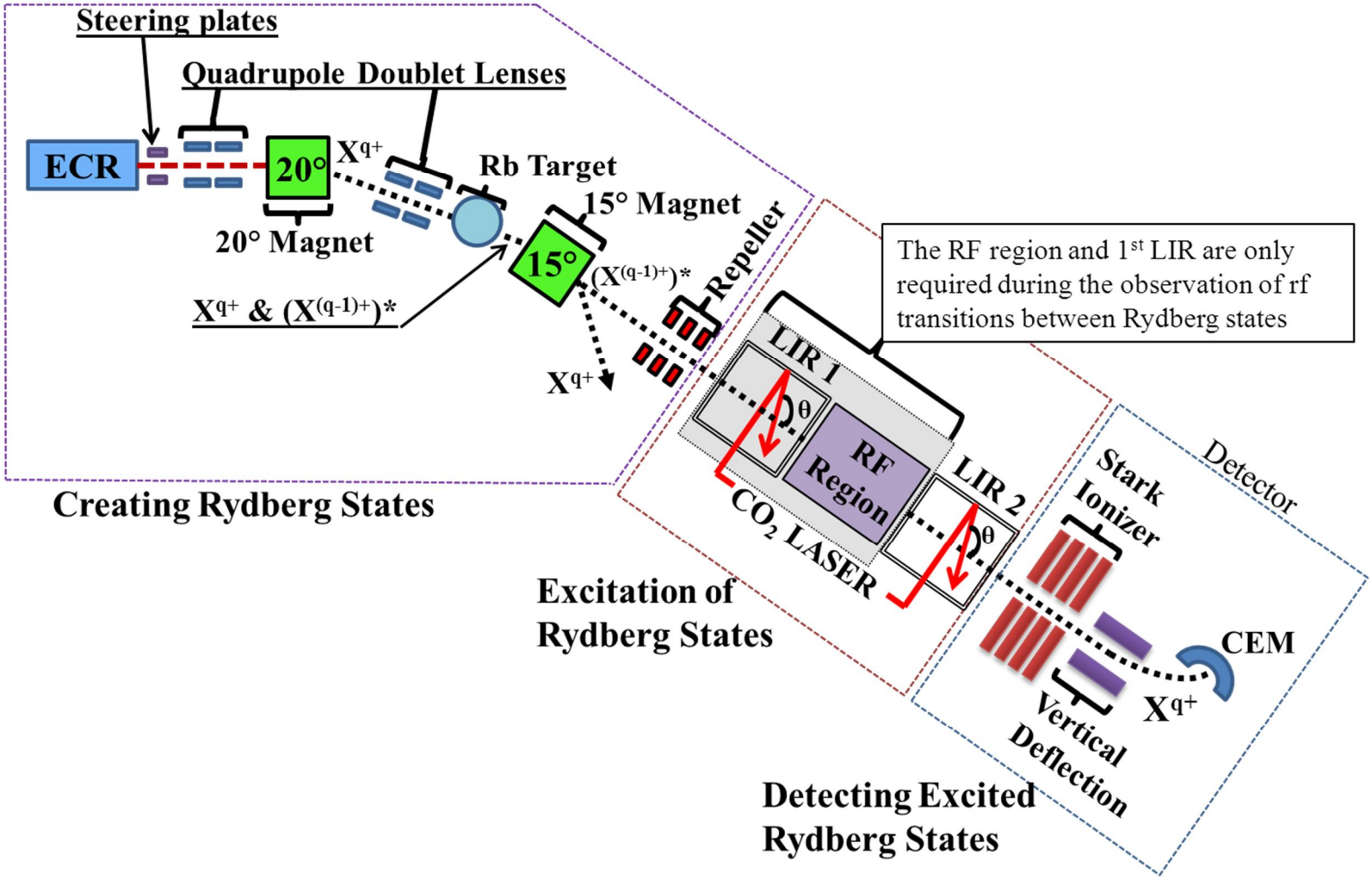


Figure 2.13: Schematic of the rf RESIS apparatus the three major areas of the apparatus are indicated.

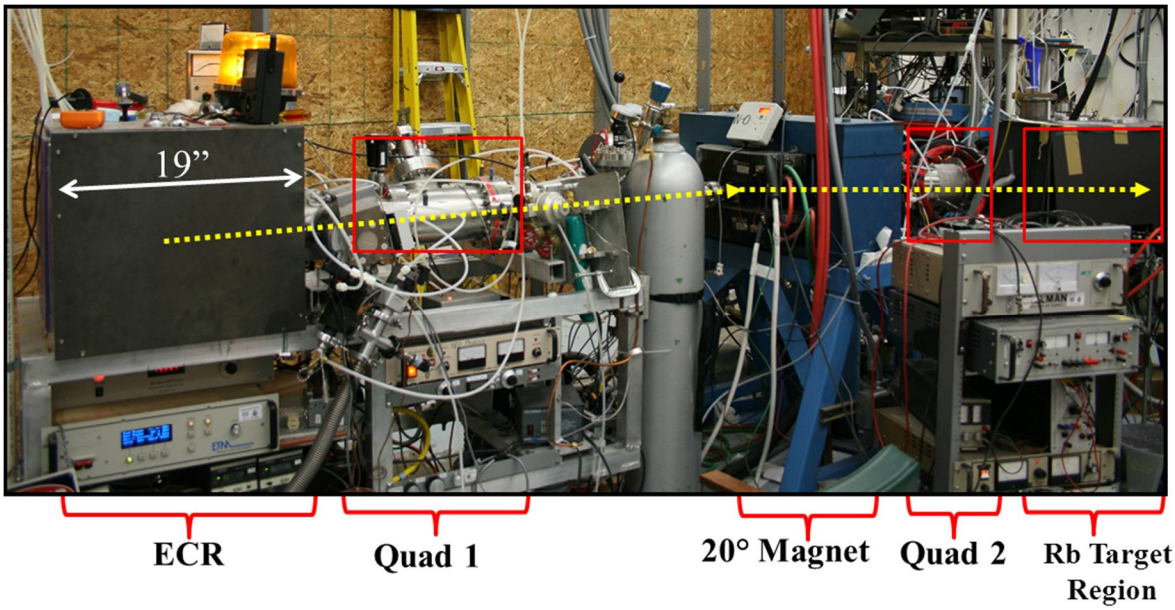


Figure 2.14: Picture of the first part of the RESIS apparatus, starting with the ECR on the left side going through the Rb target region, shown on the right side of the picture. To add scale to the picture the side of the box containing the ECR is approximately 19” wide.

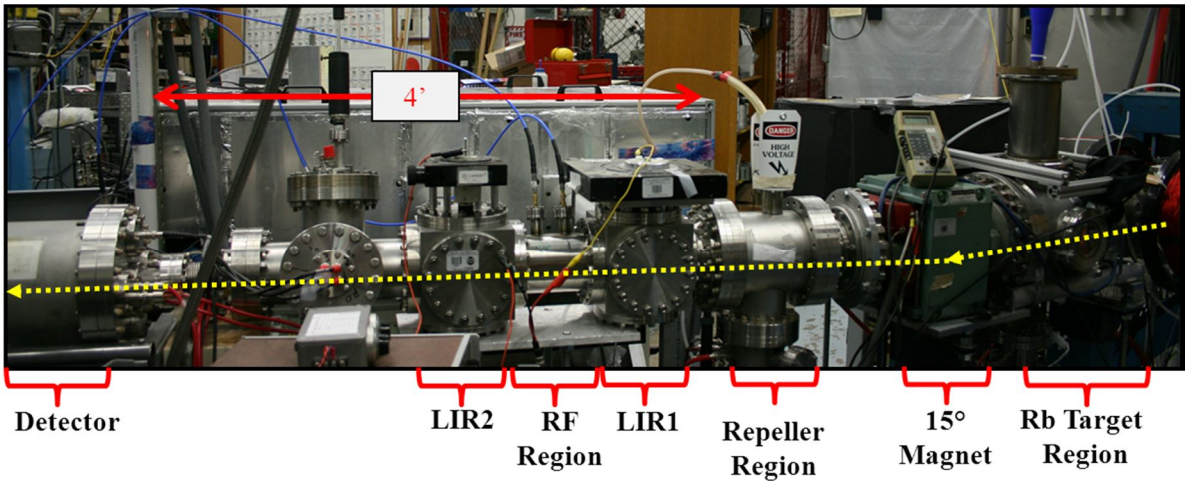


Figure 2.15: Picture of the second part of the RESIS apparatus, starting with the Rb target region on the right side of the picture and ending with the front flange of the detector region on the left side of the picture. To add scale to the picture, the box behind the beam line, containing the $CO_2$ laser is approximately 4’ wide.

The rf RESIS technique uses the optical RESIS technique as a way to detect direct transitions between levels of the same $n$ with sub-MHz precision. The observation of the rf resonance between levels can be accomplished with the addition of only the rf region to the beam

line apparatus. The addition of the second laser interaction region will be discussed after the basic rf RESIS is understood. For the discussion of the rf RESIS technique the $n$=37 $Th^{3+}$ Rydberg fine structure will be used, the RESIS optical excitation spectrum for the $n$=37 to 73 $Th^{3+}$ Rydberg fine structure is shown in the Fig. 1.5 with the individual transitions identified. The rf RESIS technique works by detecting changes in the population of the states contributing to the RESIS optical excitation spectrum by inducing rf transitions between states in the lower $n$ state before the RESIS optical excitation. This is illustrated in Fig. 2.16.

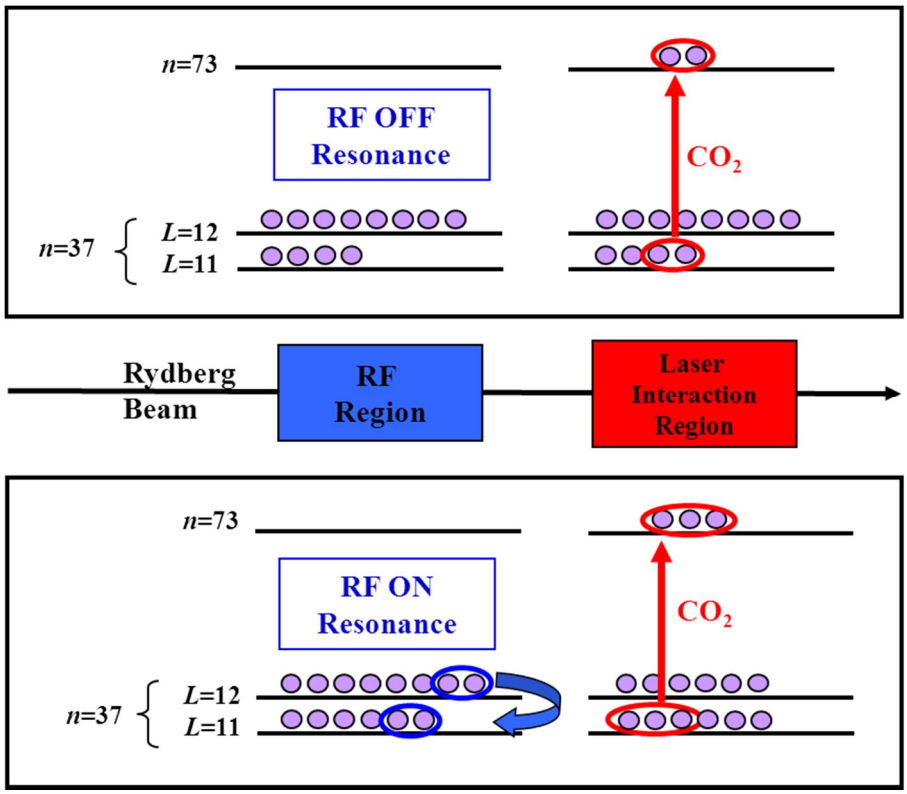


Figure 2.16: The rf RESIS technique detection scheme (one LIR), the top diagram show the population of the states when the rf is off resonance for the $n$=37 $L$=11 to $L$=12 transition. The bottom the diagram show the population when the rf is on resonance. The change in the number of ions excited to the $n$=73 level when the rf is on resonance provides a means to detect the transition.

The best way to understand this technique is to see its application to a specific case, shown in Fig. 2.16 is the setup required to observe the $n$=37 $L$=11 to $n$=37 $L$=12 transition in the

$Th^{3+}$ Rydberg fine structure. The method of creating the Rydberg states is unchanged, the beam of the Rydberg states of interest passes first through the rf region and then into the laser interaction region (LIR 2). The laser interaction region is set to a specific intersection angle so a specific transition between $n$=37 level to the $n$=73 level is excited with the $CO_2$ laser. For the example in Fig. 2.16 the $n$=37 $L$=11 is excited to $n$=73 $L$=12, this optical RESIS excitation is seen at approximately 800MHz in Fig. 1.5. The optical excitation done in the laser interaction region will excite half the population in the $n$=37 $L$=11 state to the $n$=73 $L$=12. Recall that the population of the $n$=73 level was removed from the beam during the creation of the Rydberg states of interest, therefore no population should exist in the $n$=73 level before this. The rf region before the laser interaction is then used to induce a transition between states in the $n$=37, in this case the $L$=11 and the $L$=12 states. If the rf region is on resonance with the energy difference between the two states and the population of the $L$=12 exceeds the $L$=11, the amount of population excited to the $n$=73 level and detected by the CEM will be increased. The detector region of the apparatus is unchanged, the upper state is Stark ionized and deflected into to the CEM for detection. During the scan for a rf transition the $CO_2$ laser is not chopped. Instead the rf being sent into the rf region is modulated and the lock-in is set to detect signals at that modulation frequency, thereby detecting the difference in the population of the upper state, $n$=73, when a rf transition occurs between states in the lower $n$=37 fine structure. The computer records the lock-in signal as a function of the frequency of the rf being sent to the rf region using a *Labview* program. In order for a rf transition between states to occur there must be a population difference between the two states, or the population transfer between states will not occur and thus no rf transition will be detected

To ensure the population difference between the two states an additional laser interaction region is added before the rf region, Fig. 2.17. This laser interaction region is referred to as LIR 1 and the laser interaction region after the rf region is referred to as LIR 2. The placement of a laser interaction region before the rf region allows for the RESIS excitations to be used as a way to produce a population difference between the levels in the lower state, $n$=37.

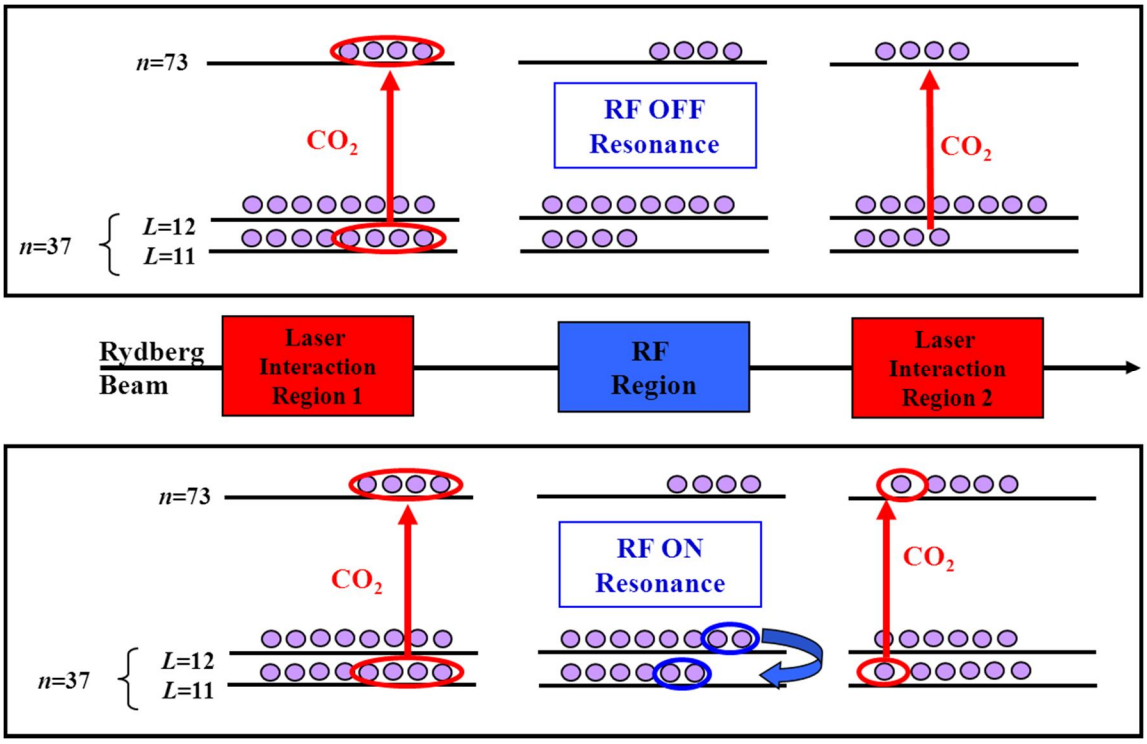


Figure 2.17: Diagram of the population of states during the rf RESIS (two LIRs), measurement of the $L$=11 to $L$=12 $n$=37 $Th^{3+}$ Rydberg fine structure interval

In the example in Fig. 2.17 LIR 1 is set to excite the $n$=37 $L$=11 to $n$=73 $L$=12, this excitation decreases the population of the $L$=11 states in $n$=37. When the rf is on resonance some of the $n$=37 $L$=11 population is replenished by the rf transition between the $L$=11 and $L$=12 in $n$=37. When LIR 2 excites the population of the $n$=37 $L$=11 state again, the amount excited will be increased if the rf region is on resonance with a transition between states. The observation of the $n$=37 $L$=11 to 12 rf resonance is shown Fig. 1.6. The fit of the resonance determined the

frequency difference between the $L$=11 and=12 to within $0.2MHz$ and resolved the $L$=12 location in the $n$=37 $Th^{3+}$ Rydberg fine structure. In the optical RESIS excitation spectrum Fig. 1.5, the $L$=12 state was not resolved from the high-$L$, the rf RESIS technique resolved its location and with a level of precision not possible with the optical RESIS technique.

The rf transitions observed in the Rydberg fine structure are limited by the selection rules that determine which states can be connected in each $n$. The transitions discussed in this section are single photon, meaning that the rf transitions in this section can only connect states that the differ in angular momentum by one unit. Therefore, in a single photon transition the angular momentum, $L$, must change by either plus or minus one, $\Delta L = \pm 1$, in addition the total angular momentum, $K$, must either remain unchanged or only change by plus or minus one, $\Delta K = 0, \pm 1$. The discussion of possible multi-photon transitions, transitions that connect levels separated by more than $\Delta L = \pm 1$ in the fine structure levels, is reserved for the next section of this chapter, since they do not follow the traditional selection rules. The fine structure of both the thorium ions of interest reported in this work relied on both single and multi-photon transitions.

The beam line in Kansas had to be modified for the rf RESIS technique with the addition of the additional laser interaction region and the rf region. These additions to the beam line would not limit the experimental apparatus to one of the RESIS experimental techniques. The apparatus could be used for either the optical RESIS technique or the rf RESIS technique without the removal of the additional parts added to the beam line for the rf technique. The second laser interaction was already constructed since work with thorium was not the first rf measurements of Rydberg fine structure made by this research group. This additional laser interaction region is of the same design as the laser interaction region already on the beam line. The addition of the second LIR required that the optics for the $CO_2$ laser be reworked. A beam splitter was added so

the beam coming out of the $CO_2$ laser could be split between the two LIRs. The second component necessary for the rf study was the rf region, the rf region used on the Kansas beam line was designed and built with the thorium experiments in mind.

Previous rf experiments used one of the previously built rf regions, both of the those rf regions were 50Ω eccentric coaxial transmission lines designed for propagating $TEM_{00}$ modes. The rf regions were designed and built by previous graduate students in the research group. The first rf region was built by Phillip L. Jacobson. This region is referred to as the PLJ region, has a frequency range up to $6GHz$, the rf interaction region is 7.9 inches long, and the total length of the rf region between the two LIRs is 21.3 inches. The second rf region was built by Robert A. Komara. This region is referred to as the RAK region, its frequency range is up to $2.4GHz$, the length of the rf interaction region is 11.8 inches and the total length of the region is 19.7 inches. The geometries and the measurements of the dimension of the inner and outer conductor for both of the regions is provided in the dissertation work of Erica Snow [27], along with pictures of both regions. The big drawback for both of these rf regions for the thorium studies was their total length, the greater the distance between the two LIRS the greater the time Rydberg states being studied have to decay. The lifetimes of the Rydberg states can be estimated from a formula developed for hydrogen-like states [28], Eq. 2.15.

$$Lifetime = \frac{n^3(L+0.5)^2}{1.08x10^{10}q^4} seconds \tag{2.15}$$

If the PLJ or RAK regions were used in the measurement of the $n$=37 $Th^{3+}$ Rydberg fine structure it would be expected that on average 65% of the Rydberg states of interest would decay in the time it takes the ion to travel between the first laser excitation and the second laser excitation, assuming 25kV terminal potential. Decreasing the total rf region to 6 inches would result in the decrease in the amount of the decay to 34% on average for the states of interest in

the $n$=37 $Th^{3+}$ Rydberg fine structure, thus the size of the signal for the rf transition would be increased. Another drawback for both PLJ and RAK was that both of the rf regions contained a small aperture at the entrance and the exit of the rf interaction region, this led to both of the rf regions being susceptible to the stray electric fields as a result of the beam hitting and passing near those surfaces. This stray electric field would shift the observed transitions via DC Stark shifts, therefore the observed transitions would have to be corrected for that effect.

For the thorium experiment and the Kansas beam line it was decided that a new rf region would be built, that would improve upon the older rf region and the address the drawbacks of the previous rf regions. Looking at the lifetimes of the thorium Rydberg states of interests led to the conclusion that the total rf region should be no longer 6 inches. Even with the drawbacks of the earlier regions it was determined that given the experience of our research group with the 50Ω coaxial transmission line designed to propagate $TEM_{00}$ mode, that this type of rf region would be best. A coaxial transmission line is made up of an inner and an outer conductor. The diameters of the each conductors and the offset between them determines the impedance of the line. The impedance, $Z$, of a coaxial transmission line is defined by Eq. 2.16 [29]

$$Z(\Omega) = 60\cosh^{-1}(U) \tag{2.16}$$

where

$$U = \frac{1}{2}\left[\frac{D}{d} + \frac{d}{D} - \frac{4c^2}{dD}\right]. \tag{2.17}$$

In Eq. 2.17, $D$ in the diameter of the outer conductor, $d$ is the diameter of the inner conductor and $c$ is the distance from the center of the inner conductor to the center of the outer of conductor. The impedance wanted for this rf region is 50Ω, therefore Eq. 2.16 was set equal to that and a

multitude of dimensions for the inner and outer conductors and offset were explored. The final dimension for the rf region decided upon are given in the Fig. 2.18, the outer conductor would be the copper pipe and the inner conductor would be a non-magnetic stainless steel rod.

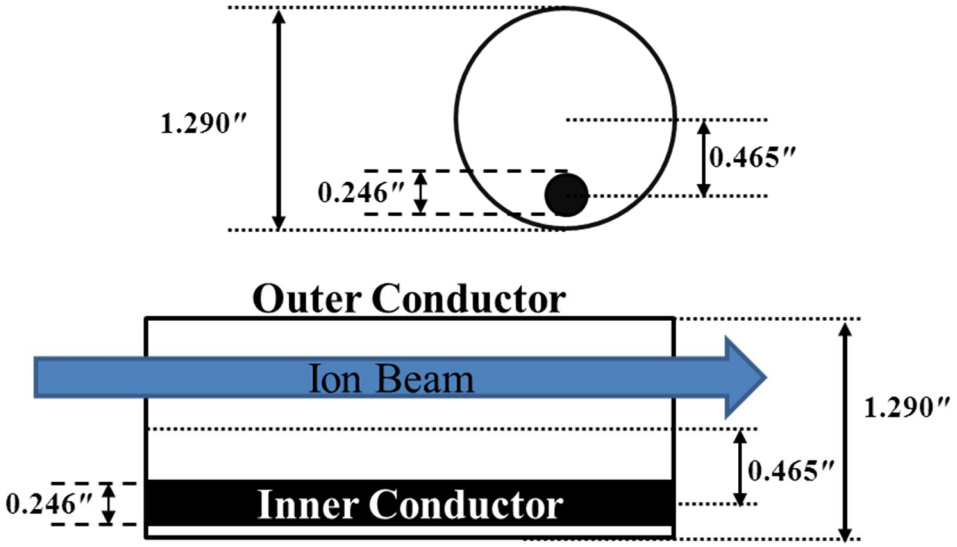


Figure 2.18: Schematic of inner and outer conductor for the rf region, all the dimension are in inches. The top drawing is looking through the rf region and the bottom drawing is a side view.

This geometry, Fig. 2.18, would make theoretical the cutoff frequency for propagation of non TEM modes approximately 5.6GHz. Therefore, transitions with frequencies all up to 5.6GHz could be observed in the region, this would enable for the full range of frequencies for the proposed thorium studies.

With the selection of the inner and outer conductors, and the offset in between them, attention turned to how to build the rf region. The questions faced in the construction were how to mount the inner conductor inside the outer conductor, how to confine the field in the rf region but still allow for the ion beam to travel through the region, and how to put the entire rf region at vacuum. The first question answered was how to put the rf region at vacuum. It was decided that the rf region would be mounted inside a 6 inch conflat tube in between the two LIRs. The

conflat tube would be only 6 inches long, so the total length of the total rf region needed to approximately 6 inches, theoretically the rf region could stick out slightly into each LIRs but not much or else it might affect the range the $CO_2$ laser could be Doppler tuned. The tube would have feedthroughs mounted on it to feed the rf into the rf region.

With an understanding of the physical restriction for the rf region, attention turned to the design of the rf region itself and answering the additional questions having to do with its construction. The inner conductor needed to be suspended inside the outer conductor and the method of suspension of the conductor would have to not interfere with the path of the ion beam. To accomplish this, an end cap was designed that would press fit into the ends of the pipe, the outer conductor. Therefore the rf region was made up initially of 4 major parts, the outer conductor, the inner conductor and two end caps, Fig. 2.19.

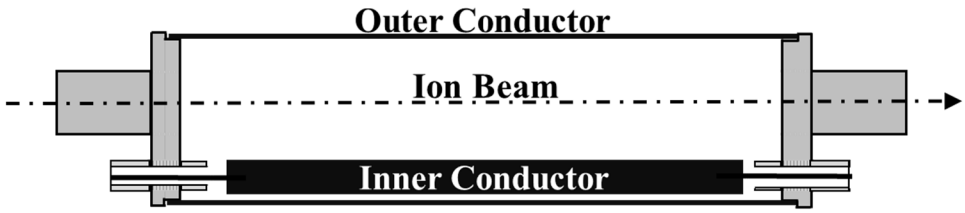


Figure 2.19: Basic schematic of the rf region with no dimension. Shown are the inner and outer conductor, the path the ion beam would take and a rough idea of what the endcaps would look like.

The ion beam would have to pass through the endcap, and the endcap would have to confine the rf in the rf region. The design of the end cap was key since it not only suspends the inner conductor; it also allows for the inner conductor to have rf fed to it. The design for the endcap is shown in the schematics and pictures of the endcap given in Fig. 2.20

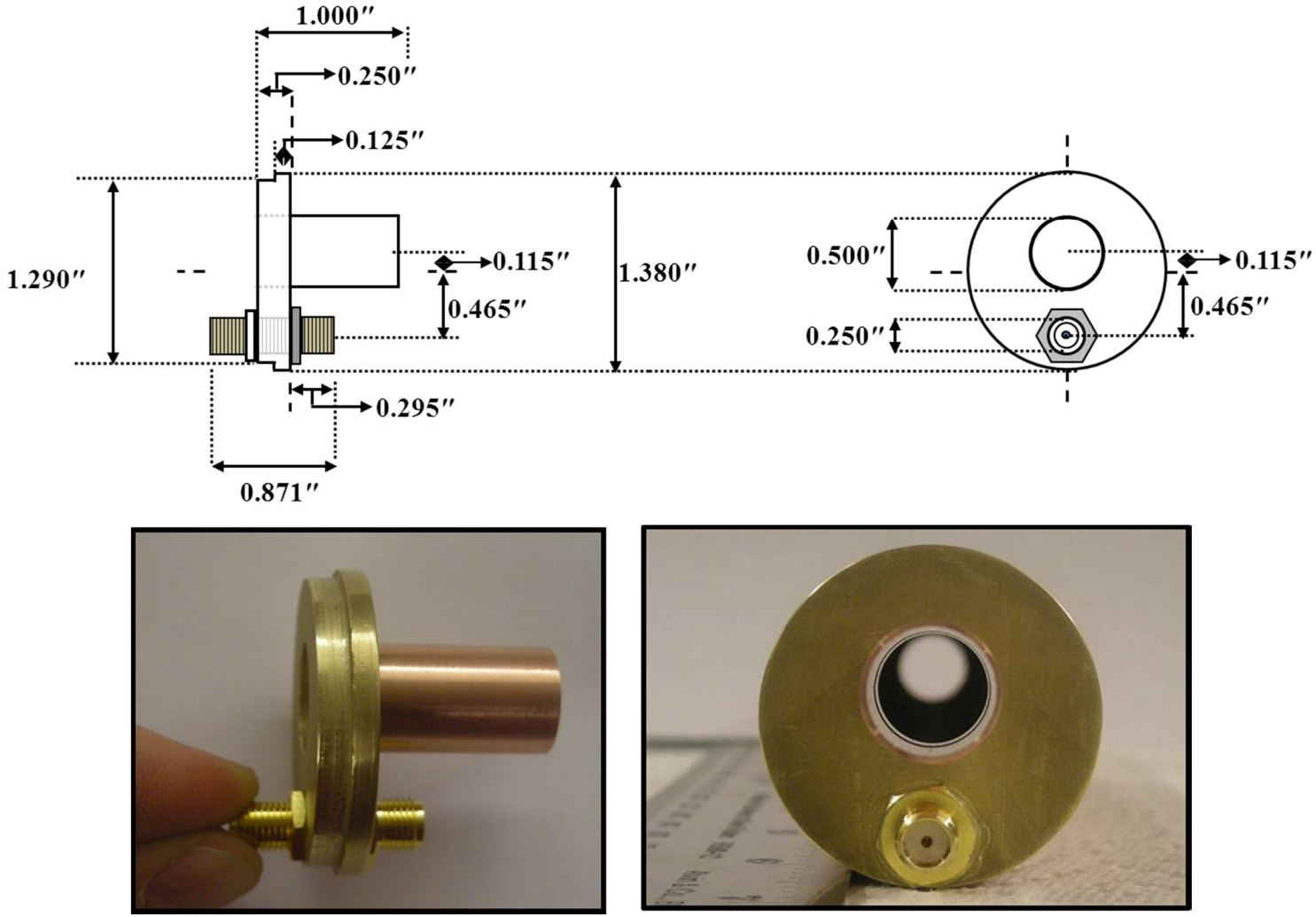


Figure 2.20: Schematic and pictures of the endcap for the rf region, all dimensions are in inches. On the left is the side view of the endcap and on the right is the view looking down the beam path.

The endcap is made up of three parts with all the parts made of non-magnetic materials. The first part is the brass pieces that act as a cap on each end of the outer conductor. The brass piece is designed so that it will be press fit into the end of the outer conductor. The brass piece has two holes in it, one for the beam to pass through and one to be used to connect and suspend the inner conductor. The inner conductor is suspended and connected to the outside by an SMA female-female bulkhead, Amplenol Connex part number 132170, which is mounted on the brass cap piece. The inner conductor has an SMA pin attached to each end of it so that when the endcap pieces are press fitted into the ends of the outer conductor, the inner conductor will be both suspended inside the outer conductor and the connected to the outside via the SMA bulkhead. The location of the hole for the SMA piece in the cap is so that the inner conductor is offset from the outer conductor, matching the conditions shown in Fig. 2.18. The third piece of the endcap is a small piece of ½" diameter copper pipe, that is press fit into the hole used as the entrance and exit for the ion beam into the rf region. This little piece of pipe is there to prevent any of the rf in the rf region of leaking out into the rest of the beam line. This is insured since there are no propagating modes in a ½" diameter circular waveguide with $f \leq 5.6MHz$.

Figure 2.21 provides a schematic of the assembled rf region with dimension and the pictures of the assembled rf region. The design and length of the inner conductor was a trial and error process. Different designs of the inner conductor were tried and the reflection in the rf region were documented over a frequency range in order to test the designs. The final design for the inner conductor is shown in Fig. 2.21, this design minimized the reflections is the region. Given the length of the inner conductor during the assembly of the rf region, an additional piece was added to the design; a plastic spacer that would act to prevent the inner conductor from coming in contact with the outer part of the SMA bulkhead which is at ground.

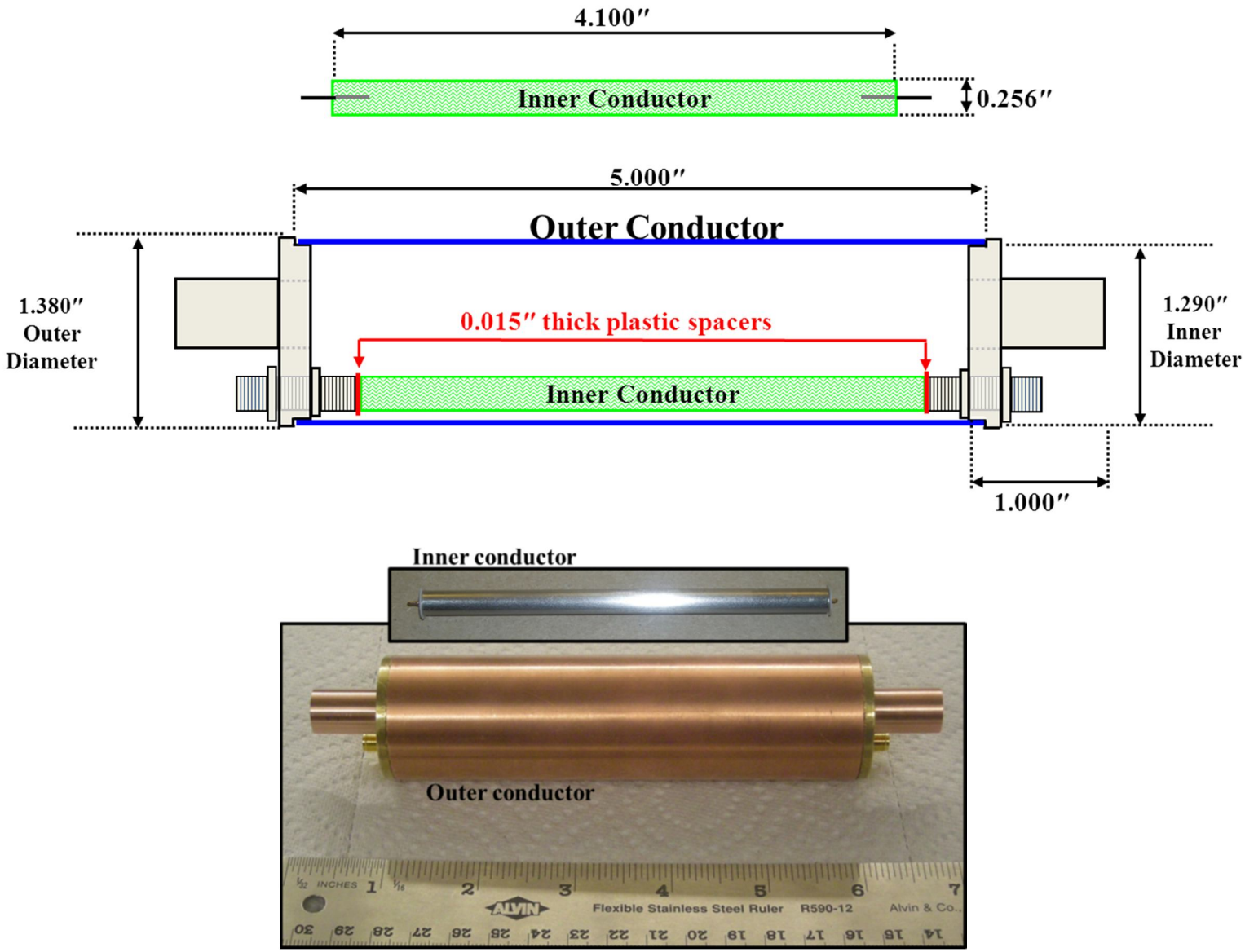


Figure 2.21: Schematic and picture of the rf region, all units are inches. Top is a schematic of the different part of the rf region. The picture below shows the actual rf region, assembled and along with a picture of the inner conductor.

The rf region is mounted in the 6 inch conflat tube that has length of 6 inches. The tube has two SMA feedthroughs mounted on mini-conflat flanges attached so rf can be fed into and out of the rf region. The SMA feedthroughs used are good to 8GHz and each of the feedthroughs is connected to the rf region with a small SMA cable. The tube the rf region is mounted in is also shielded with a μ-metal to protect the rf region from the earth's magnetic field. Figure 2.22 shows a picture of the rf region mounted in the tube and a picture of tube mounted between the two laser interaction regions with the two feedthroughs shown. The rf region does stick out of the tube slightly but not enough to be a problem for the laser interaction regions.

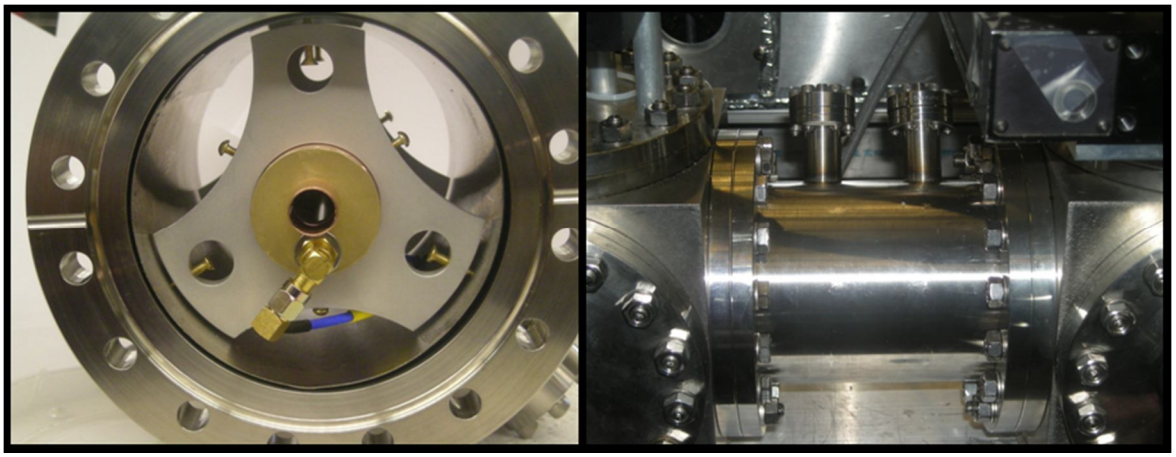

Figure 2.22: Pictures of the rf region mounted in the conflat tube and the conflat tube mounted on the beam line

The rf being sent to the rf region is produced using an HP 8648B signal generator, the generator has a range of the 9kHZ to 2000MHz. The signal generator is controlled via a *Labview* program on the computer; this program also records the signal being averaged by the lock-in. The program allows for a range of frequency to be scanned and records the frequency and the detected signal into a file. The power coming out of the rf region is also monitored with an rf power meter and the settings were recorded during data taking. The frequency range of the

function generator producing the rf was extended to 4.5GHz with the use of the multipliers, and when more power was necessary to observe transitions an amplifier was used.

Fig. 2.23 gives a scan of the reflection coefficient for the assembled rf region, terminated by 50Ω. This data shows that the reflection coefficient increases with frequency. For the rf studies presented in this dissertation the largest resonance frequency observed is approximately 3.5GHz, in that range the total reflection coefficient is ≤0.3, indicating that the refection from each end of the rf region is <0.15. If a large reflected wave existed in the rf region the observed resonance frequency could be affected, since the observed resonance experience a Doppler shift depending on the whether the ion beam and the electric field in the rf region are traveling parallel or anti-parallel.

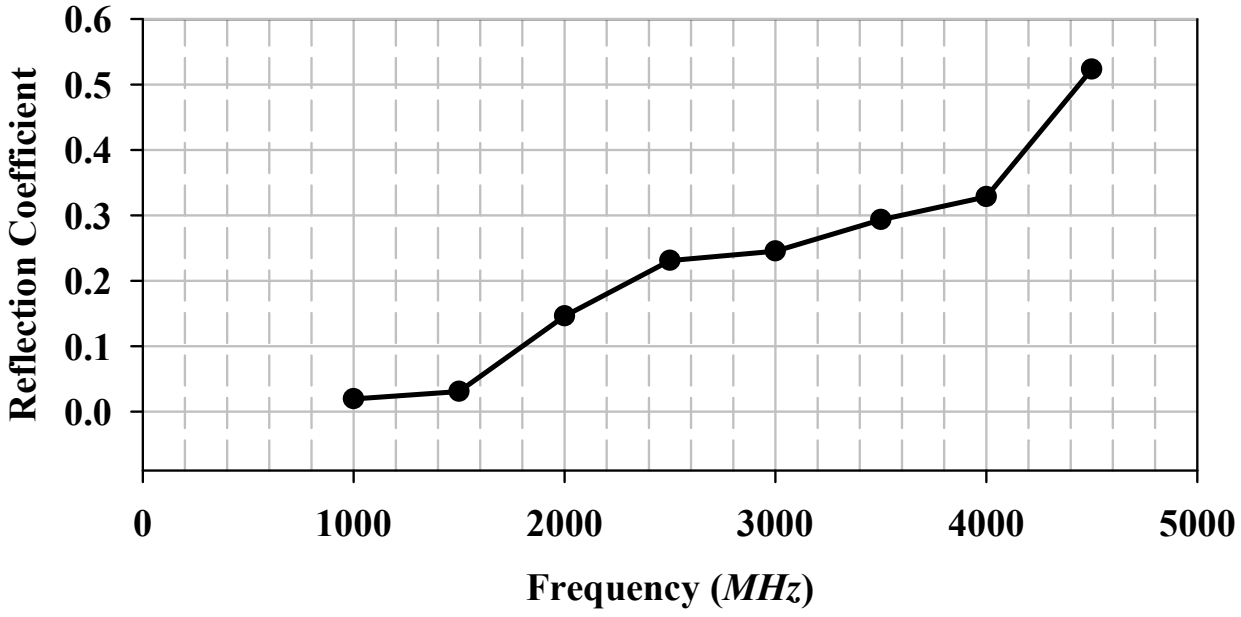


Figure 2.23: Plot of the reflection coefficient of the rf region versus the frequency for the rf region. This data was taken in JAK3-023, with the output of the rf region terminated in 50Ω.

As the frequency of the resonance increases so does the size of the Doppler shift experienced by the resonance, so if the reflection coefficient was large two resonances might be observed. One

of the resonances would be due to the ion beam and the electric field traveling parallel and one due to them traveling anti-parallel, this would therefore be a symptom of a large reflection existing in the rf region. The correction of the observed resonances for the Doppler effect will be discussed in the next section of this Chapter.

In order to observe the rf transitions it was only necessary to have a rough idea of the location of the transitions and an idea of the rf power necessary to produce the electric field in the rf region for the rf transitions between states. The location of the rf transitions observed in this work were estimated using the preliminary properties for the ions of interest found from the optical RESIS studies[3, 21]. The power setting used for the rf being sent into the rf region is essential since too much or too little power in the rf region would result in the inability to observe a resonance even when at the correct frequency. The first fine structure studied was the $n$=37 $Th^{3+}$ Rydberg fine structure. Once a transition was found the optimum power necessary to observe the transition was found by taking a saturation curve. The saturation curve is done by sitting at the center of a resonance and measuring the signal size as a function of rf power coming out of the rf region. An example of such a saturation curve is shown Fig. 2.24. This saturation curve was taken on the $n$=37 $L$=12 to 13 transition in the $Th^{3+}$ Rydberg fine structure.

The shape of the saturation curve is predicted from the two level problem. A complete formal discussion of the two level problem and the calculation of the probability of making a transition between levels is presented in the work of Ramsey [30]. The probability of making a transition between two levels at resonance has the form

$$P_{\alpha\to\beta} = A\sin^2(VT) \tag{2.18}$$

with $VT$ having units of radians. The $V$ is the coupling strength of the two states, $T$ is the transit time through the rf region and $A$ is the maximum amplitude of the saturation curve.

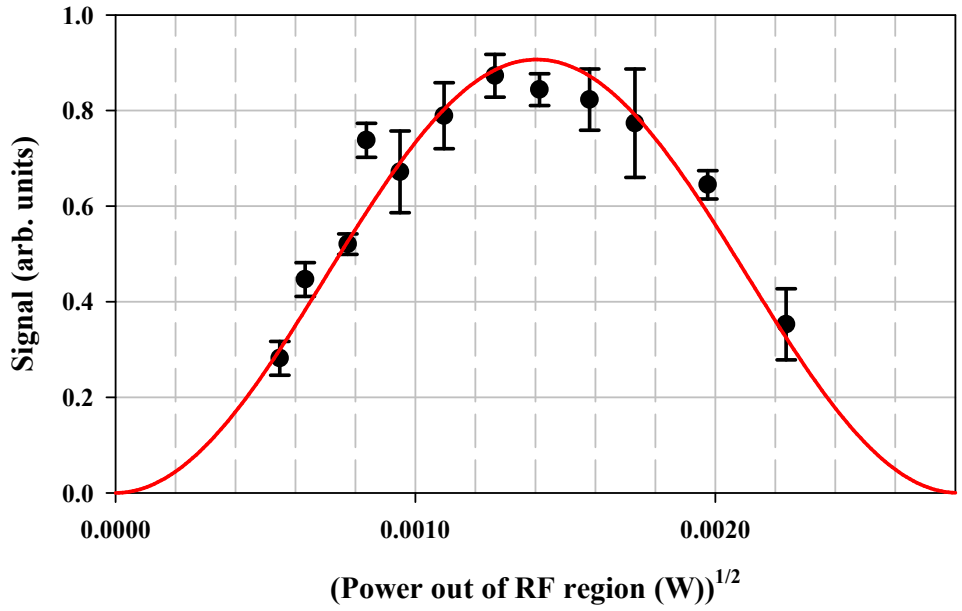


Figure 2.24: Saturation curve for $n$=37 $L$=12 to 13 single photon transition, the x-axis is the square root of the rf power coming out of the rf region in Watts and the y-axis is the signal at the given resonance frequency, 250MHz. The red line is the fit of the data, the form discussed in the text. The data for this saturation curve came from JAK6-156 and the electric field in the rf region was traveling parallel to the ion beam.

The transit time, $T$, through the rf region can be given by

$$T = \frac{Length\ of\ rf\ region}{\beta \cdot c} \tag{2.19}$$

where $\beta \cdot c$ is the beam speed and the length of the interaction part of the rf region is approximately 12.7cm, 5 inches. Therefore, for the case of the $Th^{3+}$ Rydberg fine structure where $\beta$=0.0009620 (assuming a 25kV terminal) the transit time through the rf region was 0.44μs. The coupling strength $V$ is given by

$$V(rads/s) = \frac{e Z_{rms} E_{rf}}{2\hbar} \tag{2.20}$$

where $E_{rf}$ is the electric field in the rf region, and $Z_{rms}$ is the average $Z$ matrix element for a given transition. The electric field in the rf region has the form $E_{rf}\cos(\omega t)$, it is oscillatory with time. The $Z_{rms}$ for a $\Delta L$=+1 transition is given by the Eq. 2.21, defined in term of $n$, $L$ and $q$ [31].

$$Z_{rms}(n, L \to n, L+1) = \frac{3}{2} n \frac{\sqrt{n^2 - (L+1)^2}}{q} \sqrt{\frac{(L+1)}{3(2L+1)}} a_0 \tag{2.21}$$

Eq. 2.21 neglects the total angular momentum, $K$, for the $Th^{3+}$ Rydberg fine structure this is adequate since $J_c = 0$. For the case of the $Th^{2+}$ Rydberg fine structure when $J_c = 5/2$, this it is not adequate, and this will be discussed further in the section dealing with the $Th^{2+}$ Rydberg fine structure measurements. Looking at Eq. 2.18 it can be seen that the highest probability for transition occurring is when $VT$ is equal to $\pi/2$. Therefore to find what the optimum electric field for a specific transition, $VT$ is set equal to $\pi/2$, which result in Eq. 2.22.

$$E_{rf} = \frac{h}{2eTZ_{rms}} \tag{2.22}$$

For the case of the $n$=37 $L$=12 to 13 transition the optimum $E_{rf}$ is $0.44 V/m$ since the $Z_{rms}$ is $200.1a_0$ ($1.06\text{x}10^{-8}$m) and the transit time through the rf region is 0.44μs. During the experiment though there is no direct measurement of the electric field in the rf region instead the power exiting the rf region is monitored. The electric field can be written as being proportional to the square root of power exiting the rf region. The fit of the saturation curve, Fig. 2.24, determines the optimum power exiting the rf region, $P_0$, to observe the $L$=12 to 13 transition. The saturation curve in Fig. 2.24 was fit to the form $A\sin^2\left(\frac{\pi}{2}\sqrt{\frac{P_{exit}}{P_0}}\right)$, from the fit $P_0$ was found to be $1.98(7)\text{x}10^{-6}$ watts. Knowing the calculated optimum field for the $L$=12 to 13 transition

and the observed optimum power the electric field can be written in terms of the power exiting the rf region, Eq. 2.23

$$E_{rf} = (0.44V/m)\left(\frac{P_{exit}(\mu W)}{1.98\mu W}\right)^{1/2}. \tag{2.23}$$

Eq. 2.23 gives the conversion between the power and electric field for this new rf region, making the future work of searching for transitions easier because the power level to make the observation will be known.

A check of this calculation of the connection between the electric field and the power exiting the region is provided by the known impedance of the region. The power exiting the region is the average power and therefore the potential on the inner conductor will be given by Eq. 2.24, where $U_0$ is the amplitude of the rf potential on the inner conductor and $P_{exit}(W)$ is the power reading on the output of the rf region.

$$U_0 = \sqrt{2\cdot(50\Omega)\cdot P_{exit}(W)} \tag{2.24}$$

The electric field is then just the ratio of the potential on the inner conductor divided by the effective distance, $D_{eff}$, Eq. 2.25.

$$E_{rf} = \frac{U_0}{D_{eff}} \tag{2.25}$$

For the case of the $n$=37 $L$=12 to 13, the potential on the inner conductor, $U_0 = 0.0141(3)V$, would make the effective distance be 3.20(7)cm or 1.26(3)inches. This effective distance seems very plausible given the geometry of the rf region, Fig. 2.18.

The designing and building of the rf region for the Kansas beam line was just the first step undertaken for the rf studies of the $Th^{2+}$ and $Th^{3+}$ Rydberg fine structure. With the

installation of the rf region and the second LIR, months of searching for the transitions necessary to the map out the fine structures of interests began. The transitions necessary to map out the fine structures for the two ions of interests will be discussed in a future section of this work. In the case of both the Rydberg fine structure measurements reported here, additional levels of the fine structure were measured with multi-photon transitions. Multi-photon transitions are a different category of transitions that can occur between levels of the fine structure, and these transitions require special treatment.

**2.3 Multi-photon rf transitions**

Multi-photon transitions are transitions that connect states that differ in angular momentum, $L$, by more than one unit. These transitions are not allowed under traditional selection rules discussed in the previous section. The observation of the multi-photon transitions in the thorium Rydberg fine structure requires a higher power than the single photon transitions and these multi-photon transitions are also susceptible to AC shifts. The calculation of multi-photon transitions is a time dependent problem, described by a time dependent Hamiltonian. The time dependent Hamiltonian can be transformed to a time independent Hamiltonian when the states involved are described by Floquet states. Then standard techniques of static perturbation theory can be used to determine the strength of the coupling of the states involved in the multi-photon transitions and the AC shifts. The work of Shirley [32] pioneered use of Floquet states and how that enables the replacement of the time dependent Hamiltonian with the time independent Hamiltonian. The time independent Hamiltonian is represented by an infinite matrix that is periodic. This technique of using Floquet states and the time independent Hamiltonian to approximate the multi-photon transition has been discussed previously in the work with multi-photon transitions in $He_4^+$ [33].

The Floquet state for a system such as the one here is given by $|L, p\rangle$ were $L$ is the atomic state and $p$ is the photon state. An rf transition between two pure states occurs when the electric field in the rf region is it at the same frequency as the energy difference between the states. The pure states $|L, p\rangle$ act as basis states of an infinite dimensional time independent Hamiltonian. The diagonal term of this time independent Hamiltonian are $E(L) + p \cdot \hbar\omega$. The off-diagonal terms obey the selection rules $\Delta L = \pm 1$, $\Delta p = \pm 1$, and for simplicity they are approximated by a constant $V$. Since selection rules limit the transition by $\Delta L$=±1 and $\Delta p$=±1, it would appear that multi photon transitions between pure states are not possible. But that assumption assumes that the states remain pure in the presence of the electric field in the rf region. For example the ability to observe the $L$=12 to 14 transition in the $n$=37 $Th^{3+}$ Rydberg fine structure, becomes clear when the transition is described in terms of Floquet states, as seen in Fig. 2.25. In Fig. 2.25, only the dominant Floquet states that contribute to the ability to see the two photon transition, $L$=12 to 14, are shown. The crossing between Floquet states that enables the observation of the two-photon transitions are denoted by dots in Fig. 2.25 marking the crossing of the Floquet states, in reality though those are not the locations of crossing but anti-crossing. In the presence of an electric field the dot would be the locations where states repelled each other, and then when the field is turned off the two states would decouple leaving each of the states with population possibly due in part to the other state.

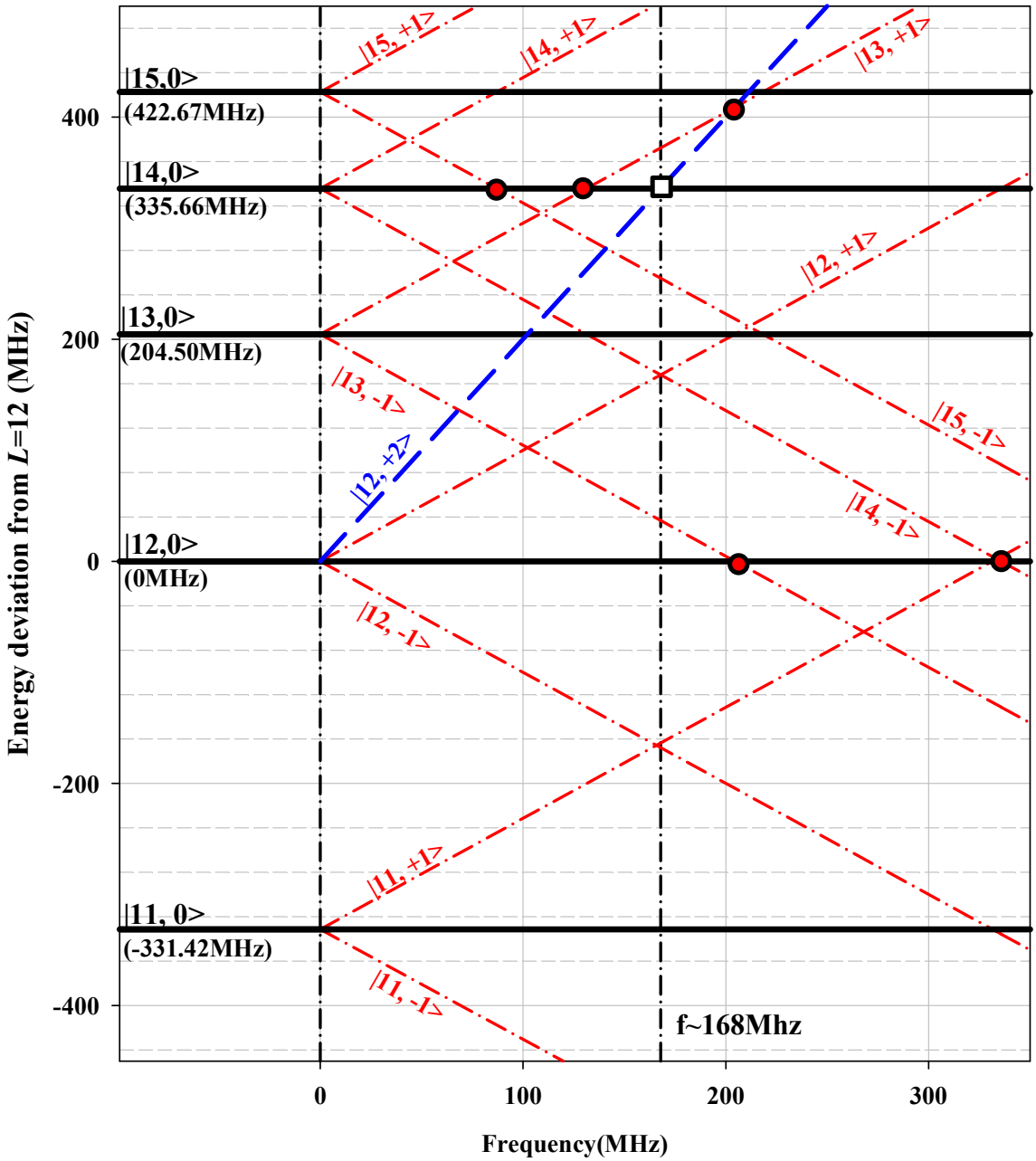


Figure 2.25 The multi-photon transition of the $L$=12 to 14. described in term of Floquet states, $|L, p\rangle$. The y-axis is in the energy deviation from the $|12,0\rangle$ in MHz. On the x-axis the two photon resonance between the $|12,+2\rangle$ and $|14,0\rangle$ is marked, 168MHz. The Floquet state for each of the $|L,0\rangle$ states is denoted by the horizontal line at the energy for each of the states. The Floquet states for each of the $|L, p\rangle$ is denoted by a dashed line. The crossing of Floquet states that observed the selection rules are denoted by dots. The crossing of the $|12,+2\rangle$ and the $|14,0\rangle$ is denoted by square.

Thus the two photon transitions becomes possible since the states are not pure. Each of the states is a linear combination of the states that can couple to it, observing the selection rules. When all the possible anti-crossings are taken into account, the Floquet states used to determine the power necessary and the AC shift for the $L$=12 to 14 transition would be given by

$$
\begin{aligned}
"\left|12,0\right\rangle" &= \left|12,0\right\rangle + \varepsilon\left|13,+1\right\rangle + \varepsilon\left|13,-1\right\rangle + \varepsilon\left|11,+1\right\rangle + \varepsilon\left|11,-1\right\rangle \\
"\left|14,0\right\rangle" &= \left|14,0\right\rangle + \varepsilon\left|13,+1\right\rangle + \varepsilon\left|13,-1\right\rangle + \varepsilon\left|15,+1\right\rangle + \varepsilon\left|15,-1\right\rangle \\
"\left|12,+2\right\rangle" &= \left|12,+2\right\rangle + \varepsilon\left|13,+1\right\rangle + \varepsilon\left|13,+3\right\rangle + \varepsilon\left|11,+1\right\rangle + \varepsilon\left|11,+3\right\rangle
\end{aligned}
\tag{2.26}
$$

where each of the perturbed eigenstates, $"\left|L,p\right\rangle"$, is a linear combination of the original basis set, observing the selection rules, $\Delta L = \pm 1$, $\Delta p = \pm 1$. The ε describes the strength of the mixing between states.

Once the makeup of the Floquet states of interest are known in terms of the other states, the strength of the coupling, the coefficients ε, can be determined. This coupling strength can be found by looking at the result of the two level time independent problem in quantum mechanics. With two levels $A$ and $B$ separated by energy, $\omega_0$, it can be found that the perturbed eigenstates can be described by

$$
\begin{aligned}
"\left|A\right\rangle" &= \left|A\right\rangle + \frac{V}{\omega_0}\left|B\right\rangle \\
"\left|B\right\rangle" &= \left|B\right\rangle - \frac{V}{\omega_0}\left|A\right\rangle
\end{aligned}
\tag{2.27}
$$

and that the perturbed energies are:

$$
\begin{aligned}
"E_A" &\rightarrow E_A + \frac{V^2}{\omega_0} \\
"E_B" &\rightarrow E_B - \frac{V^2}{\omega_0}
\end{aligned}
\tag{2.28}
$$

For Eq. 2.27 and Eq. 2.28 $A$ is above $B$, and $V$ is the dipole coupling between the two levels when $V << \omega_0$. Therefore the coupling strength for the states in Eq. 2.26 would be $\varepsilon = \pm V/\omega_0$ with the sign depending on its location in reference to the other states. In the case of the Eq. 2.26 the $\omega_0$ will be the frequency difference between the basis states near the resonance frequency of interest. For example looking at the $|14,0\rangle$ and the $|13,+1\rangle$ near the resonance frequency, Fig. 2.25, it is found that they are separated by approximately 37MHz with the $|13,+1\rangle$ above the $|14,0\rangle$ at resonance. Therefore, the coefficient in front of the basis state $|13,+1\rangle$ in the perturbed eigenstate "$|14,0\rangle$" in Eq. 2.26 will be $\varepsilon \approx -V/37$. Looking near the resonance frequency, the energy difference between the Floquet states, $\omega_{0,}$ was found for all the couplings in Eq 2.26. Then the states in Eq. 2.26 were rewritten with the coefficients to describe their coupling, Eq. 2.29, where $V$ is the single photon coupling potential, assuming that all the couplings are equal.

$$"|12,0\rangle" = |12,0\rangle - \frac{V}{372.33}|13,+1\rangle - \frac{V}{36.67}|13,-1\rangle + \frac{V}{163.59}|11,+1\rangle + \frac{V}{499.23}|11,-1\rangle$$

$$"|14,0\rangle" = |14,0\rangle - \frac{V}{36.67}|13,+1\rangle + \frac{V}{298.99}|13,-1\rangle - \frac{V}{254.84}|15,+1\rangle + \frac{V}{80.82}|15,-1\rangle$$

$$"|12,+2\rangle" = |12,+2\rangle - \frac{V}{372.33}|13,+3\rangle - \frac{V}{36.67}|13,+1\rangle + \frac{V}{163.59}|11,+3\rangle + \frac{V}{499.25}|11,+1\rangle \quad (2.29)$$

This method is an approximate treatment of the multi-photon resonances since it assumes the coupling between levels and transitions, $V$, is the same with has no dependence on $L$ or $m$.

To calculate the power necessary to observe the two photon transition the effective matrix element between the "$|12,+2\rangle$" and "$|14,0\rangle$" states has to be calculated, Eq. 2.30.

$$V_{eff} = \left|\langle 12,+2|V|14,0\rangle\right| = \left|-\frac{V^2}{36.67MHz} - \frac{V^2}{36.67MHz}\right| = \frac{V^2}{18.34MHz} \quad (2.30)$$

Most the terms used to determine Eq. 2.30 are zero since the coupling of the two states must observe the selection rules $\Delta L=\pm 1$ and $\Delta p=\pm 1$, but the sum of the nonzero terms resulted in the relationship between the effective coupling, $V_{\text{eff}}$, and the single photon coupling, $V$. The effective coupling strength, $V_{eff}$, between two states has been defined in terms of $Z_{\text{rms}}$ in Eq. 2.20 for a single photon transition, but it is also possible to estimate another way with no dependence on $L$ or $m$. From the work of the single photon it is known that the highest probability for a transition occurring is when

$$2\pi VT = \pi/2 \tag{2.31}$$

where $T$ is the transit time through the rf region. For the cases studied here $T$=0.44μs. Substituting $T$=0.44μs into Eq. 2.31 results in the determination of the coupling strength, $V_{sat}$, that has no dependence on any quantum numbers, Eq. 2.32.

$$V_{sat} = \frac{1}{4T} = \frac{1}{4\cdot(0.44\mu s)} = 0.568MHz \tag{2.32}$$

This coupling is for two states connected by a single photon transition, and it should also be the effective coupling necessary to saturate a multi-photon transition. Therefore by plugging $V_{sat}$ into Eq. 2.30 the single photon coupling strength $V$ needed to saturate the two photon transition was estimated to be 3.23MHz.

With the estimate of the saturating single photon coupling for the two photon transition, the power necessary to observe the two photon transition was determined in terms of the single photon power, by looking at the ratio of the two photon power to single photon power which is related to the ratio of the coupling strengths squared, Eq. 2.33.

$$\frac{P_{2\,photon}}{P_0(single)} = \left(\frac{V}{V_{sat}}\right)^2 = 32 \tag{2.33}$$

The single photon transition in $n$=37 $Th^{3+}$ Rydberg fine structure saturated at approximately 1.98μW, therefore the two photon transition $n$=37 $L$=12 to 14 will need approximately 64 μW for optimum observation.

The other concern for the multi-photon transitions is the possibility of AC shifts to the transitions by the electric field being produced in the rf region. The shifting of the levels can also be found from the results of the time independent two level problem. With two states $A$ and $B$ separated by $\omega_0$ with shift of the one state by another will be $\pm V^2/\omega_0$ with the sign depending on the respective locations of the levels. Therefore, the AC shift of the two photon transitions with power can also be calculated using the coefficients of the $|12,0\rangle$ and $|14,0\rangle$ states in Eq. 2.29, the shift rate of each state will just be the sum of the shifts due to each mixture, making sure to be careful with the signs. The shift to the interval will then be difference of the $|14,0\rangle$ and $|12,0\rangle$ shift rates, Eq. 2.34.

$$\Delta\nu_{12-14}(calculated) = \frac{+V^2}{157.15MHz} \tag{2.34}$$

Table 2.1 summarizes the power necessary and the AC shifts for the multi-photon transition in the observed in the $n$=37 $Th^{3+}$ Rydberg fine structure in comparison to a single photon transition. Using this same approach with Floquet states for the three photon transition, it was possible to calculate the power needed for the observation of the, $L$=12 to 15, and the AC shift rate it would experience. The results of those calculations are shown in Table 2.1. From Table 2.1 it can be seen that the power necessary to observe a multi-photon transition increases as the number of photons increase, and that for some cases the AC shifts are sizable and cannot be neglected. The model used to calculate the power and the shifts is a simplistic model that does not take into account any of the quantum number of the states involved in the transitions. This model though

at least determines an idea for the power necessary to observe transition and the approximate size for the AC shifts for the transitions. If the shift is sizable and important in determining the measured location of a transition, the AC shift can be measured for a transition. In Chapter 3 the measurement of the AC shift for the three photon transition in the $n$=37 $Th^{3+}$ Rydberg fine structure is discussed and compared with the rate calculated here. The additional multi-photon transitions for both the Rydberg fine structures reported in this work extended the measured fine structure to the higher $L$ levels which would not have been reachable with single photon transitions.

Table 2.1: Summary of the power and AC shifts for the multi-photon transitions in the $Th^{3+}$ Rydberg fine structure. The first column identifies the transitions. The second column gives the effective coupling. The third column gives the AC shift in terms of V, and the fourth column gives the V for each of the transition at saturation. The fifth column gives the saturation power, the optimum power for observing the transition of interest, and the final column gives the AC shift in MHz if the transition is observed at the saturation power.

| $L$ -$L$ ' | $V_{eff}$ | AC Shift | $V_{sat}$ (MHz) | $P_{sat}$(μW) | AC shift at $P_{sat}$ |
|---|---|---|---|---|---|
| 12-13 | $V$ | 0 | 0.57 | 1.98 | 0 |
| 12-14 | $\frac{V^2}{18.34MHz}$ | $\frac{+V^2}{157.15MHz}$ | 3.23 | 63.6 | $0.066MHz$ |
| 12-15 | $\frac{V^3}{3428.38MHz}$ | $\frac{+V^2}{229.46MHz}$ | 12.49 | 951 | $0.680MHz$ |

**2.4 Experimental correction for rf transitions**

The observation of the rf transitions, both single photon and multi-photon, have to be corrected for shifts of the transition frequency. The two shifts discussed in this section are the Doppler shift and the DC Stark shift. The Doppler shift will always occur during the observation of an rf transition, so this effect will need to be accounted for on every observation made. The

second shift discussed in this section is the DC Stark shift. This shift is the result of the stray electric fields, that may occur either in the laser interaction region or the rf region. The size of the DC stark shift is dependent of the size of the stray electric field and the shift rate of the transition of interest. During data taking every attempt is made to minimize the amount of stray electric field in the apparatus so the effect of the DC Stark shift will be minimized. The effect of both of the mechanisms of shifting observed transitions cannot be neglected. They must be understood and corrected for.

The Doppler shift discussed in this section is in the context of the rf transitions, during the observation of the rf transition the ion beam of the Rydberg states of interest is sent through the rf region in order to induce rf transition between states of the same $n$. The rf transitions are induced in the rf region by an electric field that is propagating in the rf region, oscillating at the resonance frequency. The frequency for the electric field in the rf region the ion beam sees depends on how the ion and the electric field are traveling with respect to each other. When the electric field and the ion beam are moving in the same direction the frequency of the electric field the ion beam sees is lower than the applied frequency. This effect causes an upward shift in the apparent resonance frequency, i.e. the frequency for maximum transitions. In the case of the beam line apparatus it is possible to change the relative direction of propagation between the two, by changing the feedthrough the rf is fed into.

When the ion beam and the rf in the rf region are propagating in the same direction the measurement of the rf transition is called co-prop measurement, $f_{co-prop}$, indicating the two co-propagating together. The co-prop measurements are denoted in the tables by $\rightrightarrows$. When the ion beam is traveling in opposite directions the measurement is called counter-prop, $f_{counter-prop}$, indicating the two are not propagating in the same direction. In the table of measurements of the

transitions the counter-prop transitions are denoted by ⇆. The size Doppler shift a transition will experience is dependent on the frequency and the speed of the ion beam being studied. The Doppler shifted frequency for the observation of each of the directions of propagation is given by Eq. 2.35, where $f_0$ is the un-Doppler shifted frequency of the transition, the actual position of the resonance.

$$f_{co-prop} = \frac{(1+\beta)}{\sqrt{1-\beta^2}} f_0$$
$$f_{counter-prop} = \frac{(1-\beta)}{\sqrt{1-\beta^2}} f_0 \qquad (2.35)$$

The observed transitions can be corrected for the Doppler shift if the beam speed is known, using Eq. 2.35 to determine the un-shifted position of the measured rf intervals. Another method of correcting of the Doppler shift is to observe the transition in each direction of propagation, the average of the two directions of propagation will then give un-Doppler shifted location of the transition, Eq. 2.36.

$$f_0 = \sqrt{1-\beta^2}\left[\frac{f_{co-prop} + f_{counter-prop}}{2}\right] \approx \left[\frac{f_{co-prop} + f_{counter-prop}}{2}\right] \qquad (2.36)$$

Most the time the $\sqrt{1-\beta^2}$ factor out in front of the average of the two directions of propagation, Eq. 2.36, is neglected since it is so close to one, given that $\beta < 0.001$ for most of the ions studied using the rf RESIS technique.

Using the average frequency of the two directions of propagation for a transition it is also possible to calculate the apparent $\beta$ for the transition; this can be used as a check on the observed Doppler shift. The shift between the two directions of propagation should be consistent with what would be predicted given the speed of the beam as long no sizable reflection exists in the rf region. The calculation of the apparent $\beta$ is given by Eq. 2.37.

$$apparent\ \beta = \frac{f_{co-prop} - f_{counter-prop}}{f_{co-prop} + f_{counter-prop}} = \frac{f_{co-prop} - f_{counter-prop}}{2f_0} \tag{2.37}$$

The DC Stark shift occurs when coupled states perturb each other in the presence of an electric field. In the experiment discussed in this work this type of shift occurs when a stray electric field is present in the rf region. The possible shift due to the DC Stark effect can be calculated and data can be corrected if the magnitude of the electric field is known. The DC Stark shifts occur between $L$ states for a given $n$, with the selection rule $\Delta L=\pm 1$, so an $L$ state will only be perturbed by the $L$-1 state and $L$+1state, as seen in Fig. 2.26

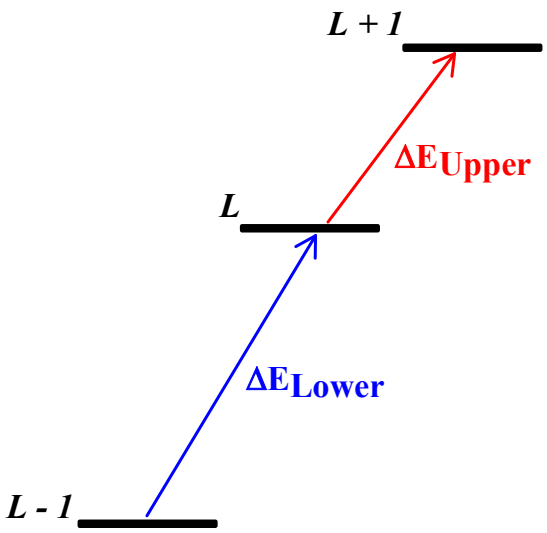


Figure 2.26: Level diagram for calculating the DC Stark shift. $\Delta E_{Lower}$ is the energy difference between the $L$-1 state and the $L$ state and the $\Delta E_{upper}$ is the energy difference between the $L$ state and the $L$+1 state. In the presence of an electric field the position of the $L$ state will be perturbed by the $L$-1 state and the $L$+1 state.

The Stark shift of a state from another state can be calculated, it is just the coupling potential squared divided by the energy difference between the states. The coupling potential between two of the levels will be given by

$$V = e Z_{rms} E \tag{2.37}$$

where $Z_{\text{rms}}$ is the $Z$ matrix element and $E$ is the electric field present. The $Z_{\text{rms}}$ was defined earlier in this chapter in Eq. 2.21 in term of $n$, $L$ and $q$. In the case discussed here and shown in Fig. 2.26, the $L$ state is only shifted by the $L$+1 state and the $L$-1 state with the direction of the shift depending on whether the perturbing state is above or below the $L$ state. When the coupled state is below the $L$ state, the shift to the $L$ state will be upward and when the coupled state is above the $L$ state, the shift to the $L$ state will then be downward. Therefore, the total shift of the $L$ state shown in Fig. 2.26 will be given by

$$DC\ Stark\ Shift = \left( \frac{(V_{Lower})^2}{\Delta E_{Lower}} - \frac{(V_{Upper})^2}{\Delta E_{Upper}} \right) \tag{2.39}$$

where the $V_{Lower}$ is the coupling between the $L$-1 state and the $L$ state and $\Delta E_{Lower}$ is the energy difference between those states. The $V_{Upper}$ is the coupling between the $L$ state and the $L$+1 state, and $\Delta E_{Upper}$ is the energy difference between those states. Then by plugging in the appropriate coupling potential and converting units it is possible to come up with an expression, Eq. 2.40, that describes the shift in MHz of an $L$ state by its neighboring $L\pm1$ states and the presence of an electric field, $E$, with units of V/cm.

$$DC\ Starkshift(MHz) = \frac{1}{3}\left( 1.28 \cdot \frac{3}{2}\frac{n}{q} \right)^2 \left\{ \frac{(n^2 - L^2)L}{(2L-1)\Delta E_{Lower}} - \frac{(n^2 - (L+1)^2)(L+1)}{(2L+1)\Delta E_{Upper}} \right\} E^2 \tag{2.40}$$

In Eq. 2.40, $\Delta E_{Lower}$ is said to be positive if the $L$-1 state is lower in energy than the $L$ state, and the $\Delta E_{Upper}$ is positive when the $L$+1 state is higher in energy than the $L$ state, both energy differences in Eq. 2.40 have units of MHz. The correction for the Stark shift can be calculated

for individual levels or for rf intervals, in the case of the rf interval the shift must be calculated for each level involved in the rf transition and the relative shift determined.

## Chapter 3: Rf RESIS study to determine properties of $Th^{4+}$

### 3.1 Background on the $Th^{4+}$ experiment

Radon-like thorium, $Th^{4+}$, was the first thorium ion of interest to be studied in this program. The optical RESIS study of the $Th^{3+}$ Rydberg states was completed by the previous grad student working on this project, Mark Hanni, and was reported in his dissertation [17] and published in Ref. [21]. This preliminary work reported the dominant properties of $Th^{4+}$ that control the $Th^{3+}$ Rydberg fine structure. The ground state of $Th^{4+}$ is $^1S_0$ , with a $J_c$=0, meaning that $Th^{4+}$ does not have any permanent moments. All the properties controlling the fine structure would be induced moments in the core, i.e. polarizabilities. The effective potential describing $Th^{3+}$ Rydberg states has only a scalar component, the first term of Eq. 1.18, since the higher order tensor ranks are not possible with $J_c$=0. The $Th^{3+}$ Rydberg fine structure produced from a scalar effective potential consists of one energy level for each $L$, with the deviation from the hydrogenic energy increasing when moving to lower $L$s. The dominant $Th^{4+}$ property determining the energy difference between $L$s is the scalar dipole polarizability. The study done by this research program in 2010 with the optical RESIS technique measured a set of RESIS optical spectra for $Th^{3+}$ Rydberg states. Three different transitions were measured: the $n$=37 to $n'$=73, the $n$=38 to $n'$=79 and the $n$=37 to $n'$=76. The optical spectra allowed for the resolution of the $L$=7, 8, 9, and 10; all other $L$s were not resolvable from the high-$L$ peak or had lifetimes too short to allow observation. An example of one of the spectra is seen in Fig. 1.5. The uncertainty in the fine structure energies from each of the $nL$ to $n'L'$ transitions was approximately 20MHz. To extract the properties of $Th^{4+}$ the observed energies differences were scaled, plotted and fitted to the effective potential model. The intercept of the scaled energy plot is related to scalar dipole

polarizability, and the slope gives information scalar quadrupole polarizability. The preliminary optical study found

$$\alpha_{D,0} = 7.61(6) a.u.$$
$$\alpha_{Q,0} = 47(11) a.u.$$

A more detailed discussion of this work is contained the published paper [21] and in the dissertation of Mark Hanni [17].

The published results from the optical RESIS measurement provided the first glimpse into the properties of $Th^{4+}$. The comparison of the experimental values with theory enabled the first test of the theoretical calculations for $Th^{4+}$. Some theoretical calculations of the scalar dipole polarizability were in very good agreement with the experimental determination, to within 1.5% [21], while other calculations differenced by more than 30% with the experimental determination. The scalar quadrupole polarizability on the other hand disagreed with the calculated value by almost 40% [17]. Prior experience with $Si^{2+}$ revealed that the determination of $\alpha_{Q,0}$ can be particularly sensitive to the higher order terms in the effective potential [34]. The $\alpha_{Q,0}$ is extracted from the initial slope of the plot of the scaled energies. If higher order terms are contributing to the fine structure then there would be curvature in the scaled energy plot, which could affect the determination of the initial slope. The fit of the optical RESIS fine structure measurements for possible curvature was limited by the precision of the optical measurements and limited range *L*s observed.

In order to increase the precision of the measured properties and clarify the possible contribution of higher order terms in the effective potential, more precise measurements of the $n$=37 $Th^{3+}$ high-$L$ Rydberg fine structure were undertaken using the rf RESIS technique. The rf RESIS technique offers a two order of magnitude improvement in precision over the optical

RESIS technique. The rf fine structure measurements also allow extension of the data to include measurements on higher *L*s, unresolved in the optical study. The increased precision in the measurement of the energy levels and the additional levels measured allowed for the more precise determination of $Th^{4+}$ properties and the inclusion of the possible of higher order terms in the analysis of the measurements. The rf RESIS measurements were completed in two parts. The first part measured the energy intervals between the $L$=9 to 15 with sub-MHz precision [35]. The second part of the study increased the precision on the positions of the higher $L$ states, $L$=14 and $L$=15, and extended the data to include the $L$=8 [36]. This chapter describes the rf measurements, the analysis of those measurements to extract $Th^{4+}$ properties, and the comparison of the resulting properties with theory.

### 3.2 Rf measurements of the $n$=37 $Th^{3+}$ Rydberg fine structure

Rf measurements of the $n$=37 $Th^{3+}$ high-$L$ Rydberg fine structure were carried out on the beam line at JRML, using the apparatus discussed in Chapter 2 of the dissertation. Illustrated in Fig. 3.1 is the $n$=37 $Th^{3+}$ Rydberg fine structure, with the observed rf transitions denoted by the colored line connecting the levels. In Fig. 3.1 the zero on the y-axis in this figure is the estimated hydrogenic energy for $n$=37, but only the relative position of the different levels were actually measured.

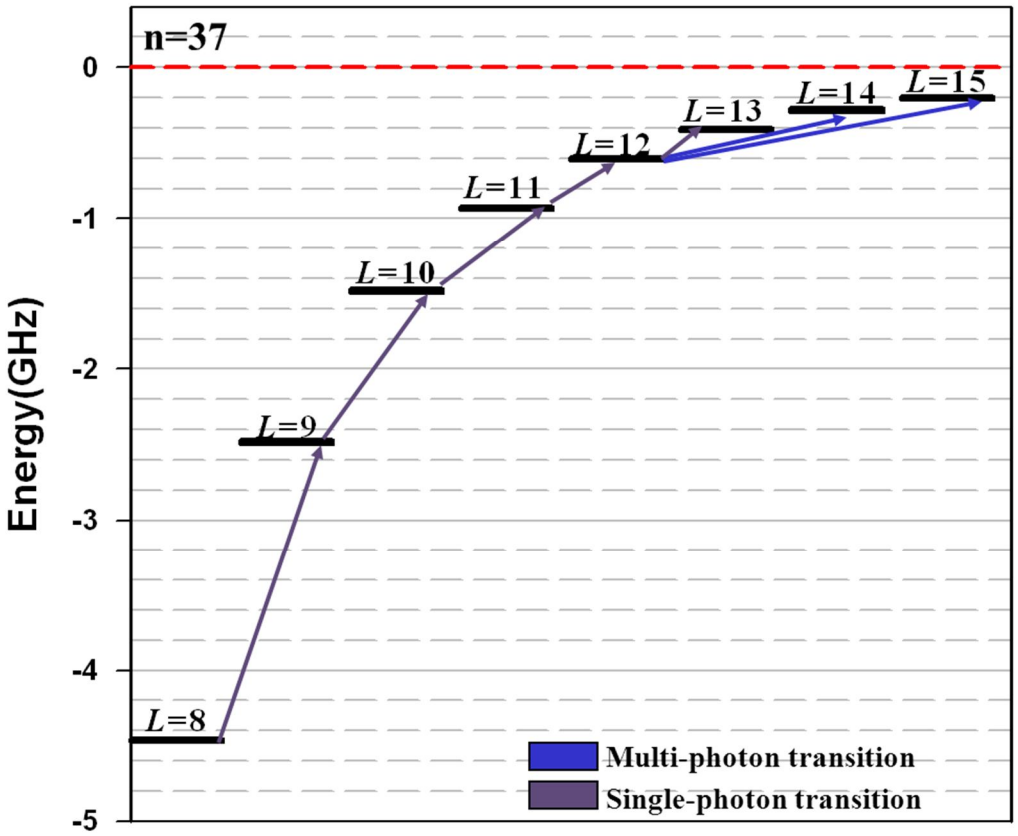


Figure 3.1: The fine structure of the $n$=37 $Th^{3+}$ Rydberg levels with the observed rf transitions denoted by the colored lines connecting the levels. In purple are the single photon transitions observed and in blue are the two and three photon transitions. The y-axis is the energy difference from hydrogenic in GHz for a given $L$ level, with the red dashed line representing the hydrogenic energy for $n$=37.

The rf transitions used to measure these fine structure intervals fall into one of two categories. The first category is the single photon transitions, this kind of transition only allows for the measurement of the energy interval over $\Delta L$=1, for example the $L$= 8 to 9 interval. The second category is the multi-photon transitions, this type of transition can measure the interval over $\Delta L$>1, the $L$=12 to 14 transition is an example of a multi-photon transition. A total of seven rf transitions were used to map out the $n$=37 $Th^{3+}$ high-$L$ Rydberg fine structure, five single photon transitions and two multi-photon transitions.

The rf measurements of this fine structure pattern for the $n$=37 $Th^{3+}$ Rydberg states relied on the RESIS technique as a way of detection. Using the resolution in the RESIS excitation spectrum $n$=37 to $n'$=73, seen in Fig. 1.5, it was possible to detect either the removal of population or the addition of population to given $L$ level. The measurement of the rf transitions of the fine structure energy intervals depended on the use of the $CO_2$ laser interaction regions (LIRs) to help create and detect population differences. Table 3.1 gives the different rf intervals measured, the $n$=37 $L$ each LIR was placed on for the detection of each of the rf transitions, the initial estimated location of each transitions given the preliminary properties [21], and the final measured positions. The use of the RESIS technique to detect the rf signal is discussed in more detail in Chapter 2. For $Th^{4+}$ the procedure was to set both LIRS on the lower $L$ of the rf transition of interest. For example, the $L$=11 to 12 transitions would be seen by placing both LIRs on the $L$=11. LIR 1 acts to deplete the $L$=11 population by exciting it from the $n$=37 level to the $n'$=73 level. The population of the $L$=11 state would then be replenished by equalizing the $L$=11 and $L$=12 population with the rf transition between the two states.

Table 3.1: Summary of the measured $n$=37 fine structure transitions in $Th^{3+}$. Column one of this table gives the $n$=37 fine structure intervals measured. Columns two and three gives the $n$=37 $L$ that LIR 1 and LIR 2 were placed on for the detections for a specific interval. Column four gives the estimated frequencies for the interval of interest, found with the preliminary properties [21]. The uncertainty in the simulated intervals was a result of altering the uncertainty in the core properties by one standard deviation and seeing how that affected the estimated intervals. The final column gives the measured frequencies for the interval determined from the rf study reported here along with their uncertainties.

| $L$ -$L$ ' | LIR 1 | LIR 2 | Estimated Interval(MHz) | Measured Interval(MHz) |
|---|---|---|---|---|
| 8-9 | 8 | 8 | 1951(29) | 1937.95(17) |
| 9-10 | 9 | 9 | 1010(13) | 1008.57(25) |
| 10-11 | 10 | 10 | 561(6) | 562.20(10) |
| 11-12 | 11 | 11 | 330(3) | 331.35(6) |
| 12-13 | 12 | 12 | 203(2) | 204.52(6) |
| 12-14 | 12 | 12 | 333(3) | 335.70(7) |
| 12-15 | 12 | 12 | 420(3) | 422.79(17) |

Then LIR 2 would again excite the $n$=37 $L$=11 to the $n$=73 level for detection. If the rf frequency was on resonance with the frequency difference between the $L$=11 and $L$=12 then more population is excited to the $n$=73 level. The rf field in the rf region was modulated and the corresponding change in the $n$=73 population was measured with a lock-in amplifier. By scanning through a possible frequency range for the $L$=11 to 12 it was possible to measure the frequency difference between the two states to sub-MHz precision, an example of such a scan is seen in Fig. 3.2.

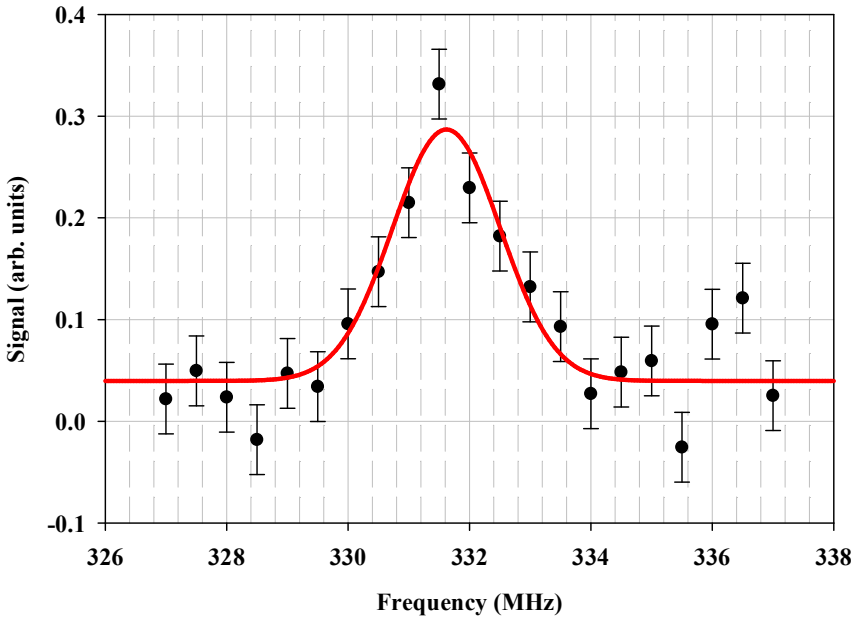


Figure 3.2: Observation of the rf transition of the $n$=37 $L$=11 to 12 in the $Th^{3+}$ Rydberg fine structure with the electric field in the rf region traveling anti-parallel to the direction of the ion beam, co-propagating. This data was taken from lab book JAK2, page 091. The red line represents the fit of the data to a four parameter Gaussian to determine its center.

The observation of rf transitions requires knowledge of the general location of the transitions and the electric field necessary to induce a specific transitions between states. The estimated location of each of the intervals is given in Table 3.1, calculated using the properties determined during the optical study [21]. Section 2 of Chapter 2 discussed the electric field necessary to observe a transition and related that to the power being read on the output of the rf region, since there is no direct measure of the electric field in the rf region. The observations of the single photon intervals between $L$=8 and $L$=13, like the $L$=11 to 12 seen in Fig 3.2 were carried out multiple times using the approximate recommended power in the rf region. An example of each of the transitions can be seen in Appendix A. The transit time through the rf region made the minimum width for a transition approximately 2.3MHz; the largest spin splitting expected would be on the $L$=8 to 9 transition, approximately 2.5MHz. While the $L$=8 to 9

transition looks broad, there was no sign of resolved spin splitting on that resonance, therefore the possibility of spin splitting was neglected when fitting observed resonances. All the observed resonance for the $n$=37 $Th^{3+}$ Rydberg fine structure were fit to four parameter Gaussians to find their centers. Each of the intervals was observed in both the co-propagating and counter-propagating directions. Table 3.2 gives all of the observations for the single photon transitions. Each transition was observed between two and seven times with the transitions involving the lower $L$s only being observed twice. To determine the final interval for the $Th^{3+}$ Rydberg fine structure it was necessary to combine and average all the data for each interval. To start, the data for each direction of propagation was combined by taking weighted average of the measurements if more than one observation occurred. A straight average of the result for each direction of propagation was then made to find the final result for the fine structure interval. This is shown in Table 3.2. The apparent $\beta$ for each transition was also calculated as a check, using Eq. 2.37, to confirm that the observed Doppler shift was consistent with what was predicted given the speed of the beam. For all of the single photon transitions observed, the apparent $\beta$ is consistent with the predicted $\beta$=0.0009620 (assuming 25kV terminal potential). For each transition in Table 3.2 the $\Delta\beta$, the difference between the calculated $\beta$ and the observed $\beta$, $\Delta\beta = apparent\ \beta - 0.000962$ has been shown, and in all cases the observed $\beta$ is within one standard deviation of the calculated.

Table 3.2: Measured single photon transitions in the $n$=37 $Th^{3+}$ Rydberg fine structure. This table has been broken into sections, one section for each of the single photon transitions intervals measured. Five single photon intervals between $L$=8 to $L$=13 were observed. The first column gives the lab book and page of the observation. The second column gives the direction of propagation of the rf electric field with respect to the ion beam. When the electric field in the rf region is propagating parallel to the ion beam it is said to be co-propagating and denoted by ⇉ in the table. If the electric field is propagating anti-parallel to the ion beam it is called counter-propagating and denoted by ⇆ in the table. The final column gives the fitted center of the observation, $f_{measured}$, in MHz. Below the measurements, the final column gives the weighted average of each directions of propagation, if more than one measurement exists. The final result, the straight average of the two directions of propagation is also given in the final column along with the apparent β. The difference between the apparent β and the calculated β from the terminal potential is also given for each transition.

***L* =8 to 9**

| Lab Book | Direction | $f_{measured}$(MHz) |
|---|---|---|
| Average of 8 passes<br>JAK7-006, 007,008 and 009 | ⇉ | 1939.68(21) |
| Average of 10 passes<br>JAK7-010, 011,012,013,and 014 | ⇆ | 1936.22(26) |
| | AVG of ⇉ and ⇆ = 1937.95(17) | |
| | Apparent β = 0.00089(9)<br>Δ β = 0.00007(9) | |

***L* =9 to 10**

| Lab Book | Direction | $f_{measured}$(MHz) |
|---|---|---|
| Average of 7 passes<br>JAK3-008, 009, 010, and 011 | ⇉ | 1009.39(38) |
| Average of 9 passes<br>JAK2-137abc, 138, 139,140,and 141 | ⇆ | 1007.74(34) |
| | AVG of ⇉ and ⇆ = 1008.57(25) | |
| | Apparent β = 0.00082(25)<br>Δ β = 0.00014(25) | |

Table 3.2 continued:

***L* =10 to 11**

| Lab Book | Direction | $f_{measured}$(MHz) |
|---|---|---|
| JAK2-095 | ⇉ | 562.32(34) |
| JAK2-095b | ⇉ | 563.00(29) |
| JAK2-096 | ⇉ | 562.64(17) |
| JAK2-114c | ⇆ | 561.90(26) |
| JAK2-115 | ⇆ | 561.52(20) |
| JAK2-115b | ⇆ | 561.94(30) |
| | Weighted AVG of ⇉ = 562.67(14) | |
| | Weighted AVG of ⇆ = 561.72(14) | |
| | AVG of ⇉ and ⇆ = 562.20(10) | |
| | | Apparent β = 0.00085(18) |
| | | Δβ = 0.00009(18) |

***L* =11 to 12**

| Lab Book | Direction | $f_{measured}$(MHz) |
|---|---|---|
| JAK2-035 & 35b | ⇉ | 331.96(43) |
| JAK2-36abc | ⇉ | 331.87(26) |
| JAK2-38 & 38b | ⇉ | 331.92(20) |
| JAK2-084 | ⇉ | 331.70(23) |
| JAK2-091 | ⇉ | 331.62(12) |
| JAK2-112 | ⇆ | 330.96(9) |
| | Weighted AVG of ⇉ = 331.73(9) | |
| | Only ⇆ = 330.96(9) | |
| | AVG of ⇉ and ⇆ = 331.35(6) | |
| | | Apparent β = 0.00116(20) |
| | | Δβ = -0.00020(20) |

Table 3.2 continued:

***L* =12 to 13**

| Lab Book | Direction | $f_{measured}$(MHz) |
|---|---|---|
| JAK2-093 | ⇉ | 204.74(8) |
| JAK2-093b | ⇉ | 204.73(6) |
| JAK2-100 | ⇆ | 204.56(9) |
| JAK2-102 | ⇉ | 204.53(11) |
| JAK2-109 | ⇆ | 203.50(9) |
| JAK7-015 | ⇆ | 204.20(5) |
| JAK7-018 | ⇉ | 204.73(6) |
| | Weighted AVG of ⇉ = 204.71(4) | |
| | Weighted AVG of ⇆ = 204.33(12) | |
| | AVG of ⇉ and ⇆ = 204.52(6) | |
| | | Apparent β = 0.00093(32) |
| | | Δβ = 0.00003(32) |

The measurement of the single photon transitions allowed for the exact energy interval for the $n$=37 $L$=8 to 13 to be precisely mapped out. This extended the measured fine structure to include two additional $L$s not included in the optical study, the $L$=12 and $L$=13. These higher-$L$s were not well resolved in the optical RESIS excitation spectrum, Fig. 3.3 shows a zoomed in look of the resolved structure around the high-$L$ for the $n$=37 to 73 transitions. The minimum width of the transitions in the $n$=37 to 73 optical excitation spectrum is on the order of a couple hundred MHz. As the $L$s states get closer together in energy they will not be resolved from each other. From Fig. 3.3 it can be seen that the $L$=10 is well resolved from the high-$L$, the $L$=11 is partial resolved from the high-$L$, but all the other higher-$L$s are not resolved from the high-$L$. The position of the $L$=12 excitation was resolved from the high-$L$ by the observation of the $L$=11 to 12 rf transition, thus enabling the observation of the $L$=12 to 13 rf transition.

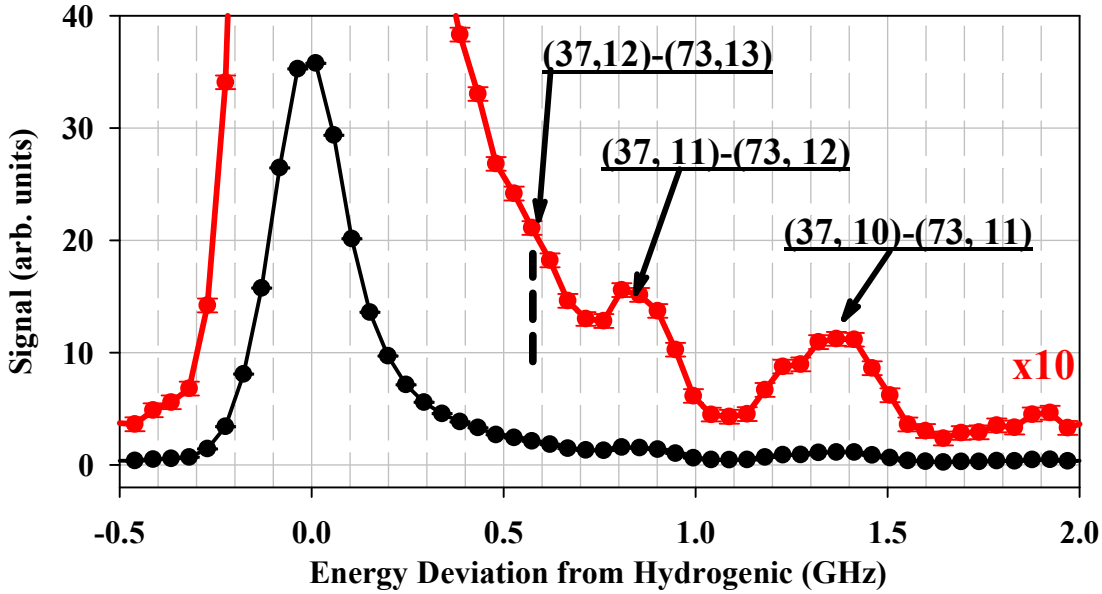


Figure 3.3: Zoomed in look of the $n$=37 to 73 RESIS optical excitation spectrum for $Th^{3+}$ Rydberg states. The x-axis is the energy deviation from hydrogenic in GHz, and the y-axis in the signal. The plot show the original signal in black and the signal times ten in red. The individual transitions are labeled. The dashed line shows the position of the $n$=27, $L$=12 excitation, inferred from the $L$=11 to 12 rf signal.

The measurement of the rf transitions using the RESIS technique relies on the ability to set both LIRs on one of the $L$ states involved in the rf transition of interest, to detect the population change produced from rf transitions. Moving to higher $L$s makes the states closer together, so it is no longer possible to optically resolve the two $L$-levels of the transitions. Thus it is problematic to set the LIRs on just one of the $L$ levels to detect the population change. Therefore, multi-photon transitions are used to measure the position of higher-$L$s with respect to the highest $L$ that can be resolved. The $L$=12 is able to be partially resolved from the high-$L$, by the $L$=11 to 12 rf transition, allowing for the detection of the population change to it by the multi-photon transitions with the $L$=14 and the $L$=15, using two photon and three photon transitions respectively.

The observation of the multi-photon transitions in the high-$L$ $Th^{3+}$ Rydberg fine structure requires higher power than the single photon transitions, and these transitions are also susceptible to AC shift, this is discussed in Section 2 of Chapter 2. Table 2.1 gave a summary of the power necessary and the calculated AC shift for the $L$=12 to 13 and $L$=12 to 15 transitions in the $n$=37 $Th^{3+}$ Rydberg fine structure. Using the estimated power necessary for the two and three photon transitions, both transitions were found, examples of both are shown in the Appendix A. For the initial observation of the transitions the power was set within a factor of two of the calculated optimum power. The size of the AC shift for a transition is a function of the amount of power being used in the observation. The AC shifts were calculated using a simplistic model that assumed that all the coupling potential between levels is not dependent on $L$ or $m$. Table 3.3 gives the AC shifts at saturation power determined by the model discussed in Chapter 2.

Table 3.3: Calculated AC shift rates for the multi-photon transitions in the $n$=37 $Th^{3+}$ Rydberg fine structure. Column one lists the transition, and column two gives the saturation power. The third column gives the AC shift expected at saturation power. The fourth column gives the calculated AC shift rate in terms of MHz/mW.

| $L$ -$L$ ' | $P_{sat}$(mW) | AC shift at $P_{sat}$ | Shift Rate (MHz/mW) |
|---|---|---|---|
| 12-14 | 0.064 | 0.066*MHz* | 1.04 |
| 12-15 | 0.956 | 0.680*MHz* | 0.72 |

To confirm the size of the AC shifts and the corrections that needed to be applied to the multi-photon transition intervals for this effect, it is necessary to measure the actual shift rate of at least one of the multi-photon transitions. Since the three photon transition experiences a larger shift, Table 3.3, its shift was measured to confirm the calculation done to predict the AC shift rates. For the three photon, $n$=37 $L$=12 to 15, four different power settings were used to observe the transition, with the power reading being taken from the rf power exiting the rf region, $P_{exit}$. With each power setting two measurements were taken, one in each direction of propagation.

The two directions of propagation were then averaged to find the Doppler corrected position of the transition for that power setting; this subset of data is in Table 3.4.

Table 3.4: A sub set of the observations of the $n$=37 $L$=12 to 15 in the $Th^{3+}$ Rydberg fine structure. The transition was observed at four different powers, with each power observed in both direction of propagation. The average position for each power was then found to correct for the Doppler shift, along with averaging the power for the two observations.

| Lab Book | Direction | $P_{exit}$ (mW) | $f_{measured}$(MHz) | $f_{AVG}$ (MHz) |
|---|---|---|---|---|
| JAK7-019 | ⇉ | 0.254 | 422.87(24) | 422.71(16) |
| JAK7-030 | ⇆ | 0.262 | 422.55(22) | $P_{AVG}$=0.26mW |
| JAK7-021 | ⇉ | 0.64 | 423.81(8) | 423.45(5) |
| JAK7-029 | ⇆ | 0.66 | 423.09(6) | $P_{AVG}$=0.65mW |
| JAK7-022 | ⇉ | 1.29 | 424.19(14) | 423.81(10) |
| JAK7-028 | ⇆ | 1.29 | 423.43(15) | $P_{AVG}$=1.29mW |
| JAK7-025 | ⇉ | 1.72 | 424.48(33) | 424.44(22) |
| JAK7-026 | ⇆ | 1.70 | 424.40(28) | $P_{AVG}$=1.71mW |

All the data taken to determine the AC shift rate was taken on one day, to limit the influence of other factors on the positions of the transitions. To find the experimental shift rate for the three photon transition the average position was plotted as a function of the rf power exiting the rf region, Fig 3.4. The data was then fitted to find the shift rate, both a weighted linear and un-weighted linear fit of the data was carried out. An average of the two different fitting methods was made to find the shift rate for the $n$=37 $L$=12 to 15 transition, the average fit of the data is shown by the red line in Fig. 3.4.

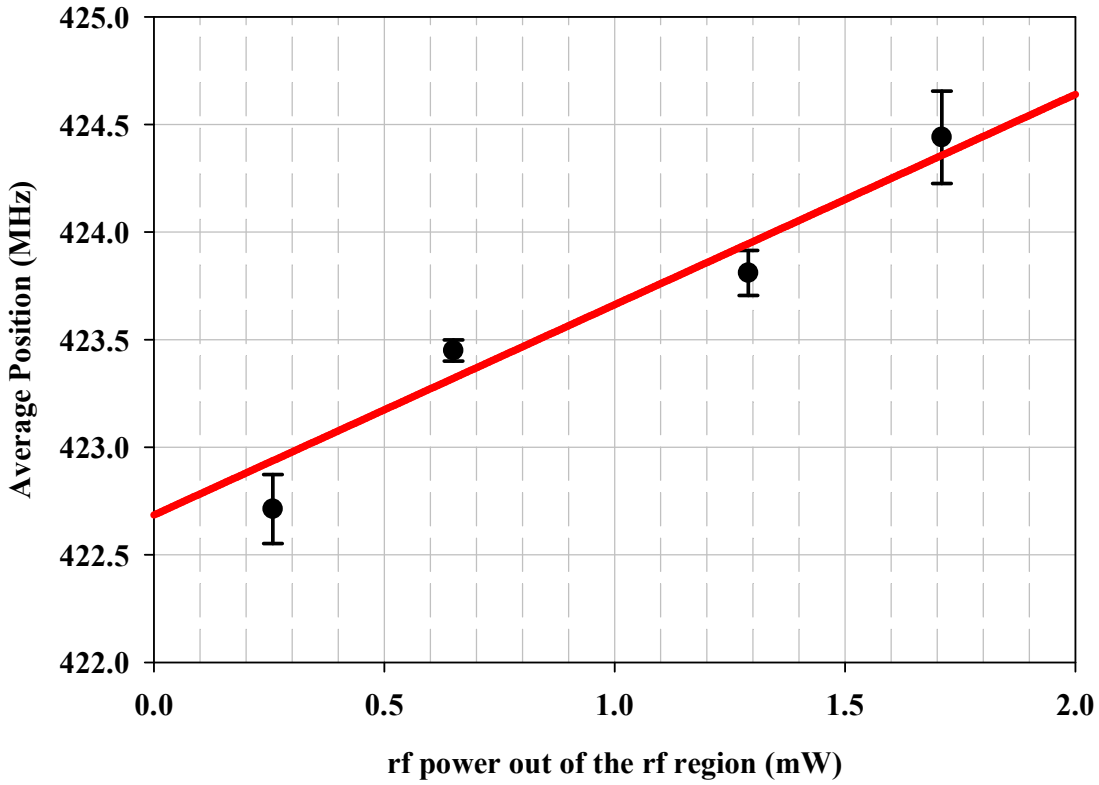


Figure 3.4: Extrapolation of the AC shift rate for the $n$=37 $L$=12 to 15, three photon transition. The x-axis is the power coming out of the rf region in mW and the y-axis is the average location of the transitions in MHz. The data for this plot came from a subset of $L$=12 to 15 observations, shown in Table 3.3. The fit of the data is the red line on the plot.

The fit of the data showed that the three photon, $n$=37 $L$=12 to 15, shift rate was 0.98(21)MHz/mW. This measured shift rate is only 1.24 standard deviations away from the calculated AC shift rate for this transition, showing the method used to approximate the multi-photon transitions is adequate. The two photon transition was then inferred using the experimentally determined three photon shift rate and the ratio of the calculated two photon and three photon shift rates. That ratio of the calculated shift rates showed that the two photon shift rate should be 1.46 times larger than the three photon shift rate. The two photon shift rate was inferred from multiplying that ratio times the experimentally determined three photon shift rate.

Therefore the AC shift rates for both of the multi-photon transitions was determined along with their errors and given to be

$$\Delta\nu_{12-14}(inferred) = +1.43(31)MHz/mW$$
$$\Delta\nu_{12-15}(measured) = +0.98(21)MHz/mW$$

with the power reading taken from the exit of the rf region in mW.

The determination of the AC shift rates for the multi-photon transitions allowed for the correction of the observation for their AC shifts. The observations for the $n$=37 $L$=12 to 14 and the $n$=37 $L$=12 to 15 are given the in Table 3.5 and examples of both are shown in Appendix A. In Table 3.5 the observed location of the transitions is given along with the direction of propagation and the power used to make the observation. Using the experimentally determined shift rates for each of the transitions, the AC shift for each observation was determined, and the observation was corrected for the AC shift. Both the shift and the corrected position of the observation are shown in the Table 3.5. Then like the single photon transitions, a weighted average of each direction of propagation was made, then a straight average of the two directions was done to correct for the Doppler shift. The error on the final result of each of the multi-photon transitions is the quadrature sum of the uncertainty in the average position of the transition and the uncertainty in the AC shift. The apparent $\beta$ for each transition was also calculated to check that the correct Doppler shift was observed. For both transitions the apparent $\beta$ was within error of the expected $\beta$, as was seen with the single photon as well. From Table 3.5 it can also be seen that the correction to the $L$=12 to 14 transition for the AC shift was on average 0.16MHz while the correction to the $L$=12 to 15 transition was 0.74 MHz on average.

Table 3.5: Measured multi-photon transitions observed in the $n$=37 $Th^{3+}$ Rydberg fine structure. In this table there is a section for each of the multi-photon transitions. The first section is for the two photon $L$=12 to 14 transition and the second section is for the three photon $L$=12 to 15. The first column gives the location in the lab book the data was taken from; the second column gives the direction of propagation. The co-propagating direction is denoted by ⇉ and the counter-propagating direction is denoted by ⇆. The third column gives what reading of the power exiting the rf region was during the observation. The fourth column gives the observed position, $f_{measured}$, in MHz of the transitions for the given power and direction of propagation. The fifth column gives the AC shift in MHz experienced by the transition given the amount of power exiting the rf region during the observation and the shift rate of the transition. The final column gives the position of the transition after it has been corrected for the AC shift, $f_{corrected}$, in MHz. The weighted average of both directions of propagation was then found for the uncorrected observation, the AC shift and the corrected observation. A straight average of the weighted averages of the two direction of propagation was then taken to find the Doppler corrected position of the transition. The final reported interval is then shown at the bottom along with the apparent $\beta$ and $\Delta\beta$, the difference between the apparent β and the β calculated from the terminal potential. The error on the final interval is the quadrature sum of the error in the AC shift and the error in the corrected average position.

**$L$ =12 to 14**

| Lab Book | Direction | $P_{exit}$ (μW) | $f_{measured}$(MHz) | AC Shift (MHz) | $f_{corrected}$(MHz) |
|---|---|---|---|---|---|
| JAK2-094 | ⇉ | 130 | 336.33(11) | 0.19(4) | 336.14(11) |
| JAK2-099 | ⇉ | 80 | 335.86(26) | 0.11(2) | 335.75(26) |
| JAK2-099b | ⇉ | 80 | 336.44(12) | 0.11(2) | 336.33(12) |
| JAK2-101 | ⇆ | 52 | 335.33(19) | 0.07(2) | 335.26(19) |
| JAK2-110 | ⇆ | 80 | 335.52(17) | 0.11(2) | 335.41(17) |
| JAK7-016 | ⇆ | 126 | 335.50(8) | 0.18(4) | 335.32(8) |
| JAK7-017 | ⇉ | 126 | 336.10(9) | 0.18(4) | 335.92(9) |
| | | Weighted AVG of ⇉ = | 336.23(10) | 0.16(3) | 336.07(10) |
| | | Weighted AVG of ⇆ = | 335.48(7) | 0.16(3) | 335.33(7) |
| | | AVG of ⇉ and ⇆ = | 335.86(6) | 0.16(3) | 335.70(6) |
| | | | | **Final =** | **335.70(7)** |
| | | | | Apparent β = | 0.00110(18) |
| | | | | Δβ = | -0.00014(18) |

Table 3.5 continued:

***L* =12 to 15**

| Lab Book | Direction | $P_{exit}$ (mW) | $f_{measured}$(MHz) | AC Shift (MHz) | $f_{corrected}$(MHz) |
|---|---|---|---|---|---|
| JAK2-094b | ⇉ | 0.92 | 424.63(34) | 0.90(20) | 424.73(34) |
| JAK2-097 | ⇉ | 0.66 | 424.17(26) | 0.65(14) | 423.52(26) |
| JAK2-097b | ⇉ | 0.42 | 423.60(42) | 0.41(9) | 423.19(42) |
| JAK2-098 | ⇉ | 0.26 | 423.98(34) | 0.25(5) | 423.73(34) |
| JAK2-111 | ⇆ | 0.64 | 423.19(47) | 0.63(14) | 422.56(47) |
| JAK2-116 | ⇆ | 0.64 | 423.56(33) | 0.63(14) | 422.93(33) |
| JAK7-019 | ⇉ | 0.25 | 422.87(24) | 0.25(5) | 422.62(24) |
| JAK7-021 | ⇉ | 0.64 | 423.81(8) | 0.63(14) | 423.18(8) |
| JAK7-022 | ⇉ | 1.29 | 424.19(14) | 1.26(27) | 422.93(14) |
| JAK7-025 | ⇉ | 1.72 | 424.48(33) | 1.68(37) | 422.80(33) |
| JAK7-026 | ⇆ | 1.70 | 424.40(28) | 1.67(36) | 422.73(28) |
| JAK7-028 | ⇆ | 1.29 | 423.43(15) | 1.26(27) | 422.17(15) |
| JAK7-029 | ⇆ | 0.66 | 423.09(6) | 0.65(14) | 422.44(6) |
| JAK7-030 | ⇆ | 0.26 | 422.55(22) | 0.26(6) | 422.29(22) |
| | | Weighted AVG of ⇉ = | 423.88(9) | 0.74(16) | 423.14(9) |
| | | Weighted AVG of ⇆ = | 423.17(7) | 0.74(16) | 422.43(7) |
| | | AVG of ⇉ and ⇆ = | 423.53(6) | 0.74(16) | 422.79(6) |
| | | | | **Final =** | **422.79(17)** |
| | | | | Apparent β = | 0.00084(13) |
| | | | | Δβ = | 0.00012(13) |

With the correction of the AC shift on the multi-photon transitions, the only other possible experimental corrections needed to the observed intervals comes from the possible DC Stark shift. This can occur on all the intervals no matter if they are single photon or multi-photon due to the possible presence of a stray electric field in the rf region during data taking. The DC Stark shift and its calculation is discussed in Section 4 of Chapter 2. Instead of calculating the shift to each state for a specific electric field strength, Eq. 2.40 was divided by electric field squared allowing for the DC Stark shift rate with units of MHz/((V/cm)$^2$) to be calculated for each of the states. The DC Stark shift rate was calculated for each of the different *L*s, *L*=8 to *L*=15 in *n*=37 and from those results the shift rates for each of the observed intervals was found, shown in Table 3.6.

Table 3.6: The *n*=37 $Th^{3+}$ Rydberg fine structure DC Stark shift rates. The first column of this table shows the transition and second column gives the observed frequency of the transition. The third column gives the DC stark shift rate for the transition, κ, in MHz/((V/cm)$^2$)

| *L* -*L* ′ | Interval (MHz) | κ(MHz/(V/cm)$^2$) |
|---|---|---|
| 8-9 | 1937.95(17) | -13.6 |
| 9-10 | 1008.57(25) | -19.9 |
| 10-11 | 562.20(10) | -17.9 |
| 11-12 | 331.35(6) | -37.5 |
| 12-13 | 204.52(6) | -48.6 |
| 12-14 | 335.70(7) | -109.3 |
| 12-15 | 422.79(17) | -182.9 |

The correcting of the transitions for the possibility of the DC Stark shift requires the knowledge of the magnitude of the stray electric field in the rf region during the data taking process. Unfortunately, the only way we have of monitoring possible stray field is by their influence on the measured interval, as was done in the determination of properties of $Si^{2+}$ [37], assuming that any such field is constant,. This method of determining the size of the stray electric field will be discussed in more detail in the next section.

### 3.3 Determination of $Th^{4+}$ properties

The measurement of the seven $n$=37 $Th^{3+}$ Rydberg fine structure intervals to sub-MHz precision presents the opportunity to extract the properties of $Th^{4+}$ with a level of precision that could rigorously test the atomic theory calculations. The determination of properties of $Th^{4+}$ from the measurement of the $Th^{3+}$ high-$L$ Rydberg fine structure requires understanding the full effective potential, and the other effects that can contribute or affect the measured fine structure intervals. Understanding these other contributions to the $Th^{3+}$ high-$L$ Rydberg fine structure allows for the correction of the measured interval so that it is possible to extract precise properties of $Th^{4+}$ from the measurements. This section discusses the corrections applied to the measured intervals and the determination of the properties of $Th^{4+}$ from the corrected intervals.

The properties of the core of the $Th^{3+}$ Rydberg state, $Th^{4+}$ determine the complexity and scale of the $Th^{3+}$ high-$L$ Rydberg fine structure. $Th^{4+}$ has a ground state of a $^1S_0$, this means that the fine structure is just a scalar fine structure whose scale is controlled by a scalar effective potential. The scalar effective potential is just the scalar component of the effective potential shown in Eq. 1.18, which shows only leading terms scalar due to the dominant scalar properties [7]. The $Th^{3+}$ high-$L$ Rydberg fine structure is primarily determined by the expectation value of the scalar effective potential, called the first order energy, $E^{[1]}$, but additional effects not included in the effective potential model contribute to the measured fine structure intervals as well. The additional effects not accounted for by the effective potential are the relativistic effect and the energy shifts due to coupling to intermediate Rydberg levels, which is referred to as $E^{[2]}(V_{eff})$. Both effects are discussed in Section 1.2. The energy of given states in the fine structure will therefore be the sum of the expectation value of the effective potential, $E^{[1]}$, the relativistic effect, $E_{\mathrm{Rel}}$ and the second order energies, $E^{[2]}(V_{eff})$. The rf measurements, $\Delta E_{obs}$,

gives the measured energies difference between $L$ states. Therefore the observed energy intervals will be the result of differences in the expectation value of the effective potential, the relativistic correction and the second order energy, Eq. 3.1

$$\Delta E_{obs} = \Delta E^{[1]} + \Delta E_{\mathrm{Rel}} + \Delta E^{[2]} \tag{3.1}$$

where

$$\Delta E^{[1]} = \left\langle nL' \middle| V_{eff} \middle| nL' \right\rangle - \left\langle nL \middle| V_{eff} \middle| nL \right\rangle \tag{3.2}$$

$$\Delta E_{\mathrm{Rel}} = E_{\mathrm{Rel}}(n, L') - E_{\mathrm{Rel}}(n, L) \tag{3.3}$$

and

$$\Delta E^{[2]} = E^{[2]}(n, L') - E^{[2]}(n, L) \tag{3.4}$$

It is possible to calculate these other effects, the relativistic effect and the second order energies so that the measurements can be corrected for them. The calculation of the relativistic corrections for the measured intervals is straight forward and given by Eq. 1.32, requiring only the input of the $n$, $L$ and $q$ for the level of interest. The correction for the relativistic effect was calculated, the correction for the measured intervals ranged in size from approximately 5 to 14MHz, well outside the uncertainty in the measured intervals. The correction $E^{[2]}(V_{eff})$ can also be calculated. The second order energies in terms of $V_{eff}$, for general $J_c$ has the form of Eq. 1.28, and for the case in this chapter when $J_c$=0, the leading term (proportional to $(\alpha_{D,0})^2$), has been simplified by Drake and Swainson [38] to be given by the analytic formula, Eq. 3.5, which only requires the input of the $n$, $q$, and $L$ of the states of interest along with an estimate of the scalar dipole polarizability, $\alpha_{D,0}$. Higher order terms should be much smaller.

$$
\begin{aligned}
E^{[2]}(n,L) &= E^{[2]}(V_{eff}) = E^{[2]}(\alpha_{D,0}\alpha_{D,0}) \\
&= -2q^6\alpha_{D,0}^2\left(\frac{(2L-3)!!}{(2L+3)!!}\right)^2\left\{\frac{(2L-5)!!}{(2L+5)!!}\frac{1}{n^7}\left[\left(\frac{9n^4}{[L(L+1)]^3}-\frac{6n^2}{[L(L+1)]^2}\right)\right.\right. \\
&\qquad \times\{45+7[89f_1(L)+520f_2(L)+80f_3(L)]\} \\
&\qquad \left.\left.+\{3+40[f_1(L)+6f_2(L)]\}\right] \right. \\
&\qquad \left.+\frac{1}{n^8}\left(\frac{27n^4}{[L(L+1)]^2}-\frac{30n^2}{[L(L+1)]}+7\right)\right\}
\end{aligned}
$$

$$
\begin{aligned}
f_1(L) &= L(L+1) \\
f_2(L) &= (L-1)L(L+1)(L+2) \\
f_3(L) &= (L-2)(L-1)L(L+1)(L+2)(L+3)
\end{aligned}
$$

(3.5)

The second order energies were calculated using the scalar dipole polarizability from the initial rf study [35], $\alpha_{D,0} = 7.720(6)$. The second order energies were later recalculated using the scalar dipole polarizability reported in this work. The slight difference in the second ordered energies, at most 0.03MHz for the $L$=8 to 9 interval, did not change the final fitted parameters. The uncertainty in the scalar dipole polarizability also does not result in a large uncertainty in the calculation of the second order energies. At most it produces 0.01MHz uncertainty in the calculation of the second order correction for the $L$=8 to 9 interval. The effect to all the other intervals is less than 0.01MHz. Values for both of the corrections to the measured intervals are shown in Table 3.7. By applying both corrections to the measured intervals the difference in the first order energies, $\Delta E^{[1]}$, were determined for each of the measured intervals, shown in Table 3.7.

Table 3.7: Corrections to the $n$=37 $Th^{3+}$ high-$L$ Rydberg fine structure measurements, necessary before the properties of $Th^{4+}$ can be extracted. Column one gives the measured intervals and column two gives the measured frequency of the intervals, $\Delta E_{obs}$ in MHz. Column three gives the relativistic correction, $\Delta E_{Rel}$ to the intervals in MHz and column four gives the second order correction, $\Delta E^{[2]}$, in MHz. Then column five gives the corrected positions, the first order energies, of each of the measured intervals in MHz.

| $L$-$L'$ | $\Delta E_{obs}$ (MHz) | $\Delta E_{Rel}$ (MHz) | $\Delta E^{[2]}$ (MHz) | $\Delta E^{[1]}$(MHz) |
|---|---|---|---|---|
| 8-9 | 1937.95(17) | 10.96 | 7.18 | 1919.81(17) |
| 9-10 | 1008.57(25) | 8.88 | 1.96 | 997.73(25) |
| 10-11 | 562.20(10) | 7.33 | 0.61 | 554.26(10) |
| 11-12 | 331.35(6) | 6.16 | 0.21 | 324.98(6) |
| 12-13 | 204.52(6) | 5.25 | 0.08 | 199.19(6) |
| 12-14 | 335.70(7) | 9.77 | 0.11 | 325.82(7) |
| 12-15 | 422.79(17) | 13.71 | 0.12 | 408.96(17) |

The difference in the first order energies extracted from the fine structure measurements can be then directly related to the difference in the expectation value of the scalar effective potential. The dominant $Th^{4+}$ property is the scalar dipole polarizability, $\alpha_{D,0}$, whose contribution to the first order energies is proportional to $\Delta\langle r^{-4}\rangle$, the difference in the hydrogenic expectation value of $r^{-4}$ [39]. Therefore, by scaling the first order energy differences, $\Delta E^{[1]}$, by the $\Delta\langle r^{-4}\rangle$, as shown in Table 3.8 the dominance of the $Th^{4+}$ scalar dipole polarizability in the fine structure pattern can be demonstrated. The ratio of the $\Delta E^{[1]}/\Delta\langle r^{-4}\rangle$ appears to be quite constant as seen in Table 3.8.

Table 3.8: The scaled first order energy intervals for the $n$=37 $Th^{3+}$ Rydberg fine structure measurement. Column one gives the interval measured and column two the gives the first order energies of the intervals in atomic units. The third column gives the difference in the hydrogenic expectation value of the $r^{-4}$ in atomic units. The column four gives the ratio of the first order energy to the difference in the hydrogenic expectation values of $r^{-4}$. The fifth column shows the ratio of the difference in the hydrogenic expectation of $r^{-6}$ over $r^{-4}$. The final column gives the DC stark shifts for the intervals scaled by the difference in the hydrogenic expectation value of $r^{-4}$, with units of $1/(V/cm)^2$ .

| $L$-$L'$ | $\Delta E^{[1]}$(a.u) | $\Delta\langle r^{-4}\rangle$ (a.u.) | $\Delta E^{[1]}/\Delta\langle r^{-4}\rangle$ | $\Delta\langle r^{-6}\rangle/\Delta\langle r^{-4}\rangle$ | $\kappa/\Delta\langle r^{-4}\rangle$ (V/cm)$^{-2}$ |
|---|---|---|---|---|---|
| 8-9 | 2.91778(26)x10$^{-7}$ | 7.36382x10$^{-8}$ | 3.9623(4) | 0.0142 | -0.03 |
| 9-10 | 1.51638(38)x10$^{-7}$ | 3.86990x10$^{-8}$ | 3.9184(10) | 0.0090 | -0.08 |
| 10-11 | 8.4238(15)x10$^{-8}$ | 2.16426x10$^{-8}$ | 3.8922(7) | 0.0060 | -0.20 |
| 11-12 | 4.9391(9)x10$^{-8}$ | 1.27367x10$^{-8}$ | 3.8779(7) | 0.0041 | -0.45 |
| 12-13 | 3.0274(9)x10$^{-8}$ | 7.36382x10$^{-9}$ | 3.8706(12) | 0.0030 | -0.94 |
| 12-14 | 4.9519(11)x10$^{-8}$ | 1.28006x10$^{-8}$ | 3.8685(8) | 0.0026 | -1.30 |
| 12-15 | 6.2155(26)x10$^{-8}$ | 1.60700x10$^{-8}$ | 3.8678(16) | 0.0024 | -1.73 |

To see the influence of the additional terms in the effective potential, the ratio of $\Delta E^{[1]}/\Delta\langle r^{-4}\rangle$ is plotted versus ratio of $\Delta\langle r^{-6}\rangle/\Delta\langle r^{-4}\rangle$, the ratio of the difference in the hydrogenic expectation values of $r^{-6}$ over $r^{-4}$, since the next term in the effective potential is proportional to $r^{-6}$. The polarizability plot, the plot of the ratio $\Delta E^{[1]}/\Delta\langle r^{-4}\rangle$ versus $\Delta\langle r^{-6}\rangle/\Delta\langle r^{-4}\rangle$ is shown in Fig. 3.5. The error on the points in the polarizability plot are due to the uncertainty in the measured interval found in Section 2 of this chapter, for some of the points the error bar is smaller than the point itself.

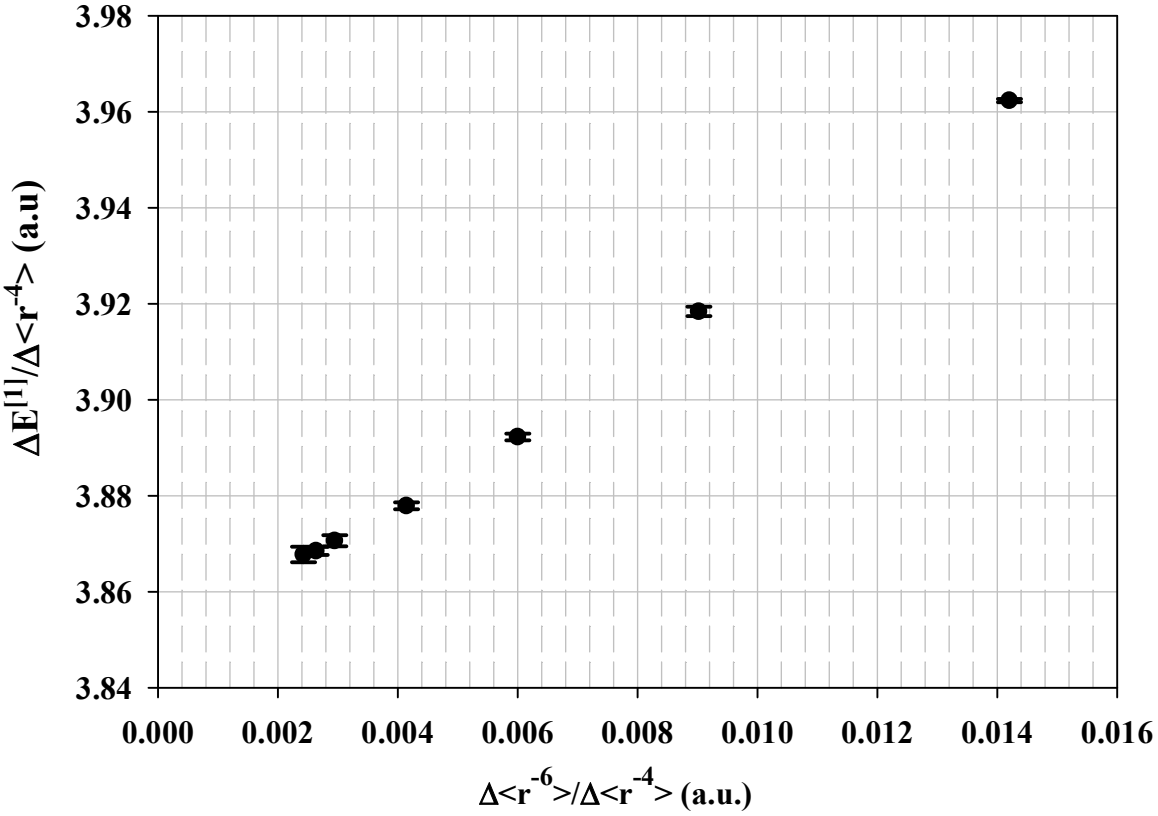


Figure 3.5: Plot of the scaled first order energies for the $Th^{3+}$ Rydberg fine structure measurements. The x-axis is the ratio of the difference in the expectations value of $r^{-6}$ over $r^{-4}$. The y-axis is the first order energies scaled by the difference in the expectation value of $r^{-4}$. The error placed on each of the points is the result of the uncertainty in the measured intervals.

Looking closely at the polarizability plot, Fig. 3.5 shows that there appears to be a slight upward curvature. This curvature cannot be explained by the effects of the possible uncorrected DC Stark shift as the scaled DC Stark shift rates, seen in Table 3.8, would cause a curvature in the data in the opposite direction than the one observed. This curvature is most likely the result higher order terms in the effective potential contributing to the fine structure intervals. To show this the data shown in Fig. 3.5 was fit to the form of Eq. 3.6,

$$\frac{\Delta E^{[1]}}{\Delta\left\langle r^{-4}\right\rangle} = B_4 + B_6 \frac{\Delta\left\langle r^{-6}\right\rangle}{\Delta\left\langle r^{-4}\right\rangle} + B_8 \frac{\Delta\left\langle r^{-8}\right\rangle}{\Delta\left\langle r^{-4}\right\rangle} + E_{SF}^2 \frac{\kappa}{\Delta\left\langle r^{-4}\right\rangle} \tag{3.6}$$

where the possibility of the higher order terms has been accounted for by the term proportional to $\Delta\left\langle r^{-8}\right\rangle \Big/ \Delta\left\langle r^{-4}\right\rangle$ and the Stark shifts have been included by the last term. In the last term $E_{SF}^2$ is the stray electric field squared, since the shift rates have units of $(a.u.)\big/(V/cm)^2$ , Table 3.8. The fit of the data to the form of Eq. 3.6 returned these parameters:

$$\begin{aligned} B_4 &= 3.8417(41) \\ B_6 &= 8.29(89) \\ B_8 &= 13(41) \\ E_{SF}^2 &= -0.0038(18) \end{aligned}$$

with the fit of the data being weighted by the uncertainty in each of the data points. The electric field squared determined by the fit was negative, which is physically impossible; the value of the electric field squared must be positive. This demonstrates that the curvature in the data of Fig. 3.5 is not of the correct sign to be due to DC Stark shifts.

Therefore the fit was redone and the stray electric field squared was constrained to be positive, Fig. 3.6 is the result of such a fit of the data. The refit found that when with the field was constrained to be positive, the quality of the fit was reduced, but the fit indicated that there was no stray electric field present in the rf region during the data taking. When the electric field in the fit is set to zero the fit returned these parameters:

$$\begin{aligned} B_4 &= 3.8500(17) \\ B_6 &= 6.59(49) \\ B_8 &= 88(26) \end{aligned}$$

with their statistical uncertainties given. The reduced chi-square of the fit is of 1.47, indicating a moderately good fit of the data (probability=21%).

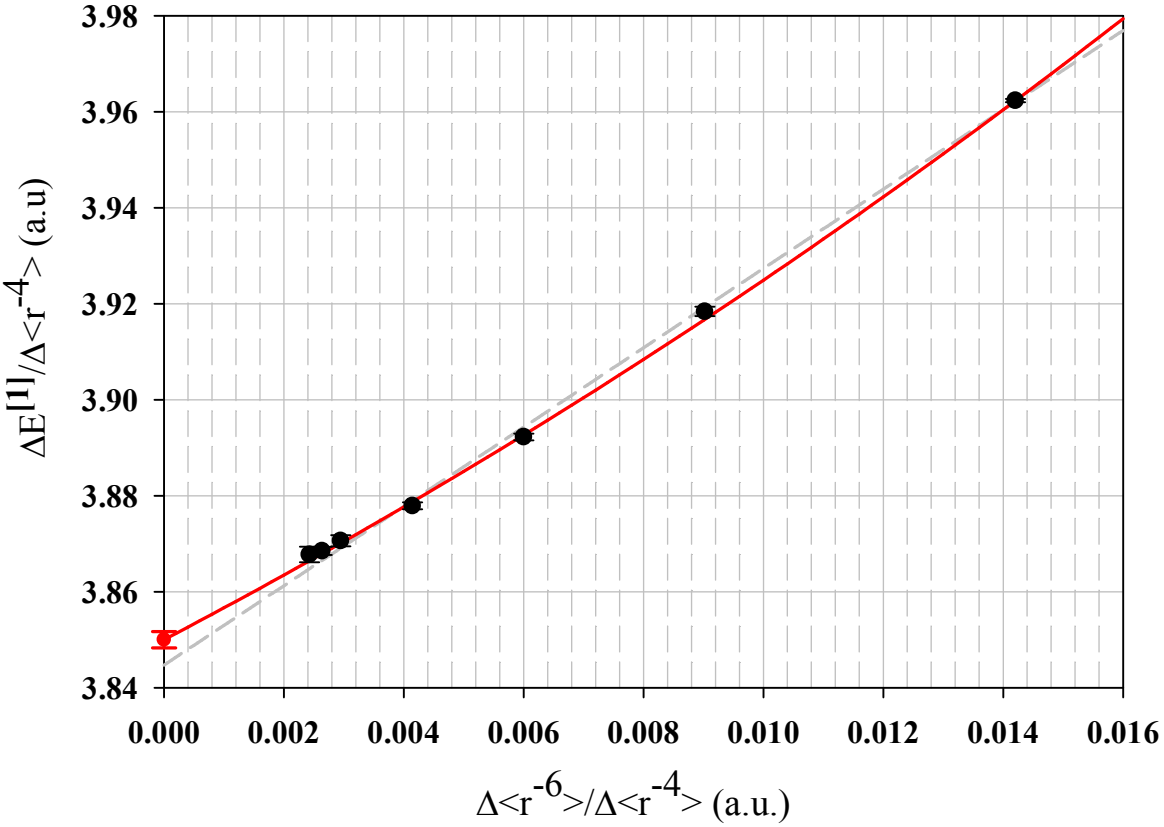


Figure 3.6: Plot of the scaled first order energies fit to determine properties of $Th^{4+}$, the data from the $n$=37 high-$L$ Rydberg fine structure measurements was fit to Eq. 3.6, with the electric field constrained to be positive. The result of such fit is shown by the red line and intercept on the y-axis. The gray dashed line represents just a weighted linear fit of the data, not allowing of term proportional to $r^{-8}$ or the term proportional to $E_{SF}^2$ in the fit.

The uncertainty in the electric field determination needs to be considered, since it will produce a systematic uncertainty in the fitted parameters in addition to their statistical uncertainty. To determine the uncertainty in the stray electric field, the quality of the fit was studied as a function of the assumed stray electric field squared. Allowing for the possibility of a stray electric field squared as large as $0.0010(\mathrm{V/cm})^2$ increased the reduced chi-square of the fit to 2.15. This corresponds to a factor of three decrease in the probability of the fit of the data. This decrease in the quality of the fit was used as a way of putting a limit on the uncertainty in the stray electric

field. A systematic uncertainty was added to each of the fitted parameters, corresponding to an uncertainty in the electric field square, $E_{SF}^2$, of 0.0010(V/cm)$^2$. The resulting fitted parameter then have two error bars placed on them

$$B_4 = 3.8500(17,22)$$
$$B_6 = 6.59(49,45)$$
$$B_8 = 88(26,20)$$

where the first number in the parentheses is the statistical uncertainty and the second number is the systematic uncertainty in the parameters due to the uncertainty in the possible stray electric field. The systematic uncertainty is comparable in size to the statistical uncertainty in the parameters so it cannot be neglected. The total uncertainty on each of the fitted parameters was then taken to be the quadrature sum of the statistical uncertainty and the systematic uncertainty, resulting in these final parameters and uncertainties

$$B_4 = 3.8500(28)$$
$$B_6 = 6.59(67)$$
$$B_8 = 88(33)$$

These fitted parameters provide the insight into the $Th^{3+}$ high-$L$ Rydberg fine structure and thereby the properties of $Th^{4+}$, such as the scalar dipole and quadrupole polarizabilities. The extraction of the scalar dipole and quadrupole polarizabilities of $Th^{4+}$ from the fitted parameters appears to be just a matter of equating the fitted parameters with the properties that contribute to each of the parameters. Eq. 1.18 only gave the leading term of the effective potential, neglecting the higher order terms. The parameters determined here show that consideration of the higher order terms in the $Th^{3+}$ high-$L$ Rydberg fine structure is necessary. Eq. 3.7 gives the difference of the first order energies scaled by the differences in the hydrogenic expectation value of $r^{-4}$, recall the first order energy is expectation value of the effective potential.

$$\frac{\Delta E^{[1]}}{\Delta\left\langle r^{-4}\right\rangle} = C_4 + C_6\frac{\Delta\left\langle r^{-6}\right\rangle}{\Delta\left\langle r^{-4}\right\rangle} + C_7\frac{\Delta\left\langle r^{-7}\right\rangle}{\Delta\left\langle r^{-4}\right\rangle} + C_{8,L(L+1)}\frac{\Delta(L(L+1))\left\langle r^{-8}\right\rangle}{\Delta\left\langle r^{-4}\right\rangle} + C_8\frac{\Delta\left\langle r^{-8}\right\rangle}{\Delta\left\langle r^{-4}\right\rangle} + \ldots \tag{3.7}$$

where

$$C_4 = \frac{\alpha_{D,0}}{2}, \qquad C_6 = \frac{(\alpha_{D,0} - \beta_{D,0})}{2}, \qquad C_7 = -\left(\frac{8q}{5}\gamma_{D,0} + \frac{\delta}{2}\right), \qquad C_{8,L(L+1)} = \frac{18}{5}\gamma_{D,0}$$

and

$$C_8 = \frac{(\alpha_{O,0} - 6\beta_{Q,0} + 72\gamma_{D,0})}{2}.$$

The first two terms are the familiar leading terms from Eq. 1.18 made up of the dominant scalar properties, the scalar dipole polarizability, $\alpha_{D,0}$, scalar quadrupole polarizability, $\alpha_{Q,0}$ and 1st non-adiabatic dipole polarizability, $\beta_{D,0}$. The additional higher order contributions come from the 2nd non-adiabatic order scalar dipole polarizability, $\gamma_{D,0}$, the adiabatic scalar octupole polarizability, $\alpha_{O,0}$ and the 1st non-adiabatic quadrupole polarizability, $\beta_{Q,0}$. All of these properties are defined in terms of matrix elements of the core and excitation energies in the work of Woods [7]. The 1st adiabatic contribution from the third-order perturbation energy, $\delta$, is not presented in the work of Woods [7], but this term's importance in the scalar effective potential has been seen in the work with the Rydberg fine structure of $Si^+$ [34].

The extraction of the scalar dipole and quadrupole polarizabilities of $Th^{4+}$ from the fitted parameters appears to be just a matter of equating the fitted parameters, $B_4$, or $B_6$ with the coefficients of Eq. 3.7, $C_4$ or $C_6$. This simplistic equating of the fitted coefficients with the properties assumes that the additional higher order terms, proportional to $\Delta\left\langle r^{-7}\right\rangle / \Delta\left\langle r^{-4}\right\rangle$ and $\Delta L(L+1)\left\langle r^{-8}\right\rangle / \Delta\left\langle r^{-4}\right\rangle$, neglected in the fitting of the data, are somehow accounted for by the $C_8$ term. The work with the determination of the $Si^{2+}$ properties showed that this assumption about

the additional higher order term is incorrect. These additional higher order terms can alter all the fitted parameters [34]. This makes the equating of coefficients in Eq. 3.7 with the fitted parameters to determine properties of $Th^{4+}$ problematic, unless the effects from the higher order terms are accounted for. It is, unfortunately, impractical to extract each $C_i$ coefficient in Eq. 3.7 independently from the data because their contributions are not linearly independent.

Table 3.9: The ratio of the hydrogenic expectation values in the $n$=37 for the $Th^{3+}$ Rydberg fine structure [39]. All values are in a.u.

| $L$-$L'$ | $\Delta\langle r^{-7}\rangle/\Delta\langle r^{-4}\rangle$ | $\Delta L(L+1)\langle r^{-8}\rangle/\Delta\langle r^{-4}\rangle$ | $\Delta\langle r^{-8}\rangle/\Delta\langle r^{-4}\rangle$ |
|---|---|---|---|
| 8-9 | $1.7128\times10^{-3}$ | $1.4287\times10^{-2}$ | $2.1310\times10^{-4}$ |
| 9-10 | $8.5781\times10^{-4}$ | $6.9317\times10^{-3}$ | $8.3319\times10^{-5}$ |
| 10-11 | $4.6188\times10^{-4}$ | $3.6441\times10^{-3}$ | $3.6056\times10^{-5}$ |
| 11-12 | $2.6339\times10^{-4}$ | $2.0390\times10^{-3}$ | $1.6897\times10^{-5}$ |
| 12-13 | $1.5738\times10^{-4}$ | $1.1993\times10^{-3}$ | $8.4448\times10^{-6}$ |
| 12-14 | $1.3418\times10^{-4}$ | $1.0186\times10^{-3}$ | $6.8910\times10^{-6}$ |
| 12-15 | $1.1964\times10^{-4}$ | $9.0609\times10^{-4}$ | $5.9878\times10^{-6}$ |

Table 3.9 provides values of the ratio of the hydrogenic expectation values involved in the higher order terms in Eq. 3.7. To understand different terms in Eq. 3.7 and their effect of the polarizability plot, each of the terms were graphed versus the $\Delta\langle r^{-6}\rangle/\Delta\langle r^{-4}\rangle$ for the seven data points in the study reported here in Fig. 3.7. Each of the terms was normalized to one for the $L$=8 to 9 point so that all of the curves could be visible on the same plot. From this plot it can be seen that the first two terms of the Eq. 3.7 contribute to the intercept and the slope for the polarizability plot.

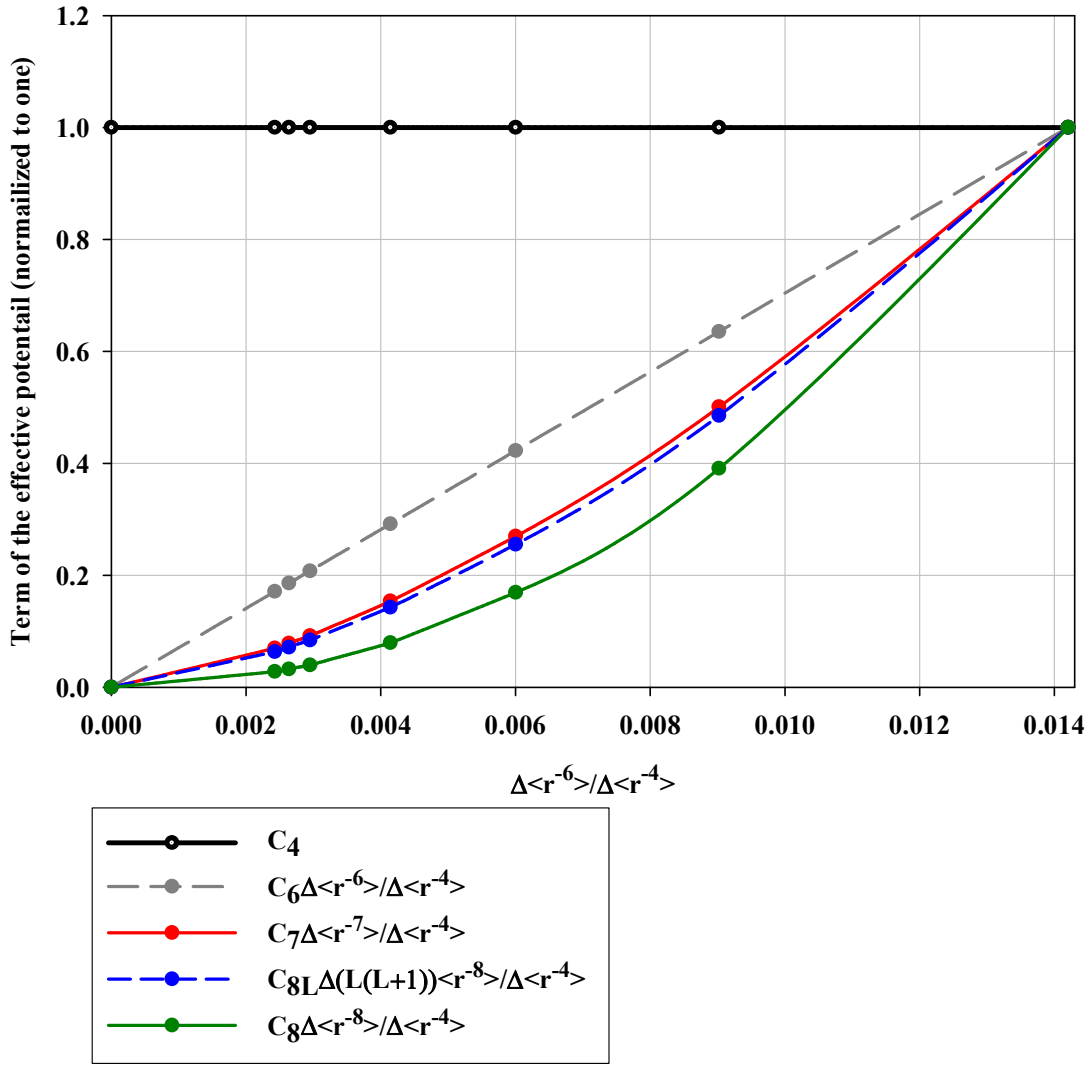


Figure 3.7: Plot of the terms in Eq. 3.7 versus the $\Delta\langle r^{-6}\rangle/\Delta\langle r^{-4}\rangle$ for the seven point measured in the study. All the terms were normalized to one for the $L$=8 to 9 point so that the terms could be on the same y-axis.

The three higher order terms would all contribute to the curvature and the initial slope. The term proportional to the $\Delta\langle r^{-7}\rangle$ and the term proportional to the $\Delta(L(L+1))\langle r^{-8}\rangle$ appear very similar in shape and are intermediate in shape between the term proportional to $\Delta\langle r^{-8}\rangle$ and $\Delta\langle r^{-6}\rangle$. In fact, both of these terms can be represented as a linear combination of $r^{-4}$, $r^{-6}$ and $r^{-8}$. As a

result, while all these higher order terms might be contributing to the scaled first order energies, the data can be accounted for by just including terms proportional to $\Delta\langle r^{-8}\rangle/\Delta\langle r^{-4}\rangle$ in the fit, like what was done in Eq. 3.6. Any contribution of the terms proportional to $\Delta\langle r^{-7}\rangle/\Delta\langle r^{-4}\rangle$ and $\Delta(L(L+1))\langle r^{-8}\rangle/\Delta\langle r^{-4}\rangle$ to the data will influence the choice of fit parameters, and this must be considered in interpreting the parameters.

The effect of these higher order terms were explored in the study of high-$L$ Rydberg states of $Si^{+}$ which determined properties of $Si^{2+}$ [34]. Following the same approach as the silicon study, the size of these additional higher order terms was taken from calculations. Their effects on the parameters extracted from the fit of the data were estimated by the parameterizing their shape. The parameterization of the additional higher order terms, $\Delta\langle r^{-7}\rangle/\Delta\langle r^{-4}\rangle$ and $\Delta L(L+1)\langle r^{-8}\rangle/\Delta\langle r^{-4}\rangle$, were carried out by fitting these additional higher order terms to Eq. 3.6, in the same ways as the data was fit, with the exclusion of the term responsible for the DC Stark shifts. The fit of the higher order terms used the same weights as the fit of the scaled first order energies and the fits of these two additional higher order terms are shown in Fig. 3.8.

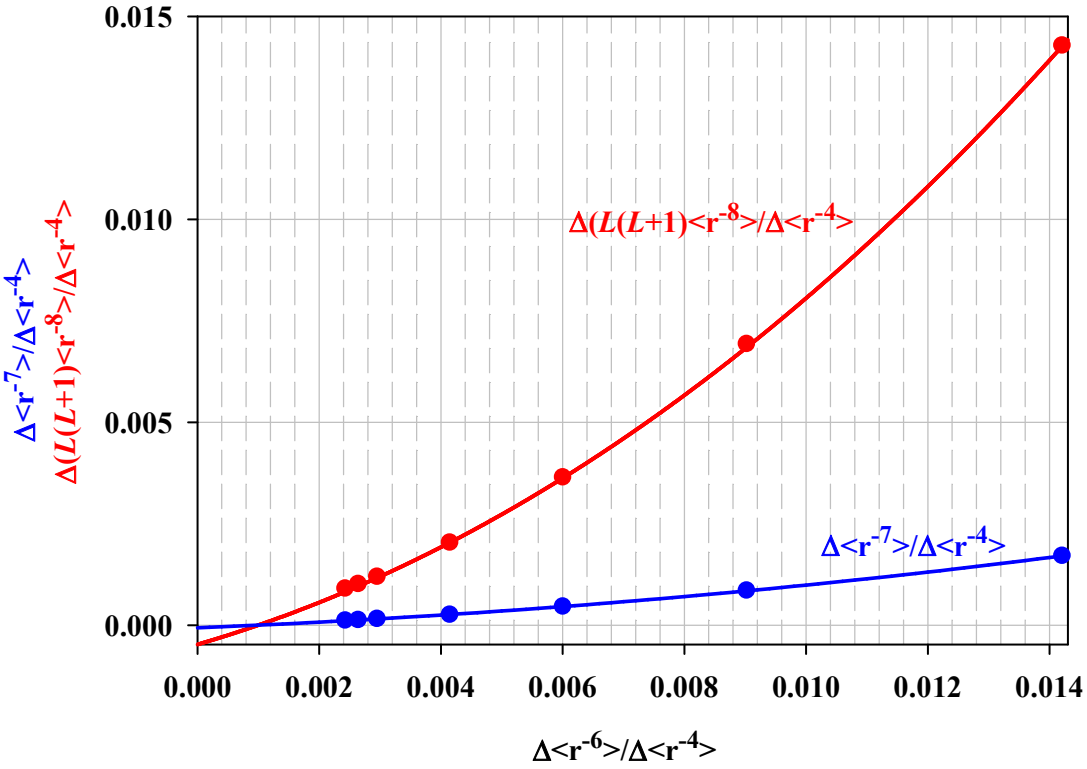


Figure 3.8: The fit of the higher order terms in the$Th^{3+}$ Rydberg fine structure for the seven points measured in $n$=37. The fit for each of set of point is shown by the solid line connecting each set of points. Each line is labeled by which higher order term it is.

The parameters determined from the fits of the additional higher order terms will show how each of the higher terms contribute to the parameter determined from the fit of the data. The fit of each of the higher order terms to Eq. 3.6 gave the resulting parameters

$$\frac{\Delta\langle r^{-7}\rangle}{\Delta\langle r^{-4}\rangle} \Rightarrow \begin{cases} B_4 = -6.46(81)x10^{-5} \\ B_6 = 0.0634(23) \\ B_8 = 4.1(1.2) \end{cases}$$

and

$$\frac{\Delta L(L+1)\left\langle r^{-8}\right\rangle}{\Delta\left\langle r^{-4}\right\rangle} \Rightarrow \begin{cases} B_4 = -4.74(59)x10^{-4} \\ B_6 = 0.455(17) \\ B_8 = 38.95(89) \end{cases}$$

With these results, the fitted parameter from the data, $B_4$, $B_6$ and $B_8$ can be written as a linear combination of the expected coefficients, $C_4$, $C_6$ and $C_8$, and the additional higher order terms $C_7$ and $C_{8,L(L+1)}$, Eq. 3.8.

$$\begin{aligned} B_4 &= C_4 - 6.46(81)x10^{-5}C_7 - 4.74(59)x10^{-4}C_{8,L(L+1)} \\ B_6 &= C_6 + 0.0634(23)C_7 + 0.455(15)C_{8,L(L+1)} \\ B_8 &= C_8 + 4.1(1.2)C_7 + 38.95(89)C_{8,L(L+1)} \end{aligned} \tag{3.8}$$

Then by substituting in the appropriate coefficients from Eq. 3.7 into Eq. 3.8, $B_4$, $B_6$ and $B_8$ can be written in terms of core properties, including four properties taken from calculations $\gamma_{D,0}$, $\delta$, $\beta_{D,0}$ and $\beta_{Q,0}$.

$$\begin{aligned} B_4 &= \frac{\alpha_{D,0}}{2} - 1.30(22)x10^{-3}\gamma_{D,0} + 3.23(41)x10^{-5}\delta \\ B_6 &= \frac{\alpha_{Q,0}}{2} - 3\beta_{D,0} + 1.23(6)\gamma_{D,0} - 0.032(1)\delta \\ B_8 &= \frac{\alpha_{O,0}}{2} - 3\beta_{Q,0} + 150(8)\gamma_{D,0} - 2.1(6)\delta \end{aligned} \tag{3.9}$$

This method of parameterizing for the higher order terms allows for the contribution of the higher order terms to be accounted for during the determining of the core properties, allowing the fitting of the actual data to be done with just the first three terms in Eq. 3.6.

The extraction of the properties from Eq. 3.9 and the parameters found from the data requires knowledge of the some of the additional properties of $Th^{4+}$. The extraction of the scalar

dipole polarizability, $\alpha_{D,0}$ and scalar quadrupole polarizability, $\alpha_{Q,0}$, from the $B_4$ and $B_6$ parameters both rely on properties that are dependent on the dipole operator. For the case of $Th^{4+}$ there exist theoretical calculations of the first non-adiabatic scalar dipole polarizability, $\beta_{D,0}$ and the 2nd non-adiabatic scalar dipole polarizability, $\gamma_{D,0}$. U. I. Safronova and M. S. Safronova used the relativistic random-phase approximation (RRPA) technique to calculate both of these properties to an estimated 5% precisions [40].

$$\beta_{D,0} = 2.97(15)\, a.u.$$
$$\gamma_{D,0} = 1.177(59)\, a.u.$$

The quoted 5% uncertainty is the result of their comparison of the calculation of the scalar dipole polarizability, $\alpha_{D,0}$ using the RRPA technique and a more accurate technique, the coupled-cluster technique, for many different ions [40], but not including $Th^{4+}$. The calculation of $\alpha_{D,0}$ relies on the same matrix elements and excitation energies as the calculation of $\beta_{D,0}$ and $\gamma_{D,0}$. But this 5% uncertainty on the RRPA calculation of $Th^{4+}$ appears to be conservative given the fact that the calculated value, $\alpha_{D,0} = 7.75$ proved to be within 1% of the determination of the scalar dipole polarizability from preliminary rf measurements [40].

While there were reported calculations for $\beta_{D,0}$ and $\gamma_{D,0}$, at the beginning of the preliminary rf measurements, there were no estimates of $\delta$. The $\delta$, is the result of the first adiabatic contribution to the third order energy and it is defined in terms of dipole and quadrupole matrix elements and excitation energies by Eq. 3.10 [34],

$$\delta = \frac{4\sqrt{2}}{15}\sum_{\lambda'\lambda''}\frac{\left\langle gJ_c=0\left\|\vec{D}\right\|\lambda' J_c=1\right\rangle\left\langle\lambda' J_c=1\left\|\vec{D}\right\|\lambda'' J_c=2\right\rangle\left\langle\lambda'' J_c=2\left\|\vec{Q}\right\|gJ_c=0\right\rangle}{\Delta E(\lambda')\Delta E(\lambda'')}$$

$$+\frac{2\sqrt{30}}{45}\sum_{\lambda'\lambda''}\frac{\left\langle gJ_c=0\left\|\vec{D}\right\|\lambda' J_c=1\right\rangle\left\langle\lambda' J_c=1\left\|\vec{Q}\right\|\lambda'' J_c=1\right\rangle\left\langle\lambda'' J_c=1\left\|\vec{D}\right\|gJ_c=0\right\rangle}{\Delta E(\lambda')\Delta E(\lambda'')} \tag{3.10}$$

where $\vec{D}$ is the dipole operator , $M^{[1]}$ and $\vec{Q}$ is the quadrupole operator, $M^{[2]}$, defined in Eq. 1.14. To calculate this parameter, δ, it is necessary to sum over two excited states so the matrix elements and the excitation energies between the states are needed. The denominator of the both the terms of $\delta$ are the product of energy differences between some excited states and ground state, unfortunately no measurements of the positions of any of energy levels of $Th^{4+}$ involved in the calculation exist. Therefore, to calculate δ it is necessary to have the excitation energies, the matrix elements connecting the ground state to the excited states, and the matrix elements that interconnect the excited states. The fifteen lowest excited states are involved in the estimating of δ, seven odd $J_c$=1 excited states and eight even $J_c$=2 excited states.

During the preliminary rf study [35] theoretical estimates of the matrix elements needed to calculate δ were determined from transition strengths provided by Don Beck [41], but that method of determining the matrix elements only gave the magnitude of the matrix elements. Therefore using the magnitude of the matrix elements involved, it was possible to only get a rough estimate of the δ,

$$\delta = 0 \pm 30\, a.u.$$

with the large uncertainty due to uncertainty in the signs of the matrix elements. This rough estimate of the δ parameter was used in the analysis of the preliminary rf data, and gave insight to the importance of the δ in extracting the $\alpha_{Q,0}$ from the measurements. After the completion of

the preliminary study it was determined that even if additional rf intervals were measured in the $n$=37 $Th^{3+}$ high-$L$ Rydberg fine structure, the analysis would be limited by the uncertainty of the estimated δ. Therefore, included in the publication of the preliminary rf results was a plea for the assistance in the calculation δ. Thankfully, M.S. Safronova undertook the calculation of the matrix elements and excitation energies necessary to calculate δ, including the sign, some of these calculations are reported in Ref. [40] while others were provided privately [42]. Two different approaches were used to calculate the necessary matrix elements and excitation energies needed to determine δ. The first approach used the multiconfiguration Dirac-Fock (MCDF) technique and that led to δ=16.8 a.u. The second approach used relativistic many body perturbation theory (RMBPT), which determined δ=14.0a.u. Given the difficulty of the calculation of δ, and with no clear indication of one method being more precise, the average of the two different approaches, MCDF and RMBPT, was taken as the result. A conservative 25% error was attached to that result to indicate the difficulty of such a calculation.

$$\delta = 15.4 \pm 3.9\, a.u.$$

Both of these results and the average are within the error bar of the previous estimate δ=0±30a.u. used to analyze the preliminary rf measurements [35]. This improved determination of δ was used in analysis presented here and in Ref. [36].

Using the theoretically calculated properties $\beta_{D,0}$, $\gamma_{D,0}$, and δ it is possible to extract the scalar dipole and quadrupole polarizabilities, using Eq. 3.9 from the $B_4$ and $B_6$ found from the fit of the data. The scalar dipole polarizability is given by

$$\begin{aligned}\alpha_{D,0} &= 2B_4 + 2.60(44)x10^{-3}\gamma_{D,0} - 6.46(82)x10^{-5}\delta \\ &= 7.700(6) + 0.0031(5) - 0.0010(3)\end{aligned}$$

which results in a determination of

$$\alpha_{D,0} = 7.702(6)\, a.u.$$

The uncertainty of the scalar dipole polarizability is only 0.08% and the net effect of the higher order terms proportional $\gamma_{D,0}$ and $\delta$ is less than the measurement uncertainty.

The scalar quadrupole polarizability is given by

$$\begin{aligned}\alpha_{Q,0} &= 2B_6 + 6\beta_{D,0} - 2.46(12)\gamma_{D,0} + 0.064(2)\delta \\ &= 13.2(1.3) + 17.8(9) - 2.9(2) + 1.0(3)\end{aligned}$$

which resulted in the determination of

$$\alpha_{Q,0} = 29.1(1.6)\, a.u.$$

The uncertainty on the scalar quadrupole polarizability is 5.5%. This large uncertainty is primarily due to the difficulty in determining the initial slope of the polarizability plot. For the scalar quadrupole polarizability the higher order terms also play a significant role in the determination of its value. Their inclusion decreases the extracted value of the scalar quadrupole polarizability by 6.5%. The determination of both of these properties with this level of precision provides the most accurate experimental determination of any $Th^{4+}$ properties to date. Both the scalar dipole polarizability and the scalar quadrupole polarizability shown here were reported in Ref. [36].

The other parameter determined from the fit of the data, $B_8$, gives information on the scalar octupole polarizability of $Th^{4+}$. The interpretation of this parameter was not the reported in Ref. [36] since it required knowledge of an additional core property that had not been estimated at the time of the publication. The additional property needed to extract the scalar octupole polarizability was the first non-adiabatic scalar quadrupole polarizability, for which no

theoretical estimates existed. The work of U. I. Safronova and M. S. Safronova [40] does calculate the matrix elements and the energies for the three lowest states and that work also estimated the location of the next highest state. Then using the formula for the first non-adiabatic scalar quadrupole polarizability presented in the work of Woods [7], it was possible to estimate this property.

$$\beta_{Q,0} = 51(3) a.u.$$

The uncertainty in this property is primarily due to the fact that the contributions from the additional states, other than the first three states, had to be estimated using the scalar quadrupole polarizability and the estimated energy of the next highest state. Plugging the estimate $\beta_{Q,0}$ into the formula for $B_8$ given in Eq. 3.9 along with the other core properties allows for the scalar octupole polarizability to be given by

$$\begin{aligned} \alpha_{O,0} &= 2B_8 + 6\beta_{Q,0} - 300(16)\gamma_{D,0} + 4.2(1.2)\delta \\ &= 176(66) + 306(18) - 354(26) + 64(24) \end{aligned}$$

which results in this determination of the scalar octupole polarizability

$$\alpha_{O,0} = 192(77)\, a.u.$$

This value for the scalar octupole polarizability is 2.5 sigma away from zero, and represents the first time that scalar octupole polarizability has been extracted from experimental measurements for $Th^{4+}$.

As the previous discussion indicated, the three $Th^{4+}$ polarizabilities, $\alpha_{D,0}$, $\alpha_{Q,0}$, and $\alpha_{O,0}$, extracted from the measurements are all dependent at some level on the calculation of other properties. Even though the extracted properties are primarily dependent on the fitted parameterization of the experimental measurements ($B_4$, $B_6$, and $B_8$) theoretical estimates of

other core properties are needed to extract the final values of the polarizabilities. To clarify this interdependence, Table 3.10 lists the polarizabilities and summarizes the measured and calculated values that enter into their determinations. Examination of Table 3.10 shows that the values obtained for the dipole polarizability is only minimally dependent on the calculated properties, but both the quadrupole and octupole polarizabilities have substantial contributions from calculated properties.

Table 3.10: Summary of the dependence of the three adiabatic polarizabilities of $Th^{4+}$ extracted from this study on the measured parameters ($B_4$, $B_6$, and $B_8$) and the calculated $Th^{4+}$ properties. Column one lists the reported polarizability and indicates its quoted precision. Column two shows the relevant measured parameters and it quoted precision. Column three shows the percentage contribution of the measured parameters to the final result for the polarizability. Column four lists the calculated properties used to obtain the final result and indicates its assumed precision. Column five shows the percentage contribution of each calculated property to the final result.

| Property (precision) | Measured (precision) | Contribution from Measured | Calculated Property (precision) | Contribution from Calculated |
|---|---|---|---|---|
| $\alpha_{D,0}$ (0.08%) | $B_4$ (0.072%) | 99.974(78)% | $\gamma_{D,0}$ (5%) | 0.040(6)% |
| | | | $\delta$ (25%) | -0.013(4)% |
| $\alpha_{Q,0}$ (5.5%) | $B_6$ (10.2%) | 45.4(4.5)% | $\beta_{D,0}$ (5%) | 61.2(3.1)% |
| | | | $\gamma_{D,0}$ (5%) | -10.0(7)% |
| | | | $\delta$ (25%) | 3.4(1.0)% |
| $\alpha_{O,0}$ (40%) | $B_8$ (37%) | 92(34)% | $\beta_{Q,0}$ (6%) | 159(9)% |
| | | | $\gamma_{D,0}$ (5%) | -184(14)% |
| | | | $\delta$ (25%) | 33(13)% |

The calculated properties $\beta_{D,0}$ and $\gamma_{D,0}$ depend on the distribution of the dipole excitation strengths and their estimated precision (5%) is likely very conservative given the 1% agreement for $\alpha_{D,0}$ obtained with the same theoretical method. Their influence on the extracted values of

$\alpha_{Q,0}$ and $\alpha_{O,0}$ is substantial but they have only slight influence on the quoted uncertainties of these extracted properties. The calculated quantity $\delta$ plays a similar role for both $\alpha_{Q,0}$ and $\alpha_{O,0}$. Its estimated 25% uncertainty is based on the level of agreement between the two calculations, as discussed. The calculated property $\beta_{Q,0}$ is important for extracting the value of the octupole polarizability $\alpha_{O,0}$, but it contributes little to its uncertainty.

### 3.4 Summary of $Th^{4+}$ properties

Before August 2010, there existed no independent experimental measurements of any kind for $Th^{4+}$ properties. The experimental work reported here in this dissertation on the determination of the properties of $Th^{4+}$ is the culmination of years of the experimental work on the measurement of the high-$L$ $Th^{3+}$ Rydberg fine structure for the purpose of extracting properties of $Th^{4+}$. The results for all experimental and theoretical determinations of the scalar dipole polarizability, scalar quadrupole polarizability, and the scalar octupole polarizability of the $Th^{4+}$ are shown in Table 3.11. All the experimental determinations of the properties, seen in Table 3.11, are the result of RESIS measurement, either optical or rf. The comparison of these experimentally determined properties of $Th^{4+}$ offer a benchmark test of the atomic theory used to calculate properties for ions like $Th^{4+}$.

The precision of the scalar dipole polarizability, 0.08%, offers the most rigorous test of any of the atomic theoretical calculations of $Th^{4+}$ to date. The 4C FSCC calculation of the scalar dipole polarizability is within 0.2% of the experimental value reported in this work [43]. The 4C FSCC acronym is not clearly defined in the Ref. [43]. The relativistic random phase approximation (RRPA) of the scalar dipole polarizability is within 0.6% current experimental value [40] and the Relativistic Coupled Cluster including single, double and partial triple excitation (RCCSD(T)) calculation comes out within 0.04% of the experimental value.

Table 3.11: The experimentally and theoretically determined properties of $Th^{4+}$. Column one gives the property being compared, either the scalar dipole polarizability, $\alpha_{D,0}$ or scalar quadrupole polarizability, $\alpha_{Q,0.}$ The second column reports all experimental determination of these two properties. The third column reports all the theoretical determination of these two properties. All properties are in atomic units.

| Property | Experiment (a.u.) | Theory (a.u.) |
|---|---|---|
| $\alpha_{D,0}$ | 7.702(6)[a] | 7.699[d] |
| | 7.720(7)[b] | 7.716[e] |
| | 7.61(6)[c] | 7.75[f] |
| | | 8.96[g] |
| | | 10.26[h] |
| $\alpha_{Q,0}$ | 29.1(1.6)[a] | 28.82[f] |
| | 21.5(3.9)[b] | 24.54[g] |
| | 47(11)[c] | |
| $\alpha_{O,0}$ | 192(77)[a*] | 192.5[f] |
| | | 148.5[g] |

[a]This work, reported in Reference [36], with the exception of the octupole polarizability*
[b]Reference [35]
[c]Reference [21]
[d]RCCSD(T), Schwerdfeger and Borschevsky [44]
[e]4C FSCC, Réal, Vallet, Clavaguéra and Dognon [43]
[f]RRPA, M.S. Safronova and U.I. Safronova [40]
[g]DHF, Safronova and U.I. Safronova [40]
[h]Fraga, Karwowski, and Saxena [2]

The experimental scalar dipole polarizability differs from the relativistic Dirac-Hartree-Fock (DHF) by 16% [40] and the non-relativistic Hartree-Fock [2] by 33%, indicating how difficult such calculations can be for a system such as $Th^{4+}$. There are only two theoretical calculations of the scalar quadrupole polarizability and the comparison with theory is limited by the 5.5%

precision of the experimental. The theoretical calculation of the scalar quadrupole polarizability with RRPA comes out within 1% of the experimental value, while the DHF result differs by more than 15% [40]. Both of the theoretical calculations of the scalar octupole polarizability are within the error of the experimental determined value, with the value from the RRPA calculation closer than the value determined from DHF calculation [40].

While the scalar dipole polarizability was determined very precisely, the precision of the scalar quadrupole polarizability is only moderate. This is mostly due to the precision of the initial slope, $B_6$, determined from the polarizability plot. The precision of the $B_6$ might be improved if an additional transition, the $L$=7 to 8 in $n$=37, was measured adding an additional point to the polarizability plot, but that might prove experimentally challenging. This additional fine structure measurement would also allow the possible improvement of the precision of the fitted curvature of the data; therefore the precision of the scalar octupole polarizability might be improved as well, but only if the precision of the theoretical properties used in the extraction of the properties from the fitted parameter were also improved. The measurement of the properties of $Th^{4+}$ present in this work provide a benchmark test for the theoretical calculation of systems such as $Th^{4+}$ and it is hoped that additional calculations of the properties of $Th^{4+}$ will be conducted and tested against the results presented here.

## Chapter 4: $Th^{3+}$ experiment-optical study

### 4.1 Background on the $Th^{3+}$ experiment

Francium-like thorium, $Th^{3+}$, was the second thorium ion of interest for this program of study. The fine structure for the high-$L$ $Th^{2+}$ Rydberg states is much more complicated than the fine structure for the high-$L$ $Th^{3+}$ Rydberg states explored in the previous chapter, since the ground state of $Th^{3+}$ is ${}^2F_{5/2}$ with $J_c$=5/2. Instead of the one energy level for each $L$ seen in the previous chapter with the Rydberg fine structure of $Th^{3+}$, the Rydberg fine structure of $Th^{2+}$ has six levels for each $L$. Each energy level will be denoted by its $L$ and $K$ values. The scale and the separation between the energy levels in this complex Rydberg fine structure will be determined by not only polarizabilities but also permanent moments of the core, $Th^{3+}$. For example, Fig. 4.1 shows the simulated fine structure of high-$L$ $Th^{2+}$ Rydberg levels in $n$=28, for $L$=9 to 12. The splitting of the six levels for each $L$ in the simulation, Fig. 4.1, is determined primarily by the permanent quadrupole moment of $Th^{3+}$ and the shifting of the center of gravity of the levels for each $L$ away from hydrogenic determined primarily by the scalar dipole polarizability. Unlike the Rydberg fine structure of $Th^{3+}$ seen in the previous chapter , the fine structure explored in this Chapter will have a scalar, vector, 2nd rank tensor, 3rd rank tensor and 4th rank tensor component, all of the component seen in the effective potential, Eq. 1.18.

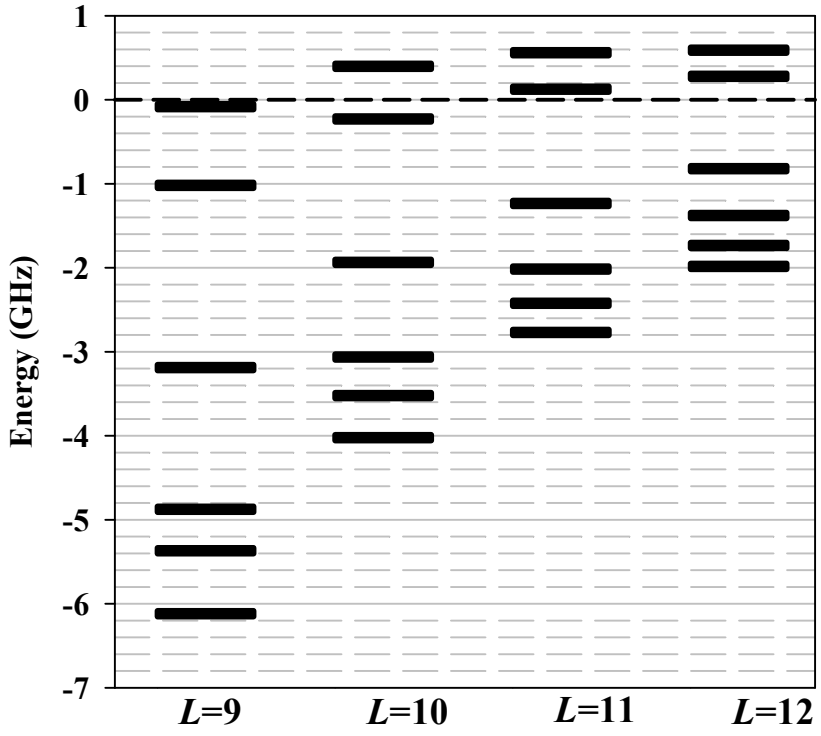


Figure 4.1: Simulated fine structure for $n$=28 $Th^{2+}$ Rydberg states $L$=9 to 12. This structure was simulated assuming the theoretical estimates of the permanent quadrupole moment and the scalar dipole polarizability. The y-axis has unit of the GHz.

The only other time that an ion with $J_c$=5/2 has been studied with the RESIS technique is the recent study of nickel [11]. To gain experience with this type of fine structure pattern, $Ni^+$ with ground state $^2D_{5/2}$ was studied with both optical [20] and rf RESIS [11]. The study of nickel was crucial to expanding knowledge of Rydberg fine structure, without which the study of the $Th^{2+}$ Rydberg fine structure would most likely not have been possible. Like the study of the $Th^{4+}$ ion, the study of the $Th^{3+}$ ion began with the optical RESIS study, so that preliminary properties of $Th^{3+}$ could be determined. The results of the optical study are reported in this chapter. Chapter 5 deals with measurements of the $Th^{2+}$ Rydberg fine structure with the rf RESIS technique and Chapter 6 with the extraction of the properties of $Th^{3+}$.

## 4.2 Optical measurements of the $Th^{2+}$ Rydberg fine structure

The optical RESIS technique was used for the initial study of the $Th^{2+}$ Rydberg fine structure. This work is discussed in this chapter and has also been reported in Ref.[3]. Chapter 2 discussed the technique and gave details of the experimental apparatus. The application of this technique to measure the Rydberg fine structure of $Th^{2+}$ required no major changes to the optical RESIS apparatus. At the time of $Th^{2+}$ Rydberg fine structure measurement, the $Th^{3+}$ Rydberg fine structure was also being measured, so the ECR already had thorium installed and was producing thorium beams. The observation of the $Th^{2+}$ Rydberg fine structure required that the $Th^{3+}$ beam coming out of the ECR be selected and tuned down the beam line instead of the $Th^{4+}$. Chapter 2 gave details on the different components of the experimental apparatus used in the observation of the optical RESIS. The setting of some components, the repeller and detector, had to change for the observation of the specific $Th^{2+}$ Rydberg fine structure, but the changes were predicted by the discussion of the technique presented in Chapter 2.

The selection of a specific RESIS optical excitation for observation is limited by the $CO_2$ laser frequency range and upper $n$ state that the detector can detect. The $CO_2$ laser used in this study has 65 different laser lines near 10μm, the transition selected for observation has to have a hydrogenic frequency near a laser line frequency. The laser line selected for the RESIS excitation must not be shared by another detectable RESIS excitation; otherwise the observed fine structure might be confused with the fine structure from another transition. The transitions selected for observation also had to be able to be detected by the detector. The voltage on the long gap Stark ionizer cannot exceed the voltage limit of the feedthroughs used, approximately 7000V. Therefore the $n_{upper}$ must be greater than $n$=57. The voltage on the Stark ionizer also needs to be high enough so that the location of the signal is as far from the regenerated primary

in the deflection voltage as possible, so that the background caused by the regenerated primary is minimized. With the consideration of the laser and the detector in mind, three transitions for the observation of the $Th^{2+}$ Rydberg fine structure were selected: the $n$=27 to 60, the $n$=28 to 66 and the $n$=29 to 72. The hydrogenic frequency of the three different transitions and the respective laser line used for their observation is given in Table 4.1.

Table 4.1: Transitions used to observed the $Th^{2+}$ Rydberg fine structure, column one lists the specific transitions. Column two gives the hydrogenic transition frequency for the transition in $cm^{-1}$. The third column gives the laser line selected for the observation of the transition, along with the frequency of the laser line in $cm^{-1}$. The fourth column gives the voltage necessary for the long gap stripper to detected the transition, calculated using Eq. 2.9

| $n_{lower}$- $n_{upper}$ | $E_{hyd}$ ($cm^{-1}$) | Laser Frequency ($cm^{-1}$) | $V_{Long}$(V) |
|---|---|---|---|
| 27-60 | 1080.4358 | 9R(24) = 1081.0874 | 5949 |
| 28-66 | 1033.0072 | 9P(24) = 1033.4880 | 4063 |
| 29-72 | 983.8404 | 10R(34) = 984.3832 | 2869 |

The observation of the three spectra are in the MH series of lab books, since Mark Hanni was the senior graduate student on the apparatus at the time of the data taking, he was not responsible for the actual data taking or the analysis of the spectra seen in this section though. The three spectra can be seen in MH-12 and MH-13, each of the spectra was observed multiple times. The multiple observations of each spectrum were then averaged and combined at the completion of data taking.

The spectra are observed as a function of the angle recorded by the computer, which is converted into the angle of the intersection between the ion beam and the $CO_2$ laser using Eq. 2.8 and the calibrated value of $\theta_{\perp}$ given in Chapter 2. The intersection angle is then converted into an energy using Eq. 2.7, this conversion requires the speed of the ion beam being studied and the frequency of the laser line being used, Table 4.1. Chapter 2 gives the calibration of the dial

reading of the high voltage power supply used to accelerate the beams, for the three spectra observed here the high voltage dial was set to

$$HVDial = 8.335$$

this corresponds to a terminal potential of

$$V_{\text{terminal}} = 24938(25)V$$

and a beam speed in terms of $\beta$ of

$$\beta = 0.0008320(4).$$

Using this beam speed and the calibration of the $\theta_{\perp}$ all three spectra were plotted as a function of the energy deviation from hydrogenic, the Doppler tuned frequency of the laser minus the hydrogenic frequency in GHz. Fig. 4.2 shows all three spectra. The original signal in each spectra is shown with black points, the blue is signal time five and the red is the signal times twenty. The large peak around hydrogenic in all three spectra is the high-$L$, made up all the unresolved levels around hydrogenic. Unlike the high-$L$ seen in the optical $Th^{3+}$ Rydberg fine structure spectrum, Fig. 1.5, the high-$L$ in all three of the $Th^{2+}$ Rydberg fine structure spectra has a "dip" right at hydrogenic, splitting the high-$L$ into two parts.

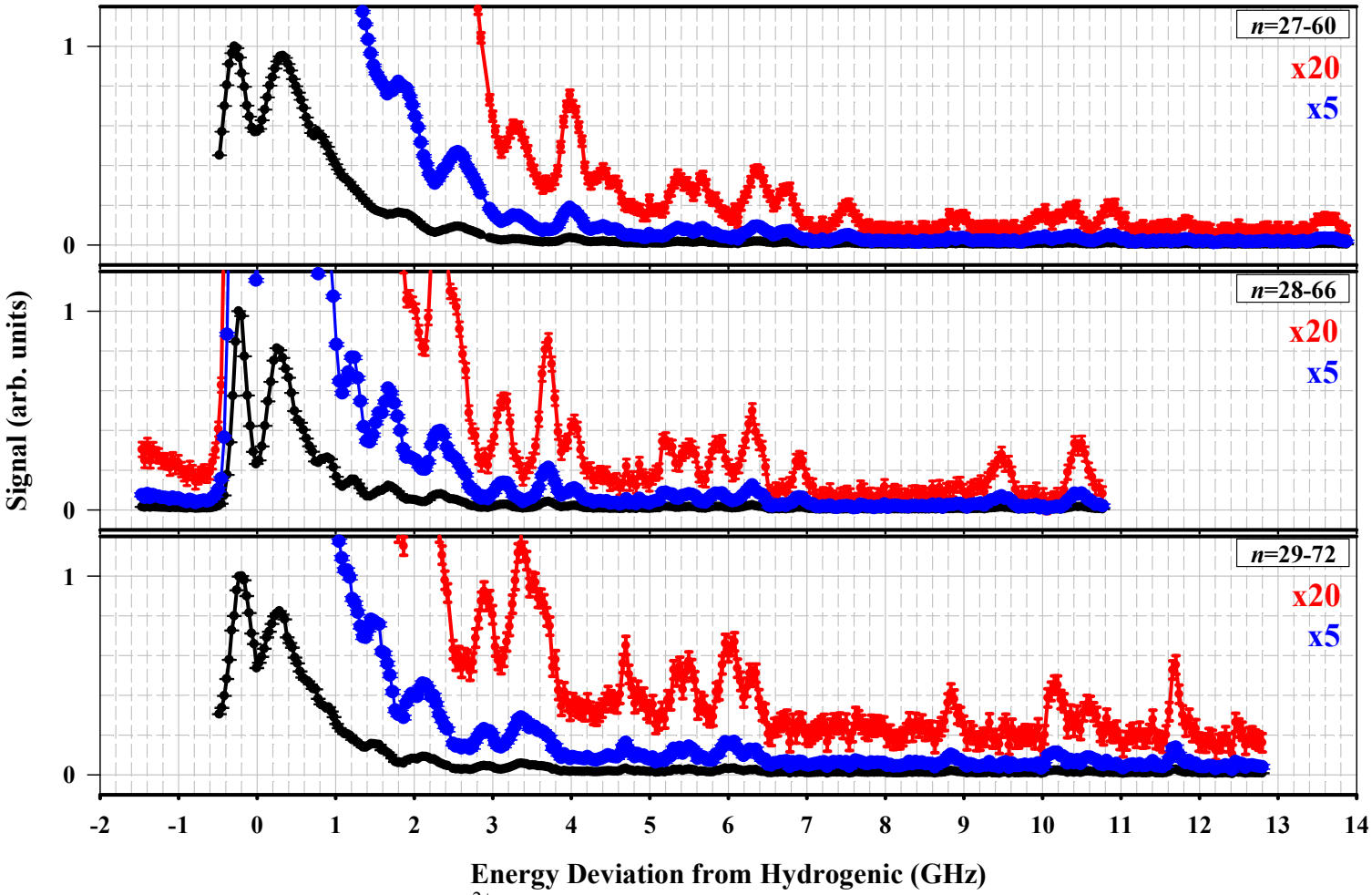


Figure 4.2: RESIS optical spectra for high-$L$ $Th^{2+}$ Rydberg levels , three different transitions were observed. The x-axis is the energy deviation from hydrogenic in GHz, in black is the original signal, blue is signal time five and red is signal times twenty.

This splitting of the high-$L$ has never before been observed on any of the different multiple charged ions studied using the RESIS technique, but $Th^{3+}$ is the first multiple charged ion studied that has a permanent quadrupole moment. Therefore the "dip" feature could be used as a way to put limits on the possible size of the $Th^{3+}$ permanent quadrupole moment. All three of the spectra also have resolved structure on the right side of the high-$L$, these structure are of varying size and separations. The observed spectra were made up of an average of multiple runs in order to get the adequate signal to noise to observe the resolved fine structure in the each of the spectra. The observation of these three spectra with the optical RESIS technique was just the first step required to determine properties of $Th^{3+}$.

### 4.3 Deciphering the $Th^{2+}$ Rydberg fine structure

In order to extract properties of $Th^{3+}$ from the measurements the $Th^{2+}$ RESIS spectra, the pattern of resolved structures must be understood and specific states identified. To gain understanding of the features that could be expected in the $Th^{2+}$ high-$L$ Rydberg fine structures, each of the observed transition fine structures were simulated using the two dominant terms in the effective potential, Eq 1.18, the scalar dipole polarizability and the permanent quadrupole moment. Theoretical estimates of the scalar dipole polarizability [45], $\alpha_{D,0} = 15.1 a.u.$ and the permanent quadrupole [46], $Q = 0.62 a.u.$, were used as a starting point for these simulations. The dominant type of transition observed in a high-$L$ Rydberg fine structures observed with the optical RESIS technique is $L' = L + 1$ and $K' = K + 1$, therefore the fine structure for both the lower and upper state must be simulated. The energy deviation from hydrogenic is the energy of the upper state minus the energy of the lower state. The result of the initial simulation for each of the observed spectra, using the estimated properties, is shown in Fig. 4.3, with the x-axis being the energy deviation from hydrogenic in GHz. The simulated signal size is seen in black,

the blue is the simulated signal times five and the red is the simulated signal times twenty. The "dip" feature in each of the observed spectra is reproduced in each of the simulated spectra and the simulation also includes many resolved features with varying sizes and separations on the right side of the high-$L$ feature. The reproduction of the dip in the high-$L$ can only occur if the number of $L$ states in the simulation is limited. This seems plausible given that the probability of exciting transitions between $n_{\text{lower}}$ and $n_{\text{upper}}$ decreases as $L$ increases since the probability of the excitation is dependent on the Z matrix element connecting the states, Eq. 2.3 in Reference [17]. In the case of the simulation included in this chapter of the three RESIS optical only $L \leq 17$ were included. All three of the simulated spectra look very similar, with the deviation of the resolved features from hydrogenic decreasing like $1/n^3$. These similarities between the spectra are not observed in the actual observed spectra, Fig. 4.2. Those spectra show clear difference, especially if one looks between the 8 and 13GHz range, the number of peaks in that range is different for each the spectra. The spacing and grouping of the five peaks in the 4.5 to 8 GHz range is also different for each of the observed spectra. Close inspection of the three of the observed spectra, Fig. 4.2, shows that the spectra are clearly different. These differences cannot be explained by any additional terms in the effective potential model or changes to any of the core properties in the effective potential used to simulate the spectra, these differences must therefore be caused by something not accounted for in the effective potential model.

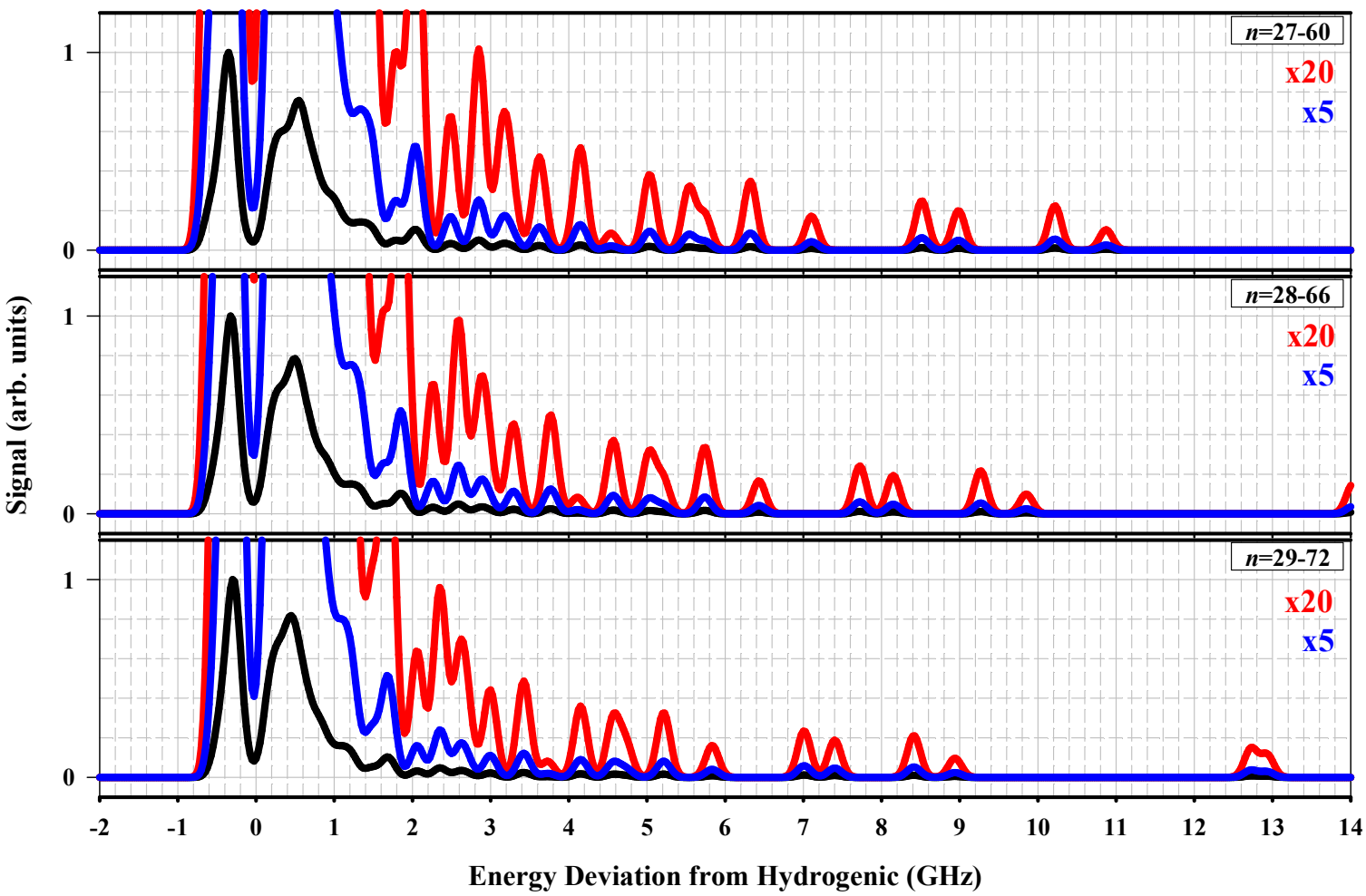


Figure 4.3: Simulated RESIS optical spectra using the theoretical estimated scalar dipole polarizability and quadrupole moment and assuming the adequacy of the effective potential model. The x-axis is the energy deviation from hydrogenic in GHz, the black is the simulated signal size, the blue is the simulated signal times five and the red is the simulated signal times twenty.

Once it was seen that the effective potential model was not adequately describing the observed fine structure, attention was turned to the derivation of the effective potential and possible effects that might be left out of it. The effective potential is derived using three different expansions, the first is static perturbation theory, Eq. 1.9, the second is the multipole expansion of the potential describing the interaction of the Rydberg electron and the core ion, Eq. 1.13, and the third expansion is the adiabatic expansion, Eq. 1.15. Looking at the measured excited levels of $Th^{3+}$ [9, 13] it was found that there are two states, the $^2D_{3/2}$ and the $^2D_{3/2}$, that lie very close to the ground state. The adiabatic expansion, Eq. 1.15, used to derive the effective potential requires that the core excitation energy, $\Delta E(\lambda', J_c')$ be much greater than the Rydberg energy difference, $\Delta E_{Ryd}$. For the case of the two low-lying *D* states this requirement is not met. This leads to the failure of the adiabatic expansion, and thus the failure of the effective potential to adequately describe interactions with excited states containing those two low-lying *D* states.

The failure of the adiabatic expansion will not affect all the terms of the effective potential since some components of the effective potential are derived without it. The permanent moments are the result of the first order perturbation energies of the potential which do not contain energy denominators and therefore do not rely on the adiabatic expansion. A majority of the effective potential, the polarizabilities, are the result of the second order perturbation energies, Eq. 4.1,

$$E^{[2]}(nLK) = -\sum_{n'L'\lambda'J_c'} \frac{\left\langle 5^2F_{5/2}, nL; K \middle| V \middle| \lambda' J_c', n'L'; K \right\rangle \left\langle \lambda' J_c', n'L'; K \middle| V \middle| 5^2F_{5/2}, nL; K \right\rangle}{\Delta E(\lambda', J_c') - E(n') + E(n)} \tag{4.1}$$

where *V* is the potential, Eq. 1.13 and the intermediate core states is denoted $\lambda' J_c'$, and the intermediate Rydberg level is identified by $n'L'$. The application of the adiabatic expansion to the second order energy, Eq. 4.1 allows the second order energy to be rewritten as a sum of

terms, In Eq. 4.2, the first term is the adiabatic term, the second term is the 1st non-adiabatic term, and the third term is the 2nd non-adiabatic term.

$$E^{[2]}(V) = E^{[2]}_{\mathrm{Ad}}(V) + E^{[2]}_{\mathrm{1st\,NonAd}}(V) + E^{[2]}_{\mathrm{2\,ndNonAd}}(V) + \ldots \tag{4.2}$$

If the adiabatic expansion is valid, the use the adiabatic expansion to expand out the denominator allows for the second order energies to be rewritten in terms of core properties and expectation values of *r*. A test for whether the adiabatic expansion is valid is to see if the 1st non-adiabatic term is much smaller than the adiabatic term, by looking at the ratio of the 1st non-adiabatic term to the adiabatic term. The ground state is primarily connected to the $^2D_{3/2}$ and the $^2D_{5/2}$ via the dipole coupling therefore the ratio 1st non adiabatic second order energy to the adiabatic second order energy for dipole coupling will be the focus of the discussion. The ratio of the 1st non-adiabatic second order energy to the adiabatic second order energy is given by Eq. 4.3

$$\frac{E^{[2]}_{\mathrm{1st\,NonAd}}}{E^{[2]}_{\mathrm{Ad}}} = \frac{\Delta\bar{E}_{nLL'}}{\Delta E(\lambda' J'_c)} \tag{4.3}$$

where $\Delta\bar{E}_{nLL'}$ is the average Rydberg energy difference between the Rydberg state of interest and intermediate Rydberg state. The average Rydberg energy difference for dipole coupling is given by Eq. 4.4. It simplifies to a multiple of the ratio of expectation values of $r^{-6}$ to $r^{-4}$ using the relations presented in the work of Woods [7].

$$\Delta\bar{E}_{nLL'} = \frac{\sum_{n'}\left[E(n') - E(n)\right]\left\langle nL\left|r^{-2}\right|n'L'\right\rangle^2}{\sum_{n'}\left\langle nL\left|r^{-2}\right|n'L'\right\rangle^2}$$

$$= \frac{\left[4 - L(L+1) + L'(L'+1)\right]}{2}\frac{\left\langle r^{-6}\right\rangle_{nL}}{\left\langle r^{-4}\right\rangle_{nL}} \tag{4.4}$$

This ratio of the 1st non-adiabatic to the adiabatic second order energy, $E^{[2]}_{\text{1st NonAd}} / E^{[2]}_{\text{Ad}}$ was calculated for $n$=28 for both cases, $L' = L \pm 1$ as a test of the validity of the adiabatic expansion, and the results are shown in Table 4.2 for both the of the excited core states, $^2D_{3/2}$ and $^2D_{5/2}$.

Table 4.2: The ratio of the $E^{[2]}_{\text{1st NonAd}}$ to $E^{[2]}_{\text{Ad}}$ for the case of the $^2D_{3/2}$ and $^2D_{5/2}$ for the $L' = L \pm 1$ in $n$=28, $L$=8 to 13. Column one gives the $L$, column two gives the ratio for the $L' = L + 1$ term and column three gives the ratio for $L' = L - 1$ term. The top half of the table is for the $^2D_{3/2}$ state and the bottom part of the table is for the $^2D_{5/2}$ state.

| $L$ | Ratio ($L'$=$L$+1) | Ratio ($L'$=$L$-1) |
|---|---|---|
| $^2D_{3/2}$ | | |
| 8 | 1.37 | -0.75 |
| 9 | 0.93 | -0.54 |
| 10 | 0.66 | -0.40 |
| 11 | 0.48 | -0.31 |
| 12 | 0.36 | -0.24 |
| 13 | 0.27 | -0.19 |
| $^2D_{5/2}$ | | |
| 8 | 0.87 | -0.48 |
| 9 | 0.59 | -0.34 |
| 10 | 0.42 | -0.26 |
| 11 | 0.30 | -0.20 |
| 12 | 0.23 | -0.15 |
| 13 | 0.17 | -0.12 |

From Table 4.2 it can be seen that for both the $^2D_{3/2}$ and $^2D_{5/2}$, the 1st non-adiabatic second order energy is comparable in size to the adiabatic second order energy for $L$=8. This indicates that the average Rydberg energy difference is the same order of magnitude as the excitation energies for the two low-lying $D$ core states, and thus the failure of the adiabatic expansion for that $L$. The ratio does decrease as $L$ increases. This is due to the fact that the averaged Rydberg energy difference decreases since it is proportional to the ratio expectation values $r^{-6}$ over $r^{-4}$. The convergence of this ratio with increasing $L$ indicates that as $L$ increases

the use of the adiabatic expansion will be become valid. This means that for the lower $L$s the contribution to $E^{[2]}$ from states containing the $^2D_{3/2}$ and $^2D_{5/2}$ core states will not be well described by the effective potential, but if the $L$ is high enough the effective potential will be adequate. This explains why the high-$L$ features look similar but the resolved structure did not when comparing observed spectra, Fig. 4.2, with the spectra simulated that assumed the adequacy of the effective potential model, Fig. 4.3.

Figure 4.4 shows the respective Rydberg series for each of the three core states of interest, the ground state and the two low-lying $D$ states. For reference the location of the $n$=28 in the Rydberg series of the ground state is denoted by a dashed black line, in Fig. 4.4. The excitation energy of the $^2D_{3/2}$ is $9193.2461(9)cm^{-1}$ and $^2D_{5/2}$ is $14486.4017(9)cm^{-1}$ [9]. The $n$=28 Rydberg state bound to the $^2F_{5/2}$ is in between the $n'$=9 and $n'$=10 intermediate Rydberg states bound to the $^2D_{3/2}$ and in between the $n'$=7 and $n'$=8 bound to the $^2D_{5/2}$. These nearby intermediate Rydberg states will couple with the Rydberg states being studied, resulting in the Rydberg states of interest being perturbed. The strength of the coupling is dependent on the separation between the states. For example the $n$=28 Rydberg state bound to the $^2F_{5/2}$ will couple more strongly to the $n'$=10 than the $n'$=11 bound to the $^2D_{3/2}$. Since the coupling between the states connecting the $^2F_{5/2}$ and either the $^2D_{3/2}$ or the $^2D_{5/2}$ is primarily due to the dipole term in the multipole expansion the change in $L$ between the $L$ of the Rydberg state bound to the ground state and the intermediate Rydberg state, $L'$, that is bound to either the $^2D_{3/2}$ or the $^2D_{5/2}$ can only be $\pm 1$.

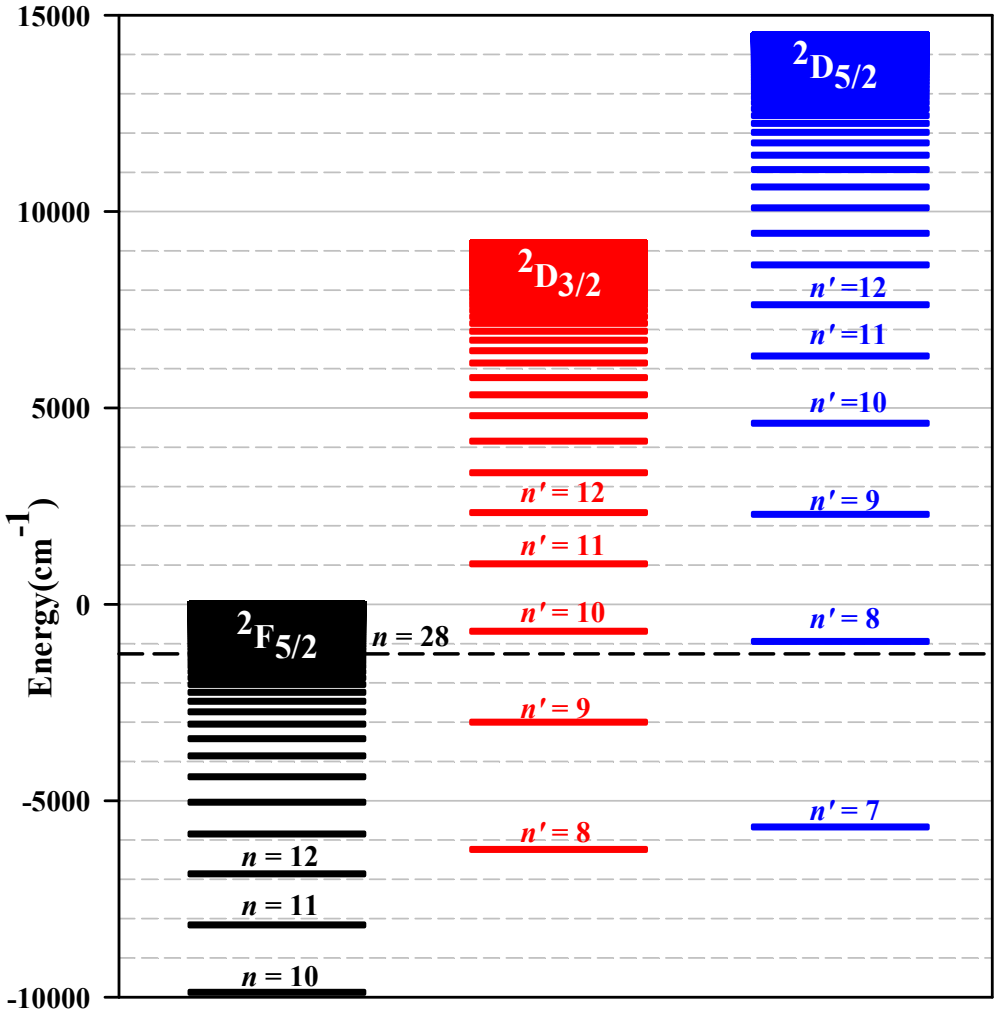


Figure 4.4: The Rydberg series bound to the $^2F_{5/2}$, $^2D_{3/2}$, and the $^2D_{5/2}$, the y-axis is the energy in $cm^{-1}$.

The presence of the low-lying core states, the $^2D_{3/2}$ and the $^2D_{5/2}$, introduces non-adiabatic effects into the observed Rydberg fine structure in the lower $L$ levels. These non-adiabatic effects would not be the same for each of the transition spectra, since they depend on the specific $nL$ of the transition. Both the lower and upper $n$ of the RESIS excitation transitions will be affected by the low-lying $D$ states. The contributions of these two low-lying core states to the observed energy cannot be described by the effective potential derived using the adiabatic

expansion, therefore they must be dealt with another way. For all other excited states of $Th^{3+}$, the requirement for the use of the adiabatic expansion is met so the use of the adiabatic expansion is valid. The contribution from other excited states will then be accurately described by an effective potential model but the contributions from the two low-lying core states must be treated separately. The failure of the adiabatic expansion has occurred before in the study of Rydberg levels of the Barium by Gallagher et al. [47] and Snow et al. [48]. In the barium study there were low lying states that produced non-adiabatic effects that had to be taken into account [48] in order to extract the properties of $Ba^{+}$. Using a similar approach with $Th^{2+}$ Rydberg levels, the effective potential model can be corrected for effects of the $^2D_{3/2}$ and $^2D_{5/2}$ levels.

The contributions of the $^2D_{3/2}$ and $^2D_{5/2}$ to the $Th^{2+}$ Rydberg fine structure can be determined by calculating the full second order perturbation energy from intermediate states where either the $^2D_{3/2}$ or $^2D_{5/2}$ are the intermediate core states in Eq. 4.1, without using the adiabatic expansion. The $^2D_{3/2}$ and $^2D_{5/2}$ excited states can only connect to the ground state of $Th^{3+}$, $^2F_{5/2}$, via odd terms in the multipole expansion of the full potential, Eq. 1.13. The first odd term of the multipole expansion is when $\kappa = 1$, the dipole term, which is given by

$$V = M^{[1]} \frac{C^{[1]}(\hat{r})}{r^2} \tag{4.5}$$

where the $M^{[1]}$ is the dipole operator that acts on wave function of the core. This dipole term in the multipole expansion is responsible for the different types of the dipole polarizabilities in the effective potential, such as the scalar dipole polarizability, the tensor dipole polarizability and the 1st non-adiabatic dipole polarizability to name a few. Plugging the dipole term of the potential into Eq. 4.1 second order perturbation energies involving the intermediate $^2D_{3/2}$ and $^2D_{5/2}$ states

can be found, Eq. 4.6 and 4.7, in terms of reduced matrix elements, 3J symbols, and 6J symbols [7].

$$E^{[2]}(^2D_{3/2}) = -\left\langle 5^2F_{5/2}\left\|M^{[1]}\right\|6^2D_{3/2}\right\rangle^2 \sum_{n'L'}\begin{Bmatrix} K & L & 5/2 \\ 1 & 3/2 & L' \end{Bmatrix}^2 \begin{pmatrix} L & 1 & L' \\ 0 & 0 & 0 \end{pmatrix}^2 (2L+1)(2L'+1)$$

$$\times \frac{\left\langle nL\left\|r^{-2}\right\|n'L'\right\rangle\left\langle n'L'\left\|r^{-2}\right\|nL\right\rangle}{\Delta E(6^2D_{3/2}) + E(n') - E(n)} \tag{4.6}$$

$$E^{[2]}(^2D_{5/2}) = -\left\langle 5^2F_{5/2}\left\|M^{[1]}\right\|6^2D_{5/2}\right\rangle^2 \sum_{n'L'}\begin{Bmatrix} K & L & 5/2 \\ 1 & 5/2 & L' \end{Bmatrix}^2 \begin{pmatrix} L & 1 & L' \\ 0 & 0 & 0 \end{pmatrix}^2 (2L+1)(2L'+1)$$

$$\times \frac{\left\langle nL\left\|r^{-2}\right\|n'L'\right\rangle\left\langle n'L'\left\|r^{-2}\right\|nL\right\rangle}{\Delta E(6^2D_{5/2}) + E(n') - E(n)} \tag{4.7}$$

In the case of the both Eq. 4.6 and 4.7 everything can be calculated up to a constant, the matrix elements connecting the ground state to the excited state of interest. For a dipole transition the sum over $L'$ has only two term, $L' = L \pm 1$, with the $L'$ being the angular momentum of the intermediate Rydberg electron. The sum over $n'$ can be carried out numerically using the Dalgarno-Lewis method [10], and can be calculated very accurately since the excitation energies for both the $^2D_{3/2}$ and $^2D_{5/2}$ have been precisely measured [9].

$$\Delta E(6^2D_{3/2}) = 9193.2461(9)cm^{-1}$$
$$\Delta E(6^2D_{5/2}) = 14486.4017(9)cm^{-1}$$

The only thing unknown in Eq. 4.6 and 4.7 is the matrix element that connects the ground state to the excited state, so initially a unit matrix element was used to get a sense of the size and behavior of the second perturbation order energies due to the intermediate $^2D_{3/2}$ and $^2D_{5/2}$ states.

These energies must be calculated for each specific $nLK$ state of interest in the $Th^{2+}$ Rydberg fine structure pattern.

The energy of a specific $nLK$ level in the $Th^{2+}$ Rydberg fine structure, $E^{Mod}(nLK)$, will be the sum the of the expectation value of a modified effective potential, $E^{[1]}(V_{eff}^{Mod})$ and two explicitly calculated second order perturbation energies due to the intermediate $^2D_{3/2}$ and $^2D_{5/2}$ states, Eq. 4.8,

$$E^{Mod}(nLK) = E^{[1]}(V_{eff}^{Mod}) + \left|\left\langle 5^2F_{5/2}\left\|M^{[1]}\right\|6^2D_{3/2}\right\rangle\right|^2 E^{[2]}(D_{3/2})^* + \left|\left\langle 5^2F_{5/2}\left\|M^{[1]}\right\|6^2D_{5/2}\right\rangle\right|^2 E^{[2]}(D_{5/2})^* \tag{4.8}$$

where $E^{[2]}(D_{3/2})^*$ and $E^{[2]}(D_{5/2})^*$ denote the calculation of the second order energies with unit matrix elements. Since the second order perturbation energies were calculated with unit matrix elements in Eq. 4.8 a factor was placed in the front of each to allow for their adjustments, that factor is the dipole matrix element squared that couples each the ground state to the excited states. The modified effective potential, $V_{eff}^{Mod}$, Eq. 4.9, contains properties that have contributions from the $^2D_{3/2}$ and $^2D_{5/2}$ states missing.

$$V_{eff}^{Mod} = -\frac{\alpha_{D,0}^{Mod}}{2r^4} - \left(\frac{Q}{r^3} + \frac{\alpha_{D,2}^{Mod}}{2r^4}\right) \times \frac{X^{[2]}(J_c)\cdot C^{[2]}(\hat{r})}{\begin{pmatrix} 5/2 & 2 & 5/2 \\ -5/2 & 0 & 5/2 \end{pmatrix}} + \ldots \tag{4.9}$$

To simulate the energy deviation from hydrogenic for the transitions seen in the observed RESIS excitation spectra, the energies of both the lower states, $nLK$, and the upper states, $n'L'K'$ must be calculated. For the RESIS excitation the dominant transition to observe is $L' = L + 1$ and $K' = K + 1$, therefore the energy deviation from hydrogenic will be given by

$$\Delta E(nLK \rightarrow n'L'K') = E^{Mod}(n'L'K') - E^{Mod}(nLK) \tag{4.10}$$

where the $E^{Mod}(nLK)$ denotes the energy of the lower states and $E^{Mod}(n'L'K')$ denotes the energy of the upper state, both given by Eq. 4.8. Both $E^{Mod}(nLK)$ and $E^{Mod}(n'L'K')$ are defined in terms of core properties, expectation values and matrix elements by Eq. 4.8. For both the lower and upper states the full second order perturbation energies due to the $^2D_{3/2}$ and $^2D_{5/2}$ had to be calculated for every state to be included in a simulation of the spectra.

Initial simulations of the spectra were constructed assuming the theoretical estimates of the properties of $Th^{3+}$ [45, 46],

$$Q = 0.62 a.u. \quad \alpha_{D,0}^{Mod} = 8.58 a.u. \quad \alpha_{D,2}^{Mod} = -0.47 a.u.$$
$$\left|\left\langle 5^2 F_{5/2} \left\| M^{[1]} \right\| 6^2 D_{3/2} \right\rangle\right| = 1.530 a.u.$$
$$\left|\left\langle 5^2 F_{5/2} \left\| M^{[1]} \right\| 6^2 D_{3/2} \right\rangle\right| = 0.412 a.u.$$

where $\alpha_{D,0}^{Mod}$ is the modified scalar dipole polarizability and $\alpha_{D,2}^{Mod}$ is the modified tensor dipole polarizability, both excluding contributions from the $^2D_{3/2}$ and $^2D_{5/2}$. The simulations of the spectra using the theoretical estimates of the five key core parameters did not match the observed spectra very well. So using the key features of the observed spectra limits for the five parameters were determined. The five parameters were then varied inside those limits until the simulated spectra reasonably matched for all three of the observed spectra. Then using the simulations of the $Th^{2+}$ Rydberg fine structures as a guide, preliminary identifications of the transitions in the resolved structure were made, Fig 4.5. Each letter represents a specific ($L$, $K$) state, a total of eight different ($L$, $K$) states were identified in the spectra.

A total of fourteen specific transitions were clearly identified in the three observed spectra, labeled by the letters without parentheses in Fig. 4.5, the letters with parentheses are estimated locations of transitions.

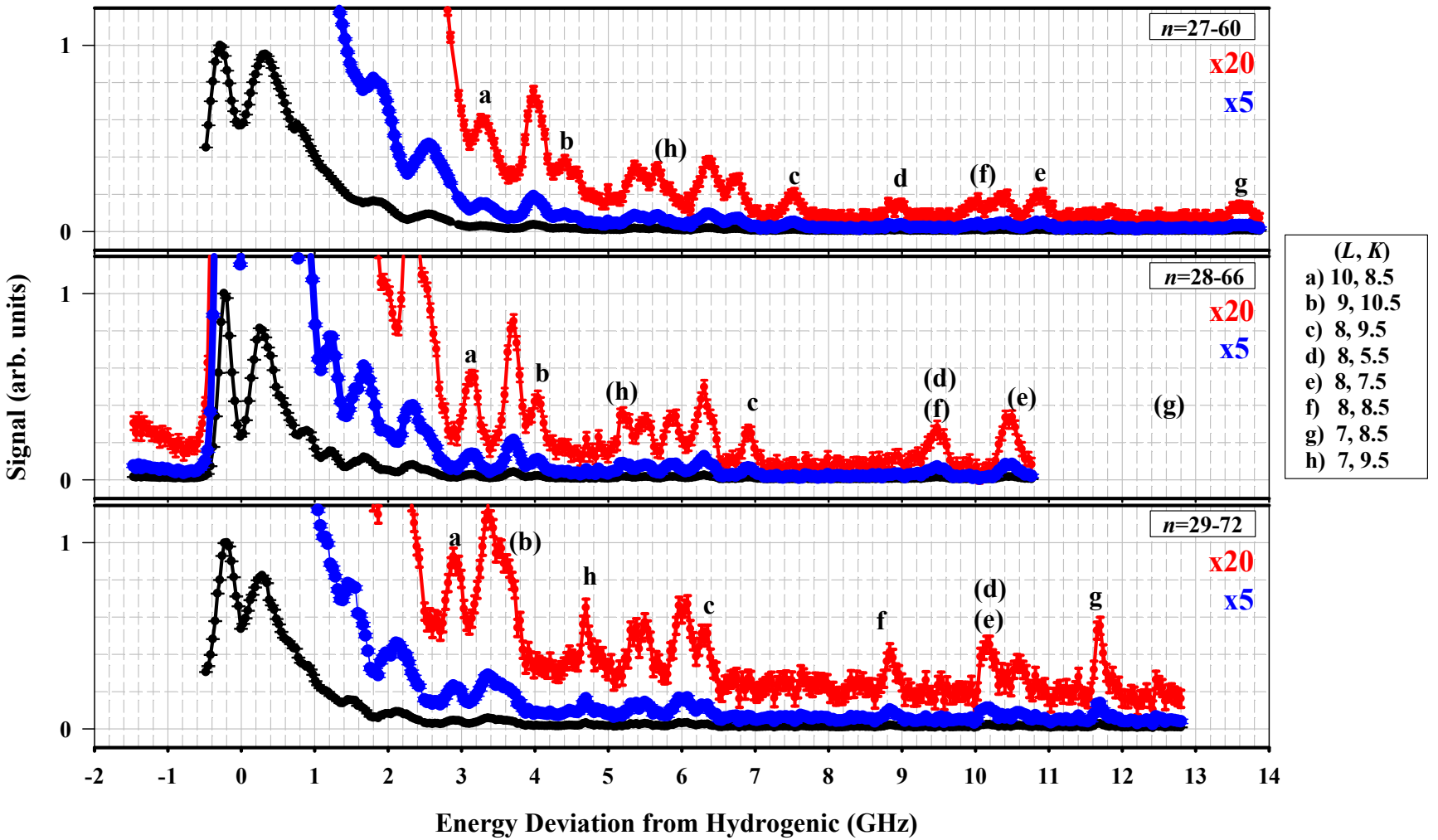


Figure 4.5: RESIS optical spectra of $Th^{2+}$ Rydberg fine structure with preliminary identification of transitions each letter represents a different (L, K) state. The letters without parentheses were included in the fit to determined properties of $Th^{3+}$.

The transitions identified, without parentheses, were transitions that were well resolved from others, thereby representing a single excitation. It was these transitions that were fit to determine properties of $Th^{3+}$. Each of the identified transitions was then fit with a Gaussian to determine its fitted position in the spectra, a list of identified transitions and the positions of the transitions is given in Table 4.3, the transitions are labeled by the ($L$, $K$). The uncertainty on each of the positions is due to the uncertainty of the fit of the peak for each of the transitions. The uncertainty in the energies due to uncertainty of the beam speed and the $\theta_{\perp}$ used to convert the angle recorded by the computer into energy will be dealt with separately, since those uncertainties are correlated.

Before the transitions in Table 4.3 could be fit to determined properties of $Th^{3+}$, the energies of the identified transitions had to be corrected for effect not included in the effective potential model, effects discussed in Chapter 1. The relativistic effect, Eq. 1.32 and the second order energy due to the exclusion of the ground electronic states from the derivation of the effective potential, Eq. 1.28, were calculated for each of the states identified. For the $Th^{2+}$ Rydberg fine structure measurements, it was determined that the second order energies due to coupling to intermediate Rydberg levels were negligible, therefore the observations were only corrected for the relativistic effect, Eq. 4.11.

$$\Delta E(nLK \rightarrow n'L'K') = E_{obs} - \Delta E_{\mathrm{Rel}} \tag{4.11}$$

The correction for the relativistic effect is shown in Table 4.3. The corrected positions were then fit to Eq. 4.8 to determine the dominant properties controlling $Th^{2+}$ Rydberg fine structure, the fit was weighted by the uncertainty in the positions of each of the identified transitions.

Table 4.3: Summary of the observed and fitted positions of the identified $Th^{2+}$ Rydberg fine structure transitions. Column one lists the transitions, column two gives the identifier used to label the transition in Fig. 4.5. The third column gives the observed position of the transitions, column five gives the relativistic correction was applied, and the sixth column gives the corrected position of the transitions. The seventh column gives the predicted positions of the transitions, determined from fitting corrected positions to Eq. 4.8. The final column gives the difference between the fitted positions and the corrected observed positions. All energies are in MHz.

| Transition ($L$ , $K$ ) | Fig 4.5 Identifier | $E_{obs}$(MHz) (MHz) | $\Delta E_{Rel}$ (MHz) | $E_{obs}$-$\Delta E_{Rel}$ (MHz) | Fitted positions (MHz) | Difference (MHz) |
|---|---|---|---|---|---|---|
| $n$ =27 to 60 | | | | | | |
| (10,8.5) | a | 3288(8) | 44 | 3244 | 3295 | 51 |
| (9,10.5) | b | 4428(16) | 50 | 4378 | 4325 | -53 |
| (8,9.5) | c | 7514(8) | 59 | 7455 | 7588 | 133 |
| (8, 5.5) | d | 8932(17) | 59 | 8873 | 8848 | -25 |
| (8,7.5) | e | 10874(9) | 59 | 10815 | 10762 | -53 |
| (7, 8.5) | g | 13617(9) | 69 | 13548 | 13501 | -47 |
| $n$ =28 to 66 | | | | | | |
| (10, 8.5) | a | 3133(8) | 41 | 3092 | 3077 | -15 |
| (9, 10.5) | b | 4030(8) | 47 | 3983 | 3924 | -59 |
| (8, 9.5) | c | 6905(17) | 54 | 6851 | 6791 | -60 |
| $n$ =29 to 72 | | | | | | |
| (10, 8.5) | a | 2903(7) | 38 | 2865 | 2891 | 26 |
| (8,9.5) | c | 6320(16) | 50 | 6270 | 6262 | -8 |
| (8, 8.5) | f | 8851(8) | 50 | 8801 | 8815 | 14 |
| (7, 8.5) | g | 11691(8) | 59 | 11632 | 11643 | 11 |
| (7, 9.5) | h | 4695(8) | 59 | 4636 | 4634 | -2 |

Table 4.3 gives the fitted positions of the transitions; the fit determined below properties for the $Th^{3+}$.

$$Q = 0.54(4)\,a.u. \quad \alpha_{D,0}^{Mod} = 9.67(15)a.u. \quad \alpha_{D,2}^{Mod} = 1.5(1.3)a.u.$$
$$\left|\left\langle 5^2 F_{5/2} \left\| M^{[1]} \right\| 6^2 D_{3/2} \right\rangle\right| = 1.435(10)a.u.$$
$$\left|\left\langle 5^2 F_{5/2} \left\| M^{[1]} \right\| 6^2 D_{3/2} \right\rangle\right| = 0.414(24)a.u.$$

The error on each of the properties is the statistical uncertainty in the parameters. The uncertainty in the properties, due to the uncertainty in the beam speed and $\theta_\perp$, was negligible. Table 4.3 gives the differences between the predicted positions for the transitions and the observed corrected positions; the average of the absolute value of the differences is 40MHz. The deviation between the predicted and the observed corrected positions is most likely due to a combination of small errors in the beam speed or the determination of $\theta_\perp$, drifts in the $CO_2$ laser frequency ($\leq$30MHz) or beam trajectory, small stray electric fields, and contributions from additional terms of the effective potential. Additional core properties of $Th^{3+}$ were included in the fit on a trial basis, such as the permanent hexadecapole moment, $\Pi$, and the scalar quadrupole polarizability, $\alpha_{Q,0}$, but the quality of the fit failed to be improved and there were no significant changes to the five parameters included in the original fit. Table 4.4 gives a breakdown of the contributions of the different components of Eq. 4.8 to the total predicted position for each of the transitions assuming the properties given above. This breakdown shows that the contributions from the low-lying core *D* states to the observed Rydberg fine structure energies are very significant, the same order of magnitude as the contributions from the quadrupole moment and the scalar dipole polarizability.

Table 4.4: Predicted $Th^{2+}$ RESIS transition frequencies using the properties of $Th^{3+}$ determined from the fit of the optical RESIS data. The quantity tabulated represents the difference from the hydrogenic transition frequency. The first column identifies the transition with ($L$, $K$) of the lower state. The second through fourth column gives the contributions from the scalar dipole polarizability, the permanent quadrupole moment and the tensor dipole polarizability respectively to the total fitted energy. The fifth and sixth columns give the contributions from the low-lying $D$ states. The final column fives the total predicted energy determined from the. All energies are in MHz.

| Transition ($L$ , $K$) | $E^{[1]}(V_{eff}^{Mod})$ (MHz) | | | $E^{[2]}(6^2D_{3/2})$ (MHz) | $E^{[2]}(6^2D_{5/2})$ (MHz) | Predicted positions (MHz) |
|---|---|---|---|---|---|---|
| | $\alpha_{D,0}^{Mod}$ | $Q$ | $\alpha_{D,2}^{Mod}$ | | | |
| $n$ =27 to 60 | | | | | | |
| (10,8.5) | 1389 | -169 | -9 | 2038 | 46 | 3295 |
| (9,10.5) | 2327 | 1218 | 81 | 600 | 98 | 4325 |
| (8,9.5) | 4123 | 1807 | 152 | 1075 | 431 | 7588 |
| (8, 5.5) | 4123 | -4468 | -375 | 9346 | 222 | 8848 |
| (8,7.5) | 4123 | 2216 | 186 | 3663 | 574 | 10762 |
| (7, 8.5) | 7839 | 2825 | 309 | 1411 | 1117 | 13501 |
| $n$ =28 to 66 | | | | | | |
| (10, 8.5) | 1264 | -153 | -8 | 1932 | 42 | 3077 |
| (9, 10.5) | 2114 | 1104 | 73 | 543 | 90 | 3924 |
| (8, 9.5) | 3740 | 1638 | 138 | 821 | 455 | 6791 |
| $n$ =29 to 72 | | | | | | |
| (10, 8.5) | 1150 | -138 | -7 | 1849 | 38 | 2891 |
| (8,9.5) | 3396 | 1486 | 125 | 749 | 506 | 6262 |
| (8, 8.5) | 3396 | 2706 | 228 | 1784 | 701 | 8815 |
| (7, 8.5) | 6443 | 2320 | 253 | 1163 | 1465 | 11643 |
| (7, 9.5) | 6443 | -3676 | -402 | 2216 | 53 | 4634 |

These measurements provided the first experimental determinations of any $Th^{3+}$ properties, despite the failure of the effective potential model to adequately describe the data. The $Th^{3+}$ properties determined from the optical RESIS study were the result of fitting fourteen transitions in three different spectra. Fitting of that data set did not allow for the complete determination of all of the $Th^{3+}$ properties possible in the full effective potential, Eq. 1.18. Nevertheless, the reported properties and matrix elements for $Th^{3+}$ offer the first opportunity to test the theoretical calculation of the properties. To compare all the determined properties with the theory, the total scalar dipole polarizability and tensor dipole polarizability had to be calculated, including the contribution from the $^2D_{3/2}$ and $^2D_{5/2}$ core states. Both the scalar dipole polarizability and the tensor dipole polarizability are defined in terms of the matrix elements, excitation energies and constants [7]; so it is therefore possible to calculate the $^2D_{3/2}$ and $^2D_{5/2}$ contributions to both. For example the scalar dipole polarizability is given by Eq. 1.24, which only requires the dipole matrix elements that connect the ground state to the excited state, which was found from the fit of the data, and the excitation energy energies, which have been precisely measured. Therefore, using the determined matrix element and excitation energies it was possible to find and report the total scalar dipole polarizability, $\alpha_{D,0}$ and the total tensor dipole polarizability, $\alpha_{D,2}$.

$$\alpha_{D,0} = \alpha_{D,0}^{Mod} + \alpha_{D,0}^{D_{3/2}} + \alpha_{D,0}^{D_{5/2}} = 9.67(15) + 5.46(8) + 0.29(3) = 15.42(17)$$
$$\alpha_{D,2} = \alpha_{D,2}^{Mod} + \alpha_{D,2}^{D_{3/2}} + \alpha_{D,2}^{D_{5/2}} = 1.5(1.3) - 5.46(8) + 0.33(4) = -3.6(1.3)$$

Table 4.5 shows the results of the optical RESIS study. These results were reported in Ref. [3], and in that reference they were compared with the theoretical estimates. This dissertation will reserve that discussion until Chapter 6, so that both the result of the optical study and rf study can be compared with theory.

Table 4.5: $Th^{3+}$ properties determined from the optical RESIS study of $Th^{2+}$ Rydberg fine structures, these properties were reported in Ref. [3]. All properties are in atomic units.

| Property | Optical RESIS (a.u.) |
|---|---|
| $\alpha_{D,0}^{Mod}$ | 9.67(15) |
| $\alpha_{D,0}$ | 15.42(17) |
| $Q$ | 0.54(4) |
| $\alpha_{D,2}^{Mod}$ | 1.5(1.3) |
| $\alpha_{D,2}$ | -3.6(1.3) |
| $\left\|\left\langle 5^2F_{5/2}\left\|M^{[1]}\right\|6^2D_{3/2}\right\rangle\right\|$ | 1.435(10) |
| $\left\|\left\langle 5^2F_{5/2}\left\|M^{[1]}\right\|6^2D_{5/2}\right\rangle\right\|$ | 0.414(24) |

As a final test of the properties determined from the fit of the optical RESIS data for the $Th^{2+}$ Rydberg fine structure, they were used to simulate all three spectra to see if more transitions could be identified. The simulation of the three spectra is shown in Fig. 4.6, with the x-axis of the simulation being the energy deviation from hydrogenic in GHz with the simulated signal represented by the black line. The simulated signal times five is the blue line and times twenty is the red line in Fig. 4.6. For the most part the simulation of each of the spectra is consistent with the observed spectra, with only slight differences between the simulation and the observation around the 5 to 6 GHz range. The features in the high-$L$ are clearly reproduced in the simulation and the simulations enabled the identification of additional transitions. In Fig. 4.7, the observed spectra are shown with the transitions labeled by their $(L, K)$ values. The transitions with the labels in green indicate transitions included in the fit to determine the properties of $Th^{3+}$. The transitions with black labels are inferred identifications given the simulation of the spectra from

the determined $Th^{3+}$ properties. All the transitions in the observed spectra have been given probable identifications with no transition left unidentified or unexplained, showing that the properties determined from the fit of the data are able to reproduce all three of the observed spectra.

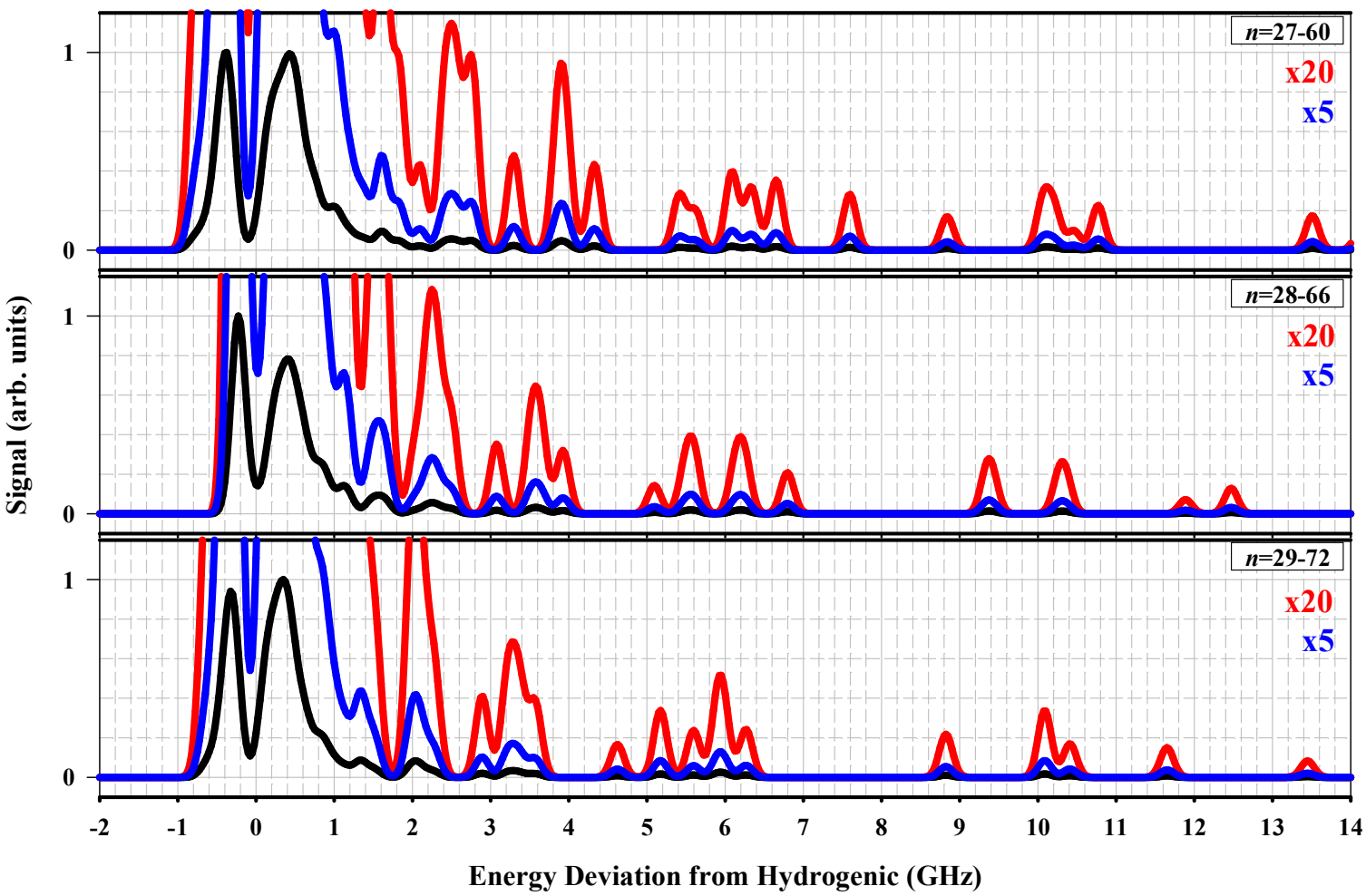


Figure 4.6: Simulated RESIS optical spectra using the determined $Th^{3+}$ properties and matrix elements [3]. The x-axis is the energy deviation from hydrogenic in GHz. The simulated signal is seen in black, the simulated signal time five is seen in blue and the simulated signal times twenty is seen in red.

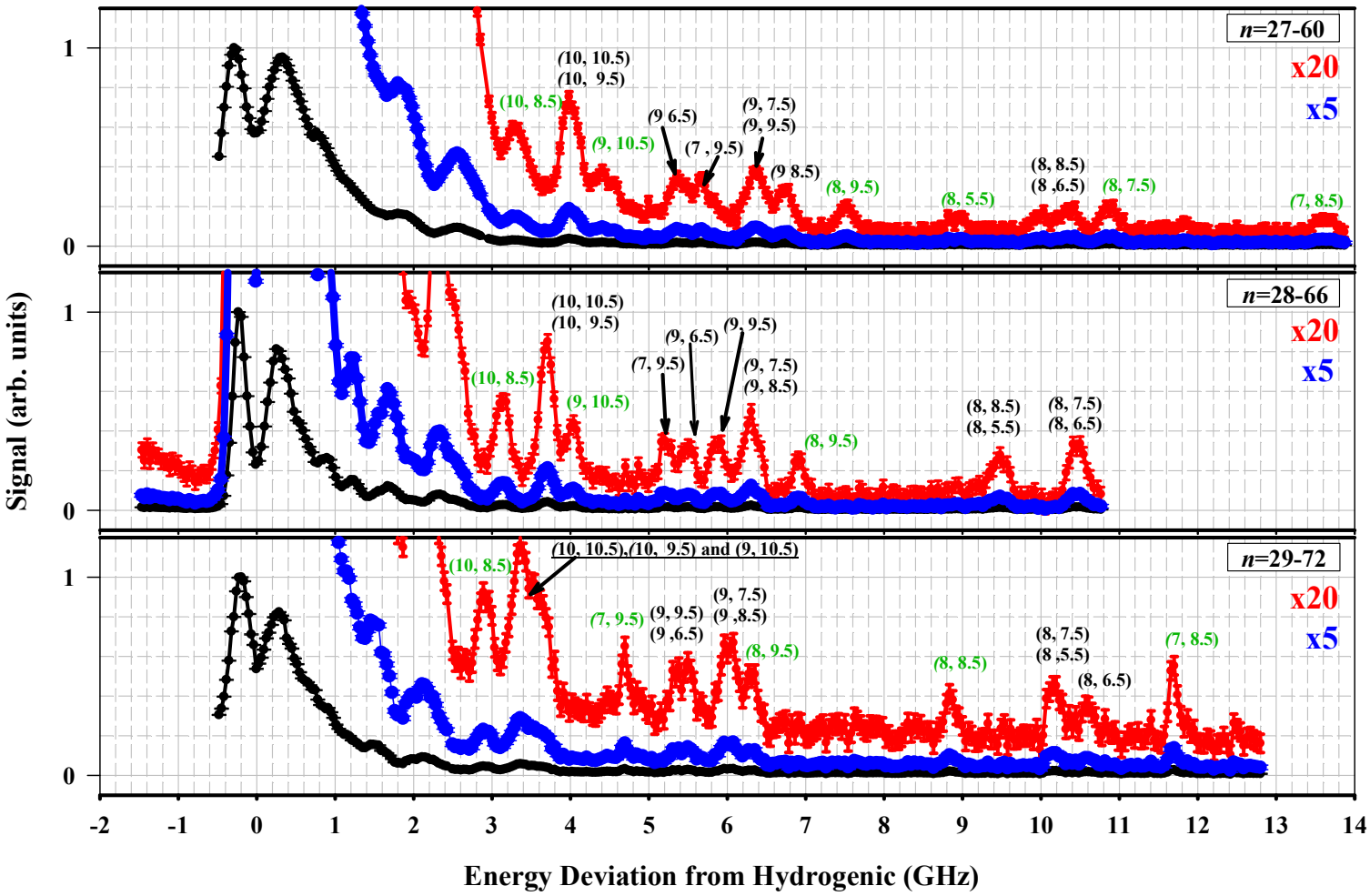


Figure 4.7: RESIS optical spectra for high-$L$ $Th^{2+}$ Rydberg levels with the transitions identified, the x-axis is the energy deviation from hydrogenic in GHz. The black is the original signal, blue signal time five and red signal times twenty. The transitions are labeled by ($L$, $K$) with the labels in green denoting transitions used in the fit to determine properties [3]. The transitions denoted by black labels are inferred identification given the simulated positions of the transition from the determined properties.

## Chapter 5: Rf measurments of $n$=28 $Th^{2+}$ Rydberg states

### 5.1 Why make rf measurements of the $Th^{2+}$ Rydberg fine structure?

The optical study of $Th^{2+}$ Rydberg structure was limited in ability to resolve the fine structure. A total of fourteen individual transitions in the three optical spectra shown in the previous chapter were identified and fit to determine properties of $Th^{3+}$. The rf RESIS technique is capable of resolving parts of the Rydberg fine structure pattern not resolvable with the optical technique and providing measurements of much higher precision. The rf study also has other advantages. For example, the rf measurement depends only on the structure of the lower $n$ state in the RESIS transition, so it is not complicated by questions of structure or perturbations in the upper state. All of these advantages were illustrated in the rf study of $Th^{3+}$ Rydberg levels described in Chapter 3.

The rf study of the $Th^{2+}$ Rydberg fine structure is a much more complex project, but it offers the opportunity to learn more about $Th^{3+}$ and more fully explore the effective potential model used to extract the properties of $Th^{3+}$ from the $Th^{2+}$ Rydberg fine structure. In the case of the $Th^{2+}$ Rydberg fine structure, the optical study showed that the effective potential model was not adequate in the interpretation the $Th^{2+}$ Rydberg fine structure without corrections for the low-lying $D$ states. By improving on the optical measurement the effects of the low-lying $D$ states on the Rydberg fine structure could be explored and the method of correcting the effective potential for these effects could be put to the test. With a goal of improving upon the optical RESIS measurements, an rf study of the $n$=28 $Th^{2+}$ Rydberg fine structure was undertaken. The experimental results are presented in this chapter.

## 5.2 Measuring the $n$=28 $Th^{2+}$ Rydberg fine structure with rf transitions

Using the apparatus at JRML, discussed in detail in Chapter 2 of this work, rf measurement of the $n$=28 $Th^{2+}$ high-$L$ Rydberg fine structure were undertaken. The lower $n$=28 state was chosen for closer study due the resolution of the $n$=28 to 66 spectrum seen in Fig. 4.7. Several transitions were better resolved in that spectrum than the other two observed spectra shown in that figure, specifically $L$=10 $K$=8.5 and $L$=9 $K$=10.5. In order for an rf study to proceed the states of interests must be resolved in the optical excitation spectrum, since the rf transitions are detected by detecting changes in the amount of population that is excited by the RESIS excitation. This study was started by assuming all the identifications in the $n$=28 to 66 spectrum in Fig. 4.7 were correct. The optical $n$=28-66 excitation spectrum clearly resolved some of the $L$=8, $L$=9 and $L$=10 states but due to frequency range of the rf generator being used to make the rf measurements, the fine structure measured would only be able to include states with $L$>8.

Figure 5.1 shows the fine structure of $n$=28, $L$=9 to $L$=12, simulated using the results of the optical study of the $Th^{2+}$ Rydberg fine structure. The y-axis of Fig 5.1 gives the energy difference from hydrogenic in GHz for each level. The levels in the fine structure pattern are labeled by their $L$, $K$ and series value, denoted by $(L, K, series)$. At other times in the text the levels are just labeled by $(L, K)$ alone, because the series value is just another way of writing the $K$ value. There are six different series given the $J_c$ of $Th^{3+}$. Series value ranges from $L-5/2$ to $L+5/2$, just like the $K$ value. Two different colors of lines in Fig. 5.1 denote the locations of each of the levels. The levels denoted with black lines indicate levels that are resolved and identified in the optical spectrum, Fig. 4.7. The levels denoted with grey lines are levels whose

positions are not optically resolved in the optical spectrum. The location of the some of these levels were discovered with the assistance of the rf transitions.

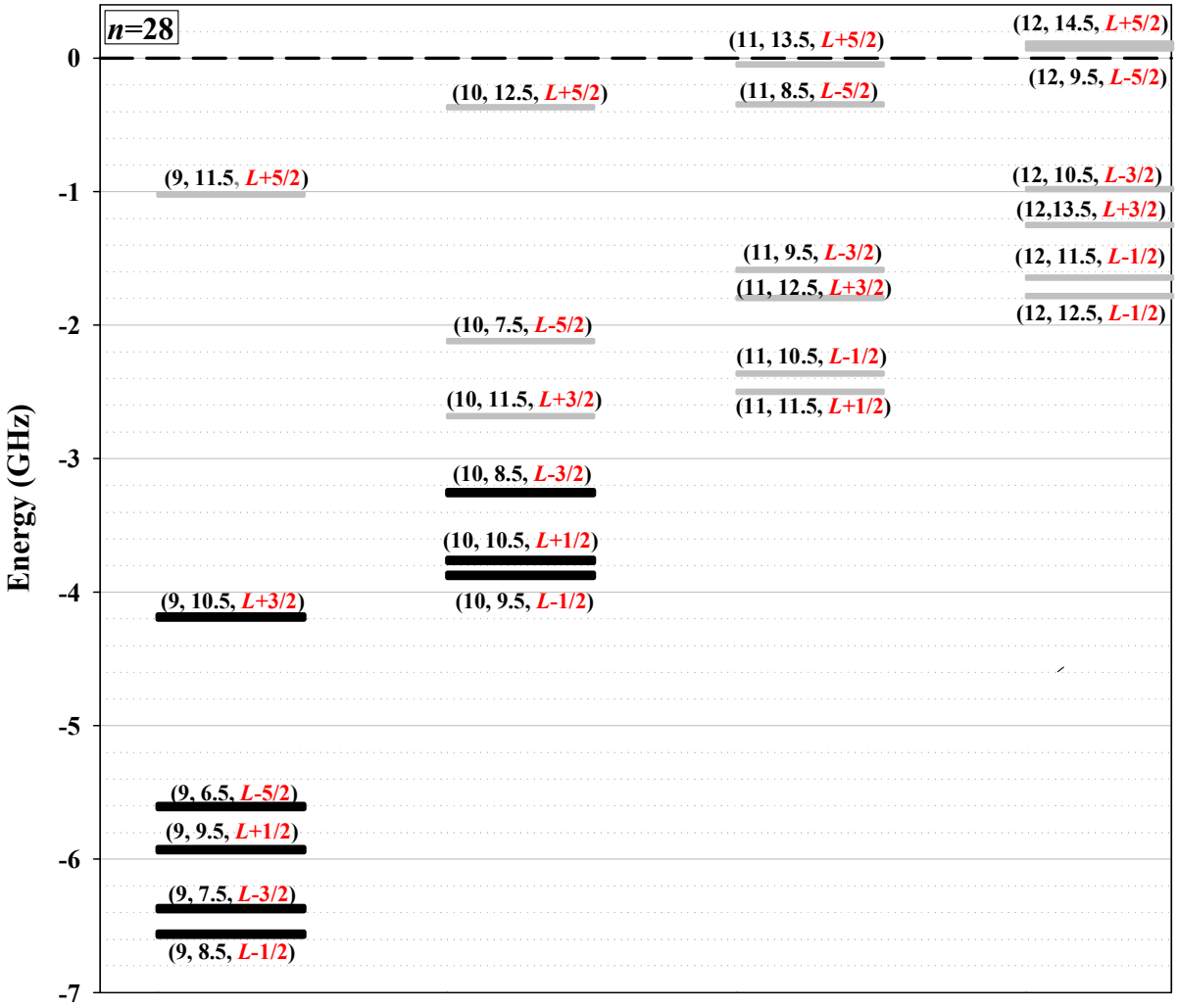


Figure 5.1: $Th^{2+}$ Rydberg level diagram for $n$=28 $L$=9 to 12, simulated using the result of the optical study. The y-axis is the energy in GHz, each level in the fine structure is labeled by its $(L, K, series)$ values. Levels denoted in grey are not resolved in the optical $n$=28-66 excitation spectrum, levels denoted with black lines are resolved.

The mapping out of the fine structure pattern relies on the interconnecting of the all the levels in the fine structure with rf transitions. Determining this fine structure pattern with the RESIS rf technique is very challenging due the number of levels involved in the fine structure

pattern and the fact that a majority of the transitions in the $n$=28 to 66 optical spectrum are not well resolved. In order for the rf study of the $Th^{2+}$ Rydberg fine structure to be successful, the fine structure needed to be measured in a minimum of three $L$s with the positions of as many of the six levels as possible for each $L$ determined. The measurement of this complex fine structure relies on both single and two photon transitions to interconnect all of the states. The single photon transitions are limited by two selection rules, the first one is $L' = L \pm 1$ and the second is $K' = K, K \pm 1$. The most likely transitions to occur for a state is $L' = L + 1$ and $K' = K + 1$, this type of transition connects states in the same series. The next most likely single photon transition is the $L' = L + 1$ and $K' = K$, this type of transition can interconnect levels of different series. The third type of transition used in the measuring the $n$=28 fine structure was two photon transition following the selection rule $L' = L + 2$ and $K' = K + 2$. This allowed for the measured fine structure pattern to be expanded to include levels in higher $L$, that were not reachable with single photon transitions. Each of these different types of rf transitions require different levels of power to make observations of the transitions. The discussion of the power level used in the observation will be reserved until later.

The measuring of such a complex fine structure can be overwhelming, so to begin with the fine structure of each individual series was focused on and measured. The levels in the $L$-5/2 series are denoted by the black lines in Fig. 5.2. The blue lines interconnecting the states indicate the transitions necessary to interconnect the levels, dashed lines representing single photon transitions, and the solid line representing a two photon transition. The four states in the $L$-5/2 series are the $L$=9 $K$=6.5, the $L$=10 $K$=7.5, the $L$=11 $K$=8.5 and the $L$=12 $K$=9.5.

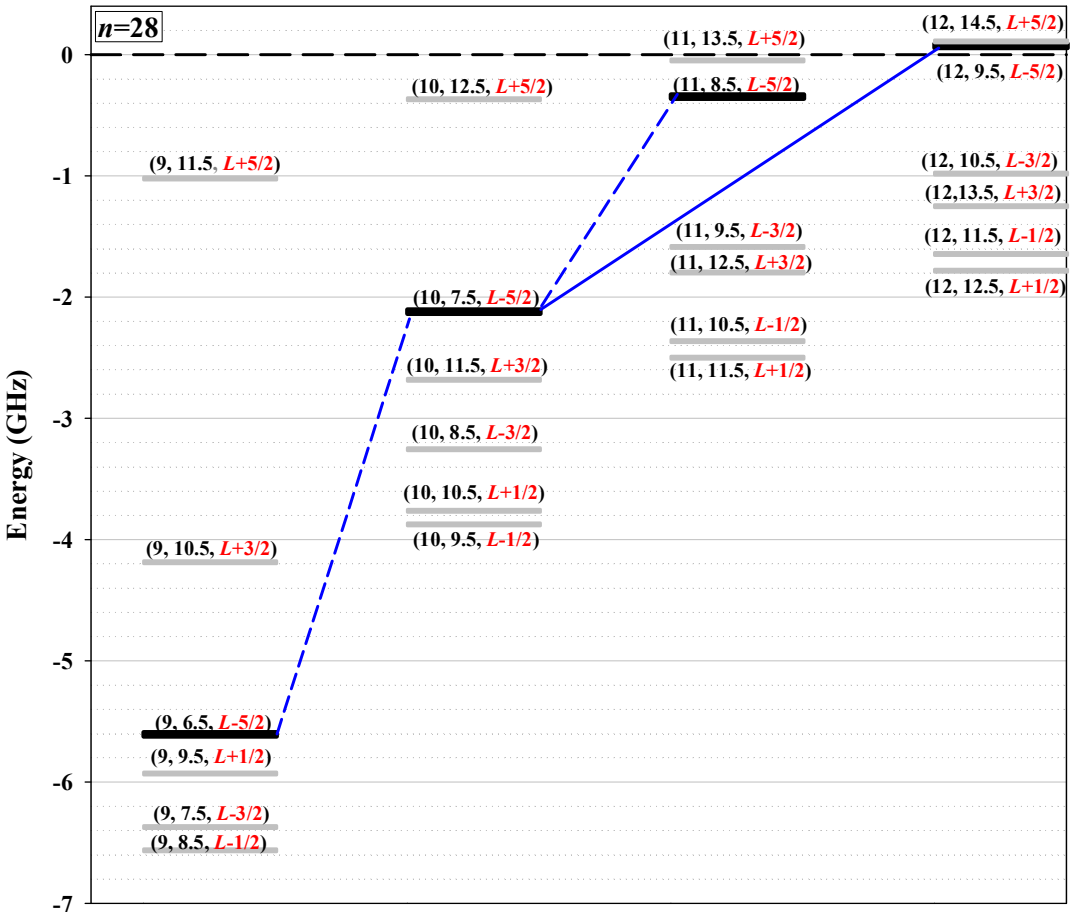


Figure 5.2: Diagram of the $L$-5/2 transitions in the $n$=28 $Th^{2+}$ Rydberg fine structure. The blue lines represent single photon (dashed) and two photon (solid) transitions.

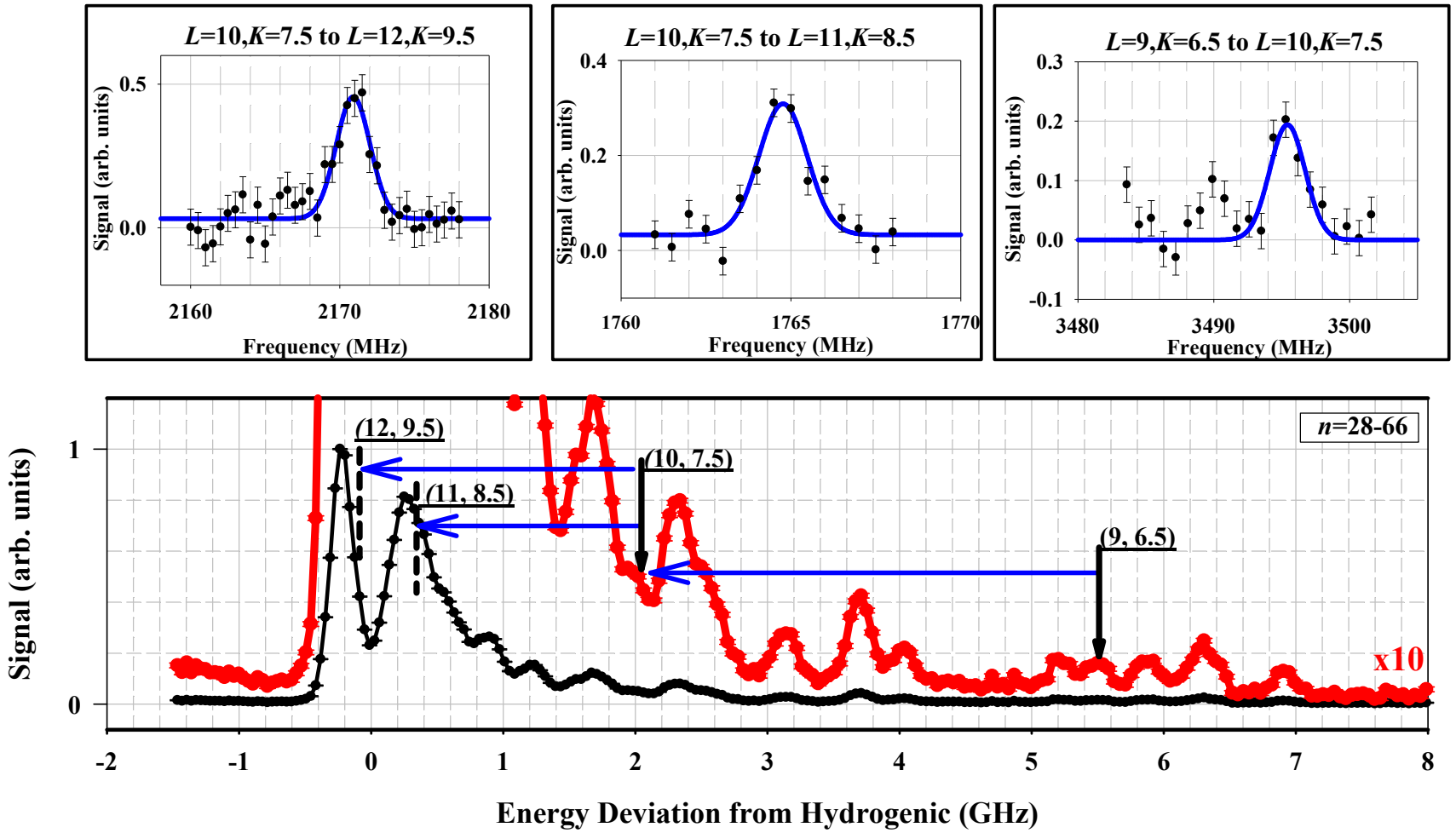


Figure 5.3: Measuring the $L$-5/2 series in the $n$=28 $Th^{2+}$ Rydberg fine structure. The bottom graph is the optical excitation spectrum for the $n$=28-66 transition, the locations of each of the excitation used to observe rf transitions is denoted by a solid vertical. The dashed vertical lines indicate the estimated position of levels that are not optically resolved. The blue lines that connect the vertical lines indicate rf transitions used to connect the levels. The graphs on top give examples of each of the rf transitions that interconnect the states in the $L$-5/2 series in $n$=28.

The measurement of the $L$-5/2 series, began by locating the $L$=9 $K$=6.5 in the $n$=28-66 optical spectrum, located at approximately 5.5GHz in Fig 5.3, where it is resolved from the states near it. Both LIRs were placed on the $L$=9 $K$=6.5 optical excitation. LIR 1 acted to deplete the $L$=9 $K$=6.5 population in $n$=28 by exciting it up to the $n$=66 level. LIR 2 was used to excite the $L$=9 $K$=6.5 population again to $n$=66 level after the $L$=9 $K$=6.5 population had been replenished by a rf transition in the rf region. If the rf is on resonance with the $L$=9 $K$= 6.5 to $L$=10 $K$=7.5 energy difference, population from the $L$=10 $K$=7.5 will transfer to the $L$=9 $K$=6.5 causing the excitation of more population to $n$=66 level by the LIR 2. The increase in the population of the $n$=66 level is detected as the signal, since the field in the rf region is modulated and resulting modulation of the $n$=66 population is measured. The frequency of the $L$=9 $K$=6.5 to $L$=10 $K$=7.5 resonance was estimated from the optical study [3] to be at approximately 3486±55MHz and the actual $L$=9 $K$=6.5 to $L$=10 $K$=7.5 transition was found at a Doppler-corrected frequency 3492.42±0.11MHz. The observation of the signal is seen in Fig. 5.3. In the observation of this transition there is a slight peak on the left side of the resonance, located at approximately 3490MHz. The small peak is due to an unusually larger reflection coefficient in the rf system. The presence of the additional peak was considered when fitting the resonance.

To measure the next rf transition in the $L$-5/2 series, the $L$=10 $K$=7.5 had to be located in the $n$=28-66 optical spectrum so that both LIRs could be placed on it. This state is not optically resolved in the $n$=28-66 spectrum. The location of the $L$=10 $K$=7.5 in the optical spectrum has been simulated using the properties determined from the optical study, the simulation accounts for the fine structure of both the lower $n$ and upper $n$ state. The measurement of the rf transition provides the energy differences between the $L$=9 $K$=6.5 to $L$=10 $K$=7.5 in the $n$=28, so it also provides an estimate of the location of the $L$=10 $K$=7.5 in the optical excitation spectrum. This

estimation would lack the contribution of the $n$=66 fine structure to the location of the optical excitation of the $L$=10 $K$=7.5 in the optical spectrum though. The combination of the rf transition and the simulation of the location from the properties determined from the optical study were both used to identify an estimated location of the $L$=10 $K$=7.5 excitation in the $n$=28-66 optical spectrum, at approximately 2GHz in Fig. 5.3. The $L$=9 $K$=6.5 to $L$=10 $K$=7.5 rf transition itself was then used to confirm the location of $L$=10 $K$= 7.5 optical excitation. To do this the $L$=9 $K$=6.5 to $L$=10 $K$=7.5 rf resonance was first measured with both LIRS on the $L$=9 $K$=6.5. LIR 2 was then moved off the $L$=9 $K$=6.5 making the rf signal go away since LIR 2 can no longer detect the population change to the $L$=9 $K$=6.5 when the second LIR is tuned off the optical excitation. LIR 2 was then scanned across the estimated location of the $L$=10 $K$=7.5 in the optical spectrum, to detect the depletion of the $L$=10 $K$=7.5 by the rf transition. A negative signal was observed when LIR 2 was at the exact location of the $L$=10 $K$=7.5 in the optical spectrum. The first LIR was then moved the same amount to sit on the $L$=10 $K$=7.5 and the search for the $L$=10 $K$=7.5 to $L$=11 $K$=8.5 rf resonance began. The $L$=10 $K$=7.5 to $L$=11 $K$=8.5 rf resonance was estimated at around 1775±27MHz, and it was discovered to be at approximately 1763.64±0.08MHz. These two single photon transitions interconnected three $L$s in the $L$-5/2 series. To add an additional $L$ to this series it was necessary to do a two photon transition between the $L$=10 $K$=7.5 and the $L$=12 $K$=9.5 since even with the knowledge gained in the optical study and the $L$=10 $K$=7.5 to $L$=11 $K$=8.5 rf resonance, it was not possible to resolve the location of the $L$=11 $K$=8.5 in the optical excitation spectrum. The estimated location of the $L$=11 $K$=8.5 in the optical spectrum is overlapping with the high-$L$, as can be seen in Fig. 5.3. The estimated location of the $L$=11 $K$=8.5 has been denoted by dashed line at approximately 300 to 400MHz on the optical excitation spectrum. A two photon transition connecting the $L$=10

$K$=7.5 to $L$=12 $K$=9.5 was estimated to be at 2192±54MHz, and it was observed at a Doppler-corrected frequency of 2168.86±0.07MHz. These three transitions interconnect four $L$s in the $n$=28 fine structure and establish the positions of three levels that were not resolved in the optical study.

Using the same techniques used with the $L$-5/2 series, four more series were measured and mapped out in the $n$=28 $Th^{2+}$ Rydberg fine structure. The observation of each of the other series is summarized with two figures and one table for each series. For each series one figure identifies the transitions involved in the series on a diagram of the $n$=28 fine structure, another figure that identifies the transitions in relation to the optical spectrum and shows examples of the observed rf transitions. A table for each of the series gives a list of the transitions involved in each series, the estimated locations of the transitions and the measured Doppler-corrected frequencies. The second series, the $L$-3/2 series, is shown in Fig. 5.4, Fig. 5.5 and Table 5.1. The transitions for the third series, the $L$-1/2 series, are shown in Fig.5.6, Fig. 5.7 and Table 5.2. The fourth series, the $L$+1/2 series, is presented in Fig. 5.8, Fig. 5.9 and Table 5.3. The fifth series, the $L$+3/2 series, is shown in Fig. 5.10, Fig. 5.11 and Table 5.4.

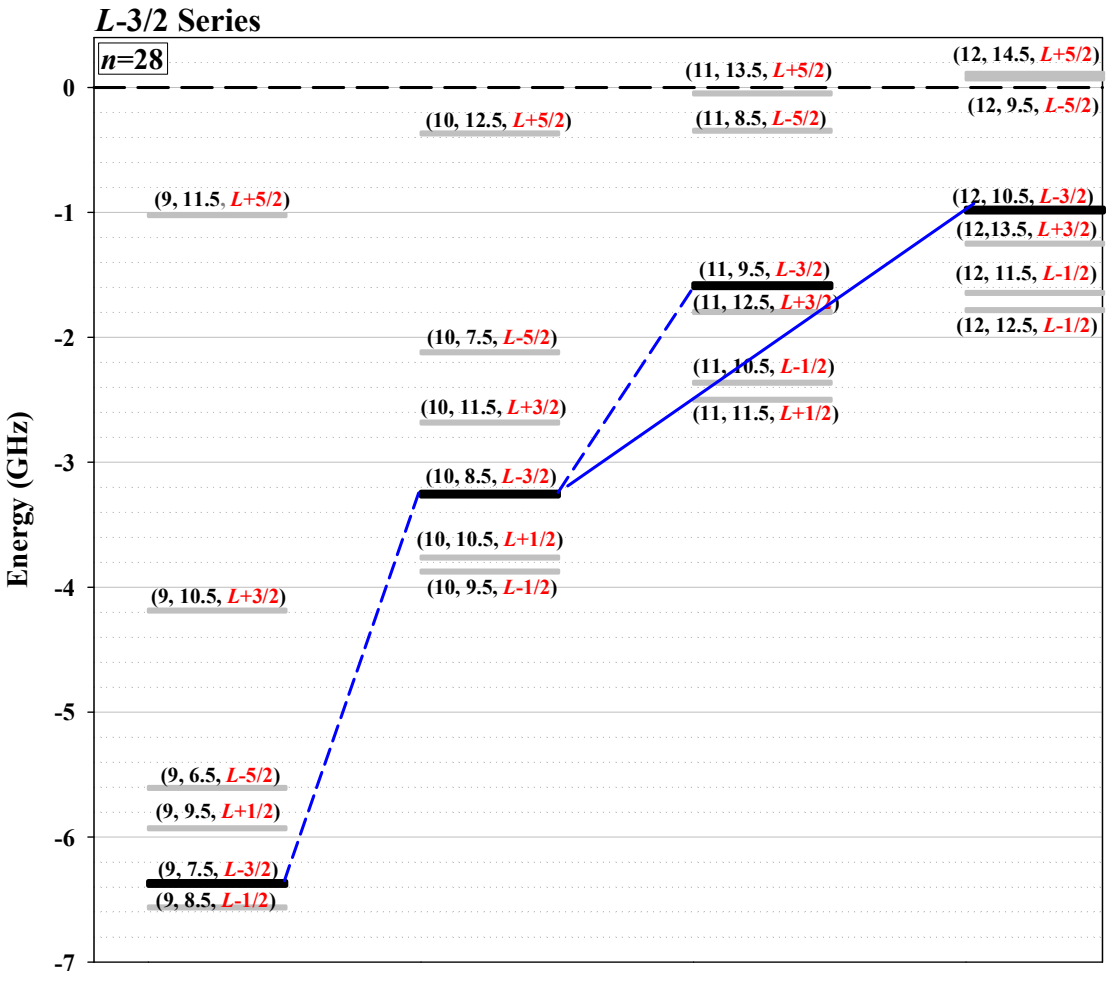


Figure 5.4: Diagram of the $L$-3/2 transitions in the $n$=28 $Th^{2+}$ Rydberg fine structure. The blue lines represent single photon (dashed) and two photon (solid) transitions.

Table 5.1: List of the transitions in the $L$-3/2 series. Column one identifies the transition, column two gives the estimated location for the transition and the third column gives the Doppler-corrected frequency for the transition.

| $(L, K)$ to $(L', K')$ | Estimated Interval (MHz) | Measured Interval (MHz) |
|---|---|---|
| (9,7.5) to (10,8.5) | 3117(30) | 3126.56(11) |
| (10,8.5) to (11,9.5) | 1669(16) | 1663.47(8) |
| (10,8.5) to (12,10.5) | 2273(22) | 2262.15(11) |

***L*-3/2 Series**

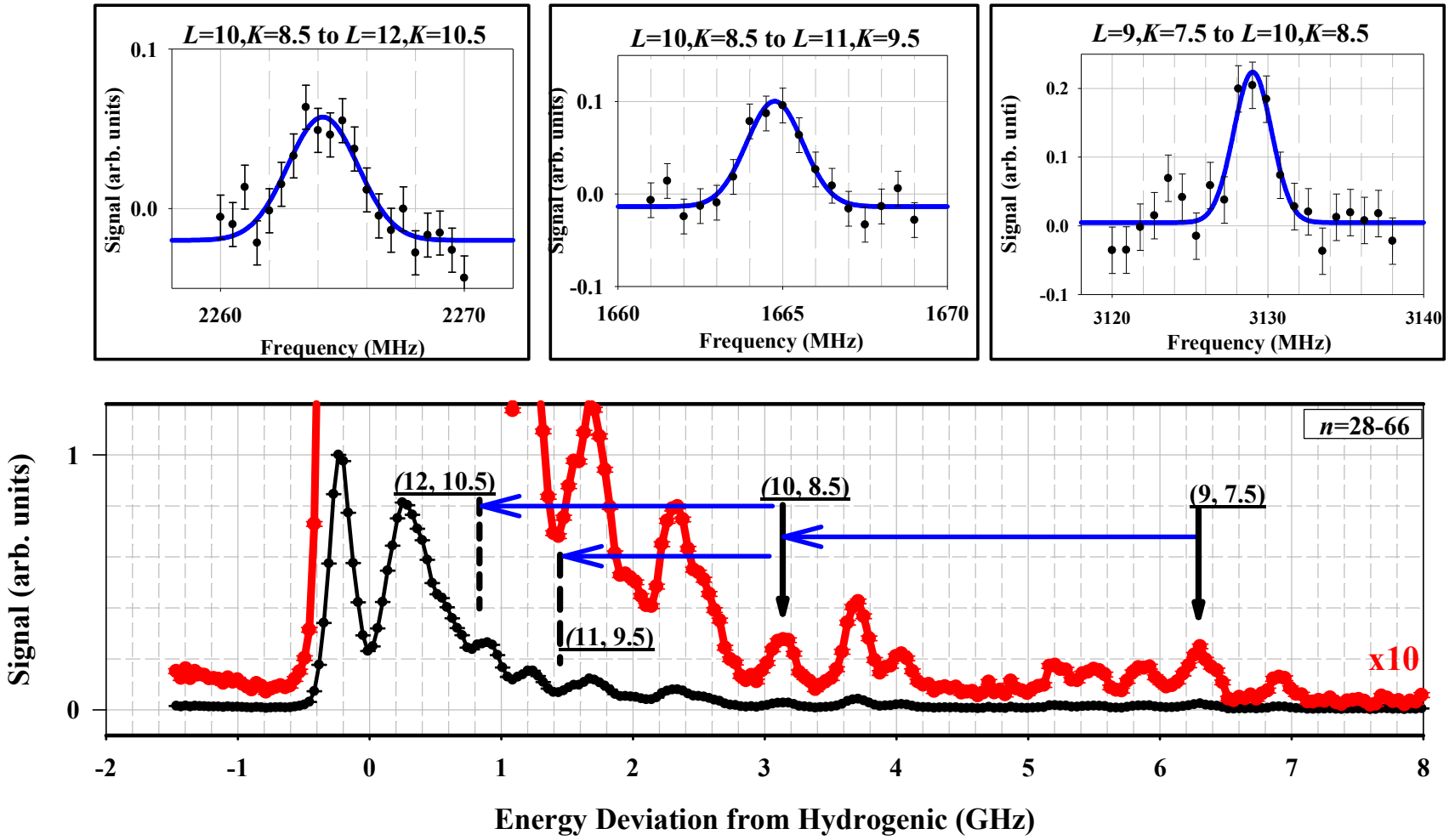


Figure 5.5: Measuring the *L*-3/2 series in the *n*=28 $Th^{2+}$ Rydberg fine structure. The bottom graph is the optical excitation spectrum for the *n*=28-66 transition, the locations of each of the excitation used to observe rf transitions is denoted by a solid vertical. The dashed vertical lines indicate the estimated position of levels that are not optically resolved enough to be used to observe an rf transition. The blue lines that connect the vertical lines indicate rf transitions used to connect the levels. The graphs on top give examples of each of the rf transitions that interconnect the states in the *L*-3/2 series in *n*=28.

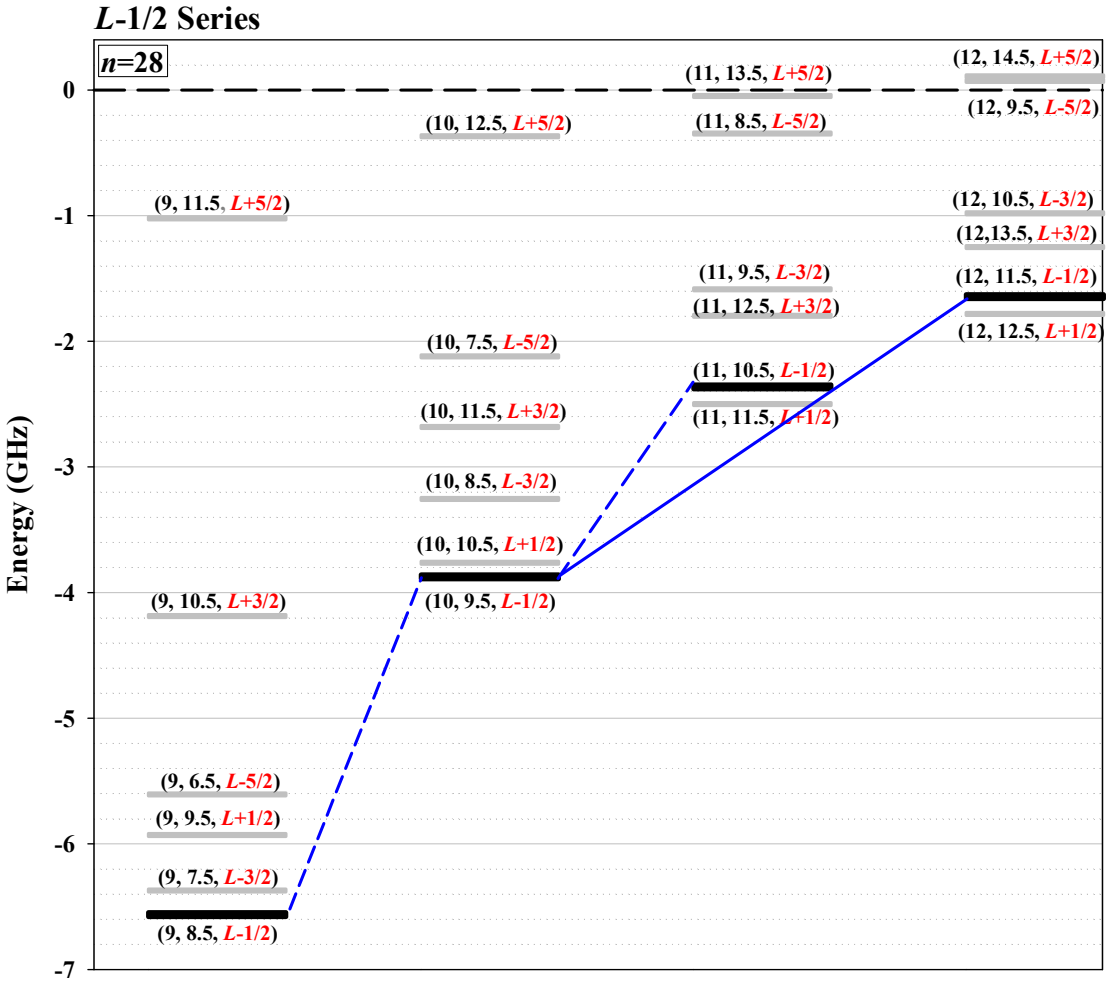


Figure 5.6: Diagram of the $L$-1/2 transitions in the $n$=28 $Th^{2+}$ Rydberg fine structure. The blue lines represent single photon (dashed) and two photon (solid) transitions.

Table 5.2: List of the transitions in the $L$-1/2 series. Column one identifies the transition, column two gives the estimated location for the transition and the third column gives the Doppler-corrected frequency for the transition.

| $(L, K)$ to $(L', K')$ | Estimated Interval (MHz) | Measured Interval (MHz) |
|---|---|---|
| (9,8.5) to (10,9.5) | 2689(78) | 2683.02(16) |
| (10,9.5) to (11,10.5) | 1511(47) | 1504.90(11) |
| (10,9.5) to (12,11.5) | 2230(75) | 2221.73(12) |

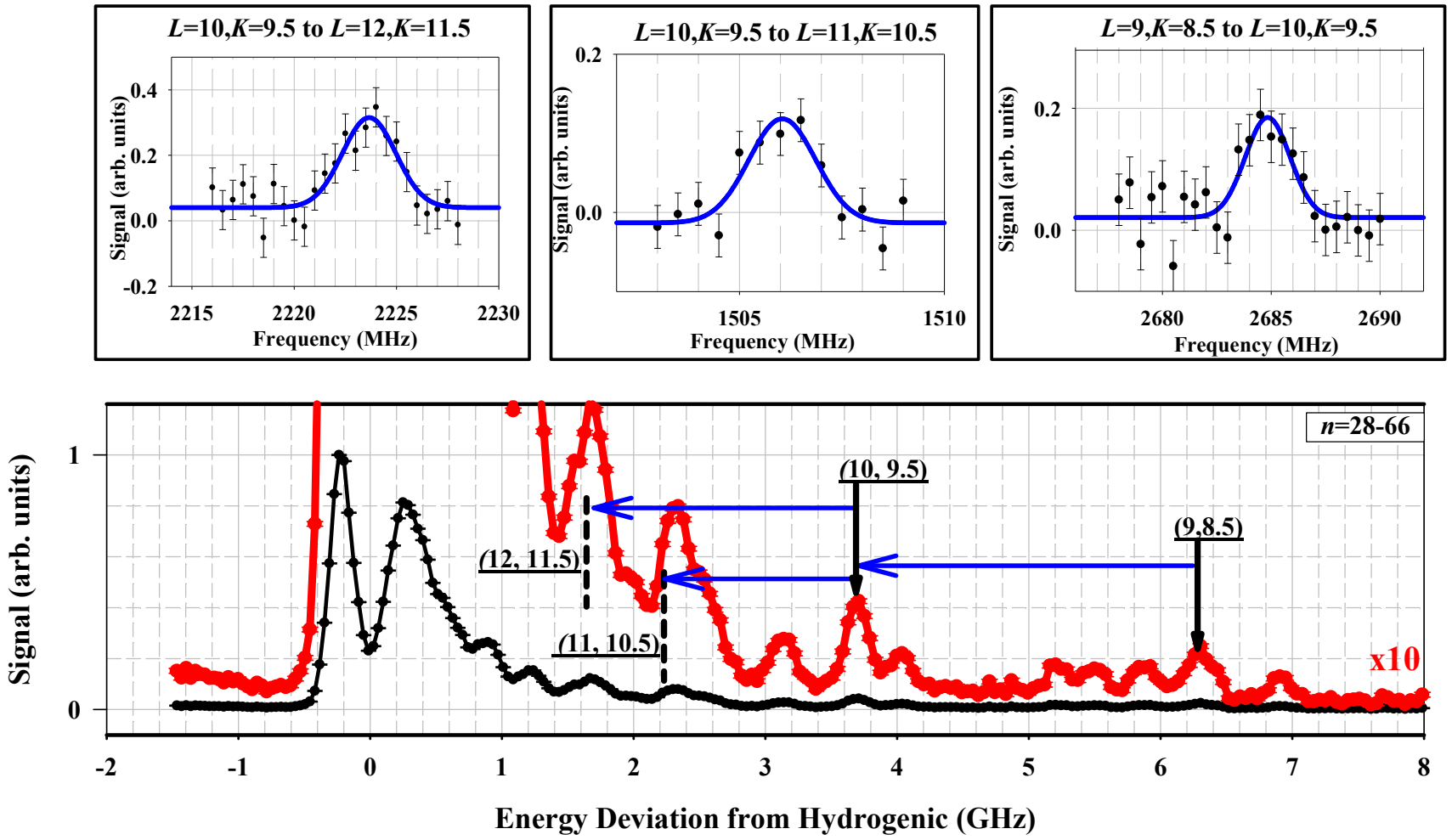


Figure 5.7: Measuring the $L$-1/2 series in the $n$=28 $Th^{2+}$ Rydberg fine structure. The bottom graph is the optical excitation spectrum for the $n$=28-66 transition, the locations of each of the excitation used to observe rf transitions is denoted by a solid vertical. The dashed vertical lines indicate the estimated position of levels that are not optically resolved enough to be used to observe an rf transition. The blue lines that connect the vertical lines indicate rf transitions used to connect the levels. The graphs on top give examples of each of the rf transitions that interconnect the states in the $L$-1/2 series in $n$=28.

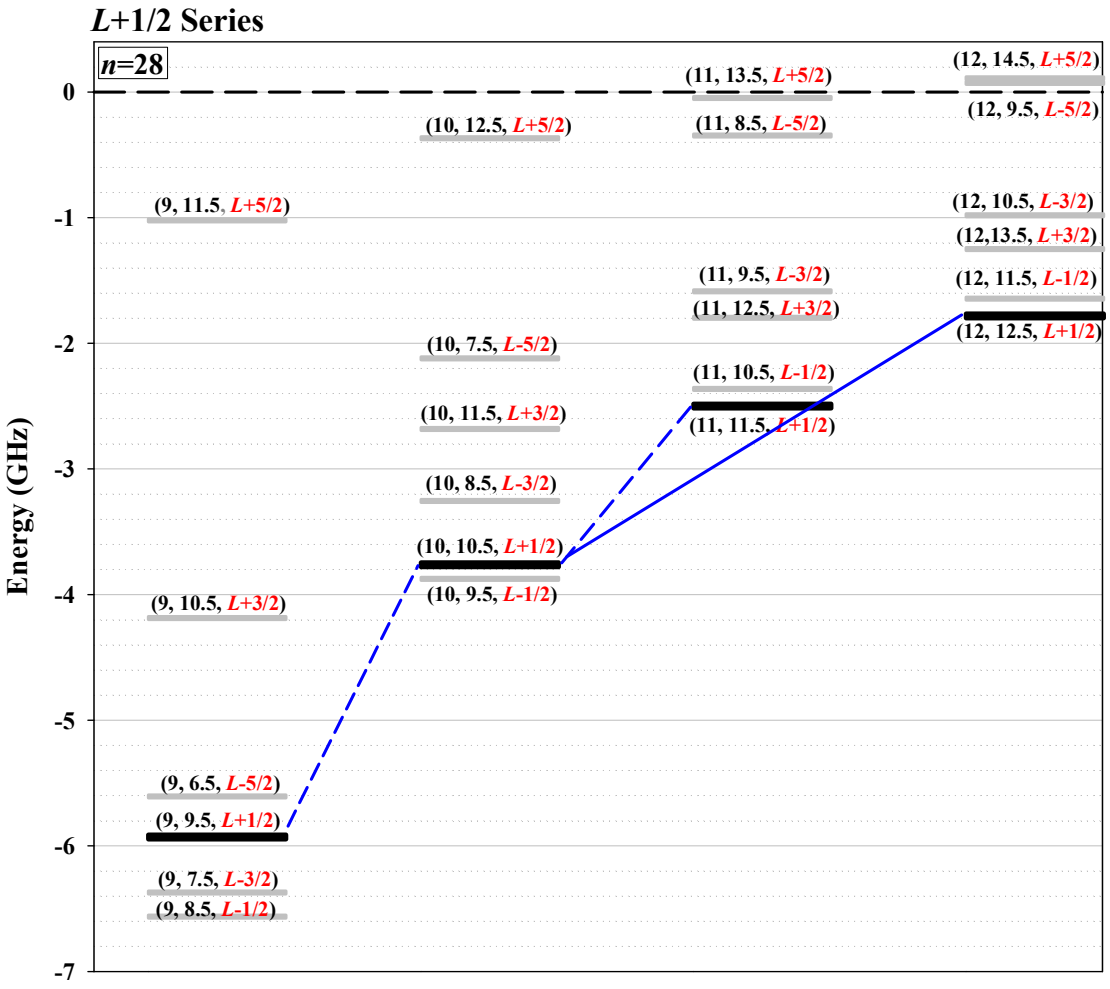


Figure 5.8: Diagram of the L+1/2 transitions in the $n$=28 $Th^{2+}$ Rydberg fine structure. The blue lines represent single photon (dashed) and two photon (solid) transitions.

Table 5.3: List of the transitions in the $L$+1/2 series. Column one identifies the transition, column two gives the estimated location for the transition and the third column gives the Doppler-corrected frequency for the transition.

| $(L, K)$ to $(L', K')$ | Estimated Interval (MHz) | Measured Interval (MHz) |
|---|---|---|
| (9,9.5) to (10,10.5) | 2166(93) | 2257.30(25) |
| (10,10.5) to (11,11.5) | 1264(56) | 1270.18(13) |
| (10,10.5) to (12,12.5) | 1981(91) | 1989.52(5) |

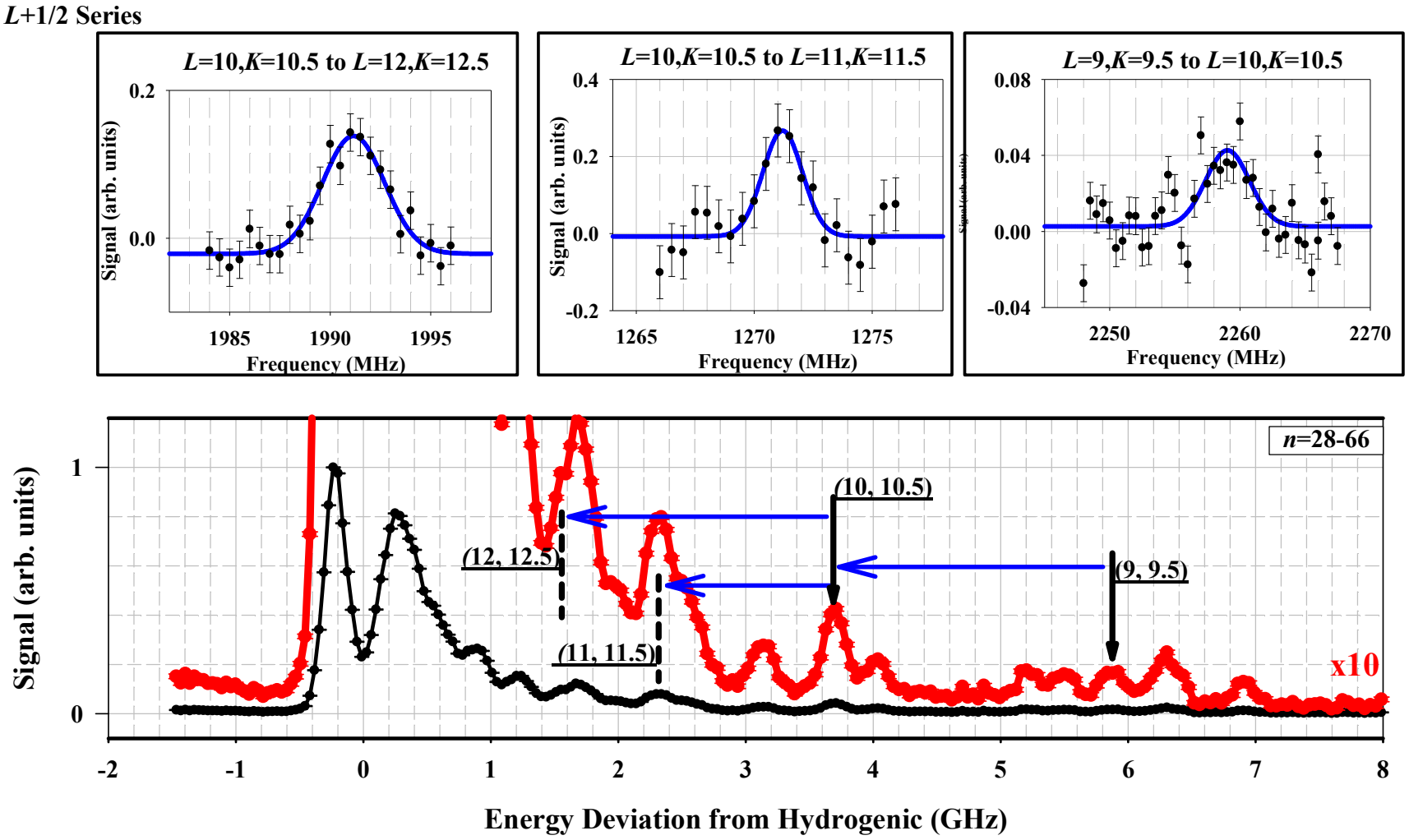


Figure 5.9: Measuring the $L$+1/2 series in the $n$=28 $Th^{2+}$ Rydberg fine structure. The bottom graph is the optical excitation spectrum for the $n$=28-66 transition, the locations of each of the excitation used to observe rf transitions is denoted by a solid vertical. The dashed vertical lines indicate the estimated position of levels that are not optically resolved enough to be used to observe an rf transition. The blue lines that connect the vertical lines indicate rf transitions used to connect the levels. The graphs on top give examples of each of the rf transitions that interconnect the states in the $L$+1/2 series in $n$=28.

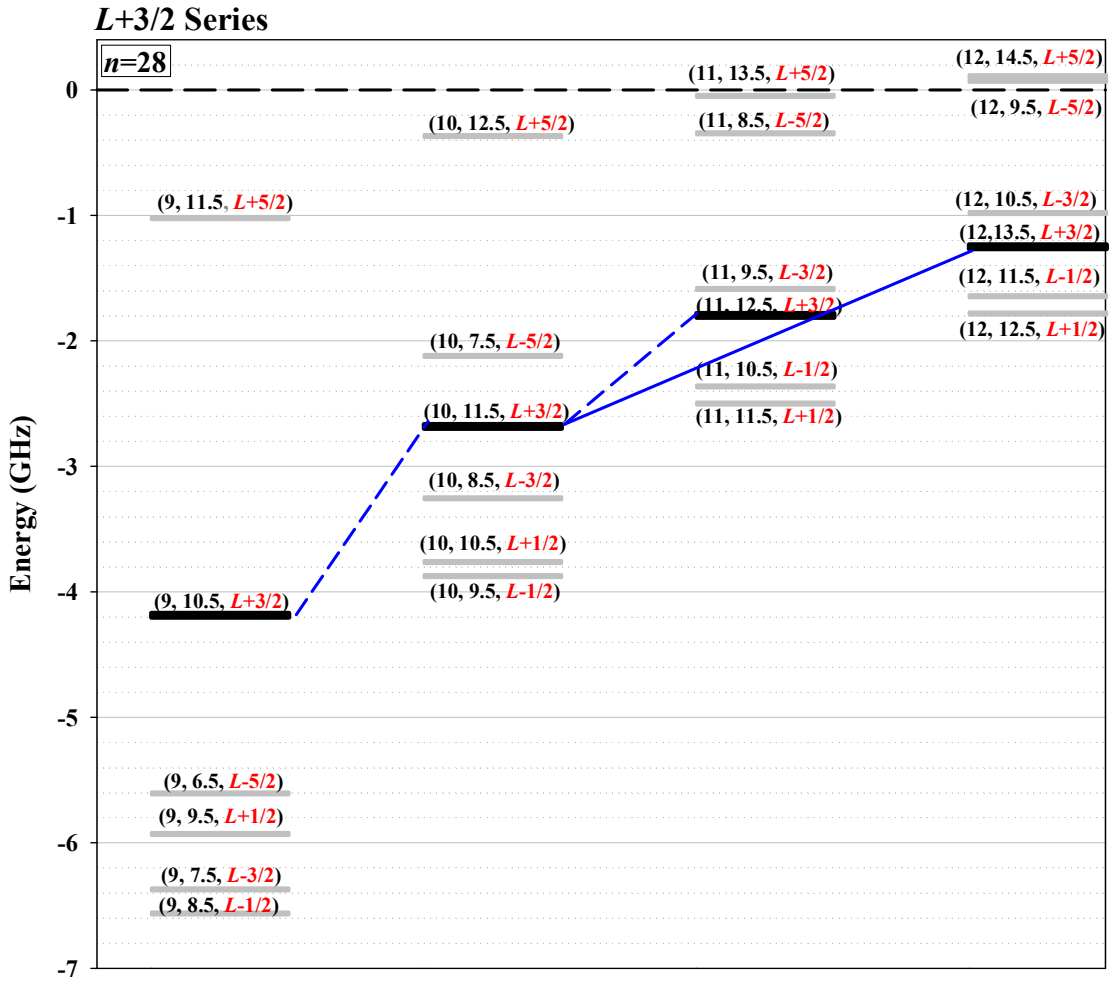


Figure 5.10: Diagram of the $L$+3/2 transitions in the $n$=28 $Th^{2+}$ Rydberg fine structure. The blue lines represent single photon (dashed) and two photon (solid) transitions.

Table 5.4: List of the transitions in the $L$+3/2 series. Column one identifies the transition, column two gives the estimated location for the transition and the third column gives the Doppler-corrected frequency for the transition.

| $(L, K)$ to $(L', K')$ | Estimated Interval (MHz) | Measured Interval (MHz) |
|---|---|---|
| (9,10.5) to (10,11.5) | 1505(59) | 1501.69(7) |
| (10,11.5) to (11,12.5) | 884(34) | 884.60(6) |
| (10,11.5) to (12,13.5) | 1431(56) | 1433.91(10) |

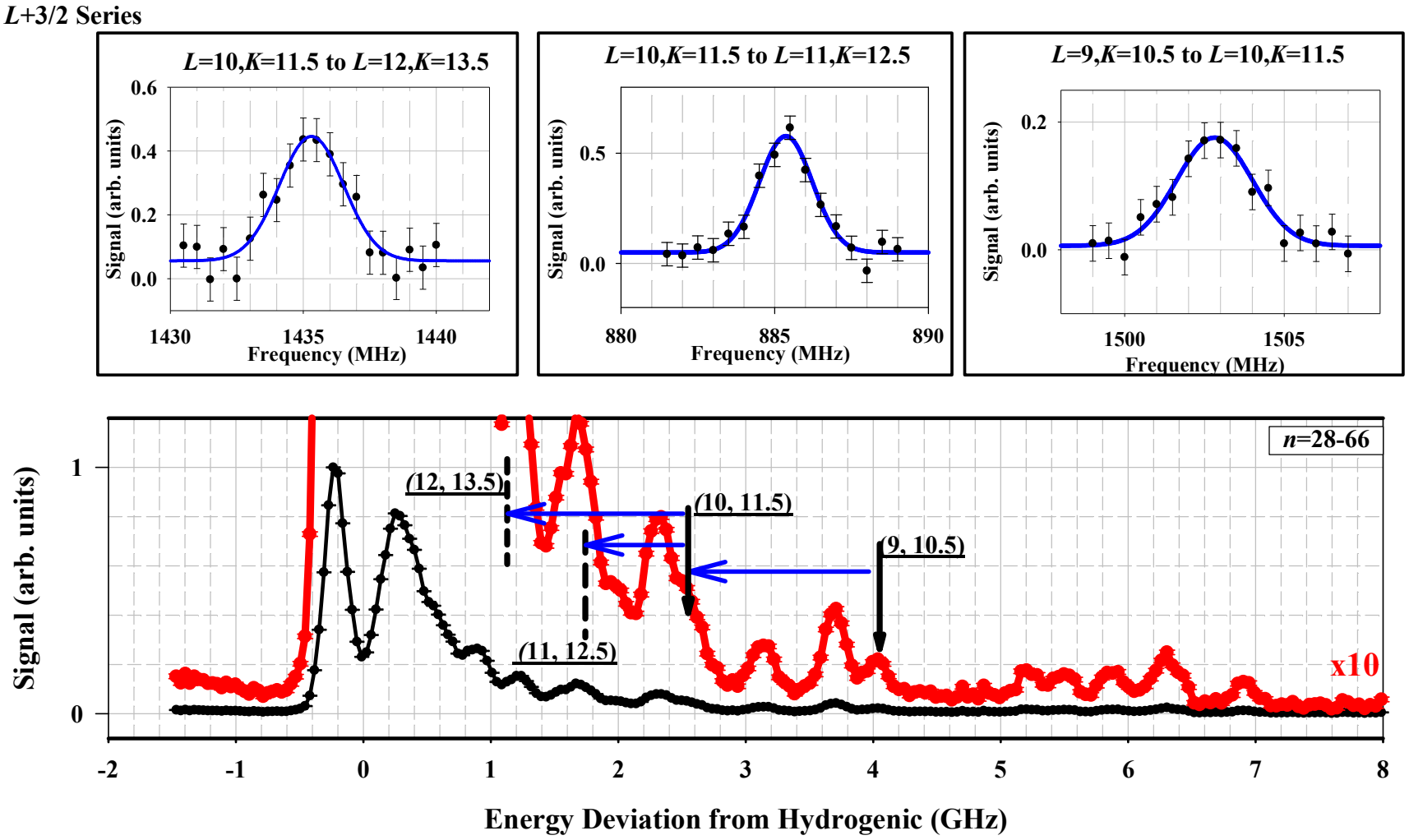


Figure 5.11: Measuring the $L$+3/2 series in the $n$=28 $Th^{2+}$ Rydberg fine structure. The bottom graph is the optical excitation spectrum for the $n$=28-66 transition, the locations of each of the excitation used to observe rf transitions is denoted by a solid vertical. The dashed vertical lines indicate the estimated position of levels that are not optically resolved enough to be used to observe an rf transition. The blue lines that connect the vertical lines indicate rf transitions used to connect the levels. The graphs on top give examples of each of the rf transitions that interconnect the states in the $L$+3/2 series in $n$=28.

The sixth series, the $L$+5/2 series, which includes the $L$=9 $K$=11.5, the $L$=10 $K$=12.5, the $L$=11 $K$=13.5, and the $L$=12 $K$=14.5 was not measured since none of the transitions in that series were optically resolved in the $n$=28-66 excitation spectrum, Fig. 5.12. The estimated location of each of the levels is given in Fig 5.12 and also the estimated frequency difference between the levels. The $L$=9 $K$=11.5 is located very close to the high-$L$ structure and is located in an area with an estimated five other transitions so its location cannot be clearly determined. The absence of this series from the data pattern is unfortunate, but it will not significantly limit the analysis of the measured fine structure pattern. The measurements of the five series only gives the relative location of the four states in each series with respective to the other states in the series.

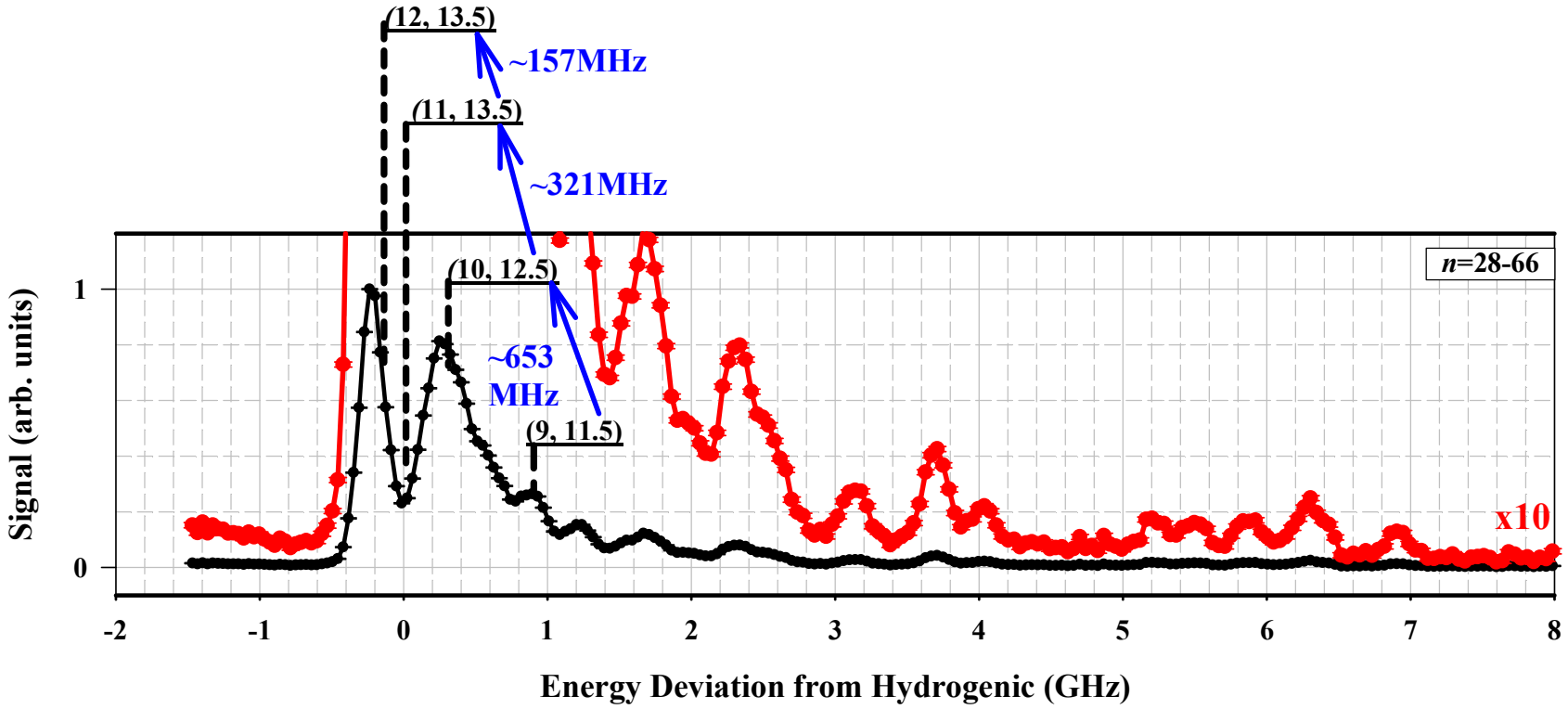


Figure 5.12: The $L$+5/2 series in $n$=28 $Th^{2+}$ Rydberg fine structure, none of the optical excitation in this series are resolved. The locations of the states in this series are denoted by the vertical line dashed lines. The blue lines interconnecting the states represent the estimated frequency difference between the states in $n$=28.

To complete the mapping out of the fine structure it was necessary to interconnect the five series so that the locations of all twenty states are determined relative to each other. This interconnecting of the series is completed by observing four $L' = L + 1$ $K' = K$ transitions. The four selected transitions used to interconnect the series are listed and shown in Fig. 5.13. The observation of the four interconnecting transitions relied on the transitions in the optical excitation spectrum that have already been identified, resolved, and used to the observed other rf transitions.

With the completion of the four $K' = K$ transitions and the measurement of the five series, a total nineteen rf transitions were measured interconnecting twenty of the twenty-four levels in $n$=28 $L$=9 to 12. Figure 5.14 shows all the rf transitions measured. Examples of all nineteen of the rf transitions measured can be seen in Appendix B. Five of the six levels for $L$=9, 10, 11, and 12 were located, providing a much more complete measurement of the $Th^{2+}$ Rydberg fine structure pattern than the reported optical RESIS measurements [3]. The third section of this chapter will provide a table for each of the observed transitions and discuss the relative positions of the levels, for now the discussion will turn to some of the details about what was needed in order to observe the transitions

.

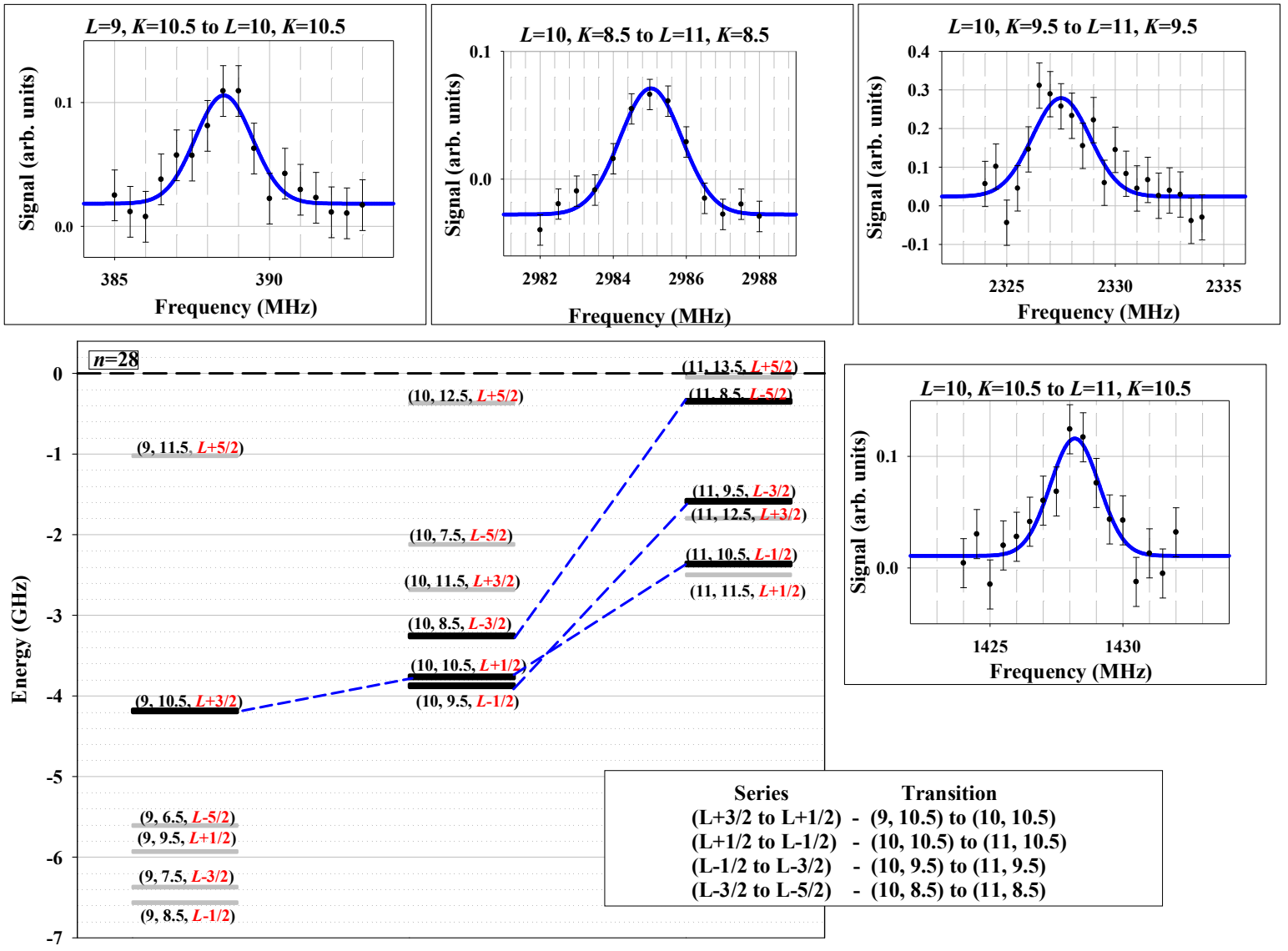


Figure 5.13: The $K'=K$ transitions that interconnect the series in the $n=28$ $Th^{2+}$ Rydberg fine structure. Four transitions connect the five series, an example of each is shown.

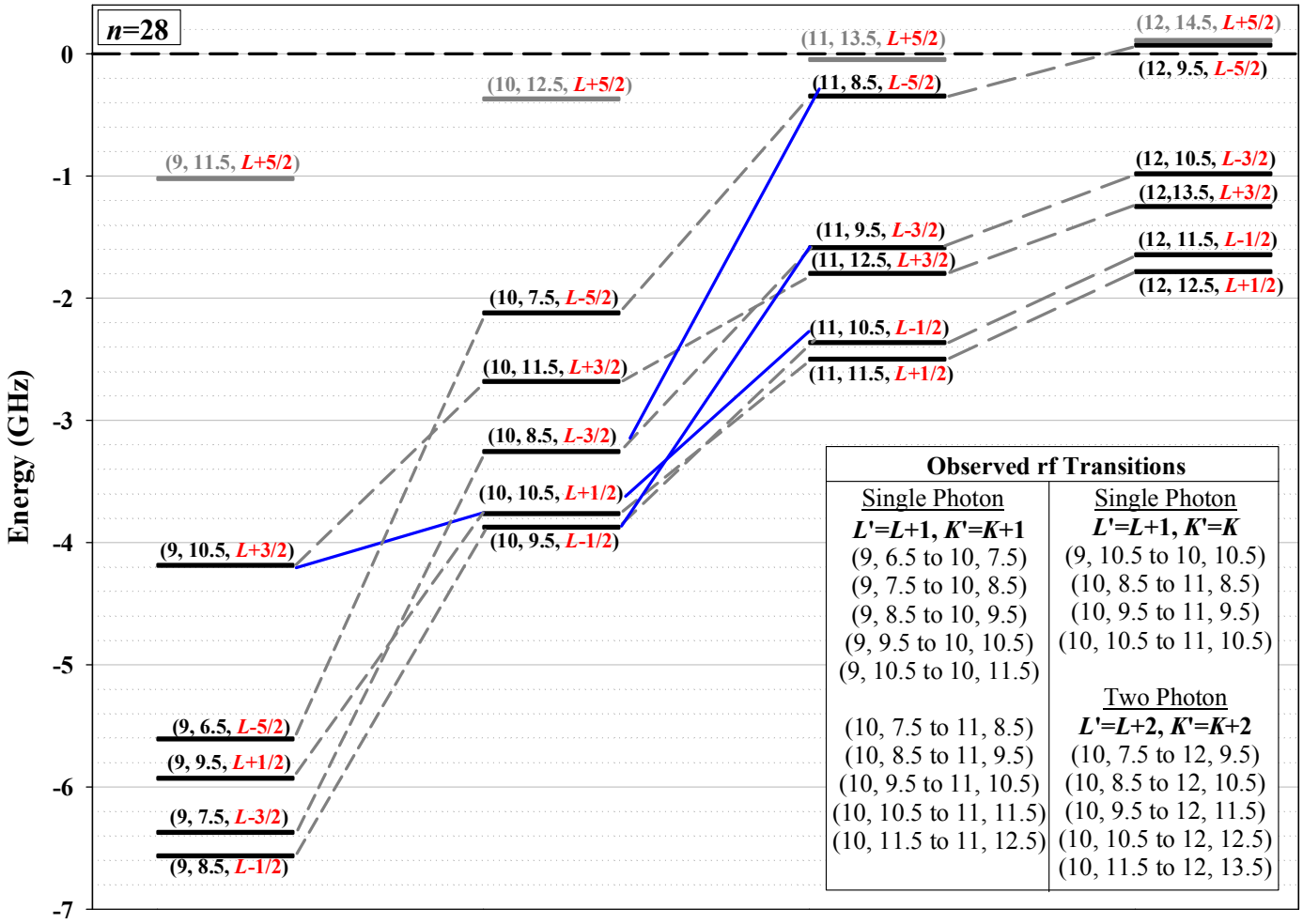


Figure 5.14: The fine structure of the $n$=28 $Th^{2+}$ Rydberg levels observed with rf transitions each level in the fine structure is labeled by $(L, K, series)$. The y-axis is the energy deviation from hydrogenic in GHz. The lines interconnecting the levels represent the rf transitions used to measure the relative positions of all the levels, a complete list of the transitions is seen in the box on the diagram. The grey dashed lines represent the $L' = L+1$ $K' = K+1$ intervals, the blue lines are the $L' = L+1$ $K' = K$ transitions.

In order to complete the observation of the nineteen rf transitions, located and observed in the $n$=28 $Th^{2+}$ Rydberg fines structure, it was necessary to have estimates of all the transitions frequencies and the estimates of the correct power for the observations. Table 5.5 gives a list of the transitions observed and the optical excitation transition each of the LIRs was set on for the observations. The final two columns of Table 5.5 give the estimated frequency of the transition and the observed frequency.

Table 5.5: List of the observed $n$=28 rf transitions used to measure the $Th^{2+}$ Rydberg fine structure. Column one gives the transition and then column two and three gives the optical signal LIR one and two were placed on in order to detect the rf resonance. Column four gives the estimated frequency of the rf resonance in MHz. The final column gives the positions of the measured interval for the transitions in MHz.

| $(L,K)$ to $(L',K')$ | LIR 1 | LIR 2 | Estimated Interval (MHz) | Measured Interval (MHz) |
|---|---|---|---|---|
| (9,6.5) to (10,7.5) | (9,6.5) | (9,6.5) | 3486(35) | 3492.42(11) |
| (9,7.5) to (10,8.5) | (9,7.5) | (9,7.5) | 3117(30) | 3126.56(11) |
| (9,8.5) to (10,9.5) | (9,8.5) | (9,8.5) | 2689(78) | 2683.02(16) |
| (9,9.5) to (10,10.5) | (9,9.5) | (9,9.5) | 2166(93) | 2257.30(25) |
| (9,10.5) to (10,11.5) | (9,10.5) | (9,10.5) | 1505(59) | 1501.69(7) |
| | | | | |
| (10,7.5) to (11,8.5) | (10,7.5) | (10,7.5) | 1775(27) | 1763.64(8) |
| (10,8.5) to (11,9.5) | (10,8.5) | (10,8.5) | 1669(16) | 1663.47(8) |
| (10,9.5) to (11,10.5) | (10,9.5) | (10,9.5) | 1511(47) | 1504.90(11) |
| (10,10.5) to (11,11.5) | (10,10.5) | (10,10.5) | 1264(56) | 1270.18(13) |
| (10,11.5) to (11,12.5) | (10,11.5) | (10,11.5) | 884(34) | 884.60(6) |
| | | | | |
| (9,10.5) to (10,10.5) | (9,10.5) | (9,10.5) | 423(23) | 388.52(11) |
| (10,8.5) to (11,8.5) | (10,8.5) | (10,8.5) | 2909(155) | 2982.60(12) |
| (10,9.5) to (11,9.5) | (10,9.5) | (10,9.5) | 2288(138) | 2328.73(19) |
| (10,10.5) to (11,10.5) | (10,10.5) | (10,10.5) | 1400(81) | 1427.10(10) |
| | | | | |
| (10,7.5) to (12,9.5) | (10,7.5) | (10,7.5) | 2192(54) | 2168.86(7) |
| (10,8.5) to (12,10.5) | (10,8.5) | (10,8.5) | 2273(22) | 2262.15(11) |
| (10,9.5) to (12,11.5) | (10,9.5) | (10,9.5) | 2230(75) | 2221.73(12) |
| (10,10.5) to (12,12.5) | (10,10.5) | (10,10.5) | 1981(91) | 1989.52(5) |
| (10,11.5) to (12,13.5) | (10,11.5) | (10,11.5) | 1431(56) | 1433.91(10) |

The frequencies of the transitions were simulated from the properties found during the optical study [3]. In the end all of the rf transitions were observed within 100MHz of the predicted frequency of the transitions, and the rf measurements confirmed the preliminary identification of all of the transitions in the optical spectrum. The amount of power required in the rf region to product an electric field adequate to induce the transition between the two states of interest was estimated using the approach presented in Chapter 2, Eq. 2.22 and Eq. 2.23. Initially the *K* dependence in the transitions was neglected when estimating the rf power necessary to observe these transitions. The optimum electric field, Eq. 2.22, was calculated using the average *Z* matrix element, Eq. 2.21, which does not include *K* dependence. The transit time through the rf region is $0.51\mu s$ given $\beta = 0.0008320$ for the 75keV $Th^{3+}$ beam. Therefore, for a *L*=10 to 11 transition in the $Th^{2+}$ Rydberg fine structure, the estimated optimum electric field was found to be $0.51V/m$ with $Z_{rms} = 150.6a_0$. The optimum electric field was then rewritten in terms as power exiting the rf region using Eq. 2.23, determining the optimum power to observe *L*=10 to 11 transitions $P_{exit} = 2.64(10)\times 10^{-6} W$. All the single photon $K' = K + 1$ transitions observed should require approximately the same power since the average Z matrix elements without *K* dependence for a *L*=9 to 10 transition and a *L*=10 to 11 transition differ by less than 2%.

To determine whether this estimate of the power necessary to observe the single photon rf transition in the $Th^{2+}$ Rydberg fine structure was correct, a saturation curve was taken on the first discovered rf transition. The data for the saturation curve was taken on the *L*=10 *K*=8.5 to *L*=11 *K*=9.5 rf transition, which is a $K' = K + 1$ transition. The saturation curve was completed by sitting at the experimentally determined resonance frequency for the *L*=10 *K*=8.5 to *L*=11 *K*=9.5 transition and measuring the observed signal as a function of the power exiting the rf region in Watts. The resulting saturation curve is seen in Fig. 5.15, with the x-axis being the square root

of the power reading on the exit of the rf region in Watts. The saturation curve was fit to the function $A\sin^2\left(\frac{\pi}{2}\sqrt{\frac{P_{exit}}{P_0}}\right)$, where $P_0$ is the optimum power to observe the transition.

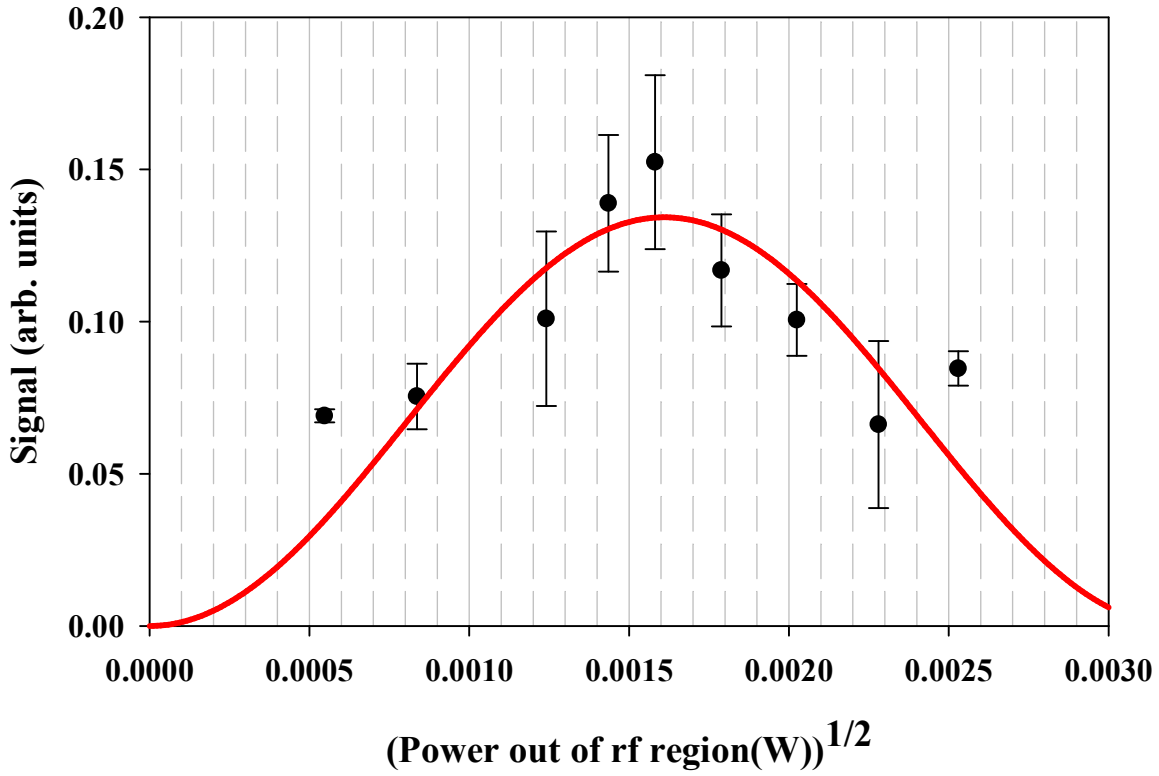


Figure 5.15: Saturation curve for the $n$=28 $L$=10, $K$=8.5 to $L$=11, $K$=9.5 in the $Th^{2+}$ Rydberg fine structure. The x-axis is the square root of the power coming out of rf region in W and the y-axis is the signal size at the resonance frequency of 1665MHz with the electric filed in the rf region traveling parallel to the direction of the ion beam. Each point is the average of several points, with the error the standard deviation of the mean of those points. The fit of the data, shown by the red line, is discussed in the text. This data came from JAK3-040.

The fit of the saturation curve is the red line in Fig 5.15, from which the optimum power to observe the $L$=10 $K$=8.5 to $L$=11 $K$=9.5 transition was determined to be $P_0 = 2.6(2)\times10^{-6}W$. The result of the fit of the saturation curve is completely consistent with the power predicted by calculating the optimum electric field, assuming no $K$ dependence in the average $Z$ matrix element, $Z_{rms}$, for a $K' = K+1$.

Not all the single photon transitions will require the same amount of power for observation, since the $K$ dependence in the average $Z$ matrix elements cannot be neglected. Therefore the magnitude of the average $Z$ matrix elements for both the $K' = K + 1$ and $K' = K$ transitions with $L' = L + 1$ had to be calculated, shown respectively by Eq. 5.1 and 5.2.

$$\left|Z_{rms}(n, L, K \to n, L+1, K+1)\right| = \frac{3}{2}\frac{n}{q}\sqrt{n^2 - (L+1)^2}\sqrt{\frac{(L+1)}{3(2K+1)}}$$

$$\times\sqrt{\frac{(K+L+J_c+2)(K+L+J_c+3)(K+L-J_c+1)(K+L-J_c+2)}{(2K+2)(2L+1)(2L+2)(2L+3)}}a_0 \tag{5.1}$$

$$\left|Z_{rms}(n, L, K \to n, L+1, K)\right| = \frac{3}{2}\frac{n}{q}\sqrt{n^2 - (L+1)^2}\sqrt{\frac{(L+1)}{3}}$$

$$\times\sqrt{\frac{(K+L+J_c+2)(K+L-J_c+1)(L-K+J_c+1)(K-L+J_c)}{K(2K+2)(2L+1)(2L+2)(2L+3)}}a_0 \tag{5.2}$$

The power necessary to make a transition between states is related to the inverse of the average $Z$ matrix element squared. The average Z matrix elements, $Z_{rms}$, for all the $K' = K + 1$ transitions observed are approximately the same, differ only within a few percent. Therefore, the same power level determined by the saturation curve, Fig. 5.15, was used to take all the measurements of the $K' = K + 1$ transitions observed. The average Z matrix element, $Z_{rms}$, for a $K' = K$ transition is approximately five to six times smaller than the average Z matrix element for $K' = K + 1$ transitions, indicating that the $K' = K$ transitions will need additional power to be observed. The ratio the power needed for a $K' = K$ to the power needed for a $K' = K + 1$ transition is just the average Z matrix element for the $K' = K$ divided by the average $Z$ matrix element for $K' = K + 1$ squared, Eq. 5.3.

$$\frac{P_{rf}(n,L,K\rightarrow n,L+1,K)}{P_{rf}(n,L,K\rightarrow n,L+1,K+1)}=\left[\frac{Z_{rms}(n,L,K\rightarrow n,L',K+1)}{Z_{rms}(n,L,K\rightarrow n,L',K)}\right]^2$$

$$=\frac{K(K+L+J_c+3)(K+L-J_c+2)}{(2K+1)(L-K+Jc+1)(K-L+J_c)} \tag{5.3}$$

For the case of $Th^{2+}$ Rydberg fine structure where $J_c=5/2$, the $K'=K$ transitions observed needed on average thirty times more power than their $K'=K+1$ counterparts. The need for increased power to observe the $K'=K$ transitions was confirmed by taking a saturation curve on the *L*=10 *K*=8.5 to *L*=11 *K*=8.5 transition, Fig. 5.16. The fitting of the saturation curve for the *L*=10 *K*=8.5 to *L*=11 *K*=8.5 to $A\sin^2\left(\frac{\pi}{2}\sqrt{\frac{P_{exit}}{P_0}}\right)$ showed that the optimum power to observe the $K'=K$ transitions was $P_0(K'=K)=73(11)\times10^{-6}W$. This is slightly under the predicted power necessary if one uses the ratio, Eq. 5.3. For this specific transition the optimum power was determined from the saturation curve, Fig. 5.15, to be $P_0(K'=K+1)=2.6(2)\times10^{-6}W$. The predicted power for this specific $K'=K$ transition was $P_{predict}(K'=K)=106(8)\times10^{-6}W$, which differs from the observed by $33(14)\times10^{-6}W$. This difference is slight when you consider the quality of the data in both of the saturation curves, Fig. 5.15 and 5.16. The observation of all the single photon transitions were done at the approximate estimated powers for the s

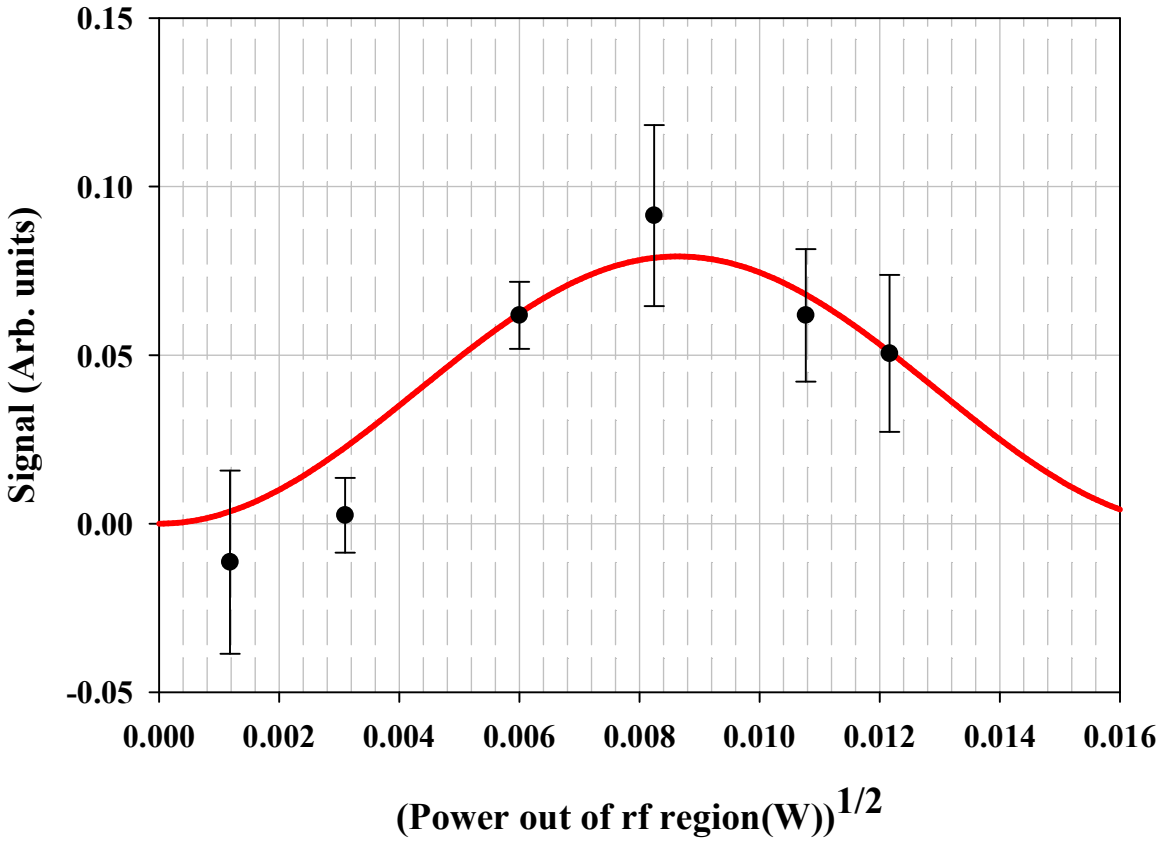


Figure 5.16: Saturation curve for the $n$=28 $L$=10, $K$=8.5 to $L$=11, $K$=8.5 in the $Th^{2+}$ Rydberg fine structure. The x-axis is the is the square root of the power exiting the rf region in W. The y-axis is the average signal while sitting at the resonance frequency, the fit of the data is shown by the red line. This data is from JAK5-023.

The calculation of the power necessary to observe multi-photon transitions is different, as was discussed in Chapter 2. Traditionally, multi-photon transitions would not be allowed due to selections rules that only allow for transitions between states that observe the selection rule, $L' = L \pm 1$. But as discussed in the case of the $Th^{3+}$ Rydberg fine structure in Chapter 2 multi-photon transitions can occur due to the coupling of the population of different levels with others. For the case of the $Th^{2+}$ Rydberg fine structure, the transitions observed were $L' = L + 2$ and $K' = K + 2$. The ability to observe multi-photon transitions requires careful consideration of the

power level needed to make the transitions and understanding that the transitions are susceptible to AC shifts that must be corrected for. The calculation of the power and the shift rates for the two photon transitions is a time dependent problem. Using the approach discussed in Chapter 2, states involved in the two photon transitions were described in terms of Floquet states and the time dependent problem was simplified into a time independent problem[32]. This technique of simplifying the time dependent problem into a time independent problem is an approximation, but this approximation has proven to be adequate with the description of multi-photon transitions in $He^{+}$ [33] and the multi-photon transitions in the $Th^{3+}$ Rydberg fine structure discussed in Chapter 3. Therefore, using this approximation technique discussed in Chapter 2, estimates of the power necessary to observe each transition were made along with estimates of the AC shift each transition might experience at its saturating power, Table 5.6.

Table 5.6: The calculated power and AC shifts for the two photon transitions in the $n$=28 $Th^{2+}$ Rydberg fine structure, in reference to a single photon transitions, shown in the first row. The first column gives the transitions, the second column gives the effective coupling and the third column gives the AC shift in term of V. The fourth column gives the V for each of the transitions in MHz. The fifth column gives saturation power necessary to observe the transition and the final column gives the AC shift the transition would experience if it was observed at the saturation power, in MHz.

| *(L, K)* -(*L'*, *K'*) | $V_{eff}$ | AC Shift | *V(MHz)* | $P_{sat}$(μW) | AC shift at $P_{sat}$ |
|---|---|---|---|---|---|
| (10,8.5)-(11,9.5) | $V$ | 0 | 0.49 | 2.6 | 0 |
| (10,7.5)-(12,9.5) | $\frac{+V^2}{340.07MHz}$ | $\frac{+V^2}{1529.05MHz}$ | 12.92 | 1808 | $0.11MHz$ |
| (10,8.5)-(12,10.5) | $\frac{+V^2}{266.16MHz}$ | $\frac{+V^2}{1316.48MHz}$ | 11.42 | 1412 | $0.10MHz$ |
| (10,9.5)-(12,11.5) | $\frac{+V^2}{196.99MHz}$ | $\frac{+V^2}{1132.04MHz}$ | 9.83 | 1046 | $0.09MHz$ |
| (10,10.5)-(12,12.5) | $\frac{+V^2}{137.70MHz}$ | $\frac{+V^2}{889.92MHz}$ | 8.21 | 730 | $0.08MHz$ |
| (10,11.5)-(12,13.5) | $\frac{+V^2}{83.80MHz}$ | $\frac{+V^2}{666.01MHz}$ | 6.41 | 445 | $0.06MHz$ |

The power necessary to observe the two photon transitions is between 0.4mW and 1.8mW depending on which transition is being studied. The predicted AC shifts in Table 5.6 assumes they are observed at their saturation power, all the two photon transitions were observed with power that was within a factor of two of the saturation power and thus all the corrections to the AC shifts were small. Looking at all the observations and the power at which they were observed, the largest AC shift experience for the five two photon transitions would be approximately 0.2MHz. The corrections to the two photon intervals are small and not very significant to the measured two photon interval. The size of the shift rates and their insignificance to the measured interval led to the correcting of the measured intervals with the calculated shift rates, none of the shift rates were measured. It would be experimentally very hard to measure shift rates this small, and the model of approximating these shift rates appears to be quite adequate. Therefore, each observation of a two photon transition will be corrected by its respective shift rate, Eq. 5.4, given in terms of MHz/mW.

$$\Delta\upsilon_{(10,7.5)-(12,9.5)} = +0.061(5)\frac{MHz}{mW}$$

$$\Delta\upsilon_{(10,8.5)-(12,10.5)} = +0.070(5)\frac{MHz}{mW}$$

$$\Delta\upsilon_{(10,9.5)-(12,11.5)} = +0.082(6)\frac{MHz}{mW}$$

$$\Delta\upsilon_{(10,10.5)-(12,12.5)} = +0.104(8)\frac{MHz}{mW}$$

$$\Delta\upsilon_{(10,11.5)-(12,13.5)} = +0.139(10)\frac{MHz}{mW} \qquad (5.4)$$

The uncertainty in each of the AC shift rates is due to the uncertainty in the single photon saturation power determined from the fit of Fig. 5.15.

### 5.3 Results of the $n$=28 $Th^{2+}$ Rydberg fine structure rf measurements

A total of nineteen rf transitions made up the mapping out of the $n$=28 $L$=9 to 12 fine structure. Each of these transitions was observed multiple times and the resulting observations were fit and combined by averaging them. Single photon transitions makeup the majority of the measurements, with a total of fourteen out of the nineteen transitions being of that type. The single photon transitions were observed in both directions of propagations, with each transition observed between two and five times. None of the single photon transitions showed evidence of resolved spin splitting, so the resonances were fit to a single four parameter Gaussian to determine their centers. The data for each transition was combined by taking a weighted average of the data for each direction of propagation, if more than one measurement existed. The weighted averages of the two directions of propagation were combined by taking a straight average to give the un-Doppler shifted locations. Table 5.7 shows the measurements for each of the single photon transitions, the averages for each direction of propagation for each transition, and the resulting Doppler corrected position of each of the single photon transitions. The apparent $\beta$ for each transition was also calculated and compared with the $\beta$ calculated from using the terminal potential, $\beta = 0.0008320$. On average the observed $\beta$ were consistent calculated $\beta$, within 1.3 sigma.

Table 5.7: Single photon transitions observed in the $n$=28 $Th^{2+}$ Rydberg fine structure, a total of fourteen transitions. This table has been broken into fourteen sections, with one transition in each section, with each section labeled by its specific transitions and its transition type, $K' = K + 1$ or $K' = K$. In each section the first column shows the lab book and page of the observation. The second column gives the direction of propagation of the rf electric field for the observation. The ⇉ denotes the rf electric propagating parallel to ion bean and ⇆ denotes the electric field propagating anti-parallel to the ion beam. The final column gives the fitted center of each of the observations, $f_{measured}$, in MHz. Underneath all of the measurements in each section is the weighted average for each of the directions of propagation, when multiple measurements exist and the final straight average of the two directions of propagation. The apparent $\beta$ from the observed Doppler shift was also calculated for each transition. The difference between the apparent $\beta$ and the $\beta$ calculated from the terminal potential, $\Delta\beta$ is shown below the apparent $\beta$.

| $K'=K+1$ | $L$=9 $K$=6.5 to $L'$=10 $K'$=7.5 | |
|---|---|---|
| Lab Book | Direction | $f_{measured}$(MHz) |
| JAK6-085,86 & 87 | ⇉ | 3495.33(18) |
| JAK6-096 | ⇆ | 3489.51(30) |
| JAK7-111 | ⇆ | 3489.51(12) |
| | Only ⇉ = | 3495.33(18) |
| | Weighted Avg ⇆ = | 3489.51(11) |
| | AVG of ⇉ and ⇆ = | 3492.42(11) |
| | Apparent β = | 0.00083(3) |
| | Δβ = | 0.0000(3) |

| $K'=K+1$ | $L$=9 $K$=7.5 to $L'$=10 $K'$=8.5 | |
|---|---|---|
| Lab Book | Direction | $f_{measured}$(MHz) |
| JAK6-069 | ⇉ | 3128.31(72) |
| JAK6-070 | ⇉ | 3129.03(15) |
| JAK6-071 | ⇉ | 3129.03(18) |
| JAK6-072 | ⇆ | 3124.11(18) |
| | Weighted AVG ⇉ = | 3129.01(11) |
| | Only ⇆ = | 3124.11(18) |
| | AVG of ⇉ and ⇆ = | 3126.56(11) |
| | Apparent β = | 0.00078(3) |
| | Δβ = | 0.0005(3) |

Table 5.7 continued

| $K'=K+1$ | $L=9$ $K=8.5$ to $L'=10$ $K'=9.5$ | |
|---|---|---|
| Lab Book | Direction | $f_{measured}$(MHz) |
| JAK6-005 | ⇉ | 2685.16(16) |
| JAK6-006 | ⇆ | 2681.28(11) |
| JAK6-063 & 66 | ⇉ | 2684.84(18) |
| JAK7-105 | ⇆ | 2680.72(24) |
| | Weighted AVG ⇉ = 2685.02(16) | |
| | Weighted AVG ⇆ = 2681.02(28) | |
| | AVG of ⇉ and ⇆ = 2683.02(16) | |
| | Apparent β = 0.00075(6) | |
| | Δβ = 0.0008(6) | |

| $K'=K+1$ | $L=9$ $K=9.5$ to $L'=10$ $K'=10.5$ | |
|---|---|---|
| Lab Book | Direction | $f_{measured}$(MHz) |
| JAK5-153 | ⇉ | 2259.04(36) |
| JAK5-154 | ⇆ | 2255.56(36) |
| | AVG of ⇉ and ⇆ = 2257.30(25) | |
| | Apparent β = 0.00077(11) | |
| | Δβ = 0.0006(11) | |

| $K'=K+1$ | $L=9$ $K=10.5$ to $L'=10$ $K'=11.5$ | |
|---|---|---|
| Lab Book | Direction | $f_{measured}$(MHz) |
| JAK5-135 | ⇉ | 1502.82(9) |
| JAK5-138 | ⇆ | 1500.45(16) |
| JAK7-085 | ⇉ | 1502.84(20) |
| JAK7-089 | ⇆ | 1500.66(16) |
| | Weighted AVG ⇉ = 1502.82(8) | |
| | Weighted AVG ⇆ = 1500.56(11) | |
| | AVG of ⇉ and ⇆ = 1501.69(7) | |
| | Apparent β = 0.00075(5) | |
| | Δβ = 0.0008(5) | |

Table 5.7 continued

| $K'=K$ | $L=9$ $K=10.5$ to $L'=10$ $K'=10.5$ | |
|---|---|---|
| Lab Book | Direction | $f_{measured}$(MHz) |
| JAK5-136 | ⇉ | 388.53(10) |
| JAK5-137 | ⇆ | 388.30(12) |
| JAK7-086 | ⇉ | 389.11(20) |
| JAK7-086b | ⇉ | 389.19(31) |
| JAK7-088 | ⇆ | 388.41(16) |
| | Weighted AVG ⇉ = 388.69(19) | |
| | Weighted AVG ⇆ = 388.34(10) | |
| | AVG of ⇉ and ⇆ = 388.52(11) | |
| | Apparent β = 0.00045(27) | |
| | Δβ = 0.00038(27) | |

| $K'=K+1$ | $L=10$ $K=7.5$ to $L'=11$ $K'=8.5$ | |
|---|---|---|
| Lab Book | Direction | $f_{measured}$(MHz) |
| JAK6-091 & 91b | ⇉ | 1764.81(9) |
| JAK6-095 | ⇆ | 1762.58(16) |
| JAK7-113 | ⇆ | 1762.29(16) |
| JAK7-114 | ⇉ | 1764.95(18) |
| | Weighted AVG ⇉ = 1764.84(8) | |
| | Weighted AVG ⇆ = 1762.44(14) | |
| | AVG of ⇉ and ⇆ = 1763.64(8) | |
| | Apparent β = 0.00068(5) | |
| | Δβ = 0.00015(5) | |

Table 5.7 continued

| $K'=K+1$ | $L=10$ $K=8.5$ to $L'=11$ $K'=9.5$ | |
|---|---|---|
| Lab Book | Direction | $f_{measured}$(MHz) |
| JAK5-111 | ⇉ | 1664.76(8) |
| JAK5-113 | ⇆ | 1662.23(20) |
| JAK7-076 | ⇆ | 1662.23(14) |
| JAK7-082 | ⇉ | 1664.44(18) |
| | Weighted AVG ⇉ = 1664.71(11) | |
| | Weighted AVG ⇆ = 1662.23(11) | |
| | AVG of ⇉ and ⇆ = 1663.47(8) | |
| | Apparent β = 0.00075(5) | |
| | Δβ = 0.00008(5) | |

| $K'=K$ | $L=10$ $K=8.5$ to $L'=11$ $K'=8.5$ | |
|---|---|---|
| Lab Book | Direction | $f_{measured}$(MHz) |
| JAK5-117 | ⇉ | 2985.04(6) |
| JAK5-116 | ⇆ | 2980.34(14) |
| JAK7-074 | ⇉ | 2985.22(10) |
| JAK7-075 | ⇆ | 2979.90(14) |
| | Weighted AVG ⇉ = 2985.08(8) | |
| | Weighted AVG ⇆ = 2980.12(22) | |
| | AVG of ⇉ and ⇆ = 2982.60(12) | |
| | Apparent β = 0.00083(4) | |
| | Δβ = 0.00000(4) | |

Table 5.7 continued

| $K'=K+1$ | $L=10$ $K=9.5$ to $L'=11$ $K'=10.5$ | |
|---|---|---|
| Lab Book | Direction | $f_{measured}$(MHz) |
| JAK5-087 | ⇉ | 1506.05(13) |
| JAK5-090 | ⇆ | 1503.51(14) |
| JAK7-051 | ⇉ | 1505.95(21) |
| JAK7-054 | ⇆ | 1503.93(11) |
| | Weighted AVG ⇉ = 1506.02(11) | |
| | Weighted AVG ⇆ = 1503.77(20) | |
| | AVG of ⇉ and ⇆ = 1504.90(11) | |
| | Apparent β = 0.00075(8) | |
| | Δβ = 0.00008(8) | |

| $K'=K$ | $L=10$ $K=9.5$ to $L'=11$ $K'=9.5$ | |
|---|---|---|
| Lab Book | Direction | $f_{measured}$(MHz) |
| JAK5-102 | ⇉ | 2330.40(18) |
| JAK5-103 | ⇆ | 2326.72(14) |
| JAK7-071 | ⇆ | 2327.50(20) |
| JAK7-072 | ⇉ | 2330.50(10) |
| | Weighted AVG ⇉ = 2330.48(8) | |
| | Weighted AVG ⇆ = 2326.98(38) | |
| | AVG of ⇉ and ⇆ = 2328.73(19) | |
| | Apparent β = 0.00075(8) | |
| | Δβ = 0.00008(8) | |

Table 5.7 continued

| $K'=K+1$ | $L=10$ $K=10.5$ to $L'=11$ $K'=11.5$ | |
|---|---|---|
| Lab Book | Direction | $f_{measured}$(MHz) |
| JAK5-086 | ⇉ | 1271.21(13) |
| JAK5-089 | ⇆ | 1269.23(14) |
| JAK7-049 | ⇉ | 1270.83(9) |
| JAK7-055 | ⇆ | 1269.58(14) |
| | Weighted AVG ⇉ = 1270.95(18) | |
| | Weighted AVG ⇆ = 1269.41(18) | |
| | AVG of ⇉ and ⇆ = 1270.18(13) | |
| | Apparent β = 0.00061(10) | |
| | Δβ = 0.00022(10) | |

| $K'=K$ | $L=10$ $K=10.5$ to $L'=11$ $K'=10.5$ | |
|---|---|---|
| Lab Book | Direction | $f_{measured}$(MHz) |
| JAK5-088 | ⇉ | 1427.86(19) |
| JAK5-091 | ⇆ | 1426.11(27) |
| JAK5-091b | ⇆ | 1425.89(12) |
| JAK7-052 | ⇉ | 1428.19(12) |
| JAK7-053 | ⇆ | 1426.31(13) |
| | Weighted AVG ⇉ = 1428.10(15) | |
| | Weighted AVG ⇆ = 1426.09(14) | |
| | AVG of ⇉ and ⇆ = 1427.10(10) | |
| | Apparent β = 0.00070(7) | |
| | Δβ = 0.00013(7) | |

Table 5.7 continued

| $K'=K+1$ | $L=10$ $K=11.5$ to $L'=11$ $K'=12.5$ | |
|---|---|---|
| Lab Book | Direction | $f_{measured}$(MHz) |
| JAK5-143 | ⇉ | 885.05(9) |
| JAK5-140 | ⇆ | 883.86(11) |
| JAK7-093 | ⇆ | 883.92(8) |
| JAK7-094 | ⇉ | 885.37(5) |
| | Weighted AVG ⇉ = 885.29(12) | |
| | Weighted AVG ⇆ = 883.90(6) | |
| | AVG of ⇉ and ⇆ = 884.60(6) | |
| | Apparent β = 0.00079(7) | |
| | Δβ = 0.00004(7) | |

The measurement of the fourteen single photon transitions mapped out the relative location of a total fifteen levels in the $n$=28 $Th^{2+}$ Rydberg fine structure with sub-MHz precision. These measurements of the single photon resonances confirmed the preliminary identification of all resolved structures in the $n$=28-66 optical spectrum, Fig. 4.7, as being correct. The measurements of these single photon resonances also helped to solidify the accuracy of the predicted rf resonances, simulated from the five preliminary parameters of $Th^{3+}$ reported [3]. Nine out of fourteen of the single photon resonances came out within ±20 MHz of their estimated positions, Table 5.5, and the remaining five transitions were found within 100 MHz of their predicted locations.

Measurements of the $n$=28 $Th^{2+}$ Rydberg fine structure were expanded to include an additional $L$, the $L$=12, by the observation of the two photon transitions between the $L$=10 states and the $L$=12 states. Table 5.8 has a section for each of the five two photon transitions, with column one providing the lab book and page of the observation. Column two provides the propagation direction of the observation, and column three gives the power at which the

transition was observed. As with the single photon resonance none of the two photon resonances showed any evidence of spin splitting, so the resonances were fit to single four parameter Gaussians to determine their center, the resulting fitted center for each observation is given in column four of Table 5.8. Column five gives the calculated AC shift corrections for the observation, determined from the calculated shift rates, Eq. 5.4 and the power reading during the observations, column three. The final column of Table 5.8 gives the corrected positions for each of the observations. The data for each transition was then averaged to find its final Doppler corrected positions. First a weighted average of the data for each direction of propagation was made. Then a straight average of the two directions of propagation determined the Doppler corrected positions. The apparent $\beta$ for each transition was also calculated and compared with the $\beta$ determined by the terminal potential. The difference between the calculated $\beta$ and the apparent $\beta$ was determined, $\Delta\beta$, on average the apparent β was consistent with the $\beta$ calculated from the terminal potential.

Table 5.8: Two photon transitions observed in the $n$=28 $Th^{2+}$ Rydberg fine structure, this table has a separate section for each of the five two photon transitions observed with each section labeled for the specific transition. Column one gives the lab book and page of the observation. Column two give the direction propagation of the observation, with ⇉ indicating the rf electric field propagating parallel to the ion beam and ⇆ indicating the rf electric field propagating anti-parallel to the ion beam. Column three gives the power reading on the exit of the rf region during the observation in mW. Column four gives the fitted center of the observation in MHz. The fifth column gives the AC shift given the power at which the observation occurred and the calculated shift rate. Column six gives the AC corrected position of the observation in MHz. The weighted average of the data for each direction propagation is also shown for each transitions and the straight average of the result for each direction of propagation determined the Doppler corrected final positions of each of the rf intervals. The apparent $\beta$ for each of the transitions was also found. The apparent $\beta$ was then compared to the $\beta$ found from assuming the terminal potential, $\Delta\beta$.

$L$=10, $K$=7.5 to $L'$=12, $K'$= 9.5

| Lab Book | Direction | $P_{exit}$ (mW) | $f_{measured}$(MHz) | AC Shift (MHz) | $f_{corrected}$(MHz) |
|---|---|---|---|---|---|
| JAK6-093 | ⇉ | 2.00 | 2170.90(10) | 0.12(1) | 2170.78(10) |
| JAK6-094 | ⇆ | 1.90 | 2167.20(10) | 0.12(1) | 2167.08(10) |
| JAK7-112 | ⇆ | 3.00 | 2166.98(18) | 0.18(2) | 2166.80(18) |
| JAK7-115 | ⇉ | 3.00 | 2170.80(12) | 0.18(2) | 2170.62(12) |
| | | Weighted AVG of ⇉ = | 2170.86(8) | 0.15(1) | 2170.71(8) |
| | | Weighted AVG of ⇆ = | 2167.15(12) | 0.13(1) | 2167.01(12) |
| | | AVG of ⇉ and ⇆ = | 2169.01(7) | 0.14(1) | 2168.86(7) |
| | | | | | **Final = 2168.86(7)** |
| | | | | | Apparent β = 0.00085(3) |
| | | | | | Δβ = -0.00002(3) |

Table 5.8 continue

$L$ =10, $K$ =8.5 to $L'$=12, $K'$= 10.5

| Lab Book | Direction | $P_{exit}$ (mW) | $f_{measured}$(MHz) | AC Shift (MHz) | $f_{corrected}$(MHz) |
|---|---|---|---|---|---|
| JAK5-112 | ⇉ | 2.60 | 2264.20(14) | 0.18(1) | 2264.02(14) |
| JAK5-114 | ⇆ | 2.60 | 2260.54(14) | 0.18(1) | 2260.36(14) |
| JAK7-077 | ⇆ | 2.10 | 2259.99(30) | 0.15(1) | 2259.84(30) |
| JAK7-081 | ⇉ | 2.20 | 2264.18(16) | 0.15(1) | 2264.03(16) |
| | | Weighted AVG of ⇉ = | 2264.19(11) | 0.17(1) | 2264.02(11) |
| | | Weighted AVG of ⇆ = | 2260.44(20) | 0.17(1) | 2260.27(20) |
| | | AVG of ⇉ and ⇆ = | 2262.32(11) | 0.17(1) | 2262.15(11) |
| | | | | | **Final = 2262.15(11)** |
| | | | | | Apparent β = 0.00083(5) |
| | | | | | Δβ = 0.00000(5) |

$L$ =10, $K$ =9.5 to $L'$=12, $K'$= 11.5

| Lab Book | Direction | $P_{exit}$ (mW) | $f_{measured}$(MHz) | AC Shift (MHz) | $f_{corrected}$(MHz) |
|---|---|---|---|---|---|
| JAK5-107 | ⇉ | 2.10 | 2223.38(22) | 0.17(1) | 2223.21(22) |
| JAK5-108 | ⇆ | 1.86 | 2220.38(16) | 0.15(1) | 2220.23(16) |
| JAK7-069 | ⇉ | 1.64 | 2223.66(16) | 0.13(1) | 2223.53(16) |
| JAK7-070 | ⇆ | 1.64 | 2220.02(14) | 0.13(1) | 2219.89(14) |
| | | Weighted AVG of ⇉ = | 2223.56(15) | 0.14(1) | 2223.42(15) |
| | | Weighted AVG of ⇆ = | 2220.18(18) | 0.16(1) | 2220.04(18) |
| | | AVG of ⇉ and ⇆ = | 2221.87(12) | 0.15(1) | 2221.73(12) |
| | | | | | **Final = 2221.73(12)** |
| | | | | | Apparent β = 0.00076(5) |
| | | | | | Δβ = 0.00007(5) |

Table 5.8 continue

$L$ =10, $K$ =10.5 to $L'$=12, $K'$= 12.5

| Lab Book | Direction | $P_{exit}$ (mW) | $f_{measured}$(MHz) | AC Shift (MHz) | $f_{corrected}$(MHz) |
|---|---|---|---|---|---|
| JAK5-104 | ⇆ | 0.96 | 1988.12(12) | 0.10(1) | 1988.02(12) |
| JAK5-105 | ⇉ | 0.92 | 1991.16(10) | 0.10(1) | 1991.06(10) |
| JAK7-056 | ⇆ | 0.90 | 1988.00(10) | 0.09(1) | 1987.91(10) |
| JAK7-058 | ⇉ | 0.91 | 1991.20(10) | 0.09(1) | 1991.10(10) |
| | | Weighted AVG of ⇉ = | 1991.18(7) | 0.10(1) | 1991.08(7) |
| | | Weighted AVG of ⇆ = | 1988.05(8) | 0.09(1) | 1987.96(8) |
| | | AVG of ⇉ and ⇆ = | 1989.62(5) | 0.10(1) | 1989.52(5) |
| | | | | | **Final = 1989.52(5)** |
| | | | | | Apparent β = 0.00078(3) |
| | | | | | Δβ = 0.00005(3) |

$L$ =10, $K$ =11.5 to $L'$=12, $K'$= 13.5

| Lab Book | Direction | $P_{exit}$ (mW) | $f_{measured}$(MHz) | AC Shift (MHz) | $f_{corrected}$(MHz) |
|---|---|---|---|---|---|
| JAK5-141 | ⇆ | 0.92 | 1432.30(20) | 0.13(1) | 1432.17(20) |
| JAK5-142 | ⇉ | 0.93 | 1435.24(20) | 0.13(1) | 1435.11(20) |
| JAK7-092 | ⇆ | 0.72 | 1432.82(8) | 0.10(1) | 1432.72(8) |
| JAK7-095 | ⇉ | 0.71 | 1435.30(10) | 0.10(1) | 1435.20(10) |
| | | Weighted AVG of ⇉ = | 1435.29(9) | 0.11(1) | 1435.18(9) |
| | | Weighted AVG of ⇆ = | 1432.75(18) | 0.10(1) | 1432.60(18) |
| | | AVG of ⇉ and ⇆ = | 1432.02(10) | 0.11(1) | 1433.91(10) |
| | | | | | **Final = 1433.91(10)** |
| | | | | | Apparent β = 0.00089(7) |
| | | | | | Δβ = -0.00006(7) |

With the measurement of the five two photon transitions, the fine structure pattern in the $n$=28 was expanded to include the relative positions of twenty out of the twenty-four levels in $L$=9 to 12. Examples of all nineteen of the rf transitions measured can be seen in Appendix B. Five of the six levels for $L$=9, 10, 11, and 12 were located, providing a much more complete measurement of the $Th^{2+}$ Rydberg fine structure pattern than the reported optical RESIS measurements [3]. Before the analysis of the fine structure could begin, an additional experimental uncertainty in the measured fine structure rf intervals must be accounted for. The possible presence of a stray electric field in the rf region during the data taking and the effect it would have on the measured intervals. All nineteen of the measured rf transition intervals to varying degrees are susceptible to DC Stark shifts induced by the possible presence of a stray electric field in the rf region. To gain understanding in the possible size of shifts that could be present, the DC Stark shift rates were calculated for each $n$=28 levels in $L$=9, 10, 11 and 12, Table 5.9, with units of $MHz/(V/cm)^2$. The calculation of the DC stark shift rates in Table 5.9 used the same approach as in Chapter 2, Eq. 2.40, neglecting the $K$ dependence. Each $(L,K)$ state is dominantly shifted by two states, the $(L+1,K+1)$ state and the $(L-1,K-1)$ state. Using Eq. 2.40, the DC Stark shift rate for each $(L,K)$ state was calculated with the lower state being the $(L-1,K-1)$ state and upper state being the $(L+1,K+1)$ state. These calculations of the DC Stark shifts of the $n$=28 $Th^{2+}$ Rydberg states allowed for the determination of which states would be sensitive to stray electric fields. From these shift rates it was determined that shifts on the order of 1 MHz could be expected if the stray field was as large as $0.10 V/cm$. In order to determine the size of the stray electric field in the rf region, a transition who has been previously studied was observed. The location and DC Stark shift rate is well known, so therefore any shift

in positions of the transition can detect the presence and size of the stray electric field in the rf region.

Table 5.9: DC Stark shift rates for the $n$=28 $Th^{2+}$ Rydberg fine structure levels. Column one gives the $L$ and $K$ of the $n$=28 states and column two gives the DC Stark shift rate, κ, in MHz/(V/cm)$^2$. The states with asterisks on them were states not observed in the $Th^{2+}$ Rydberg fine structure reported in this section, but the shift rates for the states were calculated for completeness.

| ($L$ , $K$ ) | κ(MHz/(V/cm)$^2$) |
|---|---|
| (9, 6.5) | -0.66 |
| (9, 7.5) | -2.66 |
| (9, 8.5) | -4.84 |
| (9, 9.5) | -6.77 |
| (9, 10.5) | -12.36 |
| (9, 11.5)* | -29.68 |
| (10, 7.5) | -10.04 |
| (10, 8.5) | -10.20 |
| (10, 9.5) | -10.34 |
| (10, 10.5) | -12.20 |
| (10,11.5) | -16.39 |
| (10, 12.5)* | -56.79 |
| (11, 8.5) | -67.10 |
| (11, 9.5) | -37.34 |
| (11, 10.5) | -25.14 |
| (11,11.5) | -20.42 |
| (11, 12.5) | -23.05 |
| (11, 13.5)* | -111.85 |
| (12, 9.5) | -137.03 |
| (12, 10.5) | -44.68 |
| (12,11.5) | -27.43 |
| (12, 12.5) | -24.09 |
| (12, 13.5) | -31.92 |
| (12, 14.5)* | -247.78 |

During the data taking process for the transitions presented in this section, the $L$=12 to 14 transition in $n$=37 $Th^{3+}$ Rydberg fine structure was periodically monitored and used as an electric field diagnostic. The location of the $L$=12 to 14 transition, reported in Table 3.5, was determined with sub-MHz precision and the analysis of the $Th^{3+}$ Rydberg levels reported in Chapter 3 showed that the observation of the $Th^{3+}$ Rydberg fine structure levels occurred at virtually zero field. All the periodic measurements of the location of the $L$=12 to 14 transition taken during the data collection of the $Th^{2+}$ Rydberg fine structure in this chapter were all consistent within error of the position determined in Chapter 3. This indicated that the measurements of the $Th^{2+}$ Rydberg fine structure occurred at zero field. The uncertainty on the zero field determination for the $Th^{3+}$ Rydberg fine structure data, in Chapter 3, was $0.001(V/cm)^2$, so to be conservative the same uncertainty was assigned to be the uncertainty on the electric field during the measurement in this chapter. If this uncertainty in the electric field was large it would have to be accounted for as an additional experimental uncertainty, and it would need to be applied to either the rf transitions or the relative positions of the levels. In the case of this study, the uncertainty in the stray electric field is small, and resulting uncertainty in the relative position of the levels due to this effect would be at most 0.14MHz for the $L$=12 $K$=9.5 and smaller for all other states. Given the size of the possible uncertainty in the relative position due to the stray electric, this effect on the $n$=28 $Th^{2+}$ Rydberg fine structure was neglected

With this additional experimental uncertainty in the observed rf transition understood, the relative positions of the twenty levels involved in the nineteen rf transitions measured were determined. The location of the $L$=12 $K$=9.5 was assumed to be zero, and using the measured rf transitions the relative locations of all the levels were determined. In Table 5.10, column one gives the identity of the states in spectroscopy notation and column two gives just the $(L,K)$ of

the state; the notation used in this work to identify the states. The third column gives the relative positions of the states in MHz. The error on each of the relative positions of each of the levels in the $n$=28 $Th^{2+}$ Rydberg fine structure are the result of propagating the uncertainty in the rf transitions through. The results in the Table 5.10 are the final experimental results of the $n$=28 $Th^{2+}$ study, in the remaining parts of this dissertation these experimental determined positions are analyzed, the properties of the $Th^{3+}$ are extracted, and the resulting properties are compared with theoretical estimates of the properties. It should be noted that when these experimental results are published, it may prove possible to analyze them with alternative theoretical methods, as has been done for the structure of neon Rydberg levels [8].

Table 5.10: The relative positions of the states measured in the $n$=28 $Th^{2+}$ Rydberg fine structure with the zero position being the location of the $n$=28, $L$=12, $K$=9.5. Column one labels the states using spectroscopic notation, $nL_K$ . Column two labels the state in the convention used in this work. Column three gives the position relative to the $n$=28, $L$=12, $K$=9.5 in MHz and the uncertainty in the position

| $nL_K$ | $(L, K)$ | $E_{obs}$ (MHz) |
|---|---|---|
| $28M_{6.5}$ | (9, 6.5) | -5661.28(13) |
| $28M_{7.5}$ | (9, 7.5) | -6514.38(16) |
| $28M_{8.5}$ | (9, 8.5) | -6736.10(31) |
| $28M_{9.5}$ | (9, 9.5) | -6232.58(39) |
| $28M_{10.5}$ | (9, 10.5) | -4363.80(32) |
| $28M_{11.5}$ | (9, 11.5) | -- |
| $28N_{7.5}$ | (10, 7.5) | -2168.86(7) |
| $28N_{8.5}$ | (10, 8.5) | -3387.82(16) |
| $28N_{9.5}$ | (10, 9.5) | -4053.08(26) |
| $28N_{10.5}$ | (10, 10.5) | -3975.28(30) |
| $28N_{11.5}$ | (10,11.5) | -2862.11(33) |
| $28N_{12.5}$ | (10, 12.5) | -- |
| $28O_{8.5}$ | (11, 8.5) | -405.22(11) |
| $28O_{9.5}$ | (11, 9.5) | -1724.35(18) |
| $28O_{10.5}$ | (11, 10.5) | -2548.18(28) |
| $28O_{11.5}$ | (11,11.5) | -2705.10(33) |
| $28O_{12.5}$ | (11, 12.5) | -1977.51(33) |
| $28O_{13.5}$ | (11, 13.5) | -- |
| $28Q_{9.5}$ | (12, 9.5) | 0.00 |
| $28Q_{10.5}$ | (12, 10.5) | -1125.67(19) |
| $28Q_{11.5}$ | (12,11.5) | -1831.35(29) |
| $28Q_{12.5}$ | (12, 12.5) | -1985.76(30) |
| $28Q_{13.5}$ | (12, 13.5) | -1428.20(34) |
| $28Q_{14.5}$ | (12, 14.5) | -- |

## Chapter 6: Interpretation of the $n$=28 $Th^{2+}$ Rydberg fine structure

### 6.1 Model for fitting the fine structure

The rf measurements of the $n$=28 $Th^{2+}$ Rydberg fine structure described in Chapter 5 promise an improved determination of the properties of $Th^{3+}$. The previous conclusions based on the optical measurements in Chapter 4 were limited by the measurement precision (±20MHz) and the number of levels clearly identified (fourteen). These limitations in the optical study data set only allowed for the five dominant parameters of $Th^{3+}$ to be determined [3] and did not allow for the exploration any of the other additional properties that might be controlling the $Th^{2+}$ Rydberg fine structure pattern. The rf measurements reported in Chapter 5 determined the relative positions of five levels each in $L$=9, 10, 11, and 12, a total of twenty of the twenty-four levels in $n$=28, with sub-MHz precision. This more complete and much more precise data set enables a more comprehensive analysis and a clearer determination of the properties of $Th^{3+}$.

If the effective potential described all the interactions between the core and the Rydberg electron, then the measured fine structure pattern could be fit directly to an effective potential. Just as the effective potential has tensor components, so does the observed fine structure, so the first step to extracting the properties of $Th^{3+}$ from the data would be to extract the fitted structure parameters, $A_b$, seen in Eq. 6.1 from the data.

$$E_{corrected} = \left\langle nL_K \left| V_{eff} \right| nL_K \right\rangle = A_0(L) + A_1(L)(\vec{L}\cdot\vec{J}_c) + A_2(L)\frac{X^{[2]}(J_c)\cdot C^{[2]}(\hat{r})}{\begin{pmatrix} J_c & 2 & J_c \\ -J_c & 0 & J_c \end{pmatrix}}$$

$$+ A_3(L)(X^{[3]}(J_c)\cdot T^{[3]}(\hat{r})) + A_4(L)\frac{X^{[4]}(J_c)\cdot C^{[4]}(\hat{r})}{\begin{pmatrix} J_c & 4 & J_c \\ -J_c & 0 & J_c \end{pmatrix}} \quad (6.1)$$

The fitted structure parameters are referred to by their tensor ranks, for example the $A_0$ is the scalar component, the $A_1$ is the vector component, $A_2$ is the 2nd rank tensor component, $A_3$ is the 3rd rank tensor component, and $A_4$ is the 4th rank tensor component. The levels for each $L$ would be fit to determine the structure parameters for each $L$, and then those fitted parameters for each $L$ would be scaled by the appropriate hydrogenic expectation values of $r$ and equated with the core properties contributing to each of the fitted structure parameters. Normally, prior to this step, the observed energies would be corrected for two relatively minor effects, $E_{\mathrm{Rel}}$, the relativistic correction and $E^{[2]}(V_{eff})$, a correction due to the coupling to other Rydberg levels, Eq. 6.2.

$$E_{corrected} = E_{obs} - E_{\mathrm{Rel}} - E^{[2]}(V_{eff}) \tag{6.2}$$

This type of fitting of a fine structure pattern was used in the study of the properties of $Ni^+$ from rf measurements of the $n$=9 Ni Rydberg fine structure [11]. There it was found that the model, Eq. 6.1, was adequate since $Ni^+$ contained no low-lying excited states.

As discussed in Chapter 4, the optical study, $Th^{3+}$ is not well described by the effective potential model alone due to the fact that there are two low-lying $D$ states. These low-lying $D$ states produce non-adiabatic effects that are not described by the adiabatic effective potential model. Therefore two additional terms had to be added to the model used to fit the observed transitions in the optical study, Eq. 6.3.

$$\begin{aligned} E_{corrected} = \left\langle nL_K \left| V_{eff}^{Mod} \right| nL_K \right\rangle + \left| \left\langle 5^2F_{5/2} \left\| M^{[1]} \right\| 6^2D_{3/2} \right\rangle \right|^2 E^{[2]}(^2D_{3/2})* \\ + \left| \left\langle 5^2F_{5/2} \left\| M^{[1]} \right\| 6^2D_{5/2} \right\rangle \right|^2 E^{[2]}(^2D_{5/2})* \end{aligned} \tag{6.3}$$

These two additional terms were the full second order dipole-dipole energies due to each of the low-lying $D$ states. The modified effective potential, $V_{eff}^{Mod}$, in Eq. 6.3 excludes contributions these two states in the core properties. Given the limitation of the optical study, only the dominant terms in the modified effective potential model and the matrix elements for the low-lying $D$ states were determined from the fit of the optical data to Eq. 6.4.

$$E_{corrected} = -\frac{\alpha_{D,0}^{Mod}}{2}\left\langle r^{-4}\right\rangle_{nL} - \left(Q\left\langle r^{-3}\right\rangle_{nL} + \frac{\alpha_{D,2}^{Mod}}{2}\left\langle r^{-4}\right\rangle_{nL}\right)\times\frac{X^{[2]}(J_c)\cdot C^{[2]}(\hat{r})}{\begin{pmatrix} 5/2 & 2 & 5/2 \\ -5/2 & 0 & 5/2 \end{pmatrix}}$$
$$+\left|\left\langle 5^2F_{5/2}\left\|M^{[1]}\right\|6^2D_{3/2}\right\rangle\right|^2 E^{[2]}(^2D_{3/2})*$$
$$+\left|\left\langle 5^2F_{5/2}\left\|M^{[1]}\right\|6^2D_{5/2}\right\rangle\right|^2 E^{[2]}(^2D_{5/2})* \qquad (6.4)$$

That fit of the optical data confirmed the large size of the contributions to the fine structure from the low-lying $D$ states. Those contributions were the same order of magnitude as the contributions from $\alpha_{D,0}^{Mod}$ and $Q$, as illustrated in Table 4.4. The fit of the optical data also showed that the ratio of the dipole matrix element coupling the ground state to the low-lying $D$ states was consistent with the ratio predicted by $LS$ coupling and that the shifts due to the $^2D_{5/2}$ were much smaller than the $^2D_{3/2}$ shifts. If $LS$ coupling scheme is assumed, the dipole matrix element between the ground state and the $^2D_{5/2}$ can be written in terms of the dipole matrix element between the ground state and the $^2D_{3/2}$, Eq. 6.5.

$$\left|\left\langle 5^2F_{5/2}\left\|M^{[1]}\right\|6^2D_{5/2}\right\rangle\right|^2 = \frac{1}{14}\left|\left\langle 5^2F_{5/2}\left\|M^{[1]}\right\|6^2D_{3/2}\right\rangle\right|^2 \qquad (6.5)$$

This means that both of the dipole matrix elements are not required in Eq. 6.4. It would have been sufficient given the precision of the measurements to write both of the full second order

dipole-dipole energies in terms of the dipole matrix element coupling the $^2D_{3/2}$ and the ground state.

The model used to fit the rf data will certainly have to include large non-adiabatic contributions from the low-lying *D* states, as was done in the optical study. With the much richer data pattern, it should be possible to explore the possibility of the contributions from other properties not consider in the optical study. To accomplish this one would think that the data should be fit to a model like Eq. 6.1, with additional terms added to account for the large non-adiabatic effects, Eq. 6.6. The additional terms that would account for the non-adiabatic effects would be the full second order dipole-dipole energies due to the low-lying *D* states.

$$E_{Corrected} = A_0(L) + A_1(L)(\vec{L}\cdot\vec{J}_c) + A_2(L)\frac{X^{[2]}(J_c)\cdot C^{[2]}(\hat{r})}{\begin{pmatrix} J_c & 2 & J_c \\ -J_c & 0 & J_c \end{pmatrix}} +$$

$$+A_3(L)X^{[3]}(J_c)\cdot T^{[3]}(\hat{r}) + A_4(L)\frac{X^{[4]}(J_c)\cdot C^{[4]}(\hat{r})}{\begin{pmatrix} J_c & 4 & J_c \\ -J_c & 0 & J_c \end{pmatrix}}$$

$$+\left|\left\langle 5^2F_{5/2}\left\|M^{[1]}\right\|6^2D_{3/2}\right\rangle\right|^2\left(E^{[2]}(^2D_{3/2})^* + \frac{1}{14}E^{[2]}(^2D_{5/2})^*\right) \tag{6.6}$$

Fitting the measured fine structure to Eq. 6.6 with the structure parameters for each *L* determined independently requires that the structure parameters and the matrix element be independent from each other. They are not. The full second order dipole-dipole energies for each *L* can be fit perfectly to scalar, vector, and 2nd rank tensor structure parameters, but the resulting structure parameters do not scale in the fashion predicted by the effective potential model since they are highly non-adiabatic. The fact that the second order energies included in Eq. 6.6 can be broken into structure parameter that are also contained in the model makes it impossible to fit the fine

structure to both the structure parameters and matrix element since they are not linearly independent. .

To break the linear dependence between the structure parameters and the matrix element controlling the second order dipole-dipole energies it is necessary to constrain the structure parameter to scale in the fashion predicted by the effective potential model. This is accomplished by writing the structure parameters in the Eq. 6.6 explicitly in terms of expectations values and the properties of $Th^{3+}$, Eq. 6.7 through Eq. 6.11.

$$A_0(L) = -\frac{\alpha_{D,0}^{Mod}}{2}\left\langle r^{-4}\right\rangle_{nL} - \frac{(\alpha_{Q,0} - 6\beta_{D,0}^{Mod})}{2}\left\langle r^{-6}\right\rangle_{nL}, \tag{6.7}$$

$$A_1(L) = -\frac{\alpha_{FS}^2 g_J}{2}\left\langle r^{-3}\right\rangle_{nL} + \beta_{D,1}^{Mod}\left\langle r^{-6}\right\rangle_{nL} \tag{6.8}$$

$$A_2(L) = -Q\left\langle r^{-3}\right\rangle_{nL} - \frac{\alpha_{D,2}^{Mod}}{2}\left\langle r^{-4}\right\rangle_{nL} \tag{6.9}$$

$$A_3(L) = C_{M3}\left\langle r^{-5}\right\rangle_{nL} \tag{6.10}$$

and

$$A_4(L) = -\Pi\left\langle r^{-5}\right\rangle_{nL} - \frac{(\alpha_{Q,4} + \alpha_{DO,4}^{Mod})}{2}\left\langle r^{-6}\right\rangle_{nL} \tag{6.11}$$

For example, the scalar structure parameter is predicted from the effective potential model to be primarily controlled by the contribution of the scalar dipole polarizability which is proportional to $r^{-4}$ and the next term contributing to the scalar parameter is proportional to $r^{-6}$. It is expected that the contribution from the higher order terms in each of the structure parameters would be smaller than the leading terms, this assumption will be tested during the fit of the measured fine structure. With these restrictions in place it is possible to fit for the matrix element and the

properties of $Th^{3+}$ since they will be independent from each other. The fit of the fine structure to this improved model would return properties and the matrix element directly. This type of model is very similar to the model used to fit the optical data for the $Th^{3+}$ study, Eq. 6.4.

Before the rf measured fine structure was fit the to this model the possibility of additional effects that could be contributing to the fine structure were considered. These additional effects were neglected in the optical study due to the precision of the optical measurements. Given the precision of the rf measurements, these neglected effects had to be reconsidered. These additional effects were either added to the model used to fit the data or applied as corrections to the measured fine structure. The additional terms that had to be added to the model used to fit the data were the full second order octupole-dipole energies for the low-lying *D* states. For the case of the $^2D_{3/2}$ in $L$=9 these second order octupole-dipole energies were estimated to be as large as 100MHz. The calculation of the full second order octupole-dipole energies will be discussed in Section 6.2c. The addition of the full second order octupole-dipole energies to the model for the fine structure is seen in Eq. 6.12. The matrix elements controlling the respective second order energies in Eq. 6.12 are written out in the front of the second order energies, so they might be parameters in the fit of the fine structure.

$$E_{Corrected} = A_0(L) + A_1(L)(\vec{L}\cdot\vec{J}_c) + A_2(L)\frac{X^{[2]}(J_c)\cdot C^{[2]}(\hat{r})}{\begin{pmatrix} J_c & 2 & J_c \\ -J_c & 0 & J_c \end{pmatrix}} +$$

$$+A_3(L)X^{[3]}(J_c)\cdot T^{[3]}(\hat{r}) + A_4(L)\frac{X^{[4]}(J_c)\cdot C^{[4]}(\hat{r})}{\begin{pmatrix} J_c & 4 & J_c \\ -J_c & 0 & J_c \end{pmatrix}}$$

$$+\left|\left\langle 5^2F_{5/2}\left\|M^{[1]}\right\|6^2D_{3/2}\right\rangle\right|^2\left(E^{[2]}(^2D_{3/2})^* + \frac{1}{14}E^{[2]}(^2D_{5/2})^*\right)$$

$$+\left|\left\langle 5^2F_{5/2}\left\|M^{[1]}\right\|6^2D_{3/2}\right\rangle\right|\left|\left\langle 5^2F_{5/2}\left\|M^{[3]}\right\|6^2D_{3/2}\right\rangle\right|E_{OD}^{[2]}(^2D_{3/2})^*$$

$$+\frac{\left|\left\langle 5^2F_{5/2}\left\|M^{[1]}\right\|6^2D_{3/2}\right\rangle\right|}{\sqrt{14}}\left|\left\langle 5^2F_{5/2}\left\|M^{[3]}\right\|6^2D_{5/2}\right\rangle\right|E_{OD}^{[2]}(^2D_{5/2})^* \tag{6.12}$$

Before the measured fine structure was fit to this model to determine coefficients and matrix elements, the measured fine structure had to be corrected for effects not accounted for by this model, Eq. 6.13.

$$E_{Corrected} = E_{obs} - E_{\mathrm{Rel}} - E^{[2]}(V_{eff}) - E(\alpha_{D,2}\,shift) - E_{correction}^{[2]}(^2D_{3/2}) \tag{6.13}$$

The first three correction applied are "traditional" corrections for the studies of Rydberg fine structures. The first correction is the relativistic correction, $E_{\mathrm{Rel}}$, the calculation of this corrections is straight forward and is presented in Eq. 1.32. The second correction is $E^{[2]}(V_{eff})$ which corrects for the coupling between Rydberg levels. The $E^{[2]}(V_{eff})$ correction was discussed in the general in the Section 1.2, but a more detailed discussion of its calculation for the case of $Th^{3+}$ is discussed in the Section 6.2c. The third correction, $E(\alpha_{D,2}\,shift)$, is necessary due to

tensor coupling between levels with of the same $n$ in the Rydberg fine structure, this correction is discussed in Section 6.2d. The last correction that needs to be applied to the measured fine structure in Eq. 6.13 is $E^{[2]}_{correction}(^2D_{3/2})$. The $E^{[2]}_{correction}(^2D_{3/2})$ correction accounts for the neglect of the fine structure of the intermediate Rydberg states when calculating the full second order dipole-dipole energies due to the low-lying $^2D_{3/2}$. This correction is discussed in Section 6.2a at the same time as the calculation of the full second order dipole-dipole energies.

The remaining sections in this chapter will discuss the calculation of the corrections, the application of the corrections and the extraction of the properties from the measured fine structure. Section 6.2 will discuss in detail the calculation of all additional terms for the model, Eq. 6.12 and the all corrections applied to the measured fine structure, Eq. 6.13. Section 6.3 will show the application of the corrections to the observed fine structure and the fitting of the fine structure to the model. Section 6.4 will compare the values of the properties extracted from the fit with the results from the optical study and the theoretical calculations.

## 6.2 Effects contributing to the $Th^{2+}$ Rydberg fine structure

### 6.2a Dipole coupling with the low-lying *D* states

The dominance of the second order energies due to the dipole-dipole coupling with the two low-lying $D$ states in the model for the $Th^{2+}$ Rydberg fine structure requires that careful attention be paid to these calculations. The calculation of the full second order energies for dipole-dipole coupling with the $^2D_{3/2}$ and $^2D_{5/2}$ was discussed in the Chapter 4. The second order dipole-dipole energies for the $^2D_{3/2}$ and $^2D_{3/2}$ were given respectively by Eq. 4.6 and Eq. 4.7, and repeated here in Eq. 6.14 and 6.15 respectively for convenience.

$$E^{[2]}(^2D_{3/2}) = -\left\langle 5^2F_{5/2}\left\|M^{[1]}\right\|6^2D_{3/2}\right\rangle^2 \sum_{n'L'}\begin{Bmatrix} K & L & 5/2 \\ 1 & 3/2 & L' \end{Bmatrix}^2 \begin{pmatrix} L & 1 & L' \\ 0 & 0 & 0 \end{pmatrix}^2 (2L+1)(2L'+1)$$

$$\times \frac{\left\langle nL\left\|r^{-2}\right\|n'L'\right\rangle\left\langle n'L'\left\|r^{-2}\right\|nL\right\rangle}{\Delta E(6^2D_{3/2}) + E(n') - E(n)} \tag{6.14}$$

$$E^{[2]}(^2D_{5/2}) = -\left\langle 5^2F_{5/2}\left\|M^{[1]}\right\|6^2D_{5/2}\right\rangle^2 \sum_{n'L'}\begin{Bmatrix} K & L & 5/2 \\ 1 & 5/2 & L' \end{Bmatrix}^2 \begin{pmatrix} L & 1 & L' \\ 0 & 0 & 0 \end{pmatrix}^2 (2L+1)(2L'+1)$$

$$\times \frac{\left\langle nL\left\|r^{-2}\right\|n'L'\right\rangle\left\langle n'L'\left\|r^{-2}\right\|nL\right\rangle}{\Delta E(6^2D_{5/2}) + E(n') - E(n)} \tag{6.15}$$

Everything in Eq. 6.14 and 6.15 is known except the dipole matrix elements that connect the ground state to either the $^2D_{3/2}$ or $^2D_{5/2}$. Table 6.1 gives the total second order dipole-dipole energies for the $E^{[2]}(^2D_{3/2})$ and the $E^{[2]}(^2D_{5/2})$ for each of the specific states measured in the rf study. These energies were calculated assuming the theoretical values of the dipole matrix elements [45].

$$\left|\left\langle 5^2F_{5/2}\left\|M^{[1]}\right\|6^2D_{3/2}\right\rangle\right| = 1.530 a.u.$$
$$\left|\left\langle 5^2F_{5/2}\left\|M^{[1]}\right\|6^2D_{5/2}\right\rangle\right| = 0.412 a.u.$$

From Table 6.1 it can be seen that the second order energies for both core states are not small, even in $L$=12, thus confirming yet again the necessity of including them in the model used to the fit the data. Also when these corrections are calculated with their theoretical matrix elements it can be seen that contributions due to the $^2D_{3/2}$ are much larger than the contributions due to the $^2D_{5/2}$. Even though the $^2D_{5/2}$ second order dipole-dipole energies are smaller than the

$^2D_{3/2}$ second order dipole energies, they cannot be neglected. A simplification to the model can be made though, as mentioned in the first section of this chapter.

Table 6.1: The second order dipole-dipole energies for the $n$=28 $Th^{2+}$ Rydberg states due to the $^2D_{3/2}$ and the $^2D_{5/2}$ in MHz. The first column identifies the states ($L$, $K$). The second columns gives the second order energy for the $^2D_{3/2}$ and column three gives the second order energy for the $^2D_{5/2}$. Both second order energies were calculated assuming theoretical matrix elements, 1.530a.u. for the $^2D_{3/2}$ dipole matrix element and 0.412a.u. for the $^2D_{5/2}$ dipole matrix element.

| $(L, K)$ | $E^{[2]}(^2D_{3/2})$ | $E^{[2]}(^2D_{5/2})$ |
|---|---|---|
| (9, 6.5) | -7420.58 | -37.48 |
| (9, 7.5) | -4947.05 | -83.17 |
| (9, 8.5) | -2820.68 | -113.20 |
| (9, 9.5) | -1295.33 | -119.40 |
| (9, 10.5) | -654.73 | -92.66 |
| (9, 11.5) | -1212.46 | -22.91 |
| (10, 7.5) | -3458.32 | -18.82 |
| (10, 8.5) | -2282.49 | -43.80 |
| (10, 9.5) | -1310.04 | -59.99 |
| (10, 10.5) | -654.86 | -63.49 |
| (10, 11.5) | -442.85 | -49.98 |
| (10, 12.5) | -811.90 | -14.73 |
| (11, 8.5) | -1342.74 | -10.89 |
| (11, 9.5) | -878.89 | -26.17 |
| (11, 10.5) | -519.89 | -35.93 |
| (11, 11.5) | -311.85 | -38.04 |
| (11, 12.5) | -305.27 | -30.15 |
| (11, 13.5) | -555.04 | -9.72 |
| (12, 9.5) | -748.71 | -6.78 |
| (12, 10.5) | -486.66 | -16.69 |
| (12, 11.5) | -292.89 | -22.93 |
| (12, 12.5) | -192.83 | -24.26 |
| (12, 13.5) | -214.12 | -19.30 |
| (12, 14.5) | -386.61 | -6.58 |

If *LS* coupling scheme is assumed the dipole matrix element between the ground state and the $^2D_{5/2}$ can be written in terms of the dipole matrix element between the ground state and the $^2D_{3/2}$, Eq. 6.5, shown here again for convenience.

$$\left|\left\langle 5^2F_{5/2}\left\|M^{[1]}\right\|6^2D_{5/2}\right\rangle\right|^2=\frac{1}{14}\left|\left\langle 5^2F_{5/2}\left\|M^{[1]}\right\|6^2D_{3/2}\right\rangle\right|^2$$

The optical study determined both of the matrix elements [3]. The ratio of the experimentally determined matrix elements is consistent within 1.3σ with the ratio predicted from the *LS* coupling. It is very unlikely that the ratio between these two matrix elements varies by as much 5% from the *LS* coupling ratio. (The theoretical matrix elements agree with the *LS* ratio to within 1.5%.) Given the relatively small size of the calculated contribution from the $^2D_{5/2}$ state, it should be sufficiently accurate to assume that the matrix elements ratio matches the *LS* coupling predication. Therefore, in the model used to fit the fine structure the $^2D_{5/2}$ dipole matrix element will be rewritten in term of the $^2D_{3/2}$ dipole matrix element, Eq. 6.12, allowing for one less parameter in the fit of the fine structure. This assumption of *LS* coupling will be checked when the fit of the fine structure is carried out.

The numerical precision of the calculated second order dipole-dipole energies, Table 6.1 is an important consideration since these are a dominant contribution to the fine structure. The calculation of both the of the second order energies for the $^2D_{3/2}$ and the $^2D_{5/2}$, presented in Eq. 6.14 and Eq. 6.15 respectively, both contain a sum over the intermediate Rydberg state of the form

$$\sum_{n'L'}\frac{\left\langle nL\left\|r^{-2}\right\|n'L'\right\rangle\left\langle n'L'\left\|r^{-2}\right\|nL\right\rangle}{\Delta E(\lambda' J_c')+E(n')-E(n)} \tag{6.16}$$

where $nL$ denote the Rydberg state of interest and $n'L'$ is the intermediate Rydberg states. In the case of the $^2D_{3/2}$ and $^2D_{5/2}$ second order energies the possible values of $L'$ are only $L \pm 1$. The calculation of that sum over the intermediate Rydberg state is conducted numerically through a Fortran program, $f_{nLZ}$, developed by previous members of this research group [49] to implement the Dalgarno Lewis [10] approach to completing the sum over the intermediate Rydberg state, $n'$, including both discrete and continuum states. The Dalgarno Lewis approach rewrites that infinite sum as a differential equation. The $f_{nLZ}$ program then numerically solves that differential equation. The $f_{nLZ}$ program is used in the calculation of all second order energies. Therefore understanding the accuracy of the $f_{nLZ}$ program is important to understanding possible uncertainties in calculation of corrections that will be applied to the measured fine structure.

In order test the $f_{nLZ}$ program it is necessary to be able to complete the sum over the intermediate Rydberg states in a different way that would allow for a comparison and check of the $f_{nLZ}$ result. If the adiabatic expansion was valid it would be possible to carry out the sum over the intermediate Rydberg state without the use of $f_{nLZ}$, since Eq. 6.16 can be rewritten as Eq. 6.17 with the application of the adiabatic expansion.

$$\sum_{n'} \frac{\left\langle nL \left\| r^{-2} \right\| n'L' \right\rangle \left\langle n'L' \left\| r^{-2} \right\| nL \right\rangle}{\Delta E(\lambda' J_c') + E(n') - E(n)} = \sum_{n'} \frac{\left\langle nL \left\| r^{-2} \right\| n'L' \right\rangle \left\langle n'L' \left\| r^{-2} \right\| nL \right\rangle}{\Delta E(\lambda' J_c')}$$

$$- \sum_{n'} \frac{[E(n') - E(n)] \left\langle nL \left\| r^{-2} \right\| n'L' \right\rangle \left\langle n'L' \left\| r^{-2} \right\| nL \right\rangle}{\Delta E(\lambda' J_c')^2}$$

$$+ \sum_{n'} \frac{[E(n') - E(n)]^2 \left\langle nL \left\| r^{-2} \right\| n'L' \right\rangle \left\langle n'L' \left\| r^{-2} \right\| nL \right\rangle}{\Delta E(\lambda' J_c')^3} + .. \tag{6.17}$$

Then using the completeness relation and the other relations related to the radial functions seen in Ref. [7] the three terms in Eq. 6.17 can be rewritten in terms of expectations values, and

factors that are dependent on $L$, $L'$ and the excitation energy of the excited core state, $\Delta E(\lambda' J_c')$, Eq. 6.18. If the adiabatic expansion was valid for the excited core state of interest then the result of the $f_{nLZ}$ program should closely match the result of calculating the sum using Eq. 6.18.

$$\sum_{n'} \frac{\left\langle nL \left\| r^{-2} \right\| n'L' \right\rangle \left\langle n'L' \left\| r^{-2} \right\| nL \right\rangle}{\Delta E(\lambda' J_c') + E(n') - E(n)}$$

$$= \frac{\left\langle r^{-4} \right\rangle_{nL}}{\Delta E(\lambda' J_c')} - \frac{1}{2} \frac{[4 - L(L+1) + L'(L'+1)] \left\langle r^{-6} \right\rangle_{nL}}{\Delta E(\lambda' J_c')^2}$$

$$+ \frac{1}{\Delta E(\lambda' J_c')^3} \left[ -\frac{4}{5} \left( 3 \left\langle r^{-7} \right\rangle_{nL} - L(L+1) \left\langle r^{-8} \right\rangle_{nL} \right) \right.$$

$$\left. + 7\left[ -L(L+1) + L'(L'+1) \right] \left\langle r^{-8} \right\rangle_{nL} + \frac{1}{4} \left[ -6 - L(L+1) + L'(L'+1) \right]^2 \left\langle r^{-8} \right\rangle_{nL} \right] \quad (6.18)$$

For the case of the $^2D_{3/2}$ and the $n$=28 fine structure, Table 4.2 showed that for low $L$ levels in $n$=28 the adiabatic expansion would not be valid but as $L$ increases the use of the adiabatic expansion would become valid. Therefore, if $f_{nLZ}$ was used to calculate the sum, Eq. 6.16, for the $^2D_{3/2}$ for a range of $L$, it would be expected that the value of the sum calculated using three terms of the adiabatic expansion would approach the $f_{nLZ}$ value when $L$ increases, enabling a test of the $f_{nLZ}$ program. Table 6.2 gives the results of such a test. From the table it can be seen that as a $L$ increases the values of the sum calculated using $f_{nLZ}$ and Eq. 6.18 converge and match to five digits. This test of $f_{nLZ}$ also illustrates the inadequacy of the use of the adiabatic expansion for low $L$ states in $n$=28, since the $f_{nLZ}$ result differs so dramatically from the value of the sum completed using Eq. 6.18. To determine the uncertainty on each of the $f_{nLZ}$ sums a secondary test of $f_{nLZ}$ was conducted. If the core excitation energy is large it is expected that the sum completed using $f_{nLZ}$ and the sum completed using Eq. 6.18 would match over the complete

range of $L$. Therefore to test $f_{nLZ}$, the core excitation energy in Eq. 6.16 was changed to $1,000,000 cm^{-1}$ and the sum was then completed using both the $f_{nLZ}$ program and Eq. 6.18 over the entire range of $L$. The results of completing the sum both ways are seen in Table 6.3 for $L$=9 to $L$=27 in $n$=28. The test of the $f_{nLZ}$ program shows good agreement with the completion of the sum using Eq. 6.18 with the difference between the two methods occurring either in the sixth or seventh digit. There did not appear to be correlation in the deviation of the two methods with $L$ so to be conservative an error of two was placed on the sixth digit on each of the $f_{nLZ}$ sum results used, three times the average difference of the results shown in Table 6.3 for the two methods. From these two tests it was determined that the uncertainty in the calculated second order dipole-dipole energies would be on at most 0.02MHz, for the largest second order dipole-dipole energies for the $^2D_{3/2}$ in $L$=9 . This uncertainty is much smaller than the experimental uncertainty in the measured positions of the levels, so it was neglected.

Table 6.2: Comparing the sum over intermediate Rydberg state using $f_{nLZ}$ or Eq. 6.18 to calculate the Eq. 6.16 for $n$=28 $q$=3. In the table all numbers are times $10^{-10}$ and are in atomic units.

| | | $L'=L+1$ | | $L'=L-1$ | |
|---|---|---|---|---|---|
| | $L$ | $f_{nLZ}$ result | Three Terms | $f_{nLZ}$ result | Three terms |
| $\Delta E_{core}$=9193.2461cm$^{-1}$ | 9 | 9918.62 | 29602.4 | 54601.9 | 32479.8 |
| | 10 | 6613.03 | 11651.7 | 25596.6 | 16271.0 |
| | 11 | 4504.49 | 5934.40 | 9985.79 | 9005.77 |
| | 12 | 3127.95 | 3568.68 | 5590.14 | 5368.22 |
| | 13 | 2210.53 | 2355.87 | 3447.03 | 3384.98 |
| | 14 | 1587.47 | 1638.17 | 2249.21 | 2229.62 |
| | 15 | 1156.93 | 1175.47 | 1527.14 | 1520.41 |
| | 16 | 854.598 | 861.652 | 1068.84 | 1066.38 |
| | 17 | 639.114 | 641.889 | 766.483 | 765.537 |
| | 18 | 483.389 | 484.510 | 560.789 | 560.412 |
| | 19 | 369.394 | 369.857 | 417.279 | 417.124 |
| | 20 | 284.944 | 285.138 | 315.001 | 314.936 |
| | 21 | 221.685 | 221.767 | 240.765 | 240.738 |
| | 22 | 173.809 | 173.843 | 186.021 | 186.010 |
| | 23 | 137.228 | 137.242 | 145.083 | 145.078 |
| | 24 | 109.028 | 109.034 | 114.087 | 114.086 |
| | 25 | 87.1106 | 87.1127 | 90.3595 | 90.3585 |
| | 26 | 69.9455 | 69.9462 | 72.0130 | 72.0126 |
| | 27 | 56.4073 | 56.4074 | 57.7006 | 57.7004 |

Table 6.3: Comparing the sum over intermediate Rydberg state using $f_{nLZ}$ or Eq. 6.18 to calculate the Eq. 6.16 for $n$=28 $q$=3. The excitation energy used was $1,000,000 cm^{-1}$. In the table all numbers are times $10^{-11}$ and are in atomic units.

| | | $L'=L+1$ | | $L'=L-1$ | |
|---|---|---|---|---|---|
| | $L$ | $f_{nLZ}$ result | Three Terms | $f_{nLZ}$ result | Three terms |
| $\Delta E_{core}=1,000,000 cm^{-1}$ | 9 | 1518.085 | 1518.091 | 1538.669 | 1538.668 |
| | 10 | 912.1792 | 912.1793 | 921.0895 | 921.0882 |
| | 11 | 572.9688 | 572.9683 | 577.1171 | 577.1163 |
| | 12 | 373.4156 | 373.4154 | 375.4657 | 375.4655 |
| | 13 | 251.0372 | 251.0375 | 252.1019 | 252.1023 |
| | 14 | 173.2893 | 173.2893 | 173.8658 | 173.8658 |
| | 15 | 122.3725 | 122.3724 | 122.6959 | 122.6958 |
| | 16 | 88.13738 | 88.13755 | 88.32422 | 88.32438 |
| | 17 | 64.58258 | 64.58250 | 64.69331 | 64.69323 |
| | 18 | 48.04316 | 48.04312 | 48.11021 | 48.11017 |
| | 19 | 36.21881 | 36.21871 | 36.26014 | 36.26005 |
| | 20 | 27.62821 | 27.62818 | 27.65407 | 27.65404 |
| | 21 | 21.29651 | 21.29649 | 21.31288 | 21.31286 |
| | 22 | 16.56874 | 16.56874 | 16.57919 | 16.57919 |
| | 23 | 12.99699 | 12.99697 | 13.00370 | 13.00368 |
| | 24 | 10.26967 | 10.26969 | 10.27398 | 10.27401 |
| | 25 | 8.167028 | 8.167001 | 8.169792 | 8.169765 |
| | 26 | 6.531522 | 6.531507 | 6.533278 | 6.533263 |
| | 27 | 5.249143 | 5.249130 | 5.250240 | 5.250227 |

With the numerical accuracy of the calculated second order dipole-dipole energies confirmed, the last thing to check on the calculated second order dipole-dipole energies is an assumption made in their calculation. The assumption inherent in Eq. 6.14 and 6.15 is that the fine structure energy of the intermediate Rydberg state can be neglected and just the hydrogenic energy of the of the intermediate state, $E(n')$, can be used in the denominator of the calculation of the full second order energies. Fig 4.4 shows the Rydberg series connected to each $D$ states, and from this it can be seen that the $n$=28 Rydberg level bound to the ground state of $Th^{3+}$ is near

the $n'$=9 and $n'$=10 Rydberg states bound to the $^2D_{3/2}$ and the $n'$=8 Rydberg state from the $^2D_{5/2}$. For intermediate states that are close to the $n$=28 states the energy difference in the denominator of the second order dipole energy, Eq. 6.14 and 6.15, is small. Therefore if the energy of the intermediate state deviates much from hydrogenic, it could change the contribution from that intermediate state. During the optical study the fine structure of the intermediate states was neglected, but due to the sub-MHz precision of the rf measurements it cannot be neglected here.

The size of the fine structure of the intermediate Rydberg state and its proximity to the $n$=28 $Th^{2+}$ Rydberg state bound to the $^2F_{5/2}$ will determine the size of the correction needed to the full second order energies for the $^2D_{3/2}$ and the $^2D_{5/2}$. Since the $n'$ values of the intermediate states closest to the $n$=28 are $n'$=8, 9, and 10 and these contain only $L' \le 9$ levels, the lower $L$ states in $n$=28 will be most susceptible these corrections since the $L$ values of the intermediate state, $L'$, can only be $L \pm 1$. For each $L'$ in the $^2D_{3/2}$ fine structure there will be four levels since $J_c = 3/2$, while for the $^2D_{5/2}$ there will be six levels for each $L'$. The size of the fine structure of the intermediate Rydberg states will be determined by the values of the core properties for each of the excited states. At this time there are not any measurements of any of the properties for the excited states. Therefore, to determine the size of the corrections theoretical properties for the excited $^2D_{3/2}$ and $^2D_{5/2}$ were used to simulate the intermediate fine structure. For the case of the of the low-lying $^2D_{3/2}$ state the properties were provided during private communications with both M. S. Safronova [42] and U. I. Safronova [46], with the exception of the Landé g factor, $g_J$. The Landé g factor was calculated from the definition presented in the work of Bethe and Salpeter [31].

The properties used in the simulations of the intermediate fine structure bound to the low-lying $^2D_{3/2}$ are:

$$\alpha_{D,0} = -4.5(4.5)$$
$$\alpha_{D,2} = -1.6$$
$$Q = 1.32$$
$$g_J = 0.80$$

.

The large uncertainty placed on the scalar dipole polarizabilities for the $^2D_{3/2}$ is due to the fact that the a large part of the property is due to the dipole coupling between the $^2D_{3/2}$ and the $^2F_{5/2}$. The optical study of the $Th^{2+}$ Rydberg fine structure showed that the dipole coupling of the $^2F_{5/2}$ and the $^2D_{3/2}$ is not well represented by the effective potential and the scalar dipole polarizability due to the proximity of the states to each other. This will also hold true for the scalar dipole polarizability for the excited $^2D_{3/2}$ state, therefore a large correction and uncertainty has been applied to its value, $\Delta\alpha_{D,0} = -9.0(4.5)$. Using these values the fine structure of the intermediate state was then simulated to determine whether it would produce a significant difference in the energy denominator of the second order energies compared to the energy denominator calculated assuming the hydrogenic energy for the intermediate state.

Given the $n'L'$ of the intermediate state of interest and the estimated properties for the $^2D_{3/2}$ excited core state it was found that some of the fine structure patterns for the intermediate states would span up to $\pm 10 cm^{-1}$ around hydrogenic and thus changing the energy denominator of the second order energies for some intermediate states by one to two percent. The contributions to the second order energies for some of these intermediate states are on the order of 10GHz, thus the change of a few percent could prove very important in the interpretation of rf measurements with sub-MHz precision. An example of this is seen in Fig. 6.1, the $n$=28 bound

to the $^2F_{5/2}$ is separated from the $n'=10$ bound to the $^2D_{3/2}$ by 576.62cm$^{-1}$. The fine structure of the $n'=10\,L'=8$ states spans approximately $\pm 8.5 cm^{-1}$, and thus would change the energy denominator of the second order energies for intermediate states with $n'=10\,L'=8$ by as much as 1.5%.

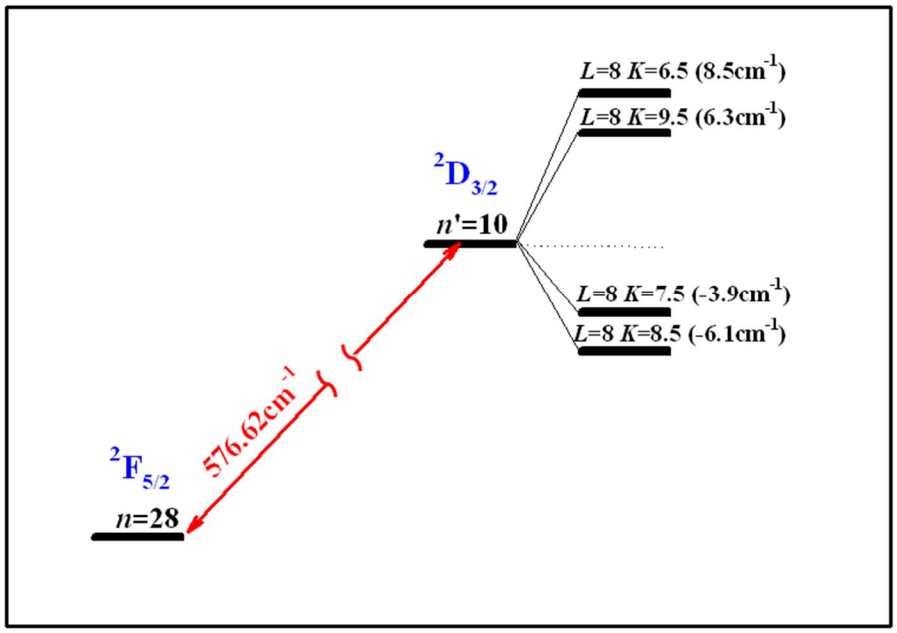


Figure 6.1: Example of the fine structure for an intermediate state $n'=10\,L'=8$ bound to the $^2D_{3/2}$. The $n$=28 bound to $^2F_{5/2}$, is separated from the $n'=10$ bound to the $^2D_{3/2}$ by 576.62cm$^{-1}$. The energies in this figure are not to scale.

To correct the second order energies for the neglect of the intermediate fine structure the contribution to the second order energies due to specific intermediate Rydberg states near the $n$=28 state of interest in Fig. 4.4, were calculated two ways. The first way assumed the hydrogenic energy for the energy of the intermediate state, $E^{[2]}_{Hyd}(\lambda' J'_c)$ and the second way used the simulated fine structure energy of the intermediate state, $E^{[2]}_{Fine}(\lambda' J'_c)$, in addition to the

hydrogenic energy. The difference between these two calculations provided the amount the full second order energy would shift due to the fine structure of the intermediate state.

$$E^{[2]}_{Correction}(\lambda' J'_c) = E^{[2]}_{Fine}(\lambda' J'_c) - E^{[2]}_{Hyd}(\lambda' J'_c) \tag{6.19}$$

This calculation was completed for all the $n$=28 states of interest and for the intermediate states bound to the $D$ states that are near the $n$=28 bound to the ground state. It would be for these states that the energy difference between $E(n)$ and $E(n')$ would be smallest, and therefore, they would be most sensitive to the possible change in the energy of intermediate state due to its possible fine structure. The calculation of the corrections to the full second order energies for the $^2D_{3/2}$ focused on the $n' = 9-11$, since those states are the nearest to the $n$=28 Rydberg state bound to $^2F_{5/2}$. Table 6.4 gives the shift to each component of the second order energies for $n' = 9-11$ and $L' = L \pm 1$, the absence of a number for a specific intermediate state indicates the nonexistence of that specific intermediate state. Thus certainty on each of the calculated shifts is the result of the uncertainty in the scalar dipole polarizability for the $^2D_{3/2}$, the uncertainty in each of the shift is propagated into the total shift for each states listed in the table.

For the case of the $^2D_{3/2}$ second order energies the corrections were only calculated for the intermediate states $n' = 9-11$ due to the fact that the corrections to the second order energies become smaller as $n'$ increases. As $n'$ increases, the intermediate Rydberg state becomes farther from the $n$=28 state bound to the ground state, Fig. 4.4, and the size of the intermediate fine structure also decreases like $1/n^3$ making the corrections to the second order energies smaller.

Table 6.4: Corrections to the second order dipole-dipole energies due to the fine structure of the intermediate state bound to the $^2D_{3/2}$ excited states. These corrections were calculated assuming the theoretical value of the dipole matrix element coupling the $^2D_{3/2}$ and the ground state, 1.53a.u. All energies are in MHz.

| $L$ | $K$ | $n'$=9 $L'=L+1$ | $n'$=9 $L'=L-1$ | $n'$=10 $L'=L+1$ | $n'$=10 $L'=L-1$ | $n'$=11 $L'=L+1$ | $n'$=11 $L'=L-1$ | $E^{[2]}_{Correction}(^2D_{3/2})$ (MHz) |
|---|---|---|---|---|---|---|---|---|
| 9 | 6.5 | - | 5.65(62) | - | 64.31(8.11) | - | 3.52(44) | 73.48 (8.15) |
| 9 | 7.5 | - | -1.76(43) | - | -20.01(5.79) | - | -1.07(30) | -22.84 (5.81) |
| 9 | 8.5 | - | -1.54(24) | - | -17.33(3.17) | 0.00 | -0.94(16) | -19.81 (3.18) |
| 9 | 9.5 | - | 0.56(9) | - | 6.46(1.10) | 0.00 | 0.35(6) | 7.37 (1.11) |
| 9 | 10.5 | - | - | - | - | 0.00 | - | 0.00 (0.00) |
| 9 | 11.5 | - | - | - | - | 0.00 | - | 0.00 (0.00) |
| 10 | 7.5 | - | - | - | 10.57(1.08) | - | 0.99(9) | 11.56 (1.08) |
| 10 | 8.5 | - | - | - | -3.76(73) | - | -0.35(6) | -4.11 (0.73) |
| 10 | 9.5 | - | - | - | -3.08(39) | - | -0.28(3) | -3.36 (0.39) |
| 10 | 10.5 | - | - | - | 1.04(14) | - | 0.10(1) | 1.14 (0.14) |
| 10 | 11.5 | - | - | - | - | - | - | - |
| 10 | 12.5 | - | - | - | - | - | - | - |
| 11 | 8.5 | - | - | - | - | - | 0.16(1) | 0.16 (0.01) |
| 11 | 9.5 | - | - | - | - | - | -0.06(1) | -0.06 (0.01) |
| 11 | 10.5 | - | - | - | - | - | -0.05(1) | -0.05 (0.01) |
| 11 | 11.5 | - | - | - | - | - | 0.02(1) | 0.02 (0.01) |
| 11 | 12.5 | - | - | - | - | - | - | - |
| 11 | 13.5 | - | - | - | - | - | - | - |
| 12 | 9.5 | - | - | - | - | - | - | - |
| 12 | 10.5 | - | - | - | - | - | - | - |
| 12 | 11.5 | - | - | - | - | - | - | - |
| 12 | 12.5 | - | - | - | - | - | - | - |
| 12 | 13.5 | - | - | - | - | - | - | - |
| 12 | 14.5 | - | - | - | - | - | - | - |

The size of the corrections also decreases with $L$, this is due to the fact in that higher $L$s require intermediate states with higher $n'$, which are farther from the $n$=28 states and have smaller fine structures. Given the fact that this correction to the second order dipole-dipole energies for the $^2D_{3/2}$ contains an uncertainty, it will be kept separate and not applied to the calculated full second order dipole-dipole energies for the $^2D_{3/2}$. This correction will instead be applied to the measured fine structure, and the uncertainty in it will be propagated into the positions of the levels.

The fine structures of the intermediate states bound to the $^2D_{5/2}$ were also studied to determine the effect of their neglect on the full second order dipole energies for the $^2D_{5/2}$. To get a sense whether they were important just the permanent quadrupole moment for the $^2D_{5/2}$ was used to simulate the fine structure of the intermediate states of interest, $Q = 2.02 a.u.$ [46]. For the case of the $^2D_{5/2}$, the nearest intermediate state to $n$=28 is the $n'$=8, the highest $L'$ contained in that state is $L'$=7, which does not contribute to any of the second order energies of interest, since they have $L \geq 9$. Given the quantum numbers and size of the fine structure of the states bound to the $^2D_{5/2}$ that are near the $n$=28 bound to the ground state, the corrections to the $^2D_{5/2}$ second order energies would be small. Table 6.5 gives the shift of the second order energies for the $^2D_{5/2}$, for $n$=28 $L$=9 due to the $n'$=9 $L'$=8 intermediate state, the closest intermediate state. The shift of the $^2D_{5/2}$ second order energies, $E^{[2]}_{Correction}(^2D_{5/2})$, were calculated assuming the theoretical dipole matrix element [45] between the ground state and the $^2D_{5/2}$. The corrections for states with $L > 9$ would be even smaller than these corrections for the $L$=9 states, since the intermediate states involved would have an even higher $n'$ value and thus would be father away from the $n$=28 state bound to the ground state. These corrections were considered negligible.

Table 6.5: The shift of the $^2D_{5/2}$ second order energies, the first column identities the $L$ and the second column identifies the $K$. The final column gives the shift assuming the theoretical dipole matrix element, 0.412a.u., for the coupling of the $^2D_{5/2}$ and the ground state. All energies are in MHz.

| $L$ | $K$ | $E^{[2]}_{Correction}(^2D_{5/2})$ (MHz) |
|---|---|---|
| 9 | 6.5 | 0.00 |
| 9 | 7.5 | -0.03 |
| 9 | 8.5 | -0.05 |
| 9 | 9.5 | -0.03 |
| 9 | 10.5 | 0.03 |
| 9 | 11.5 | - |

### 6.2b Octupole coupling with the low-lying *D* states

The full second order energies due to the dipole-dipole coupling with the low lying states proved to be very important to the deciphering of the $Th^{2+}$ Rydberg fine structure, but these second order energies only accounted for the dipole-dipole coupling between the ground state and the two low-lying excited $D$ states. The ground state and the two low-lying $D$ states can also couple via higher order odd terms in the multipole expansion. The effects of these coupling were neglected in the optical study, but given the increased precision of the rf measurements these higher order coupling must be considered. The next two coupling that can occur between the low-lying states and the ground state are octupole-dipole coupling and octupole-octupole coupling. The effect of these coupling would be smaller than the dominant dipole-dipole coupling, but just like the dipole-dipole coupling these higher order coupling would be susceptible to the failure of the adiabatic expansion for the low lying $^2D_{3/2}$ and $^2D_{5/2}$ states. The effective potential model derived using the adiabatic expansion would fail to describe these coupling to the low-lying $D$ states.

Therefore, the full second order energies due to these couplings for both of the low-lying states had to be calculated to determine their importance. The second order energies due to the octupole-dipole coupling are given by Eq. 6.20, for the two different low lying states, the $^2D_{3/2}$ and the $^2D_{5/2}$ [7].

$$E_{OD}^{[2]}(\lambda' J_c') = -2 \sum_{\lambda' J_c' n' L'} \left[ (2L+1)(2L'+1) \begin{Bmatrix} K & L & J_c \\ 3 & J_c' & L' \end{Bmatrix} \begin{Bmatrix} K & L' & J_c' \\ 1 & J_c & L \end{Bmatrix} \begin{pmatrix} L & 3 & L' \\ 0 & 0 & 0 \end{pmatrix} \begin{pmatrix} L' & 1 & L \\ 0 & 0 & 0 \end{pmatrix} \right.$$

$$\left. \times \frac{\left\langle nL \left\| r^{-4} \right\| n'L' \right\rangle \left\langle nL \left\| r^{-2} \right\| n'L' \right\rangle}{\Delta E(\lambda' J_c') + E(n') - E(n)} \left\langle gJ_c \left\| M^{[3]} \right\| \lambda' J_c' \right\rangle \left\langle gJ_c \left\| M^{[1]} \right\| \lambda' J_c' \right\rangle \right] \tag{6.20}$$

Everything in Eq. 6.20 can be calculated up to a constant, the product of the dipole and octupole matrix elements that connect the ground state to the excited state of interest. The sum over the intermediate Rydberg state, $n'$, was completed using the $f_{nLZ}$ program.

The size and importance of these second order energies depends on the size of the matrix elements, theoretical estimates of both the dipole and octupole matrix elements for the low-lying $^2D_{3/2}$ and $^2D_{5/2}$ were used in the calculation of the full second order energies initially. The dipole matrix elements for the two low-lying states have been calculated [45] to be

$$\left\langle 5^2F_{5/2} \left\| M^{[1]} \right\| 6^2D_{3/2} \right\rangle = -1.530 a.u.$$
$$\left\langle 5^2F_{5/2} \left\| M^{[1]} \right\| 6^2D_{5/2} \right\rangle = 0.412 a.u.$$

The magnitudes of the octupole matrix element were provided in private communication with M.S. Safronova [42], but the sign of each of the octupole matrix elements was determined relative to the dipole matrix elements connecting the same states by assuming a *LS* coupling scheme for the *D* and *F* states.

$$\left\langle 5^2F_{5/2}\left\|M^{[3]}\right\|6^2D_{3/2}\right\rangle = 8.394 a.u.$$
$$\left\langle 5^2F_{5/2}\left\|M^{[3]}\right\|6^2D_{5/2}\right\rangle = -7.043 a.u.$$

The full second order energies due the octupole-dipole coupling for the two low-lying state, $E_{OD}^{[2]}(^2D_{3/2})$ and $E_{OD}^{[2]}(^2D_{5/2})$, were calculated assuming the theoretical matrix elements. The results of the calculations for both of the low-lying core states are provided in Table 6.6. For the $^2D_{3/2}$ these second order octupole-dipole energies are large, at times almost 70MHz in $L$=9, but they decrease in size to be approximately 2MHz for $L$=12. While for the other low-lying state, the $^2D_{5/2}$, the second order octupole-dipole energies are less than 5MHz for $L$=9 and decrease to be less than 1MHz for $L$=12. Given the size of both of the second order octupole-dipole energies in $L$=9, neither can be neglected when fitting the observed rf fine structure for core properties. For that reason the second order octupole-dipole energies were added to the model being used to fit the measured fine structure, Eq. 6.12.

In the model being used to fit the fine structure both of the octupole matrix elements that coupling the ground state to the low-lying $D$ states have been included. The optical study of $Th^{3+}$ showed that the ratio of the dipole matrix elements that couple the ground state to the low-lying $D$ state was consistent with the ratio predicted by $LS$ coupling. This allowed for the model being used to fit the data to be simplified to include one less parameter by writing both the second order energies due to dipole coupling in terms of just one of the dipole matrix elements. Similarly it is possible to write the octupole matrix elements for the low-lying $D$ states in terms of each other if $LS$ coupling is assumed.

Table 6.6: The full second order energies due the octupole-dipole coupling between the ground state and the one of the low-lying $D$ states. The theoretical values for the both the dipole and octupole matrix elements were used in the calculation here. For the $^2D_{3/2}$ the dipole matrix element was -1.530a.u. and the octupole matrix element was 8.394a.u. For the $^2D_{5/2}$ the dipole matrix element was 0.412a.u. and the octupole matrix element was -7.043a.u. All energies are in MHz.

| $L$ | $K$ | $E_{OD}^{[2]}(^2D_{3/2})$ | $E_{OD}^{[2]}(^2D_{5/2})$ |
|---|---|---|---|
| 9 | 6.5 | -69.43 | -3.41 |
| 9 | 7.5 | 69.43 | -1.59 |
| 9 | 8.5 | 23.77 | 3.53 |
| 9 | 9.5 | -32.74 | 4.14 |
| 9 | 10.5 | 10.52 | -2.13 |
| 9 | 11.5 | -5.98 | -1.10 |
| 10 | 7.5 | -22.13 | -1.08 |
| 10 | 8.5 | 23.01 | -0.59 |
| 10 | 9.5 | 6.68 | 1.15 |
| 10 | 10.5 | -10.73 | 1.43 |
| 10 | 11.5 | 4.71 | -0.59 |
| 10 | 12.5 | -2.73 | -0.48 |
| 11 | 8.5 | -5.42 | -0.41 |
| 11 | 9.5 | 5.82 | -0.25 |
| 11 | 10.5 | 1.13 | 0.46 |
| 11 | 11.5 | -2.70 | 0.58 |
| 11 | 12.5 | 2.23 | -0.20 |
| 11 | 13.5 | -1.31 | -0.22 |
| 12 | 9.5 | -2.05 | -0.18 |
| 12 | 10.5 | 2.26 | -0.11 |
| 12 | 11.5 | 0.30 | 0.20 |
| 12 | 12.5 | -1.03 | 0.26 |
| 12 | 13.5 | 1.10 | -0.08 |
| 12 | 14.5 | -0.66 | -0.11 |

Therefore the product of the dipole and the octupole matrix elements for the $^2D_{3/2}$ can be related to the product of the dipole and the octupole matrix elements for the $^2D_{5/2}$, Eq. 6.21.

$$\left\langle 5^2F_{5/2}\left\|M^{[1]}\right\|6^2D_{5/2}\right\rangle\left\langle 5^2F_{5/2}\left\|M^{[3]}\right\|6^2D_{5/2}\right\rangle=\frac{\left\langle 5^2F_{5/2}\left\|M^{[1]}\right\|6^2D_{3/2}\right\rangle\left\langle 5^2F_{5/2}\left\|M^{[3]}\right\|6^2D_{3/2}\right\rangle}{\sqrt{21}} \tag{6.21}$$

This will allow for one of the octupole matrix element for the $^2D_{3/2}$ to be included in the fit of the fine structure as a parameter to be determined by the fit.

The full second order octupole-octupole energies were also calculated and determined to be negligible when compared to the dipole-octupole second order energies. For the $^2D_{3/2}$, the octupole-octupole second order energies were only approximately 0.2MHz in $L$=9 and become even smaller as $L$ increases. The second order octupole-octupole energies for the $^2D_{5/2}$ would be even smaller. The combined second order octupole-octupole energies for both excited core states would be within the uncertainty in the relative positions of the measured fine structure levels. Therefore they were neglected.

**6.2c Second order in the effective potential**

The second order energy in terms of the effective potential is necessary is due to the exclusion of intermediate states in which the core remains in its ground electronic configuration during the derivation of the effective potential. Since these excluded intermediates levels can be considered to be "Rydberg levels," this traditional correction can also be described as accounting for the energy shifts due to coupling to other Rydberg levels. In $Th^{3+}$ there are two states in the ground electronic state, the ground state, the $^2F_{5/2}$ and one excited level, the $^2F_{7/2}$, located $4325.394(12)cm^{-1}$ above the $^2F_{5/2}$ [9]. A discussion of these second order energies is included in Section 1.2 and in the work of Woods [7]. These works showed that they can be calculated for these Rydberg levels using the effective potential. The energy shifts are given by plugging the leading terms of the effective potential, Eq. 1.29 into Eq. 1.28. For the case of $Th^{3+}$, the second order energies in the effective potential has six terms, Eq. 1.30, repeated here for convenience.

$$E^{[2]}(V_{eff}) = E^{[2]}(\alpha_{D,0}\alpha_{D,0}) + E^{[2]}(\alpha_{D,2}\alpha_{D,0}) + E^{[2]}(Q\alpha_{D,0}) + E^{[2]}(QQ) + E^{[2]}(Q\alpha_{D,2}) + E^{[2]}(\alpha_{D,2}\alpha_{D,2})$$

Each of the terms in the Eq. 1.30 has to be evaluated separately and the size of the each of the terms is dependent on the core properties contained in each of the terms. The calculation of these corrections therefore has to be an iterative process, since the size of the correction is dependent on the properties of $Th^{3+}$. Initially the properties determined from the optical study were used, but the analysis of the rf results was iterated allowing for the properties determined from the rf data to be used in the determine the second order energies due to the excluded ground states. The iterative process was continued until there were no further changes to the determined core properties.

The first three terms in Eq. 1.30 are limited by selections rules $\Delta J_c = 0$ and $\Delta L = 0$ due to the presence of the scalar dipole polarizability in each of the terms. This means that for the first three terms the intermediate core state in the second order energy is the $^2F_{5/2}$ ground state, and the $^2F_{7/2}$ state does not play a role. The second order energy due to the scalar dipole polarizability, $E^{[2]}(\alpha_{D,0}\alpha_{D,0})$, Eq. 6.22 depends on the scalar dipole polarizability and the sum of the radial matrix elements of the Rydberg state of interest, $n$, and the intermediate Rydberg state, $n'$. This sum was carried out numerically using the $f_{nLZ}$ program.

$$E^{[2]}(\alpha_{D,0}\alpha_{D,0}) = -\frac{{\alpha_{D,0}}^2}{4} \times \left( \sum_{n'} \frac{\left\langle nL \left\| r^{-4} \right\| n'L \right\rangle \left\langle n'L \left\| r^{-4} \right\| nL \right\rangle}{E(n') - E(n)} \right) \tag{6.22}$$

This particular term in $E^{[2]}(V_{eff})$ has also been calculated analytically by Drake and Swainson [38] with the result given in Eq. 3.5. Similarly the second and third term of Eq. 1.30 can be calculated in terms of the core properties and sums over intermediate Rydberg states. The

second order energy due to the scalar dipole polarizability and the tensor dipole polarizability is given by Eq. 6.23 and the second order energy due to the quadrupole moment and the scalar dipole polarizability is given by Eq.6.24.

$$E^{[2]}(\alpha_{D,0}\alpha_{D,2}) = -\frac{\alpha_{D,0}\alpha_{D,2}}{2} \times \frac{\left\langle X^{[2]}(J_c)\cdot C^{[2]}(\hat{r})\right\rangle}{\begin{pmatrix} 5/2 & 2 & 5/2 \\ -5/2 & 0 & 5/2 \end{pmatrix}} \times \left( \sum_{n'} \frac{\left\langle nL \left\| r^{-4} \right\| n'L \right\rangle \left\langle n'L \left\| r^{-4} \right\| nL \right\rangle}{E(n') - E(n)} \right) \tag{6.23}$$

$$E^{[2]}(\alpha_{D,0}Q) = -\alpha_{D,0}Q \times \frac{\left\langle X^{[2]}(J_c)\cdot C^{[2]}(\hat{r})\right\rangle}{\begin{pmatrix} 5/2 & 2 & 5/2 \\ -5/2 & 0 & 5/2 \end{pmatrix}} \times \left( \sum_{n'} \frac{\left\langle nL \left\| r^{-3} \right\| n'L \right\rangle \left\langle n'L \left\| r^{-4} \right\| nL \right\rangle}{E(n') - E(n)} \right) \tag{6.24}$$

Both the second and third term of the second order energy, Eq. 6.23 and Eq. 6.24 depend on the $K$ of the state of interest, requiring that this correction be calculated for each individual state separately.

The remaining three terms in $E^{[2]}(V_{eff})$ have to account for the possibility that either the $^2F_{5/2}$ or the $^2F_{7/2}$ can be the intermediate core state. These remaining three terms of the second order energies are governed by the selections rules that $L' = L, L \pm 2$ and $J_c' = 7/2$ or $5/2$. Therefore the sum in each of the energies will not only be over $n'$, it will also be over $L'$ and $J_c'$. The second order energy due to the permanent quadrupole moment is given by Eq. 6.25 where $\left\langle gJ_c \left\| M^{[2]} \right\| gJ_c' \right\rangle$ is the reduced quadrupole moment matrix between core states and $\Delta E(gJ_c')$ is the excitation energy of the core state of interest. The permanent quadrupole moment is not used directly.

$$E^{[2]}(QQ) = -\sum_{J_c' n' L'} \begin{Bmatrix} K & L & J_c \\ 2 & J_c' & L' \end{Bmatrix}^2 \begin{pmatrix} L & 2 & L' \\ 0 & 0 & 0 \end{pmatrix}^2 (2L+1)(2L'+1)\left\langle gJ_c \left\| M^{[2]} \right\| gJ_c' \right\rangle^2 \times \left( \frac{\left\langle nL \left\| r^{-3} \right\| n'L' \right\rangle \left\langle n'L' \left\| r^{-3} \right\| nL \right\rangle}{\Delta E(gJ_c') + E(n') - E(n)} \right) \tag{6.25}$$

For the case of the $J_c' = 5/2$ the excitation energy $\Delta E(g^2F_{5/2}) = 0.0\,cm^{-1}$ and the reduced quadrupole matrix element, the diagonal reduced quadrupole matrix element, is related to the permanent quadrupole moment by Eq. 6.26.

$$\left\langle g^2F_{5/2} \left\| M^{[2]} \right\| g^2F_{5/2} \right\rangle = \frac{Q}{\begin{pmatrix} 5/2 & 2 & 5/2 \\ -5/2 & 0 & 5/2 \end{pmatrix}} = 2\sqrt{\frac{21}{5}}Q \tag{6.26}$$

For $J_c' = 7/2$ the excitation is $\Delta E(g^2F_{7/2}) = 4325.394(12)\,cm^{-1}$ [9] and assuming *LS* coupling quadrupole matrix element, the off diagonal reduced quadrupole matrix element is given by, Eq. 6.27.

$$\left\langle g^2F_{5/2} \left\| M^{[2]} \right\| g^2F_{7/2} \right\rangle = \sqrt{\frac{1}{6}}\left\langle g^2F_{5/2} \left\| M^{[2]} \right\| g^2F_{5/2} \right\rangle = \sqrt{\frac{14}{5}}Q \tag{6.27}$$

The remaining two terms in $E^{[2]}(V_{eff})$ contain either the tensor dipole polarizability and permanent quadrupole moment, Eq. 6.28 or the tensor dipole polarizability alone, Eq. 6.29. For both of these terms the intermediate states can be either $J_c' = 7/2$ or $5/2$ but careful attention must be paid to the permanent quadrupole moment and tensor dipole polarizability since their value is dependent on the identity of the intermediate state. As seen in the work with the second order quadrupole energy, Eq. 6.25, the value of the reduced quadrupole matrix depended on whether was $J_c' = 7/2$ or $J_c' = 5/2$, called the respectively the off diagonal or diagonal

reduced quadrupole matrix element. In the second order energies involving the tensor dipole polarizability a similar thing will occur, the tensor dipole polarizability will have two values depending on whether it is the diagonal ( $J_c' = 5/2$ ) or off-diagonal ( $J_c' = 7/2$ ).

$$E^{[2]}(Q\alpha_{D,2}) = -\sum_{J_c'n'L'} Q(J_c')\alpha_{D,2}(J_c') \begin{Bmatrix} K & L & J_c \\ 2 & J_c' & L' \end{Bmatrix}^2 \begin{pmatrix} L & 2 & L' \\ 0 & 0 & 0 \end{pmatrix}^2 (2L+1)(2L'+1) \times \left( \frac{\langle nL \| r^{-3} \| n'L' \rangle \langle n'L' \| r^{-4} \| nL \rangle}{\Delta E(gJ_c') + E(n') - E(n)} \right) \tag{6.28}$$

$$E^{[2]}(\alpha_{D,2}\alpha_{D,2}) = -\sum_{J_c'n'L'} \frac{\alpha_{D,2}(J_c')^2}{4} \begin{Bmatrix} K & L & J_c \\ 2 & J_c' & L' \end{Bmatrix}^2 \begin{pmatrix} L & 2 & L' \\ 0 & 0 & 0 \end{pmatrix}^2 (2L+1)(2L'+1) \times \left( \frac{\langle nL \| r^{-4} \| n'L' \rangle \langle n'L' \| r^{-4} \| nL \rangle}{\Delta E(gJ_c') + E(n') - E(n)} \right) \tag{6.29}$$

The diagonal tensor dipole polarizability, $\alpha_{D,2}(^2F_{5/2})$ is just the tensor dipole polarizability of $Th^{3+}$, $\alpha_{D,2}$ and the diagonal permanent quadrupole moment $Q(^2F_{5/2})$ is just the permanent quadrupole moment of $Th^{3+}$, $Q$.

The determination of the off diagonal tensor dipole polarizability requires more knowledge of the states contributing to the tensor dipole polarizability of $Th^{3+}$. For the case of $Th^{3+}$ theoretical estimates of the tensor dipole polarizability [45] show that almost all tensor dipole polarizability is due to the low-lying $^2D_{3/2}$ state, the total dipole polarizability is estimated at $\alpha_{D,2} = -6.166$ with $-6.206$ of that due to the $^2D_{3/2}$ state. Using Eq. 77 from Ref. [7], which simplifies to Eq. 6.30 for this case, it is possible to come up with a theoretical estimate of the off diagonal tensor dipole polarizability.

$$\alpha_{D,2}(^2F_{7/2}) = -\frac{5}{3}\sqrt{\frac{2}{7}}\sum_{\lambda'' J_c''}(-1)^{2J_c''}\begin{Bmatrix} J_c'' & 1 & 5/2 \\ 2 & 7/2 & 1 \end{Bmatrix}\frac{\left\langle g^2F_{5/2}\left\|M^{[1]}\right\|\lambda'' J_c''\right\rangle\left\langle\lambda'' J_c''\left\|M^{[2]}\right\|g^2F_{7/2}\right\rangle}{\Delta E(\lambda'' J_c'')} \tag{6.30}$$

This estimate of the off diagonal tensor dipole polarizability required theoretical estimates of the reduced dipole matrix elements [45] and knowledge of the excitation energies [13]. Table 8 in Ref. [45] gave a list of states contributing to the diagonal dipole polarizability, therefore this table was used as a guide in calculation the off diagonal dipole polarizability. This calculation showed that the $^2D_{3/2}$ state, which is responsible for almost all of the tensor dipole polarizability of $Th^{3+}$, does not contribute to the off diagonal tensor dipole polarizability since the $^2D_{3/2}$ cannot be a dipole coupled to the $^2F_{7/2}$. The main state contributing to the off-diagonal tensor dipole polarizability is the $^2D_{5/2}$. The contribution of all other excited states to the off diagonal dipole polarizability is minimal, two orders of magnitude smaller than the contribution from the $^2D_{5/2}$ state, so their contributions were neglected. The off diagonal tensor dipole polarizability was therefore calculated using the theoretical matrix element coupling the ground state to the $^2D_{5/2}$, presented in Ref. [45], with the sign of the matrix element determined from assuming *LS* coupling. This resulted in the determination of $\alpha_{D,2}(^2F_{7/2}) = -1.6 \pm 1.6$ with the error placed on the parameter reflecting the reliance on theoretical matrix elements and the fact that the $^2D_{5/2}$ is a state may not be well described by the adiabatic model.

The calculation of all six terms in $E^{[2]}(V_{eff})$ was carried out for all of states in the $n$=28 $Th^{2+}$ Rydberg fine structure, $L$=9 to 12, the results of which are shown in Table 6.7. The values shown are the final results of the iterative process described earlier, i.e. they were calculated using the core parameter determined from the rf measurements. The theoretical estimate of the

off diagonal tensor dipole polarizability was used without adjustment in the fitting process. In addition each of these calculated terms in $E^{[2]}(V_{eff})$ relied on a combination of 3J symbols, 6J symbols and the sums over the intermediate Rydberg states. The sums over the intermediate Rydberg states were carried out using the $f_{nLZ}$ program, which is effectively exact for this purpose. The $E^{[2]}(\alpha_{D,0}\alpha_{D,0})$ term was also calculated using Eq. 3.5, which is an analytic formula for this term, the difference in the two different calculation of this term was in the fifth digit, further confirming the accuracy of the $f_{nLZ}$ program used to carry out the sum over $n'$. Table 6.7 shows each of the components in the $E^{[2]}(V_{eff})$ and the contributions to the $E^{[2]}(V_{eff})$ from each intermediate core states for each of the states. From this table it can be seen that the largest $E^{[2]}(V_{eff})$ correction is in the $L$=9 states is on the order of one to ten MHz and decreases to less than one MHz in the $L$=12 states. Table 6.7 also show that the contribution to the total $E^{[2]}(V_{eff})$ due to the terms having to do with the off diagonal tensor dipole polarizability is less than one MHz for the $L$=9 states and less than a tenth of MHz. for the $L$=12 states.

Table 6.7: The second order energies in the effective potential for the $Th^{2+}$ Rydberg fine structure broken down into components. Column one identifies the state by (*L*, *K*), column two gives the intermediate core state and column three through eight gives the second order energy for each of the different components. Column nine gives the total second order energy. All energies are in MHz.

| *(L, K)* | | $\alpha_{D,0}\alpha_{D,0}$ | $Q\alpha_{D,0}$ | QQ | $\alpha_{D,0}\alpha_{D,2}$ | $Q\alpha_{D,2}$ | $\alpha_{D,2}\alpha_{D,2}$ | Total |
|---|---|---|---|---|---|---|---|---|
| (9, 6.5) | $^2F_{5/2}$ | -4.52 | 5.69 | -0.17 | -1.86 | 0.28 | -0.05 | -1.09 |
| | $^2F_{7/2}$ | | | -0.35 | | -0.11 | -0.01 | |
| (9, 7.5) | $^2F_{5/2}$ | -4.52 | 0.57 | 3.72 | -0.19 | -2.05 | 0.33 | -2.57 |
| | $^2F_{7/2}$ | | | -0.34 | | -0.09 | -0.01 | |
| (9, 8.5) | $^2F_{5/2}$ | -4.52 | -3.02 | 2.98 | 0.99 | -1.66 | 0.29 | -4.45 |
| | $^2F_{7/2}$ | | | 0.31 | | 0.17 | 0.02 | |
| (9, 9.5) | $^2F_{5/2}$ | -4.52 | -4.26 | -0.51 | 1.39 | 0.23 | 0.00 | -5.99 |
| | $^2F_{7/2}$ | | | 1.12 | | 0.50 | 0.05 | |
| (9, 10.5) | $^2F_{5/2}$ | -4.52 | -2.21 | -3.72 | 0.72 | 1.89 | -0.26 | -6.22 |
| | $^2F_{7/2}$ | | | 1.26 | | 0.57 | 0.06 | |
| (9, 11.5) | $^2F_{5/2}$ | -4.52 | 4.14 | -3.25 | -1.35 | 1.76 | -0.25 | -4.25 |
| | $^2F_{7/2}$ | | | -0.57 | | -0.20 | -0.02 | |
| (10, 7.5) | $^2F_{5/2}$ | -1.47 | 2.25 | 0.04 | -0.59 | 0.06 | -0.01 | 0.02 |
| | $^2F_{7/2}$ | | | -0.20 | | -0.06 | 0.00 | |
| (10, 8.5) | $^2F_{5/2}$ | -1.47 | 0.16 | 2.03 | -0.04 | -0.90 | 0.12 | -0.23 |
| | $^2F_{7/2}$ | | | -0.11 | | -0.02 | 0.00 | |
| (10, 9.5) | $^2F_{5/2}$ | -1.47 | -1.26 | 1.53 | 0.33 | -0.68 | 0.09 | -0.93 |
| | $^2F_{7/2}$ | | | 0.38 | | 0.13 | 0.01 | |
| (10, 10.5) | $^2F_{5/2}$ | -1.47 | -1.71 | -0.35 | 0.45 | 0.14 | 0.00 | -1.68 |
| | $^2F_{7/2}$ | | | 0.94 | | 0.31 | 0.02 | |
| (10,11.5) | $^2F_{5/2}$ | -1.47 | -0.85 | -2.01 | 0.22 | 0.82 | -0.09 | -2.03 |
| | $^2F_{7/2}$ | | | 0.99 | | 0.32 | 0.03 | |
| (10, 12.5) | $^2F_{5/2}$ | -1.47 | 1.69 | -1.73 | -0.44 | 0.76 | -0.09 | -1.73 |
| | $^2F_{7/2}$ | | | -0.34 | | -0.10 | -0.01 | |

Table 6.7 continue

| *(L, K)* | | $\alpha_{D,0}\alpha_{D,0}$ | $Q\alpha_{D,0}$ | QQ | $\alpha_{D,0}\alpha_{D,2}$ | $Q\alpha_{D,2}$ | $\alpha_{D,2}\alpha_{D,2}$ | Total |
|---|---|---|---|---|---|---|---|---|
| (11, 8.5) | $^2F_{5/2}$ | -0.53 | 0.97 | 0.09 | -0.21 | 0.00 | 0.00 | 0.19 |
| | $^2F_{7/2}$ | | | -0.10 | | -0.02 | 0.00 | |
| (11, 9.5) | $^2F_{5/2}$ | -0.53 | 0.05 | 1.17 | -0.01 | -0.42 | 0.04 | 0.30 |
| | $^2F_{7/2}$ | | 0.00 | -0.01 | | 0.00 | 0.00 | |
| (11, 10.5) | $^2F_{5/2}$ | -0.53 | -0.56 | 0.84 | 0.12 | -0.30 | 0.03 | 0.01 |
| | $^2F_{7/2}$ | | | 0.32 | | 0.08 | 0.01 | |
| (11,11.5) | $^2F_{5/2}$ | -0.53 | -0.74 | -0.24 | 0.16 | 0.08 | 0.00 | -0.41 |
| | $^2F_{7/2}$ | | | 0.68 | | 0.17 | 0.01 | |
| (11, 12.5) | $^2F_{5/2}$ | -0.53 | -0.35 | -1.15 | 0.08 | 0.39 | -0.04 | -0.71 |
| | $^2F_{7/2}$ | | | 0.70 | | 0.18 | 0.01 | |
| (11, 13.5) | $^2F_{5/2}$ | -0.53 | 0.75 | -0.97 | -0.16 | 0.35 | -0.03 | -0.83 |
| | $^2F_{7/2}$ | | | -0.19 | | -0.05 | 0.00 | |
| (12, 9.5) | $^2F_{5/2}$ | -0.21 | 0.45 | 0.08 | -0.08 | -0.01 | 0.00 | 0.18 |
| | $^2F_{7/2}$ | | | -0.05 | | -0.01 | 0.00 | |
| (12, 10.5) | $^2F_{5/2}$ | -0.21 | 0.01 | 0.70 | 0.00 | -0.21 | 0.02 | 0.32 |
| | $^2F_{7/2}$ | | | 0.01 | | 0.00 | 0.00 | |
| (12,11.5) | $^2F_{5/2}$ | -0.21 | -0.27 | 0.48 | 0.05 | -0.14 | 0.01 | 0.14 |
| | $^2F_{7/2}$ | | | 0.18 | | 0.04 | 0.00 | |
| (12, 12.5) | $^2F_{5/2}$ | -0.21 | -0.35 | -0.16 | 0.06 | 0.04 | 0.00 | -0.16 |
| | $^2F_{7/2}$ | | | 0.36 | | 0.08 | 0.00 | |
| (12, 13.5) | $^2F_{5/2}$ | -0.21 | -0.16 | -0.69 | 0.03 | 0.19 | -0.01 | -0.40 |
| | $^2F_{7/2}$ | | | 0.36 | | 0.08 | 0.00 | |
| (12, 14.5) | $^2F_{5/2}$ | -0.21 | 0.35 | -0.57 | -0.06 | 0.17 | -0.01 | -0.44 |
| | $^2F_{7/2}$ | | | -0.09 | | -0.02 | 0.00 | |

The only problem with calculating the $E^{[2]}(V_{eff})$ this way is that it assumes that all the states contributing to the properties, such as the scalar and tensor dipole polarizabilities, are valid in the adiabatic expansion. The result of the optical study of the $Th^{2+}$ Rydberg fine structure study, Table 4.5, showed that the almost all of the tensor dipole polarizability and a third of the scalar dipole polarizability is due to the $^2D_{3/2}$. The $^2D_{3/2}$ is low-lying and not adequately described by the adiabatic expansion, therefore the calculation of the $E^{[2]}(V_{eff})$ using the properties of $Th^{3+}$ most likely underestimates the contributes from the $^2D_{3/2}$. Close examination of Table 6.7 shows that the three dominant terms in the $E^{[2]}(V_{eff})$ are the $QQ$, the $Q\alpha_{D,0}$ and the $\alpha_{D,0}\alpha_{D,0}$. The $QQ$ term of $E^{[2]}(V_{eff})$ is not dependent on the properties that are susceptible to the failure of the adiabatic expansion so the calculation of this term shown in Table 6.7 is correct. The calculation of the other two dominant terms, the $Q\alpha_{D,0}$ and the $\alpha_{D,0}\alpha_{D,0}$, in Table 6.7 are suspect given that the scalar dipole polarizability contains a large contribution from the $^2D_{3/2}$.

The total scalar dipole polarizability, $\alpha_{D,0}(Total)$, can be thought of in two parts, the part due to the low-lying $^2D_{3/2}$, $\alpha_{D,0}(^2D_{3/2})$ and the part due to everything else, $\alpha_{D,0}(Else)$.

$$\alpha_{D,0}(Total) = \alpha_{D,0}(Else) + \alpha_{D,0}(^2D_{3/2}) \tag{6.31}$$

If the scalar dipole polarizability is thought of this way then the $E^{[2]}(Q\alpha_{D,0})$ will have two terms and the $E^{[2]}(\alpha_{D,0}\alpha_{D,0})$ will have three terms. Only terms containing $\alpha_{D,0}(^2D_{3/2})$ will be affected by the failure of the adiabatic expansion for the low-lying $^2D_{3/2}$. Table 6.8 shows the breakdown for the terms in $E^{[2]}(Q\alpha_{D,0})$ and $E^{[2]}(\alpha_{D,0}\alpha_{D,0})$, assuming the adiabatic expansion is adequate.

Table 6.8: The breakdown of the $E^{[2]}(\alpha_{D,0}\alpha_{D,0})$ and $E^{[2]}(Q\alpha_{D,0})$ assuming the adequacy of the adiabatic expansion. All units are MHz.

| $L$ | $K$ | $\alpha_{D,0}(Else)^2$ | $\alpha_{D,0}(Else)\alpha_{D,0}(^2D_{3/2})$ | $\alpha_{D,0}(^2D_{3/2})^2$ | $Q\alpha_{D,0}(Else)$ | $Q\alpha_{D,0}(^2D_{3/2})$ |
|---|---|---|---|---|---|---|
| 9 | 6.5 | -1.84 | -2.09 | -0.59 | 3.63 | 2.06 |
| 9 | 7.5 | -1.84 | -2.09 | -0.59 | 0.36 | 0.21 |
| 9 | 8.5 | -1.84 | -2.09 | -0.59 | -1.93 | -1.09 |
| 9 | 9.5 | -1.84 | -2.09 | -0.59 | -2.72 | -1.54 |
| 9 | 10.5 | -1.84 | -2.09 | -0.59 | -1.41 | -0.80 |
| 9 | 11.5 | -1.84 | -2.09 | -0.59 | 2.64 | 1.50 |
| 10 | 7.5 | -0.60 | -0.68 | -0.19 | 1.44 | 0.81 |
| 10 | 8.5 | -0.60 | -0.68 | -0.19 | 0.10 | 0.06 |
| 10 | 9.5 | -0.60 | -0.68 | -0.19 | -0.80 | -0.45 |
| 10 | 10.5 | -0.60 | -0.68 | -0.19 | -1.09 | -0.62 |
| 10 | 11.5 | -0.60 | -0.68 | -0.19 | -0.54 | -0.31 |
| 10 | 12.5 | -0.60 | -0.68 | -0.19 | 1.08 | 0.61 |
| 11 | 8.5 | -0.21 | -0.24 | -0.07 | 0.62 | 0.35 |
| 11 | 9.5 | -0.21 | -0.24 | -0.07 | 0.03 | 0.02 |
| 11 | 10.5 | -0.21 | -0.24 | -0.07 | -0.36 | -0.20 |
| 11 | 11.5 | -0.21 | -0.24 | -0.07 | -0.47 | -0.27 |
| 11 | 12.5 | -0.21 | -0.24 | -0.07 | -0.23 | -0.13 |
| 11 | 13.5 | -0.21 | -0.24 | -0.07 | 0.48 | 0.27 |
| 12 | 9.5 | -0.08 | -0.09 | -0.03 | 0.29 | 0.16 |
| 12 | 10.5 | -0.08 | -0.09 | -0.03 | 0.01 | 0.01 |
| 12 | 11.5 | -0.08 | -0.09 | -0.03 | -0.17 | -0.10 |
| 12 | 12.5 | -0.08 | -0.09 | -0.03 | -0.22 | -0.13 |
| 12 | 13.5 | -0.08 | -0.09 | -0.03 | -0.10 | -0.06 |
| 12 | 14.5 | -0.08 | -0.09 | -0.03 | 0.23 | 0.13 |

To completely understand the effect of the failure of the adiabatic expansion on the terms in $E^{[2]}(V_{eff})$, dependent on $\alpha_{D,0}(^2D_{3/2})$, these coupling would need to be calculated without use of the adiabatic expansion. The full coupling could then be compared to the coupling determined assuming the adiabatic expansion. The full scalar dipole-dipole coupling is given by Eq. 6.32 and the adiabatic scalar dipole coupling is given by Eq. 6.33.

$$V\left(Full\right)_{scalar\,dipole}=\sum_{L'=L\pm1}\frac{(2L'+1)}{18}\begin{pmatrix}L & 1 & L'\\ 0 & 0 & 0\end{pmatrix}^2\left\langle gJc\left\|M^{[1]}\right\|\lambda' J_c'\right\rangle^2$$

$$\times\sum_{n'}\frac{\left\langle nL\left\|r^{-2}\right\|n'L'\right\rangle\left\langle n'L'\left\|r^{-2}\right\|n''L\right\rangle}{\left[\Delta E(\lambda' J_c')+E(n')-E(n)\right]} \tag{6.32}$$

$$V(adiabatic)_{scalar\,dipole}=\left\langle nL\left\|\frac{\alpha_{D,0}}{2}r^{-4}\right\|n''L\right\rangle \tag{6.33}$$

Eq. 6.32 contains a sum over $n'$ that would simplify to Eq. 6.33 if the adiabatic expansion was applied to Eq. 6.32 and completeness relations were used [7].

Figure 6.2 gives the ratio of the full coupling to the adiabatic coupling for a range of $n''$. A modified form of the $f_{nLZ}$ program was used to complete the sum in the Eq. 6.32 so that the couplings could be compared. This comparison showed that the adiabatic coupling might underestimate the actual coupling by a factor between one and five depending on the $n''$.

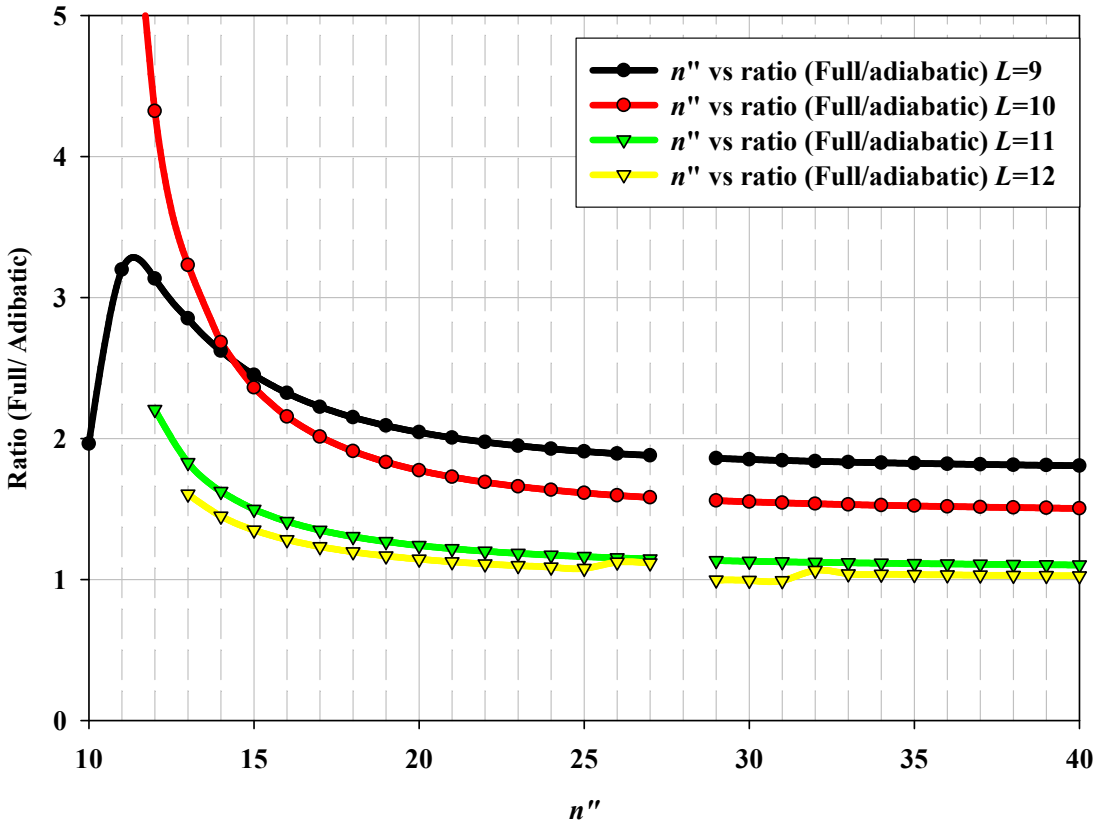


Figure 6.2: Ratio of the full coupling to the adiabatic coupling plotted versus $n''$. Each of the line represents the ratio for a different $L$. On this plot is the ratio for $L$=9, 10, 11 and 12 is shown.

This means that the contributions from specific $n''$ to $E^{[2]}(Q\alpha_{D,0})$ due to the $^2D_{3/2}$ might be underestimated by up to a factor of one to five depending on which $n''$. Since the contributions of a specific $n''$ to $E^{[2]}(\alpha_{D,0}\alpha_{D,0})$ is related to the coupling squared this means that for a specific $n''$ the contributions to $E^{[2]}(\alpha_{D,0}\alpha_{D,0})$ might be underestimated by as much as a factor of one to twenty-five depending on $n''$. As $L$ increases the discrepancy between Eq. 6.32 and Eq. 6.33 becomes smaller, for $n''$=40 the ratio between the two is smaller than two for all $L$s. These calculations can be used to improve upon the calculations of the term in $E^{[2]}(V_{eff})$ that depends on the scalar dipole polarizability due to the low-lying $^2D_{3/2}$ state.

To start with the $E^{[2]}(\alpha_{D,0}\alpha_{D,0})$ was recalculated, since the scalar dipole polarizability has two parts there will be three term in this calculation.

$$E^{[2]}\left(\alpha_{D,0}(Total)^2\right) = E^{[2]}\left(\alpha_{D,0}(Else)^2\right) + E^{[2]}\left(\alpha_{D,0}(Else)\alpha_{D,0}(^2D_{3/2})\right) + E^{[2]}\left(\alpha_{D,0}(^2D_{3/2})^2\right)$$

The first term will not be affected by the failure of the adiabatic expansion. The other two terms will be affected though since they are dependent on the scalar dipole polarizability from the low-lying $^2D_{3/2}$ state. Using the full scalar dipole coupling, Eq. 6.32 it is possible to recalculate those terms without using the adiabatic expansion for $n''$ up to 40. To estimate the contributions from the states above $n''$=40 the ratio between the full coupling, Eq. 6.32, and the adiabatic coupling, Eq. 6.33, was examined for $n''$ up to 40. It was assumed that this ratio remained constant for $n''$>40. The adiabatic contribution for $n''$>40 was then multiplied by the estimated factor between the full coupling and the adiabatic coupling and added to the part from the discrete sum of $n''$ up to 40. The ration between the full coupling and the adiabatic coupling was estimated from Fig. 6.2, by estimating the value it seems to be converging to. A conservative error was placed on each of factors equal to the half of its deviation from one. For example, from Fig. 6.2, the ratio for $L$=9 was estimated to be 1.8(4). For $L$=9, $E^{[2]}\left(\alpha_{D,0}(^2D_{3/2})^2\right)$ was estimated from the discrete sum of states up to $n''$=40 using the full coupling to be $5.22MHz$ as shown in Table 6.9. The adiabatic contribution from states above $n''$=40 was $-1.53MHz$, so to account for the states higher than 40 the adiabatic result was multiplied by factor 1.8(4) squared and added to the part from the discrete sum, as shown in Table 6.9. The factor was squared since $E^{[2]}\left(\alpha_{D,0}(^2D_{3/2})^2\right)$ depends on the full scalar dipole coupling squared.

Following this procedure each of the terms in $E^{[2]}(\alpha_{D,0}\alpha_{D,0})$ and $E^{[2]}(Q\alpha_{D,0})$ affected by the failure of the adiabatic expansion were recalculated. The breakdown of each of the

recalculated terms contributing to $E^{[2]}(\alpha_{D,0}\alpha_{D,0})$ and $E^{[2]}(Q\alpha_{D,0})$ is shown in Table 6.10. When this compared to the result in Table in 6.8 it can be seen that the result are only slightly different than what was found from assuming the adequacy of the adiabatic expansion.

Table 6.9: The calculation of $E^{[2]}\left(\alpha_{D,0}(^2D_{3/2})^2\right)$ with the full coupling , the first column gives the L. The second column gives the contribution summing states up to $n''$=40, the third column gives the contribution from states n″>40, assuming the adiabatic expansion. The fourth column gives the estimated factor between the full coupling and the adiabatic coupling for n″>40. The fifth column gives the total $E^{[2]}\left(\alpha_{D,0}(^2D_{3/2})^2\right)$ and its uncertainty. The unit on all of the energies is MHz.

| $L$ | $E^{[2]}\left(\alpha_{D,0}(^2D_{3/2})^2\right)$ up to $n''$=40 | Adiabatic contribution from states $n''$>40 | Factor | $E^{[2]}\left(\alpha_{D,0}(^2D_{3/2})^2\right)$ (Full coupling) |
|---|---|---|---|---|
| 9 | 5.217 | -1.528 | 1.8(4) | 0.27(1.96) |
| 10 | 1.406 | -0.468 | 1.50(25) | 0.35(32) |
| 11 | 0.168 | -0.156 | 1.10(5) | -0.02(2) |
| 12 | 0.052 | -0.050 | 1.030(15) | -0.002(2) |

Given the effect on the dominant terms of the $E^{[2]}(V_{eff})$ it was deemed unnecessary to recalculate the remaining terms in $E^{[2]}(V_{eff})$ that depend on the properties that have contribution from the low-lying $^2D_{3/2}$ state. The other low-lying state, the $^2D_{5/2}$ , was also neglected due to the fact the effect of that state would be even smaller than the effect of the $^2D_{3/2}$. The total values of $E^{[2]}(V_{eff})$ used to correct the measured fine structure are shown in the Table 6.11. The uncertainty in each is the result of the quadrature sum of the uncertainties in each recalculations of $E^{[2]}(\alpha_{D,0}\alpha_{D,0})$ and $E^{[2]}(Q\alpha_{D,0})$.

Table 6.10: The breakdown of the corrected $E^{[2]}(\alpha_{D,0}\alpha_{D,0})$ and $E^{[2]}(Q\alpha_{D,0})$ correcting for the inadequacy of the adiabatic expansion. All units are MHz.

| $L$ | $K$ | $\alpha_{D,0}(Else)^2$ | $\alpha_{D,0}(Else)\alpha_{D,0}(^2D_{3/2})$ | $\alpha_{D,0}(^2D_{3/2})^2$ | $Q\alpha_{D,0}(Else)$ | $Q\alpha_{D,0}(^2D_{3/2})$ |
|---|---|---|---|---|---|---|
| 9 | 6.5 | -1.84 | -2.03(2.16) | 0.27(1.96) | 3.63 | 1.42(2.60) |
| 9 | 7.5 | -1.84 | -2.03(2.16) | 0.27(1.96) | 0.36 | 0.14(26) |
| 9 | 8.5 | -1.84 | -2.03(2.16) | 0.27(1.96) | -1.93 | -0.75(1.38) |
| 9 | 9.5 | -1.84 | -2.03(2.16) | 0.27(1.96) | -2.72 | -1.06(1.95) |
| 9 | 10.5 | -1.84 | -2.03(2.16) | 0.27(1.96) | -1.41 | -0.55(1.01) |
| 9 | 11.5 | -1.84 | -2.03(2.16) | 0.27(1.96) | 2.64 | 1.03(1.89) |
| 10 | 7.5 | -0.60 | -0.35(41) | 0.35(32) | 1.44 | 0.18(60) |
| 10 | 8.5 | -0.60 | -0.35(41) | 0.35(32) | 0.10 | 0.01(4) |
| 10 | 9.5 | -0.60 | -0.35(41) | 0.35(32) | -0.80 | -0.10(33) |
| 10 | 10.5 | -0.60 | -0.35(41) | 0.35(32) | -1.09 | -0.14(45) |
| 10 | 11.5 | -0.60 | -0.35(41) | 0.35(32) | -0.54 | -0.07(22) |
| 10 | 12.5 | -0.60 | -0.35(41) | 0.35(32) | 1.08 | 0.13(45) |
| 11 | 8.5 | -0.21 | -0.18(3) | -0.02(2) | 0.62 | 0.22(5) |
| 11 | 9.5 | -0.21 | -0.18(3) | -0.02(2) | 0.03 | 0.011(2) |
| 11 | 10.5 | -0.21 | -0.18(3) | -0.02(2) | -0.36 | -0.13(3) |
| 11 | 11.5 | -0.21 | -0.18(3) | -0.02(2) | -0.47 | -0.17(3) |
| 11 | 12.5 | -0.21 | -0.18(3) | -0.02(2) | -0.23 | -0.08(2) |
| 11 | 13.5 | -0.21 | -0.18(3) | -0.02(2) | 0.48 | 0.17(4) |
| 12 | 9.5 | -0.08 | -0.054(3) | -0.002(2) | 0.29 | 0.062(6) |
| 12 | 10.5 | -0.08 | -0.054(3) | -0.002(2) | 0.01 | 0.002(2) |
| 12 | 11.5 | -0.08 | -0.054(3) | -0.002(2) | -0.17 | -0.037(3) |
| 12 | 12.5 | -0.08 | -0.054(3) | -0.002(2) | -0.22 | -0.048(4) |
| 12 | 13.5 | -0.08 | -0.054(3) | -0.002(2) | -0.10 | -0.022(2) |
| 12 | 14.5 | -0.08 | -0.054(3) | -0.002(2) | 0.23 | 0.049(4) |

Table 6.11: The total values of $E^{[2]}(V_{eff})$ applied to the measured fine structure as a correction. The first and second column identifies the state. The the third column gives the total $E^{[2]}(V_{eff})$ with its uncertainty for each state. The unit of $E^{[2]}(V_{eff})$ is MHz.

| $L$ | $K$ | $E^{[2]}(V_{eff})$ |
|---|---|---|
| 9 | 6.5 | -0.82 (3.90) |
| 9 | 7.5 | -1.72 (2.92) |
| 9 | 8.5 | -3.20 (3.22) |
| 9 | 9.5 | -4.59 (3.50) |
| 9 | 10.5 | -5.06 (3.08) |
| 9 | 11.5 | -3.81 (3.47) |
| 10 | 7.5 | 0.26 (0.79) |
| 10 | 8.5 | 0.60 (0.53) |
| 10 | 9.5 | 0.30 (0.62) |
| 10 | 10.5 | -0.32 (0.69) |
| 10 | 11.5 | -0.92 (0.57) |
| 10 | 12.5 | -1.33 (0.69) |
| 11 | 8.5 | 0.17 (0.06) |
| 11 | 9.5 | 0.40 (0.03) |
| 11 | 10.5 | 0.20 (0.04) |
| 11 | 11.5 | -0.19 (0.05) |
| 11 | 12.5 | -0.55 (0.04) |
| 11 | 13.5 | -0.82 (0.05) |
| 12 | 9.5 | 0.14 (0.01) |
| 12 | 10.5 | 0.38 (0.00) |
| 12 | 11.5 | 0.27 (0.00) |
| 12 | 12.5 | -0.02 (0.01) |
| 12 | 13.5 | -0.30 (0.00) |
| 12 | 14.5 | -0.46 (0.01) |

### 6.2d Tensor coupling

An additional effect that can contribute to the fine structure is tensor coupling between states of the same $n$. This contribution to the fine structure was not calculated in the optical measurements, but preliminary rf measurements show the importance of accounting for this

effect. In the search for the rf transitions in the $n$=28 $Th^{2+}$ Rydberg fine structure it was found that the $L$=9 $K$=9.5 to $L$=10 $K$=10.5 rf transitions was ninety-three MHz higher than the predicted location. Examination of the estimated $Th^{2+}$ Rydberg fine structure showed that the $L$=7 $K$=9.5 was very close to the $L$=9 $K$=9.5, within approximately six hundred MHz, suggesting that these two states were coupling and shifting each other. The coupling between these two states would need to observe the selection rules $\Delta n = 0$ and $\Delta L = 2$. Therefore, the most likely candidate for the cause of this coupling is due tensor coupling between the states. The primary source of tensor coupling is due to the tensor dipole polarizability, since the quadrupole coupling is zero due to the selection rule satisfied by hydrogenic radial functions, $\left\langle n, L \left\| r^{-3} \right\| n, L \pm 2 \right\rangle = 0$. The coupling strength between the two states can therefore be estimated by the tensor dipole polarizability term of the effective potential, Eq. 6.34.

$$V = -\frac{\alpha_{D,2}}{2r^4} \times \frac{X^{[2]}(J_c) \cdot C^{[2]}(\hat{r})}{\begin{pmatrix} J_c & 2 & J_c \\ -J_c & 0 & J_c \end{pmatrix}} \tag{6.34}$$

The shift of the state by this tensor dipole polarizability coupling, $E(\alpha_{D,2} shift)$, would be the coupling strength between the two states squared divided by the energy difference between the two states, Eq. 6.35.

$$E(\alpha_{D,2} shift) = \frac{\left| \left\langle nL_K \left| V \right| nL'_K \right\rangle \right|^2}{\Delta E} \tag{6.35}$$

The sign of the shift is determined by the relative locations of the two states and the size of the shift is dependent on the size of the tensor dipole polarizability and the separation of the two states. To determine the size of the possible shift of the $L$=9 $K$=9.5 state from the $L$=7 $K$=9.5, Eq. 6.34 was used to estimate the coupling strength between the two states, 215MHz, using the

theoretical estimate of the total tensor dipole polarizability, $\alpha_{D,2} = -6.22$ [45]. Given the energy separation between the two states is approximately six hundred MHz, Eq. 6.35 determines the shift of the $L$=9 $K$=9.5 state by the $L$=7 $K$=9.5 to be seventy-seven MHz, which is close to the observed ninety-three MHz. The $L$=7 $K$=9.5 would shift the $L$=9 $K$=9.5 downward, increasing the $L$=9 $K$=9.5 to $L$=10 $K$=10.5 rf interval, which is what was observed. The only problem with this calculation is the use of Eq. 6.34 to determine the coupling strength between the states. The theoretical estimates of the tensor dipole polarizability [45] showed that all of the tensor dipole polarizability is due to the low-lying $^2D_{3/2}$ state, which is not adequately described by the effective potential. Therefore the use of the tensor dipole polarizability term of the effective potential, Eq. 6.34, to estimate the coupling strength between the two states is most likely not valid and could lead to an underestimate of the coupling occurring between the two states.

Therefore, a different approach to calculate the coupling potential between two states in the $n$=28 fine structure had to be used. One that did not rely on anything derived using the adiabatic expansion. The tensor dipole coupling between two states was derived without the use of the adiabatic expansion, starting with Eq. 6.36

$$V = -\sum_{\substack{n'L' \\ \lambda' J_c'}} \frac{\left\langle gJ_c nL_K'' \left| M^{[1]} \cdot \frac{C^{[1]}}{r^2} \right| \lambda' J_c' n' L_K' \right\rangle \left\langle \lambda' J_c' n' L_K' \left| M^{[1]} \cdot \frac{C^{[1]}}{r^2} \right| gJ_c nL_K \right\rangle}{\Delta E(\lambda' J_c') + E(n') - E(n)} \tag{6.36}$$

which simplifies into Eq. 6.37 using [50].

$$V = (-1)^{J_c + J_c'} (2L'+1)\sqrt{(2L+1)(2L''+1)} \begin{Bmatrix} K & L'' & J_c'' \\ 1 & J_c' & L' \end{Bmatrix} \begin{Bmatrix} K & L' & J_c' \\ 1 & J_c & L \end{Bmatrix} \begin{pmatrix} L'' & 1 & L' \\ 0 & 0 & 0 \end{pmatrix} \begin{pmatrix} L' & 1 & L \\ 0 & 0 & 0 \end{pmatrix}$$

$$\times \left\langle gJ_c \left\| M^{[1]} \right\| \lambda' J_c' \right\rangle \left\langle \lambda' J_c' \left\| M^{[1]} \right\| gJ_c \right\rangle \frac{\left\langle nL'' \left\| r^{-2} \right\| n'L' \right\rangle \left\langle n'L' \left\| r^{-2} \right\| nL \right\rangle}{\Delta E(\lambda' J_c') + E(n') - E(n)} \tag{6.37}$$

The specific case of the tensor coupling that is occurring in the our rf measurements is $n'' = n$, $J_c'' = J_c = 5/2$, and $L' = L \pm 1$ $L'' = L \pm 2$ Since almost all of the tensor dipole polarizability is due to the $^2D_{3/2}$, the intermediate core state was taken to be the $^2D_{3/2}$, $J_c' = 3/2$. In Eq. 6.37 everything can be calculated up to a constant, the dipole matrix element that couples the ground state, $^2F_{5/2}$, to the low-lying, $^2D_{3/2}$ state. As with the other correction that rely on the matrix elements between the ground state and the low-lying states, initially the theoretical value of the dipole matrix element was used in the calculation of this coupling potential. A modified version of $f_{nLZ}$ was used to complete the sum in Eq. 6.37, given the previous testing of the $f_{nLZ}$ program the possibility of an uncertainty in the sum was the neglected.

With the tensor coupling known, the shift of each energy level due to the tensor coupling was calculated as the tensor coupling squared divided the energy difference between the two states, Eq. 6.35. The major source of the uncertainty in these calculated shifts is the uncertainty in the positions of the levels with respect to each other. The positions of only some of the levels have been measured experimentally with sub-MHz precision, the five out of six levels in the $L$=9, 10, 11, and 12. Therefore the relative positions of some of levels was reliant on a simulation of the $n$=28 $Th^{2+}$ Rydberg fine structure, to be conservative an error was placed on each of the simulated energy intervals of 100MHz. Table 6.12 shows the shift to each of the measured states in MHz due to the tensor coupling.

These shifts were calculated assuming the calculated dipole matrix element coupling the ground state and the $^2D_{3/2}$. The sign of the shift is determined by the relative position of the levels with respect to each other. Unlike the other correction due to the low-lying states this shifts is proportional to the fourth power of the dipole matrix element between the ground state and the $^2D_{3/2}$. The uncertainty placed on each of the shifts will have to be taken in to account

during the fitting of the measured fine structure. The calculated shift of the $n$=28, $L$=9 $K$=9.5 level using the theoretical estimate of the dipole matrix element [45], is -169(26)MHz. This substantially larger than the estimate derived from use of the adiabatic value of the tensor dipole polarizability, -77MHz and also larger than the apparent -93MHz shift of the (9, 9.5) to (10, 10.5) rf resonance compared to the initial estimate based on the optical results.

Table 6.12: The shifts due to the tensor coupling of states in the $n$=28 Rydberg fine structure. The theoretical value of the $^2D_{3/2}$ matrix element was assumed during the calculation, 1.53a.u. The energies are in MHz.

| $L$ | $K$ | $E$ ($\alpha_{D,2}$ shift) (MHz) |
|---|---|---|
| 9 | 6.5 | 3.95 (0.04) |
| 9 | 7.5 | 10.11 (0.10) |
| 9 | 8.5 | 17.76 (0.25) |
| 9 | 9.5 | -169.22 (26.23) |
| 9 | 10.5 | -3.98 (0.02) |
| 9 | 11.5 | 3.27 (0.21) |
| 10 | 7.5 | 1.20 (0.01) |
| 10 | 8.5 | 3.59 (0.05) |
| 10 | 9.5 | 8.57 (0.26) |
| 10 | 10.5 | -15.13 (0.97) |
| 10 | 11.5 | -2.48 (0.02) |
| 10 | 12.5 | 1.17 (0.08) |
| 11 | 8.5 | 0.43 (0.00) |
| 11 | 9.5 | 1.32 (0.00) |
| 11 | 10.5 | 3.82 (0.03) |
| 11 | 11.5 | -3.74 (0.23) |
| 11 | 12.5 | -1.69 (0.24) |
| 11 | 13.5 | 0.52 (0.04) |
| 12 | 9.5 | 0.24 (0.00) |
| 12 | 10.5 | 0.75 (0.00) |
| 12 | 11.5 | 2.39 (0.03) |
| 12 | 12.5 | -1.45 (0.10) |
| 12 | 13.5 | -1.25 (0.28) |
| 12 | 14.5 | 0.25 (0.02) |

### 6.3 Extraction of properties of $Th^{3+}$

The fitting of the $Th^{2+}$ Rydberg fine structure offers the opportunity to the gain more knowledge on $Th^{3+}$. This process of fitting the measured fine structure and extracting the properties of $Th^{3+}$ had to take into account all of the effects mentioned in Section 6.2. These effects were either added to the model being used to fit the data or applied as corrections to the measured fine structure. The model being used to fit the $Th^{2+}$ fine structure was discussed in Section 6.1, this model is shown in Eq. 6.38 with a few slight modifications.

$$E_{Corrected} = C + A_0(L) + A_1(L)(\vec{L}\cdot\vec{J}_c) + A_2(L)\frac{X^{[2]}(J_c)\cdot C^{[2]}(\hat{r})}{\begin{pmatrix} J_c & 2 & J_c \\ -J_c & 0 & J_c \end{pmatrix}} +$$

$$+A_3(L)X^{[3]}(J_c)\cdot T^{[3]}(\hat{r}) + A_4(L)\frac{X^{[4]}(J_c)\cdot C^{[4]}(\hat{r})}{\begin{pmatrix} J_c & 4 & J_c \\ -J_c & 0 & J_c \end{pmatrix}}$$

$$+\left|\left\langle 5^2F_{5/2}\left\|M^{[1]}\right\|6^2D_{3/2}\right\rangle\right|^2\left(E^{[2]}(^2D_{3/2})^* + \frac{E^{[2]}(^2D_{5/2})^*}{14}\right)$$

$$+\left\langle 5^2F_{5/2}\left\|M^{[1]}\right\|6^2D_{3/2}\right\rangle\left\langle 5^2F_{5/2}\left\|M^{[3]}\right\|6^2D_{3/2}\right\rangle\left(E_{OD}^{[2]}(^2D_{3/2})^* + \frac{E_{OD}^{[2]}(^2D_{5/2})^*}{\sqrt{21}}\right) \quad (6.38)$$

The first modification was that the *LS* coupling for the case of the octupole matrix elements in addition to the dipole matrix elements for the low-lying *D* states was assumed. Therefore, the product of the dipole and octupole matrix element for the $^2D_{5/2}$ in terms of the product of the dipole and octupole matrix element for the $^2D_{3/2}$, Eq. 6.21, for the second order octupole-dipole second order energies. The second modification was the addition of the constant, *C*, to the model. This constant is to account for the fact the rf measurements of the fine structure

determine only the relative energies. In Chapter 5 one of the states, the $L$=12 $K$=9.5, was used as the zero position and the locations of all of the states were found in reference to that using the rf transitions measured. The addition of the constant, $C$, corrects for the fact that the measured fine structure is not measured with reference to hydrogenic. In Eq. 6.38 the full second order energies due to the low-lying $D$ states are denoted with asterisks to indicate that the correction were calculated assuming unit values for each of the matrix elements. This allows for the matrix elements controlling the second order energies to be included as parameters in the fit of the measured fine structure.

The structure parameters were defined in term of properties of the $Th^{3+}$ in Section 6.1, Eq. 6.7 through Eq. 6.11, but for convenience they are rewritten here. This rewriting of the of the structure parameters also allows for them to written in terms of coefficients for which the fine structure will be fit for. Those fitted coefficients, the $B$s with the subscripts, will then be equated with the properties of $Th^{3+}$, Eq. 6.39 through Eq. 6.43.

$$A_0(L) = -\frac{\alpha_{D,0}^{Mod}}{2}\left\langle r^{-4}\right\rangle_{nL} - \frac{(\alpha_{Q,0} - 6\beta_{D,0}^{Mod})}{2}\left\langle r^{-6}\right\rangle_{nL} \Rightarrow B_{04}\left\langle r^{-4}\right\rangle_{nL} + B_{06}\left\langle r^{-6}\right\rangle_{nL} \tag{6.39}$$

$$A_1(L) = -\frac{\alpha_{FS}^2 g_J}{2}\left\langle r^{-3}\right\rangle_{nL} + \beta_{D,1}^{Mod}\left\langle r^{-6}\right\rangle_{nL} \Rightarrow B_{13}\left\langle r^{-3}\right\rangle_{nL} + B_{16}\left\langle r^{-6}\right\rangle_{nL} \tag{6.40}$$

$$A_2(L) = -Q\left\langle r^{-3}\right\rangle_{nL} - \frac{\alpha_{D,2}^{Mod}}{2}\left\langle r^{-4}\right\rangle_{nL} \Rightarrow B_{23}\left\langle r^{-3}\right\rangle_{nL} + B_{24}\left\langle r^{-4}\right\rangle_{nL} \tag{6.41}$$

$$A_3(L) = B_{35}\left\langle r^{-5}\right\rangle_{nL} \tag{6.42}$$

$$A_4(L) = -\Pi\left\langle r^{-5}\right\rangle_{nL} - \frac{(\alpha_{Q,4} + \alpha_{DO,4}^{Mod})}{2}\left\langle r^{-6}\right\rangle_{nL} \Rightarrow B_{45}\left\langle r^{-5}\right\rangle_{nL} + B_{46}\left\langle r^{-6}\right\rangle_{nL} \tag{6.43}$$

The hydrogenic expectation values of the different powers of $r$ are defined in the work of Bockasten [39] and given in Table 6.13 for the $L$s of interest here. The tensor products are defined in Eq. 1.19 through Eq. 1.22, and for the structure measured here the resulting tensor products are presented in Table 6.14, for all values of $K$ in $L$=9 to 12.

Table 6.13: The hydrogenic expectation values of the different powers of $r$ used in fitting the $Th^{2+}$ Rydberg fine structure. All values are in MHz.

| $L$ | $< r^{-3} >_{nL}$ | $< r^{-4} >_{nL}$ | $< r^{-5} >_{nL}$ | $< r^{-6} >_{nL}$ |
|---|---|---|---|---|
| 9 | 9465.106 | 458.970 | 25.255 | 1.491 |
| 10 | 7006.637 | 275.105 | 12.240 | 0.583 |
| 11 | 5331.137 | 172.523 | 6.322 | 0.247 |
| 12 | 4150.085 | 112.313 | 3.440 | 0.112 |

Table 6.14: The tensor products used in the fitting of the $Th^{2+}$ Rydberg fine structure. For the case of the $Th^{2+}$ Rydberg fine structure $J_c = 5/2$ and for the case studied here $L$=9 to 12, the tensor products for all $K$ values was calculated even though only five of the six levels for each $L$ were measured.

| $L$ | $K$ | $(\vec{L}\cdot\vec{J}_c)$ | $\frac{X^{[2]}(J_c)\cdot C^{[2]}(\hat{r})}{\begin{pmatrix} J_c & 2 & J_c \\ -J_c & 0 & J_c \end{pmatrix}}$ | $(X^{[3]}(J_c)\cdot T^{[3]}(\hat{r}))$ | $\frac{X^{[4]}(J_c)\cdot C^{[4]}(\hat{r})}{\begin{pmatrix} J_c & 4 & J_c \\ -J_c & 0 & J_c \end{pmatrix}}$ |
|---|---|---|---|---|---|
| 9 | 6.5 | -25.0 | -0.58824 | 0.7060 | 0.6471 |
| 9 | 7.5 | -17.5 | -0.05882 | -0.5648 | -1.2941 |
| 9 | 8.5 | -9.0 | 0.31261 | -0.6334 | 0.2773 |
| 9 | 9.5 | 0.5 | 0.44034 | 0.1262 | 1.0756 |
| 9 | 10.5 | 11.0 | 0.22857 | 0.7731 | -0.9193 |
| 9 | 11.5 | 22.5 | -0.42857 | -0.3741 | 0.2236 |
| 10 | 7.5 | -27.5 | -0.57895 | 0.7580 | 0.6130 |
| 10 | 8.5 | -19.0 | -0.04211 | -0.6478 | -1.2817 |
| 10 | 9.5 | -9.5 | 0.32311 | -0.6819 | 0.3295 |
| 10 | 10.5 | 1.0 | 0.43844 | 0.1717 | 1.0503 |
| 10 | 11.5 | 12.5 | 0.21739 | 0.8539 | -0.9391 |
| 10 | 12.5 | 25.0 | -0.43478 | -0.4269 | 0.2348 |
| 11 | 8.5 | -30.0 | -0.57143 | 0.8105 | 0.5865 |
| 11 | 9.5 | -20.5 | -0.02857 | -0.7295 | -1.2707 |
| 11 | 10.5 | -10.0 | 0.33143 | -0.7295 | 0.3714 |
| 11 | 11.5 | 1.5 | 0.43657 | 0.2170 | 1.0286 |
| 11 | 12.5 | 14.0 | 0.20800 | 0.9340 | -0.9556 |
| 11 | 13.5 | 27.5 | -0.44000 | -0.4801 | 0.2444 |
| 12 | 9.5 | -32.5 | -0.56522 | 0.8634 | 0.5652 |
| 12 | 10.5 | -22.0 | -0.01739 | -0.8103 | -1.2609 |
| 12 | 11.5 | -10.5 | 0.33816 | -0.7763 | 0.4058 |
| 12 | 12.5 | 2.0 | 0.43478 | 0.2621 | 1.0097 |
| 12 | 13.5 | 15.5 | 0.20000 | 1.0135 | -0.9693 |
| 12 | 14.5 | 30.0 | -0.44444 | -0.5334 | 0.2529 |

Before the observed fine structure was fit to the model in Eq. 6.38, effects not included in the model had to be applied as correction to the observed fine structure levels. For the case of the $Th^{2+}$ Rydberg fine structure each of the corrections contained in Eq. 6.13 had to be calculated

and applied to the observed energies before the observed data was fit to the model in Eq. 6.38. Eq. 6.13 is repeated here for convenience.

$$E_{Corrected} = E_{obs} - E_{\mathrm{Rel}} - E^{[2]}(V_{eff}) - E(\alpha_{D,2}\ shift) - E^{[2]}_{correction}(^2D_{3/2})$$

All the correction contained in Eq. 6.13 were discussed in the Section 6.2 with the exception of the relativistic correction, $E_{\mathrm{Rel}}$. The relativistic correction is given by Eq. 1.32 and the calculation of this correction is straight forward requiring only the charge, *n*, and *L* of the state of interest. The remaining corrections depend on either properties of $Th^{3+}$ or the matrix elements coupling the low-lying $^2D_{3/2}$ to the ground states. The calculation and application of all of the corrections to the measured fine structure is an iterative process. Initially, the results of the optical study provided guidance on the choice of properties and dipole matrix elements used in the calculation of the corrections. The data corrected with those corrections was fit and new properties were determined. The process of correcting the rf measurements and the fitting rf measurements was repeated until there was no longer any changes in the properties determined from the fit and used to calculate the corrections. In this work just the last iteration of the correcting and fitting of the data is shown and discussed, but in practice this process took multiple iterations for the parameters to be determined and converge to the values used to calculate of the correction here. The calculation of the corrections here assumed that the properties of $Th^{3+}$ were

$$Q = 0.59 a.u. \quad \alpha_{D,0} = 15.2 a.u. \quad \alpha_{D,2} = -5.3 a.u.$$

and the $^2D_{3/2}$ dipole matrix element was

$$\left|\left\langle 5^2F_{5/2}\left\|M^{[1]}\right\|6^2D_{3/2}\right\rangle\right| = 1.44 a.u.$$

The correction calculated from theses parameters are given in the Table 6.15. This table also gives the total of the corrections to be applied to each of the states in the fine structure. Three out of the four corrections that had to be applied to the measured fine structure contained uncertainties. The sources of the uncertainties were discussed in Section 6.2. The uncertainty on the total of the corrections for each states is the quadrature sum of uncertainties in the each individual corrections, this is also listed in the table. The application of these corrections to the measured fine structure is shown in Table 6.16. The first two columns identify the $n$=28 level by its $L$ and $K$ value. The third column reports the relative positions of each of the levels measured and the uncertainty in the experimentally determined position. Recall that the rf study measured the relative positions of the levels with respect to each other and not to hydrogenic, therefore the positions of one of the levels is assumed zero and the positions of all other levels are determined with respect to it. The position of the $L$=12 $K$=9.5 was arbitrarily taken as the zero positions. The uncertainty in that position was taken to be the average uncertainty of the all other $L$=12 states, to avoid excessive weight to that position in the fit Column four gives the total of the corrections applied to the measured fine structure and the uncertainty in those corrections. The final column of Table 6.16 shows the resulting positions of the levels after the subtraction of the corrections. The uncertainty in the corrected level is the quadrature sum of experimental error and the uncertainty in the correction applied. In the lower $L$ states the total uncertainty in the corrected positions is dominated by the uncertainty in the corrections. It will be these corrected positions that will be fit to determine the parameters from which the properties of $Th^{3+}$ can be determined.

Table 6.15: Calculated corrections for the $n$=28 $Th^{2+}$ Rydberg fine structure. All of the corrections have units of MHz. The first column gives the $L$ and the second column gives the $K$ of the state. The second column gives the relativistic correction, $E_{\mathrm{Rel}}$, and the third column gives the second order in $V_{\mathrm{eff}}$, $E^{[2]}(V_{eff})$. The fourth column gives the correction for the tensor coupling of states within the $n$=28 fine structure, $E(\alpha_{D,2}\, shift)$ and the fifth column gives $E^{[2]}_{correction}(^2D_{3/2})$. The final column gives the total of the corrections that need to be applied to the measured fine structure, $E_{Corrections}$.

| $L$ | $K$ | $E_{\mathrm{Rel}}$ | $E^{[2]}(V_{\mathrm{eff}})$ | $E(\alpha_{D,2}\, shift)$ | $E^{[2]}_{correction}(^2D_{3/2})$ | $E_{Corrections}$ |
|---|---|---|---|---|---|---|
| 9 | 6.5 | -50.73 | -0.82 (3.90) | 3.10 (0.03) | 65.09 (7.22) | 16.64 (8.21) |
| 9 | 7.5 | -50.73 | -1.72 (2.92) | 7.94 (0.08) | -20.23 (5.14) | -64.75 (5.92) |
| 9 | 8.5 | -50.73 | -3.20 (3.22) | 13.93 (0.20) | -17.55 (2.82) | -57.54 (4.28) |
| 9 | 9.5 | -50.73 | -4.59 (3.50) | -132.78 (20.58) | 6.53 (0.98) | -181.58 (20.90) |
| 9 | 10.5 | -50.73 | -5.06 (3.08) | -3.12 (0.02) | 0.00 (0.00) | -58.91 (3.08) |
| 9 | 11.5 | -50.73 | -3.81 (3.47) | 2.57 (0.16) | 0.00 (0.00) | -51.97 (3.48) |
| 10 | 7.5 | -44.25 | 0.26 (0.79) | 0.94 (0.01) | 10.24 (0.96) | -32.81 (1.24) |
| 10 | 8.5 | -44.25 | 0.60 (0.53) | 2.82 (0.04) | -3.64 (0.64) | -44.48 (0.83) |
| 10 | 9.5 | -44.25 | 0.30 (0.62) | 6.72 (0.20) | -2.98 (0.35) | -40.20 (0.74) |
| 10 | 10.5 | -44.25 | -0.32 (0.69) | -11.87 (0.76) | 1.01 (0.12) | -55.43 (1.04) |
| 10 | 11.5 | -44.25 | -0.92 (0.57) | -1.95 (0.02) | 0.00 (0.00) | -47.11 (0.57) |
| 10 | 12.5 | -44.25 | -1.33 (0.69) | 0.92 (0.06) | 0.00 (0.00) | -44.66 (0.69) |
| 11 | 8.5 | -38.90 | 0.17 (0.06) | 0.33 (0.00) | 0.14 (0.01) | -38.25 (0.06) |
| 11 | 9.5 | -38.90 | 0.40 (0.03) | 1.04 (0.00) | -0.05 (0.01) | -37.51 (0.03) |
| 11 | 10.5 | -38.90 | 0.20 (0.04) | 3.00 (0.02) | -0.04 (0.01) | -35.73 (0.05) |
| 11 | 11.5 | -38.90 | -0.19 (0.05) | -2.93 (0.18) | 0.02 (0.01) | -42.00 (0.19) |
| 11 | 12.5 | -38.90 | -0.55 (0.04) | -1.33 (0.19) | 0.00 (0.00) | -40.78 (0.19) |
| 11 | 13.5 | -38.90 | -0.82 (0.05) | 0.40 (0.03) | 0.00 (0.00) | -39.31 (0.06) |
| 12 | 9.5 | -34.40 | 0.14 (0.01) | 0.19 (0.00) | 0.00 (0.00) | -34.07 (0.01) |
| 12 | 10.5 | -34.40 | 0.38 (0.00) | 0.59 (0.00) | 0.00 (0.00) | -33.43 (0.00) |
| 12 | 11.5 | -34.40 | 0.27 (0.00) | 1.87 (0.02) | 0.00 (0.00) | -32.26 (0.02) |
| 12 | 12.5 | -34.40 | -0.02 (0.01) | -1.14 (0.08) | 0.00 (0.00) | -35.56 (0.08) |
| 12 | 13.5 | -34.40 | -0.30 (0.00) | -0.98 (0.22) | 0.00 (0.00) | -35.67 (0.22) |
| 12 | 14.5 | -34.40 | -0.46 (0.01) | 0.19 (0.02) | 0.00 (0.00) | -34.66 (0.02) |

Table 6.16: The corrections to measured $n$=28 $Th^{2+}$ fine structure. The first column gives the $L$, the second column gives the $K$. The third column gives the relative position of the state. The fourth column gives the total correction that need to be applied and the fifth column gives the corrected position. All the energies are in MHz.

| $L$ | $K$ | $E_{obs}$ | $E_{corrections}$ | $E_{corrected}$ |
|---|---|---|---|---|
| 9 | 6.5 | -5661.28 (0.13) | 16.64 (8.21) | -5677.92 (8.21) |
| 9 | 7.5 | -6514.38 (0.19) | -64.75 (5.92) | -6449.63 (5.92) |
| 9 | 8.5 | -6736.10 (0.31) | -57.54 (4.28) | -6678.56 (4.29) |
| 9 | 9.5 | -6232.58 (0.39) | -181.58 (20.90) | -6051.00 (20.90) |
| 9 | 10.5 | -4363.80 (0.32) | -58.91 (3.08) | -4304.89 (3.10) |
| 9 | 11.5 | -- | -51.97 (3.48) | -- |
| 10 | 7.5 | -2168.86 (0.07) | -32.81 (1.24) | -2136.05 (1.25) |
| 10 | 8.5 | -3387.82 (0.16) | -44.48 (0.83) | -3343.34 (0.84) |
| 10 | 9.5 | -4053.08 (0.26) | -40.20 (0.74) | -4012.88 (0.78) |
| 10 | 10.5 | -3975.28 (0.30) | -55.43 (1.04) | -3919.85 (1.08) |
| 10 | 11.5 | -2862.11 (0.33) | -47.11 (0.57) | -2815.00 (0.66) |
| 10 | 12.5 | -- | -44.66 (0.69) | -- |
| 11 | 8.5 | -405.22 (0.11) | -38.25 (0.06) | -366.97 (0.12) |
| 11 | 9.5 | -1724.35 (0.18) | -37.51 (0.03) | -1686.84 (0.18) |
| 11 | 10.5 | -2548.18 (0.28) | -35.73 (0.05) | -2512.45 (0.29) |
| 11 | 11.5 | -2705.10 (0.33) | -42.00 (0.19) | -2663.10 (0.38) |
| 11 | 12.5 | -1977.51 (0.33) | -40.78 (0.19) | -1936.73 (0.38) |
| 11 | 13.5 | -- | -39.31 (0.06) | -- |
| 12 | 9.5 | 0.00 (0.28) | -34.07 (0.01) | 34.07 (0.28) |
| 12 | 10.5 | -1125.67 (0.19) | -33.43 (0.00) | -1092.24 (0.19) |
| 12 | 11.5 | -1831.35 (0.29) | -32.26 (0.02) | -1799.09 (0.29) |
| 12 | 12.5 | -1985.76 (0.30) | -35.56 (0.08) | -1950.20 (0.31) |
| 12 | 13.5 | -1428.20 (0.34) | -35.67 (0.22) | -1392.53 (0.41) |
| 12 | 14.5 | -- | -34.66 (0.02) | -- |

The corrected positions were then fit to Eq. 6.38, with the fit weighted by the uncertainties in the corrected positions. The fit of the twenty levels was to twelve parameters and the parameters returned from the fit are listed here with their uncertainties.

$$C = -157.6(1.5)$$
$$B_{04} = -4.753(16)$$
$$B_{06} = -19.0(7.3)$$
$$B_{13} = -3.3(1.3)\times 10^{-5}$$
$$B_{16} = -0.04(44)$$
$$B_{23} = -0.5931(14)$$
$$B_{24} = 0.061(56)$$
$$B_{35} = 0.11(25)$$
$$B_{45} = 0.69(28)$$
$$B_{46} = -5.4(7.6)$$
$$\left|\left\langle 5^2F_{5/2}\left\|M^{[1]}\right\|6^2D_{3/2}\right\rangle\right| = 1.4355(18)$$
$$\left|\left\langle 5^2F_{5/2}\left\|M^{[3]}\right\|6^2D_{3/2}\right\rangle\right| = 3.3(1.1)$$

During the fitting process the assumption of the *LS* coupling between the two dipole matrix elements for the low-lying *D* states was checked. The ratio of the dipole matrix elements squared was varied up to 10% from the ratio determined from *LS* coupling. This variation did not result in any changes to any parameters outside of their error bars. The quality of the fit of the fine structure can be understood if the fitted parameters are used to simulate the fine structure. These parameters, the fitted coefficients and the matrix elements, represent just another way of describing the corrected relative locations of the twenty levels measured in $L$=9 to 12. By plugging the parameters determined by the fit back into the model, Eq. 6.38, a complete simulation of the $n$=28 $L$=9 to 12 is completed. The simulation also predicts the location of the sixth level in each $L$, who's position was not measured. By using these parameters to simulate the structure, Table 6.17, it is possible to see where the difference

between the predicted and the observed occur. In Table 6.17, the simulated fine structure, $E_{predicted}$ has been shown broken down by into components, the first two columns of the table identifies the *L* and *K* value of the each of the states. The third column give the part of the fine structure due to the effective potential, the *B* and *C* coefficients found from the fit. The contributions from both of the second order dipole energies are shown in column four. They were calculated using the determined dipole matrix element. The fifth column gives contributions from both of the second order octupole-dipole energies calculated using the dipole and octupole matrix element determined for the $^2D_{3/2}$. The corrections applied to the measured fine structure from Table 6.16 are shown in the sixth column. By adding together column three through six the simulation of the predicted fine structure is completed and shown in column seven. The error on the predicted location is the uncertainty from the corrections. Column nine gives the experimentally observed positions of each of the levels along with their experimental uncertainties. The final column of Table 6.17 gives the difference between the observed energies and the predicted energies. Looking at Table 6.17 it can be seen that almost all of the fine structure is due to the effective potential and the second order dipole energies for the low-lying *D* states. In *L*=11 and *L*=12 the predicted positions are within the experimental uncertainty for the levels. In *L*=9 an *L*=10 only three of the observed levels differ from the predicted by more than the uncertainty in the corrections.

Table 6.18 lists the contributions to the $\left\langle V_{eff}^{Mod} \right\rangle$ from the dominant coefficients determined during the fit of the fine structure. The sum of the contribution from the additional coefficients included in the fit are listed under the column labeled *Other* in Table 6.18. The column labeled *C* accounts for the offset of the level used as the zero position for the relative fine structure, the *L*=12 *K*=9.5, not being at hydrogenic.

Table 6.17: The breakdown of the $n$=28 $Th^{2+}$ Rydberg fine structure simulated from the parameters determinded from the fit of the fine structure. All energies are in MHz.

| $L$ | $K$ | $\langle V_{eff}^{Mod} \rangle$ | $E^{[2]}(^2D_{3/2})$ & $E^{[2]}(^2D_{5/2})$ | $E_{OD}^{[2]}(^2D_{3/2})$ & $E_{OD}^{[2]}(^2D_{5/2})$ | $E_{Corrections}$ | $E_{Predicted}$ | $E_{obs}$ | $E_{obs}$ -$E_{Predicted}$ |
|---|---|---|---|---|---|---|---|---|
| 9 | 6.5 | 936.1 | -6564.7 | -26.6 | 16.6 | -5638.6 (8.21) | -5661.3 (0.13) | -22.7 |
| 9 | 7.5 | -2045.5 | -4426.9 | 24.9 | -64.8 | -6512.3 (5.92) | -6514.4 (0.19) | -2.1 |
| 9 | 8.5 | -4109.1 | -2581.2 | 9.9 | -57.5 | -6737.8 (4.28) | -6736.1 (0.31) | 1.7 |
| 9 | 9.5 | -4816.7 | -1243.8 | -10.5 | -181.6 | -6252.6 (20.90) | -6232.6 (0.39) | 20.1 |
| 9 | 10.5 | -3654.5 | -656.7 | 3.1 | -58.9 | -4367.1 (3.08) | -4363.8 (0.32) | 3.3 |
| 9 | 11.5 | 19.4 | -1087.2 | -2.6 | -52.0 | -1122.3 (3.48) | | |
| 10 | 7.5 | 931.5 | -3060.6 | -8.5 | -32.8 | -2170.4 (1.24) | -2168.9 (0.07) | 1.5 |
| 10 | 8.5 | -1304.5 | -2047.2 | 8.2 | -44.5 | -3388.0 (0.83) | -3387.8 (0.16) | 0.1 |
| 10 | 9.5 | -2810.1 | -1205.2 | 2.9 | -40.2 | -4052.7 (0.74) | -4053.1 (0.26) | -0.4 |
| 10 | 10.5 | -3285.3 | -631.5 | -3.4 | -55.4 | -3975.7 (1.04) | -3975.3 (0.30) | 0.4 |
| 10 | 11.5 | -2382.9 | -433.2 | 1.5 | -47.1 | -2861.6 (0.57) | -2862.1 (0.33) | -0.5 |
| 10 | 12.5 | 317.7 | -727.5 | -1.2 | -44.7 | -455.6 (0.69) | | |
| 11 | 8.5 | 826.6 | -1191.4 | -2.1 | -38.3 | -405.2 (0.06) | -405.2 (0.11) | 0.0 |
| 11 | 9.5 | -892.6 | -796.4 | 2.0 | -37.5 | -1724.4 (0.03) | -1724.4 (0.18) | 0.1 |
| 11 | 10.5 | -2024.1 | -488.8 | 0.6 | -35.7 | -2548.1 (0.05) | -2548.2 (0.28) | -0.1 |
| 11 | 11.5 | -2355.0 | -307.5 | -0.8 | -42.0 | -2705.3 (0.19) | -2705.1 (0.33) | 0.2 |
| 11 | 12.5 | -1642.5 | -294.9 | 0.7 | -40.8 | -1977.4 (0.19) | -1977.5 (0.33) | -0.1 |
| 11 | 13.5 | 399.7 | -497.0 | -0.6 | -39.3 | -137.2 (0.06) | | |
| 12 | 9.5 | 699.9 | -665.0 | -0.8 | -34.1 | 0.0 (0.01) | 0.0 (0.28) | 0.0 |
| 12 | 10.5 | -650.1 | -442.9 | 0.8 | -33.4 | -1125.7 (0.00) | -1125.7 (0.19) | 0.0 |
| 12 | 11.5 | -1521.6 | -277.7 | 0.2 | -32.3 | -1831.4 (0.02) | -1831.4 (0.29) | 0.0 |
| 12 | 12.5 | -1759.1 | -190.8 | -0.3 | -35.6 | -1985.7 (0.08) | -1985.8 (0.30) | 0.0 |
| 12 | 13.5 | -1187.9 | -205.2 | 0.4 | -35.7 | -1428.4 (0.22) | -1428.2 (0.34) | 0.2 |
| 12 | 14.5 | 393.5 | -346.0 | -0.3 | -34.7 | 12.5 (0.02) | | |

Table 6.18: Breakdown of the part of the fine structure due to the effective potential in terms of the dominant coefficients determinded from the fit of the fine structure. All energies are in MHz.

| $L$ | $K$ | $C$ | $B_{04}$ | $B_{24}$ | $B_{23}$ | $B_{45}$ | $B_{13}$ | Other | $\langle V_{eff}^{Mod} \rangle$ |
|---|---|---|---|---|---|---|---|---|---|
| 9 | 6.5 | -157.5 | -2181.3 | -16.3 | 3302.2 | 11.2 | 7.8 | -30.0 | 936.1 |
| 9 | 7.5 | -157.5 | -2181.3 | -1.6 | 330.2 | -22.5 | 5.5 | -18.2 | -2045.5 |
| 9 | 8.5 | -157.5 | -2181.3 | 8.7 | -1754.9 | 4.8 | 2.8 | -31.7 | -4109.1 |
| 9 | 9.5 | -157.5 | -2181.3 | 12.2 | -2471.9 | 18.7 | -0.2 | -36.8 | -4816.7 |
| 9 | 10.5 | -157.5 | -2181.3 | 6.3 | -1283.1 | -16.0 | -3.4 | -19.5 | -3654.5 |
| 9 | 11.5 | -157.5 | -2181.3 | -11.9 | 2405.9 | 3.9 | -7.1 | -32.7 | 19.4 |
| 10 | 7.5 | -157.5 | -1307.4 | -9.6 | 2405.9 | 5.2 | 6.4 | -11.3 | 931.5 |
| 10 | 8.5 | -157.5 | -1307.4 | -0.7 | 175.0 | -10.8 | 4.4 | -7.4 | -1304.5 |
| 10 | 9.5 | -157.5 | -1307.4 | 5.4 | -1342.7 | 2.8 | 2.2 | -12.8 | -2810.1 |
| 10 | 10.5 | -157.5 | -1307.4 | 7.3 | -1822.0 | 8.8 | -0.2 | -14.2 | -3285.3 |
| 10 | 11.5 | -157.5 | -1307.4 | 3.6 | -903.4 | -7.9 | -2.9 | -7.3 | -2382.9 |
| 10 | 12.5 | -157.5 | -1307.4 | -7.2 | 1806.8 | 2.0 | -5.8 | -13.0 | 317.7 |
| 11 | 8.5 | -157.5 | -819.9 | -6.0 | 1806.8 | 2.6 | 5.3 | -4.6 | 826.6 |
| 11 | 9.5 | -157.5 | -819.9 | -0.3 | 90.3 | -5.5 | 3.6 | -3.3 | -892.6 |
| 11 | 10.5 | -157.5 | -819.9 | 3.5 | -1047.9 | 1.6 | 1.8 | -5.6 | -2024.1 |
| 11 | 11.5 | -157.5 | -819.9 | 4.6 | -1380.4 | 4.5 | -0.3 | -6.0 | -2355.0 |
| 11 | 12.5 | -157.5 | -819.9 | 2.2 | -657.7 | -4.2 | -2.5 | -2.9 | -1642.5 |
| 11 | 13.5 | -157.5 | -819.9 | -4.6 | 1391.2 | 1.1 | -4.9 | -5.7 | 399.7 |
| 12 | 9.5 | -157.5 | -533.8 | -3.8 | 1391.2 | 1.3 | 4.5 | -2.0 | 699.9 |
| 12 | 10.5 | -157.5 | -533.8 | -0.1 | 42.8 | -3.0 | 3.0 | -1.6 | -650.1 |
| 12 | 11.5 | -157.5 | -533.8 | 2.3 | -832.4 | 1.0 | 1.4 | -2.6 | -1521.6 |
| 12 | 12.5 | -157.5 | -533.8 | 3.0 | -1070.2 | 2.4 | -0.3 | -2.7 | -1759.1 |
| 12 | 13.5 | -157.5 | -533.8 | 1.4 | -492.3 | -2.3 | -2.1 | -1.2 | -1187.9 |
| 12 | 14.5 | -157.5 | -533.8 | -3.0 | 1094.0 | 0.6 | -4.1 | -2.6 | 393.5 |

With an understanding of the quality of the fit of the fine structure and the major coefficients that contribute to the fine structure having been determined, it was time to equate the coefficients found during the fit with properties of $Th^{3+}$. The extracting of the properties of $Th^{3+}$ from the coefficients began with the scalar component of the fine structure, Eq. 6.39. In the fit of the fine structures two leading component that contribute to the scalar component were found. The coefficients returned from the fit were the $B_{04}$ and the $B_{06}$. From Eq. 6.39 it can be seen that the $B_{04}$ enables the determining of the scalar dipole polarizability, $\alpha_{D,0}^{Mod}$, excluding contributions from the low-lying *D* states.

$$B_{04} = -\frac{\alpha_{D,0}^{Mod}}{2} \Rightarrow \boxed{\alpha_{D,0}^{Mod} = 9.51(3) a.u.}$$

This result gives the scalar dipole polarizability excluding contributions from the low-lying *D* states to within half a percent. The $B_{06}$ gives information on both the scalar quadrupole polarizability, $\alpha_{Q,0}$ and the 1st non-adiabatic scalar dipole polarizability, $\beta_{D,0}^{Mod}$, excluding contributions from the low-lying *D* states.

$$B_{06} = -\frac{(\alpha_{Q,0} - 6\beta_{D,0}^{Mod})}{2} \Rightarrow \boxed{(\alpha_{Q,0} - 6\beta_{D,0}^{Mod}) = 38(14) a.u.}$$

Without information on the 1st non-adiabatic scalar dipole polarizability it is not possible to the extract the scalar quadrupole polarizability. The sum of the two properties was determined with an uncertainty of 37%, so it could still be useful in the test of the theoretical calculations of the $Th^{3+}$.

The next component that contributes to the fine structure is the vector component. In the fit of the data the first two terms of the effective potential that contribute to the vector component were fit for. The first term of the vector component is due to a the magnetic dipole moment of

the core, where $g_J$ is the Landé g factor, the next term is due the 1st non-adiabatic vector dipole polarizability, $\beta_{D,1}$, called at times the vector hyperpolarizability [8]. The 1st non-adiabatic vector dipole polarizability found here will exclude contribution from the low-lying *D* states. The equating of the coefficients found with Eq. 6.40 results in these properties:

$$B_{13} = -\frac{\alpha_{FS}^2 g_J}{2} \Rightarrow \boxed{g_J = 1.24(48)}$$

$$B_{16} = \beta_{D,1}^{Mod} \Rightarrow \boxed{\beta_{D,1}^{Mod} = -0.04(44) a.u.}$$

The Landé g factor found is within 1σ of the value predicted for $Th^{3+}$. For a $^2F_{5/2}$ state $g_J$ is predicted to be $6/7$, given that $g_J$ is defined to be

$$g_J = \frac{J_c + \frac{1}{2}}{L_c + \frac{1}{2}} \tag{6.44}$$

by Bethe and Salpeter [31]. Previously rf measurement of both argon [19] and neon [51] Rydberg fine structure determined experimental values of the Landé g factor that were completely consistent with the $g_J$ predicted from Eq. 6.44. The 1st non-adiabatic vector dipole polarizability determined from the fit of the fine structure is consistent with zero.

The 2nd rank tensor component of the fine structure gives information on the permanent quadrupole moment of $Th^{3+}$ and the tensor dipole polarizability, Eq. 6.41. The $B_{23}$ is directly related to the permanent quadrupole moment.

$$B_{23} = -Q \Rightarrow \boxed{Q = 0.5931(14) a.u.}$$

This determination of the permanent quadrupole moment has an uncertainty of only a quarter of a percent.

The $B_{24}$ is just negative one half of the tensor dipole.

$$B_{24} = -\frac{\alpha_{D,2}^{Mod}}{2} \Rightarrow \boxed{\alpha_{D,2}^{Mod} = -0.12(11)a.u.}$$

The tensor dipole polarizability excluding contributions from the low-lying *D* states is almost consistent with zero. The contributions due to the low-lying *D* states will be calculated separately.

The study of $Th^{3+}$ marks only the second ion for which the 3rd rank tensor component has been determined. Experimentally the only other study that explored the possibility of the presence of the 3rd rank tensor component in the Rydberg fine structure is the rf study of the *n*=9 nickel Rydberg fine structure [11]. The leading 3rd rank tensor term is due to a possible magnetic octupole moment of the core, $C_{M3}$, this term would be proportional to $r^{-5}$. The nickel study saw no evidence for $C_{M3}$. For the case of $Th^{3+}$, there is no a theoretical estimate or evidence for a magnetic octupole in $Th^{3+}$ [42]. The equating of the coefficient found from the fit of the data showed at $C_{M3}$ consistent with zero.

$$B_{35} = C_{M3} \Rightarrow \boxed{C_{M3} = 11(25)a.u.}$$

The next term that would contribute to 3rd rank tensor term would be proportional to $r^{-8}$, since it would be so much smaller than the leading term it was not considered in the fit.

The fourth rank tensor component is controlled by two coefficients, the $B_{45}$ and the $B_{46}$. The $B_{45}$ is directly related to the permanent hexadecapole moment of $Th^{3+}$, from the fit it was determined that the permanent hexadecapole moment was nonzero.

$$B_{45} = -\Pi \Rightarrow \boxed{\Pi = -0.69(28)a.u.}$$

The study of nickel was the only other fine structure studied that determined a permanent hexadecapole moment [11]. The result here is 2.5σ away from zero. The $B_{46}$ determined from the fit is related to higher order 4th rank tensor terms, specifically the 4th rank quadrupole polarizability and the 4th rank octupole-dipole polarizability excluding contribution form the low-lying *D* states. The coefficient determined from the fit of the data is consistent with zero, so all that can be said about this term is it contribution to the fine structure is minimal.

$$B_{46} = -\frac{\left(\alpha_{Q,4} + \alpha_{DO,0}^{Mod}\right)}{2} \Rightarrow \boxed{\left(\alpha_{Q,4} + \alpha_{DO,0}^{Mod}\right) = 11(15) a.u.}$$

In addition to the properties of $Th^{3+}$ the fit of the measured fine structure also determined the dipole matrix element that couples the ground states to the low-lying $^2D_{3/2}$ state

$$\left|\left\langle 5^2 F_{5/2} \left\| M^{[1]} \right\| 6^2 D_{3/2} \right\rangle\right| = 1.436(2) a.u.$$

This matrix element was determined to a precision of two tenths of a percent. While the dipole matrix element that couples the ground states to the low-lying $^2D_{5/2}$ matrix element was not included in the fit, a value for this dipole matrix element can be extracted from the relation of the $^2D_{3/2}$ dipole matrix element and the $^2D_{5/2}$ dipole matrix element. Assuming *LS* coupling regime results, Eq. 6.5, allows for the determination of the $^2D_{5/2}$ dipole matrix element

$$\left|\left\langle 5^2 F_{5/2} \left\| M^{[1]} \right\| 6^2 D_{5/2} \right\rangle\right| = 0.384(1) a.u.$$

Both of these dipole matrix elements are important if polarizabilities are to be corrected to include the contribution from the *D* states. The properties determined from the fit had the contributions from the low-lying states excluded. The properties that have to be corrected are the scalar and tensor dipole polarizabilities, since both of the low-lying *D* states can dipole couple to the ground state and both of those properties are due to dipole coupling. This means the values

determined from fitting the data will have to be corrected to account for the effect that both of the low-lying states have on those properties. The properties have been explicitly written out in term of matrix elements and excitation energies in the work of the Woods [7]. The definition of the dipole polarizability is given in Eq. 1.24 as an example. For the $^2D_{3/2}$ and $^2D_{5/2}$ the contributions to the scalar dipole polarizability would have the form of Eq. 6.43 and Eq. 6.44 respectively.

$$\alpha_{D,0}(^2D_{3/2}) = \frac{1}{9}\frac{\left|\left\langle 5^2F_{5/2}\left\|M^{[1]}\right\|6^2D_{3/2}\right\rangle\right|^2}{\Delta E(^2D_{3/2})} \tag{6.43}$$

$$\alpha_{D,0}(^2D_{5/2}) = \frac{1}{9}\frac{\left|\left\langle 5^2F_{5/2}\left\|M^{[1]}\right\|6^2D_{5/2}\right\rangle\right|^2}{\Delta E(^2D_{5/2})} \tag{6.44}$$

The matrix elements have been determined by the fit of the fine structure and the excitation energies for these two low-lying states were measured precisely [9] to be

$$\Delta E(^2D_{3/2}) = 0.041887511(4)a.u.$$
$$\Delta E(^2D_{5/2}) = 0.066004903(4)a.u.$$

Therefore the contributions from both of the low lying states to the scalar dipole polarizability can be determined thus allowing for the total dipole polarizability, $\alpha_{D,0}$, of $Th^{3+}$ to be reported as be the sum of the scalar dipole polarizability found from the fit and the contributions from the two low-lying *D* states.

$$\begin{aligned}\alpha_{D,0} &= \alpha_{D,0}^{Mod} + \alpha_{D,0}(^2D_{3/2}) + \alpha_{D,0}(^2D_{5/2}) \\ &= 9.51(3) + 5.466(14) + 0.2478(5) \\ &\boxed{\alpha_{D,0} = 15.224(33)a.u.}\end{aligned}$$

This determines the scalar dipole polarizability to a precision of better than a quarter of a percent.

Similarly, contributions of the low-lying states to the tensor dipole polarizability were calculated. The tensor dipole polarizability for each of the low lying states was written out in term of the respective dipole matrix elements and excitation energies, Eq. 6.45 and Eq. 6.46 [7].

$$\alpha_{D,2}(^2D_{3/2}) = -\frac{1}{9}\frac{\left|\left\langle 5^2F_{5/2}\left\|M^{[1]}\right\|6^2D_{3/2}\right\rangle\right|^2}{\Delta E(^2D_{3/2})} \tag{6.45}$$

$$\alpha_{D,2}(^2D_{5/2}) = \frac{8}{63}\frac{\left|\left\langle 5^2F_{5/2}\left\|M^{[1]}\right\|6^2D_{5/2}\right\rangle\right|^2}{\Delta E(^2D_{5/2})} \tag{6.46}$$

The total dipole polarizability was then taken as the sum of the tensor dipole polarizability determined from the fit and the contributions from each of the low-lying $D$ states.

$$\begin{aligned}\alpha_{D,2} &= \alpha_{D,2}^{Mod} + \alpha_{D,2}(^2D_{3/2}) + \alpha_{D,2}(^2D_{5/2}) \\ &= -0.12(11) - 5.466(14) + 0.2832(7) \\ &\boxed{\alpha_{D,2} = -5.30(11)a.u.}\end{aligned}$$

Almost all of the tensor dipole polarizability is due to the low-lying $^2D_{3/2}$ level. The total tensor dipole polarizability is determined to a precision of the 2.1%, with the majority of the uncertainty due to the tensor dipole polarizability determined excluding contributions from the low-lying $D$ states.

### 6.4 Summary of $Th^{3+}$ Properties

The optical and the rf measurements presented in this work offered the first experimental determination of the properties of Fr-like $Th^{3+}$. Both the optical measurement and the rf measurements were discussed in this work, and the resulting properties are shown in Table 6.19. Column two gives the result of the rf study and column threes gives the results of the optical study. The first property given is the scalar dipole polarizability, both excluding and including the contributions from the low-lying states. The second property is the permanent quadrupole

moment, and the third property given is the tensor dipole polarizability, both excluding and including the contributions from the low-lying $D$ states. The fourth property listed is the permanent hexadecapole. The final two properties of $Th^{3+}$ listed are the dipole and octupole matrix elements that couples the ground state to the low-lying $^2D_{3/2}$ states. The dipole matrix element that couples the ground states and the low-lying $^2D_{5/2}$ state is not listed since it was not found independently in the rf study.

Table 6.19: The measured and calculated properties of $Th^{3+}$. Column one gives the properties. The second column gives the results extracted from the rf measurements of the $n$=28 $Th^{2+}$ Rydberg fine structure. Column three gives the result from the optical RESIS study of the $Th^{2+}$ Rydberg fine structure. The final three columns give the current theoretical results for the properties. The units on all the properties in the table are atomic units.

| Property | This Work (a.u.) | Optical [a] (a.u.) | Theory(SD) (a.u.) | Theory(DF) (a.u.) | Theory(DF+2+3) (a.u.) |
|---|---|---|---|---|---|
| $\alpha_{D,0}^{Mod}$ | 9.51(3) | 9.67(15) | 8.582[b] | -- | 8.562[g] |
| $\alpha_{D,0}$ | 15.224(33) | 15.42(17) | 15.073[b] | -- | 13.523[g] |
| $Q$ | 0.5931(14) | 0.54(4) | 0.62[c] | 0.91[e] | -- |
| $\alpha_{D,2}^{Mod}$ | -0.12(11) | 1.5(1.3) | 0.054[b] | -- | -0.014[g] |
| $\alpha_{D,2}$ | -5.30(11) | -3.6(1.3) | -6.166[b] | -- | -4.763[g] |
| $\Pi$ | -0.69(28) | -- | -0.76[d] | -- | -- |
| $\left\lvert\left\langle 5^2F_{5/2}\left\lVert M^{[1]}\right\rVert 6^2D_{3/2}\right\rangle\right\rvert$ | 1.436(2) | 1.435(10) | 1.530[b] | 2.428[f] | 1.337[g] |
| $\left\lvert\left\langle 5^2F_{5/2}\left\lVert M^{[3]}\right\rVert 6^2D_{3/2}\right\rangle\right\rvert$ | 3.3(1.1) | -- | 8.394[d] | -- | -- |

[a] Reference [3]
[b]RMBPT(SD) method from Reference [45]
[c]RMBPT(SD) method, private communications with U.I. Safronova [46]
[d]RMBPT(SD) method, private communications with M.S. Safronova [42]
[e]DF method, private communications with U.I. Safronova [46]
[f]DF method from Reference [45]
[g]DF+2+3 method from Reference [45]

Overall the two experimental measurements of all the properties appear to be in good agreement. The optical and rf used slightly different methods of fitting and extract the properties of $Th^{3+}$ from their measurements. The comparisons of the two experimental studies shows that overall the properties determined from these two studies agree. The scalar dipole polarizability from both of the studies are consistent within error of each other. The result of the rf study for the scalar dipole polarizability is more precise than the optical study. In the rf study the quadrupole moment was determined more than order of magnitude more precisely than the optical study, the two result are only 1.3σ from each other. For the tensor dipole polarizability, the rf measurements improved on the precision of the optical determination and the tensor dipole polarizability determined from each of the experimental studies agrees to within 1.3σ. The rf study also determined the $^2D_{3/2}$ dipole matrix element a factor of 5 more precisely then the optical, the resulting matrix element from both studies are completely consistent.

The third column of Table 6.19 provides the current theoretical calculation for the properties of $Th^{3+}$ using relativistic many-body perturbation theory (RMBPT) with single and double excitation (SD) technique [45]. The permanent quadrupole moment calculated from a matrix element found with the RMBPT(SD) only differs from the quadrupole moment found in the rf study by 4.5%. The hexadecapole moment found from the rf study is consistent within error of the value estimated from the theoretical matrix element [42]. The $^2D_{3/2}$ dipole matrix element determined from the study is approximately 6.5% smaller than the matrix element calculated with this first technique. The scalar dipole polarizability excluding the *D* states contributions differs from the calculated by 11%. The octupole matrix element for the $^2D_{3/2}$ found from the data is 4.7σ away from the value calculated using this technique. Given these differences, it is surprising the total calculated scalar dipole polarizability is within 1% of the

total scalar dipole polarizability determined from the fit of the rf data. In contrast the total tensor dipole polarizability differs from estimated tensor dipole polarizability calculated with RMBPT(SD) by approximately 16%, even though many of the same states that contribute to the scalar dipole polarizability also contribute to tensor dipole polarizability.

The fourth column of Table 6.19 gives the Dirac-Fock (DF) estimates of the permanent quadrupole moment [46] and the $^2D_{3/2}$ dipole matrix element [45]. This technique was not used to calculate any of the other core properties. The actual permanent quadrupole moment found from the rf study is 2/3 the predicted from the DF estimate. Similarly the $^2D_{3/2}$ dipole matrix element found from the rf study is only 59% of the DF estimates. The DF technique even though it is fully relativistic is not able to accurately predict properties of the $Th^{3+}$ ion precisely. It appears give an order of magnitude estimate. The final column gives the improved Dirac-Fock calculation [45], including second and third order corrections and referred to as DF+2+3. In the case of this technique all of the estimated properties are smaller than the properties observed in the rf study, the $^2D_{3/2}$ dipole matrix element 7.4% smaller, the scalar dipole polarizability 13% smaller and the tensor dipole polarizability 11% smaller. The inclusion of the correction factors to the DF model did improve its predictions, but they still differ from the rf determined properties by 10 to 20%. The comparison of all three of these theoretical approaches to the measured experimental properties illustrates the difficulty of calculating properties for such a relativistic ion. The experimental measurements from this work will help to test the theoretical models as they are developed.

The $Th^{3+}$ ion provided a steep challenge to the theoretical model of Rydberg fine structures [7] due to the low-lying $^2D_{3/2}$ and $^2D_{5/2}$ core states. The effective potential used in this work was corrected for the low-lying core levels in a manner that is transparent and therefore

could be applied in the future to other ions that suffer from some of the same problems as $Th^{3+}$. The properties determined from the rf study confirmed the results of the optical study and increased the level of precision of the determined properties. The rf study could be improved if more rf measurements were completed in higher $L$ levels, or if another $n$ studied, one less sensitive to the low-lying states was studied. The result of both of the optical and rf study of $Th^{3+}$ provided value of the properties of $Th^{3+}$ which can be used to rigorously test the theoretical models of the complex $Th^{3+}$ ion. Hopefully, these properties will be utilized to test the current models and provide valuable insight for future models.

**Chapter 7: Summary**

This dissertation reports the results of the rf RESIS studies of both Rn-like and Fr-like thorium ions. The study of both of the thorium ions was the culmination of years of work, exploring high charge and high angular momentum Rydberg states. The properties of $Th^{4+}$ reported in Chapter 3 and subsequently published in Ref. [36], expanded on the limited knowledge of the $Th^{4+}$ ion. The optical study to determined properties of $Th^{3+}$ is reported in Chapter 4 and published in Ref. [3]. The optical study of the properties $Th^{3+}$ was improved on with an rf RESIS study of the $n$=28 $Th^{2+}$ Rydberg fine structure. The experimental results of that study were presented in Chapter 5 and the properties extracted from those experimental measurements using the effective potential model were presented Chapter 6. The measured $Th^{3+}$ and $Th^{4+}$ properties provide information on ions that are common in actinide chemistry, but for which little had been measured. The determined properties also enable the testing of the complex theoretical models used to calculate properties of ions such as thorium.

The results of the studies of the both of the thorium ions presented in this dissertations not only expanded on the knowledge of the ions of interest, but it also expands on the knowledge of the experimental technique and the effective potential model used to extract the properties from the measurement of Rydberg fine structures. The rf RESIS technique helps to resolve fine structure levels that were not resolved in the optical RESIS studies of both of the ions. The rf studies also measured the fine structure of both ions with a higher level of precision than the optical studies. The increase in the number of levels measured and the precision of the measurements allowed for a more in-depth study of the ions with the effective potential model. The study to determine the properties of $Th^{4+}$ showed the importance of higher order terms in the effective potential and the role they play in extraction process. The study the $Th^{2+}$ Rydberg fine

structure showed the dominant effect low-lying core states have on the Rydberg fine structure and the corrections necessary to the effective potential model to account for their effect. The effect of the low-lying states in $Th^{3+}$ provided a challenge for the effective potential model [7]. The necessary modifications of the effective potential model to account for the effects of the low-lying core states were a major theme in the analysis of the data. Hopefully, in the future other models might also be tested on the $Th^{2+}$ Rydberg fine structure measurements [8]. The comparison of the properties of $Th^{3+}$ using different models might prove informative.

The thorium ions studied in this work were just two of the four ions proposed for study. The radon-like and francium-like uranium, $U^{6+}$ and $U^{5+}$, were also proposed to be studied using the RESIS technique. The study of the $U^{6+}$ would be similar to the study of $Th^{4+}$ since it too has $^1S_0$ ground states. The study to determine the properties of $U^{5+}$ would be much easier than the study to determine the properties of $Th^{3+}$. $U^{5+}$ contains no low-lying excited core states, therefore the measured $U^{4+}$ Rydberg fine structure could be fit directly to the effective potential without most of the corrections necessary in the $Th^{3+}$ study. The undertaking of both of the uranium studies began before the first study of thorium. The current observations of the optical excitation spectra for each uranium ions contain only the high-$L$ peak, with no sign of resolved levels in the fine structures. At this time the reason for the inability to observed resolved fine structure is not understood, but the effort to understand it continues. The success with the thorium study show that if resolved structure can be observed, the properties of the uranium ion can be determined.

**References**


[1] S. R. Lundeen, in *Advances in Atomic Molecular and Optical Physics*, edited by P. R. Berman, and C. C. Lin (Academic Press, New York, 2005), pp. 161.

[2] S. Fraga, J. Karwowski, and K. M. S. Saxena, *Handbook of Atomic Data,* (Elsevier Scientific Pub., Amsterdam, 1976).

[3] J. A. Keele, M. E. Hanni, S. L. Woods, S. R. Lundeen, and C. W. Fehrenbach, Phys. Rev. A **83**, 062501 (2011).

[4] Y. Ralchenko, A. Kramida, J. Reader, and NIST ASD team, NIST Atomic Spectra Database, (Version 5) (National Institute of Standards and Technology, Gaithersburg, MD, 2012)

[5] S. Civiš, M. Ferus, P. Kubelík, V. E.Chernov, and E. M. Zanozina, A&A **545**, A61 (2012).

[6] R. J. Drachman, Phys. Rev. A **26**, 1228 (1982).

[7] S. L. Woods and S. R. Lundeen, Phys. Rev. A **85**, 042505 (2012).

[8] W. Clark, C. H. Greene, and G. Miecznik, Phys. Rev. A **53**, 2248 (1996).

[9] C. J. Campbell, A. V. Steele, L. R. Churchill, M. V. DePalatis, D. E. Naylor, D. N. Matsukevich, A. Kuzmich, and M. S. Chapman, Phys. Rev Lett. **102**, 233004 (2009).

[10] A. Dalgarno and J. T. Lewis, Proc. R. Soc. A **233**, 70 (1955).

[11] S. Woods, C. Smith, J. Keele, and S. R. Lundeen, Phys. Rev. A **87**, 022511 (2013).

[12] *The Chemistry of Actnides and Transactinide Elements*, edited by L. R. Morss, N. M. Edlestein, and J. Fuger (Springer Netherland, Dordrecht, Netherlands, 2006).

[13] J. Blaise and J. F. Wyart, http://www.lac.u-psud.fr/Database/Contents.html.

[14] V. Goncharov and M. C. Heaven, J. Chem. Phys. **124**, 064312 (2006).

[15] E. Peik and C. Tamm, Europhys. Lett. **61**, 181 (2003).

[16] S. R. Lundeen and C. W. Fehrenbach, Phys. Rev. A **75**, 032523 (2007).

[17] M. E. Hanni, Ph.D Thesis, Colorado State University, (2010).

[18] M. E. Hanni, J. A. Keele, S. R. Lundeen, C. W. Fehrenbach, and W. G. Sturrus, Phys. Rev. A **81**, 042512 (2010).

[19] M. E. Hanni, J. A. Keele, S. R. Lundeen, and W. G. Sturrus, Phys. Rev. A **78**, 062510 (2008).

[20] J. A. Keele, S. L. Woods, M. E. Hanni, S. R. Lundeen, and W. G. Sturrus, Phys. Rev. A **81**, 022506 (2010).

[21] M. E. Hanni, J. A. Keele, S. R. Lundeen, and C. W. Fehrenbach, Phys. Rev. A **82**, 022510 (2010).

[22] F. J. Deck, E. A. Hessels, and S. R. Lundeen, Phys. Rev. A **48**, 4400 (1993).

[23] D. S. Fisher, Ph.D Thesis, Colorado State University, (2000).

[24] C. W. Fehrenbach, S. R. Lundeen, and O. L. Weaver, Phys. Rev. A **51**, R910 (1995).

[25] R. A. Komara, M. A. Gearba, C. W. Fehrenbach, and S. R. Lundeen, J. Phys. B **38** (2005).

[26] C. R. Quick and H. C. Bryant, J. Opt. Soc. Am. B **7**, 708 (1990).

[27] E. L. Snow, Ph.D Thesis, Colorado State University, (2006).

[28] E. S. Chang, Phys. Rev. A **31**, 495 (1985).

[29] *Reference Data for Engineers: Radio, Electronics, Computer and Communications*, edited by M. E. V. Valkenburg (SAMS, Indianapolis, 1995).

[30] N. F. Ramsey, *Molecular Beams* (Oxford University Press, London, 1956).

[31] H. A. Bethe and E. E. Salpeter, *Quantum Mechanics of One- and Two-Electron Atoms* (Dover Publications, Inc, Mineola, New York, 2008).

[32] J. H. Shirley, Phys. Rev. **138**, B979 (1965).

[33] J. R. Brandenberger, S. R. Lundeen, and F. M. Pipkin, Phys. Rev. A **14**, 341 (1976).

[34] E. L. Snow and S. R. Lundeen, Phys. Rev. A **75**, 062512 (2007).

[35] J. A. Keele, S. R. Lundeen, and C. W. Fehrenbach, Phys. Rev. A **83**, 062509 (2011).

[36] J. A. Keele, C. S. Smith, S. R. Lundeen, and C. W. Fehrenbach, Phys. Rev. A **85**, 064502 (2012).

[37] R. A. Komara, M. A. Gearba, S. R. Lundeen, and C. W. Fehrenbach, Phys. Rev. A **67**, 062502 (2003).

[38] G. W. F. Drake and R. A. Swainson, Phys. Rev. A **44**, 5448 (1991).

[39] K. Bockasten, Phys. Rev. A **9**, 1087 (1974).

[40] U. I. Safronova and M. S. Safronova, Phys. Rev. A **84**, 052515 (2011).

[41] D. R. Beck (private communication).

[42] M. S. Safronova (private communication).

[43] F. Réal, V. Vallet, C. Clavaguéra, and J.-P. Dognon, Phys. Rev. A **78**, 052502 (2008).

[44] A. Boreschevsky and P. Schwerdtfeger (private communication).

[45] U. I. Safronova, W. R. Johnson, and M. S. Safronova, Phys. Rev. A **74**, 042511 (2006).

[46] U. I. Safronova (private communication).

[47] E. S. Shuman and T. F. Gallagher, Phys. Rev. A **74**, 022502 (2006).

[48] E. L. Snow, M. A. Gearba, R. A. Komara, and S. R. Lundeen, Phys. Rev. A **71**, 022510 (2005).

[49] R. A. Komara, W. G. Sturrus, D. H. Pollack, and W. R. Cochran, Phys. Rev. A **59**, 251 (1999).

[50] A. R. Edmonds, *Angular Momentum in Quantum Mechanics,* (Princeton University Press, Princeton, New Jersey, 1996).

[51] R. F. Ward Jr., W. G. Sturrus, and S. R. Lundeen, Phys. Rev. A **53**, 113 (1995).

## Appendix A: Observations of the $n$=37 $Th^{3+}$ Rydberg Fine structure

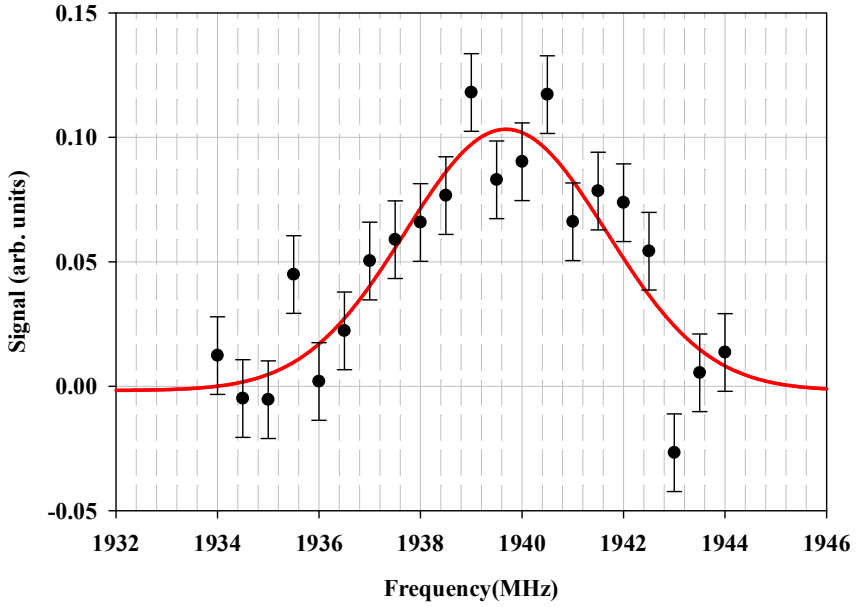


Figure A.1: $Th^{3+}$ $n$=37 $L$=8 to 9 line shape, seen in the co-propagating direction and the observation is the average of JAK7-006, 007, 008, and 009.

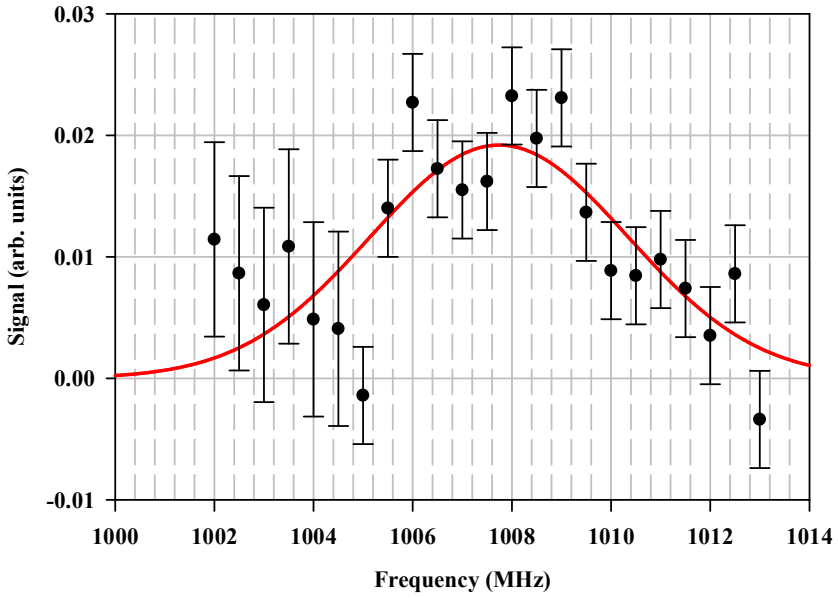


Figure A.2: $Th^{3+}$ $n$=37 $L$=9 to 10 line shape, seen in the counter propagating direction and the average of JAK2-137abc, 138, 139, 140, and 141

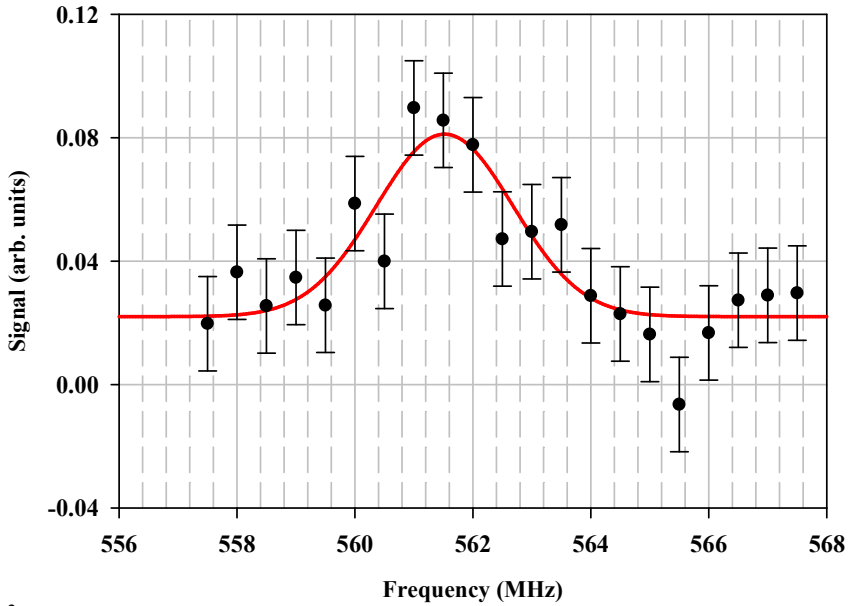


Figure A.3: $Th^{3+}$ $n$=37 $L$=10 to 11 line shape, seen in the counter- propagating direction, data from JAK2-115.

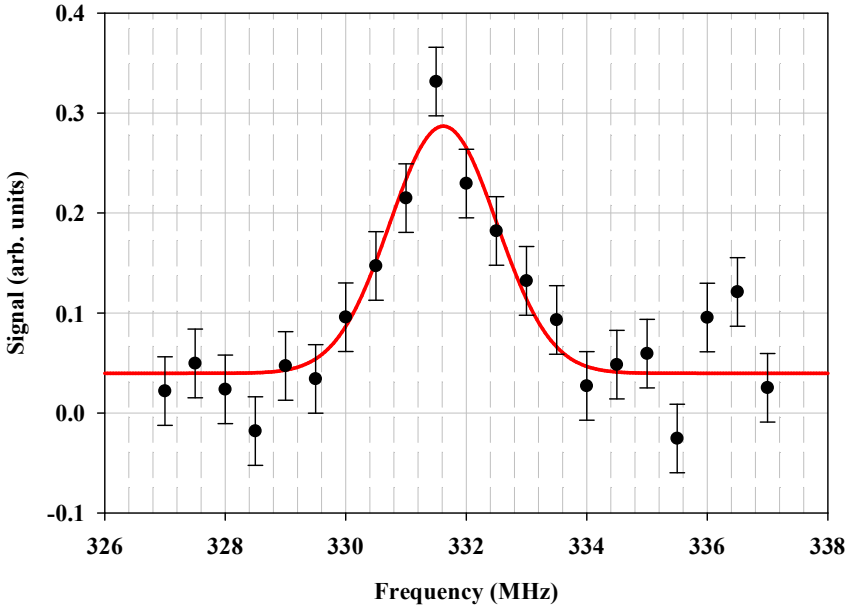


Figure A.4: $Th^{3+}$ $n$=37 $L$=11 to 12 line shape, seen in the co-propagating direction and data from JAK2-091.

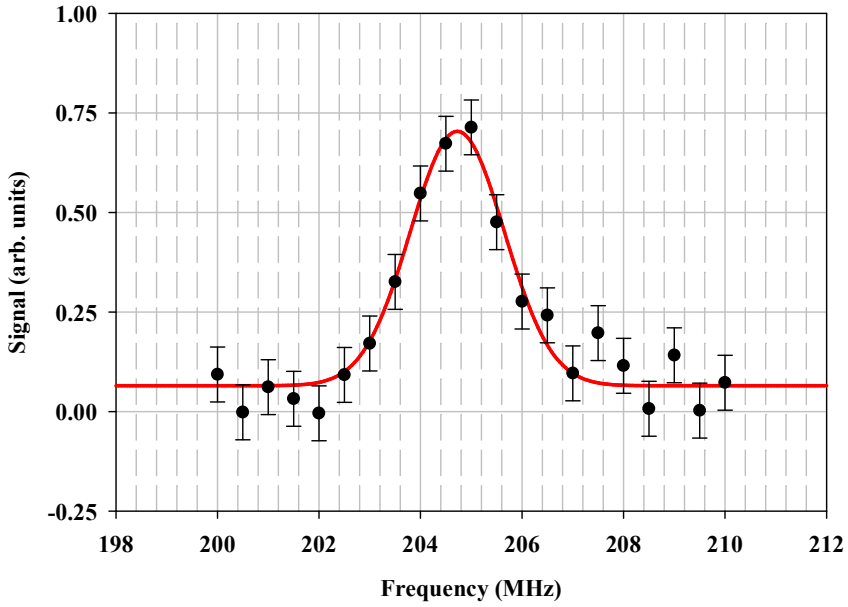


Figure A.5: $Th^{3+}$ $n$=37 $L$=12 to 13 line shape, seen in the co-propagating direction with data from JAK2-093b.

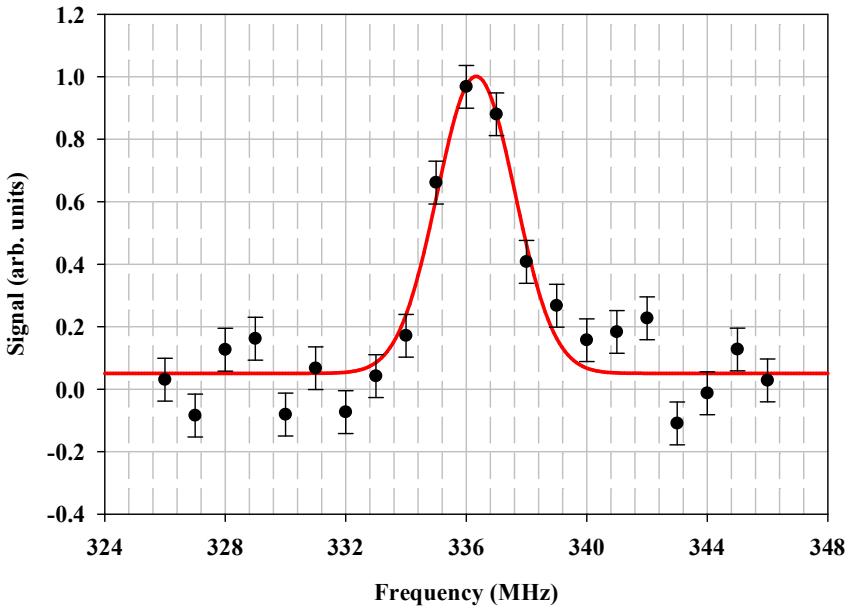


Figure A.6: $Th^{3+}$ $n$=37 $L$=12 to 14 line shape, seen in the co-propagating direction with 130μW coming out of the rf region, observation from JAK2-094.

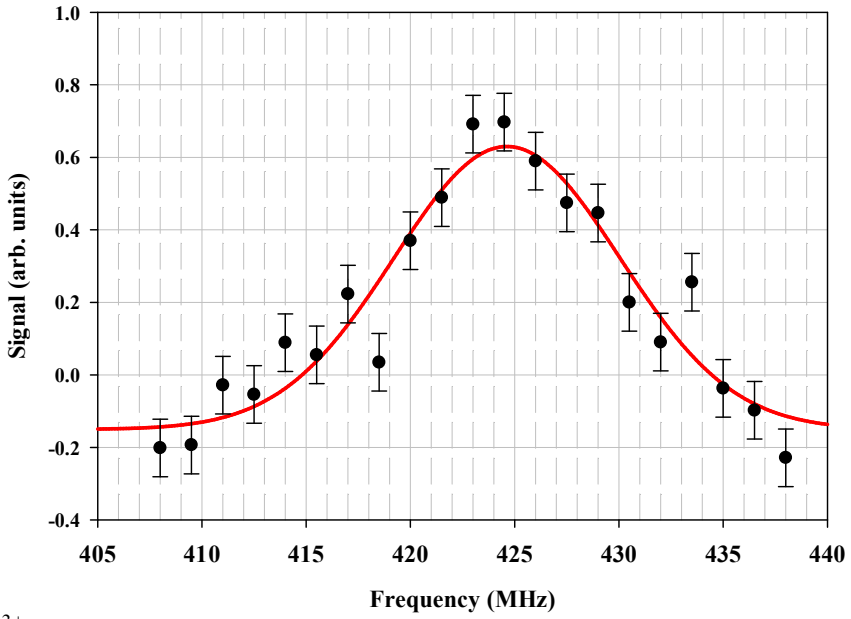


Figure A.7: $Th^{3+}$ $n$=37 $L$=12 to 15 line shape, seen in the co-propagating direction with 0.92mW coming out of the rf region, observation from JAK2-094b.

## Appendix B: Observations of the $n$=28 $Th^{2+}$ Rydberg Fine structure

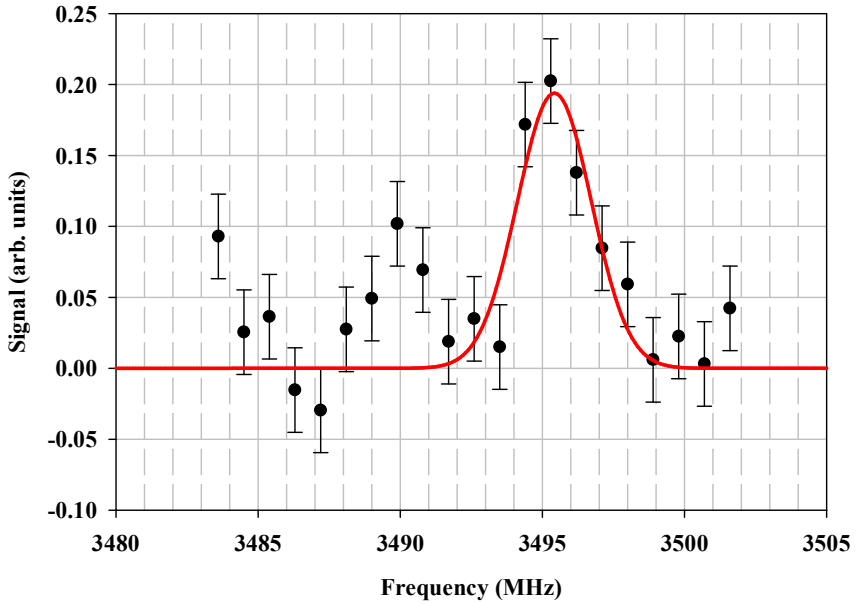


Figure B.1: $Th^{2+}$ $n$=28 $L$=9, $K$=6.5 to $L'$=10, $K'$=7.5 line shape, seen in the co-propagating direction with data from JAK6-085, 086 and 087.

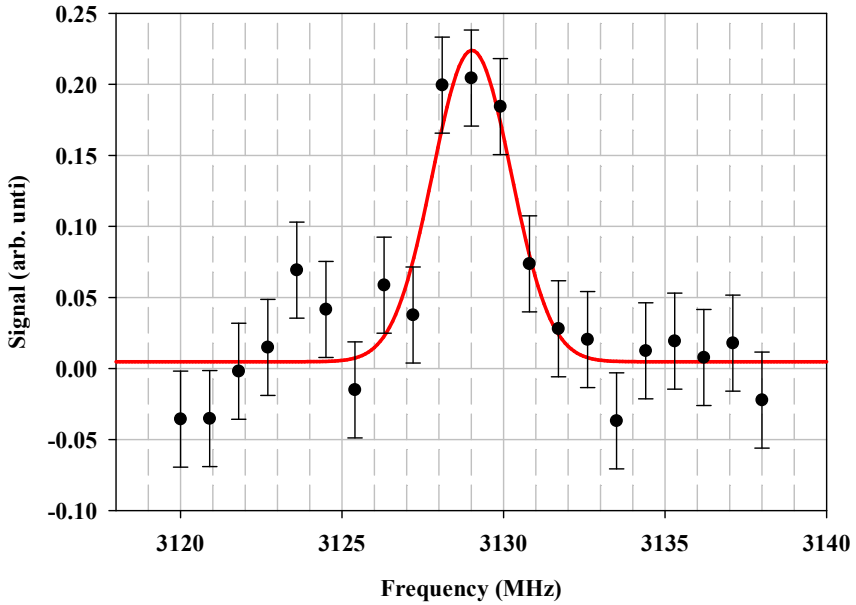


Figure B.2: $Th^{2+}$ $n$=28 $L$=9, $K$=7.5 to $L'$=10, $K'$=8.5 line shape, seen in the co-propagating direction with data from JAK6-070.

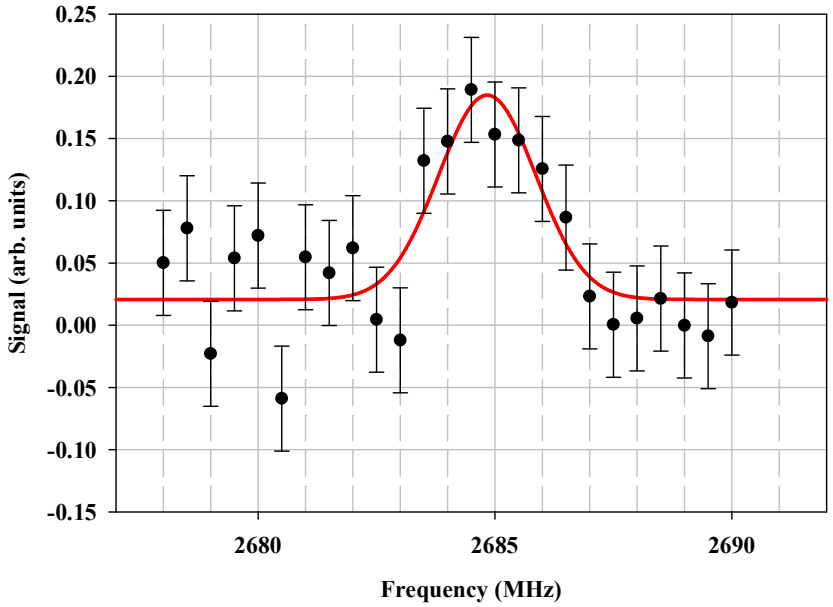


Figure B.3: $Th^{2+}$ $n$=28 $L$=9, $K$=8.5 to $L'$=10, $K'$=9.5 line shape, seen in the co-propagating direction with data from JAK6-066.

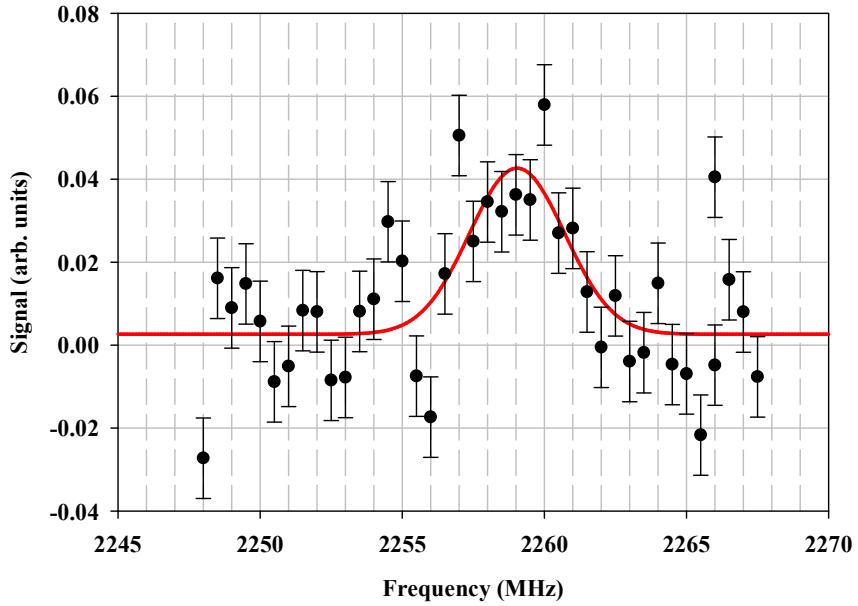


Figure B.4: $Th^{2+}$ $n$=28 $L$=9, $K$=9.5 to $L'$=10, $K'$=10.5 line shape, seen in the co-propagating direction with data from JAK5-153.

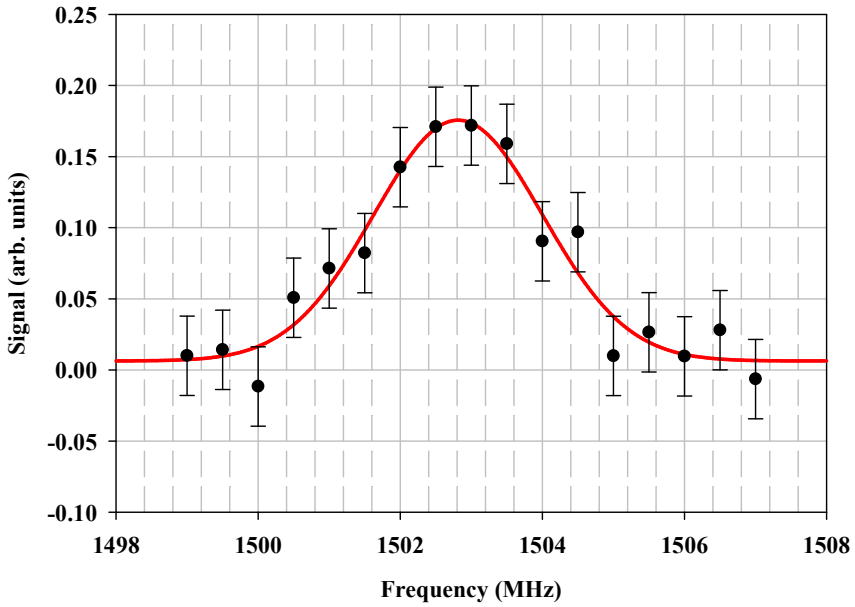


Figure B.5: $Th^{2+}$ $n$=28 $L$=9, $K$=10.5 to $L'$=10, $K'$=11.5 line shape, seen in the co-propagating direction with data from JAK5-135.

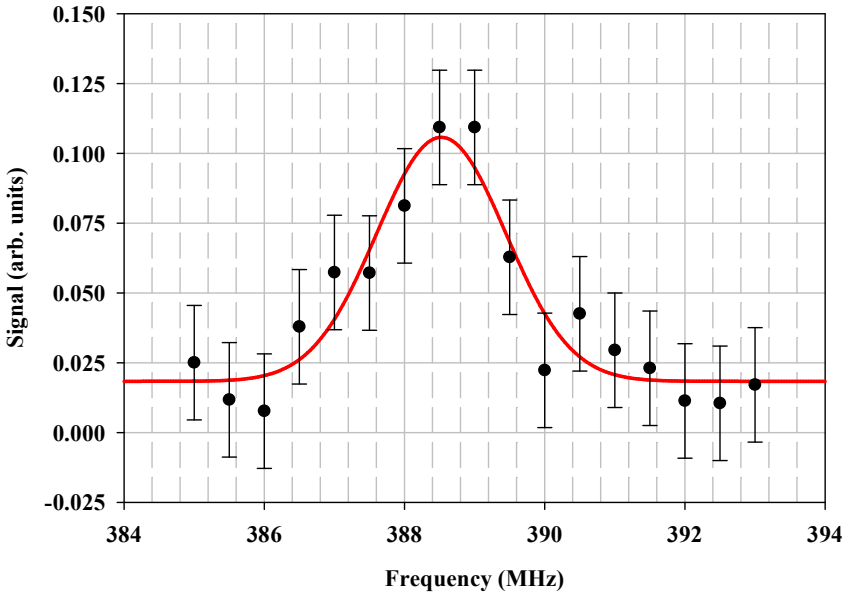


Figure B.6: $Th^{2+}$ $n$=28 $L$=9, $K$=10.5 to $L'$=10, $K'$=10.5 line shape, seen in the co-propagating direction with data from JAK5-136.

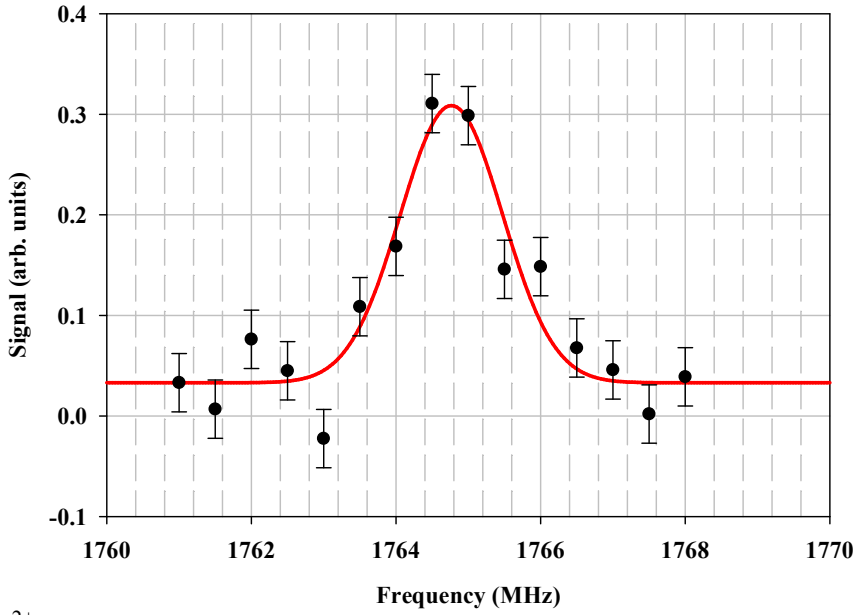


Figure B.7: $Th^{2+}$ $n$=28 $L$=10, $K$=7.5 to $L'$=11, $K'$=8.5 line shape, seen in the co-propagating direction with data from JAK6-091 and 091b.

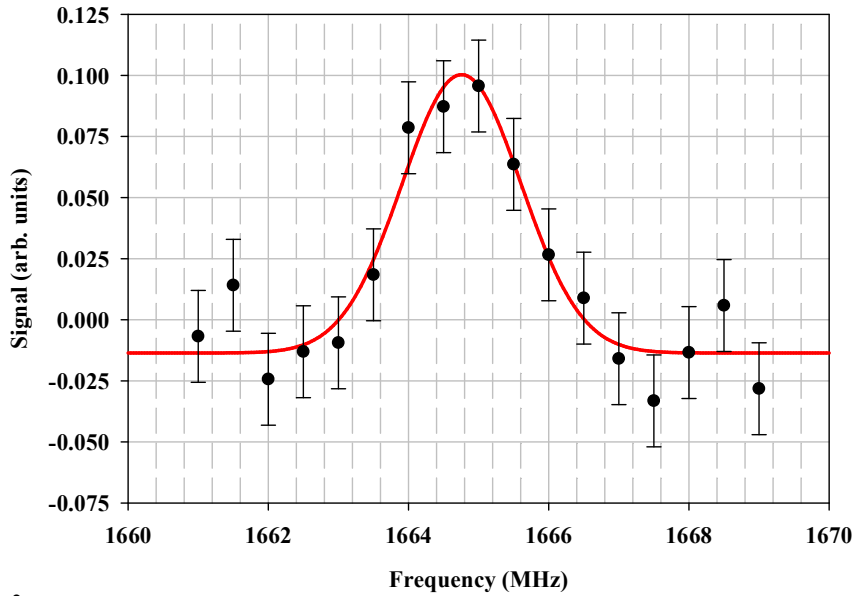


Figure B.8: $Th^{2+}$ $n$=28 $L$=10, $K$=8.5 to $L'$=11, $K'$=9.5 line shape, seen in the co-propagating direction with data from JAK5-111.

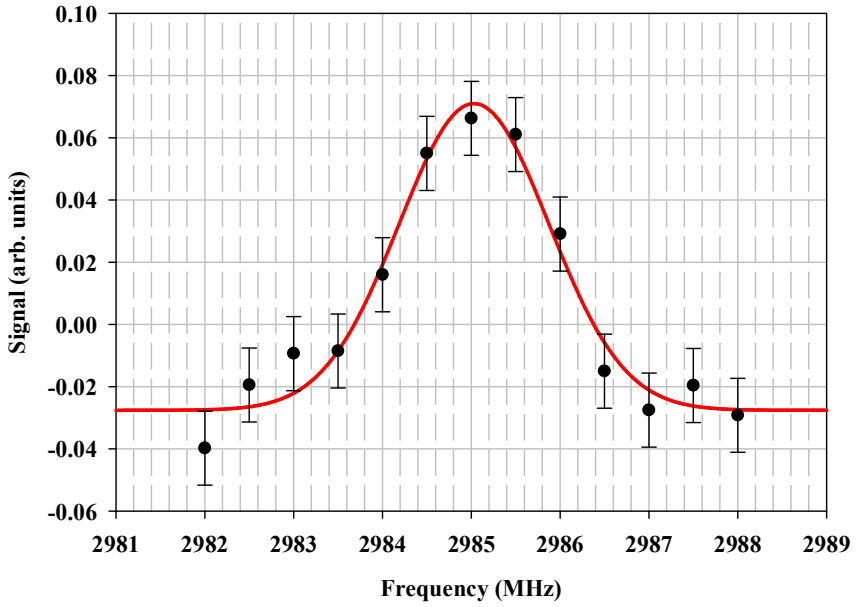


Figure B.9: $Th^{2+}$ $n$=28 $L$=10, $K$=8.5 to $L'$=11, $K'$=8.5 line shape, seen in the co-propagating direction with data from JAK5-117.

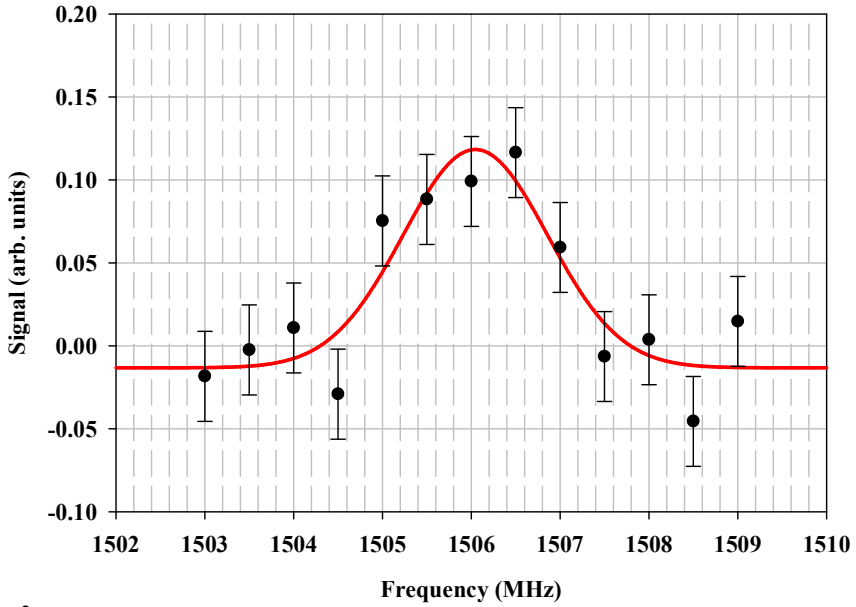


Figure B.10: $Th^{2+}$ $n$=28 $L$=10, $K$=9.5 to $L'$=11, $K'$=10.5 line shape, seen in the co-propagating direction with data from JAK5-087.

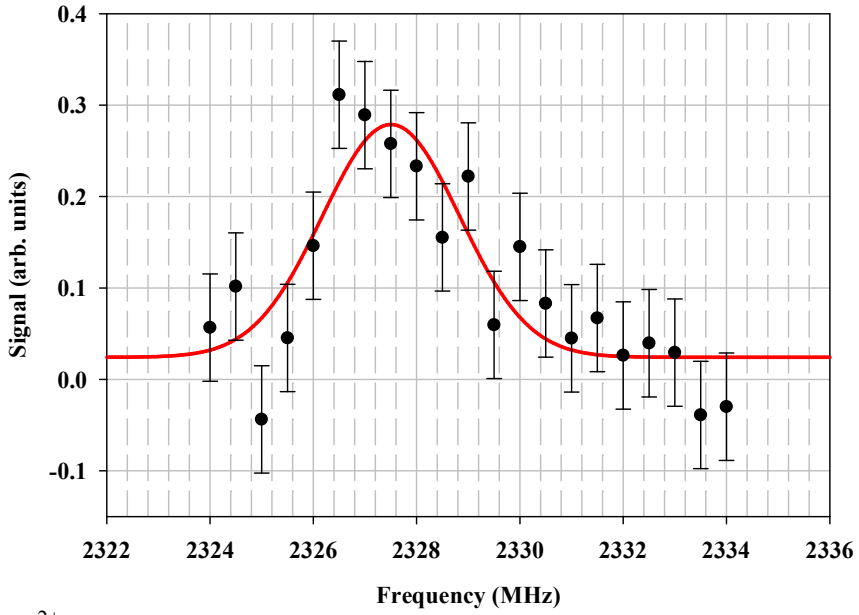


Figure B.11: $Th^{2+}$ $n$=28 $L$=10, $K$=9.5 to $L'$=11, $K'$=9.5 line shape, seen in the counter-propagating direction with data from JAK7-071.

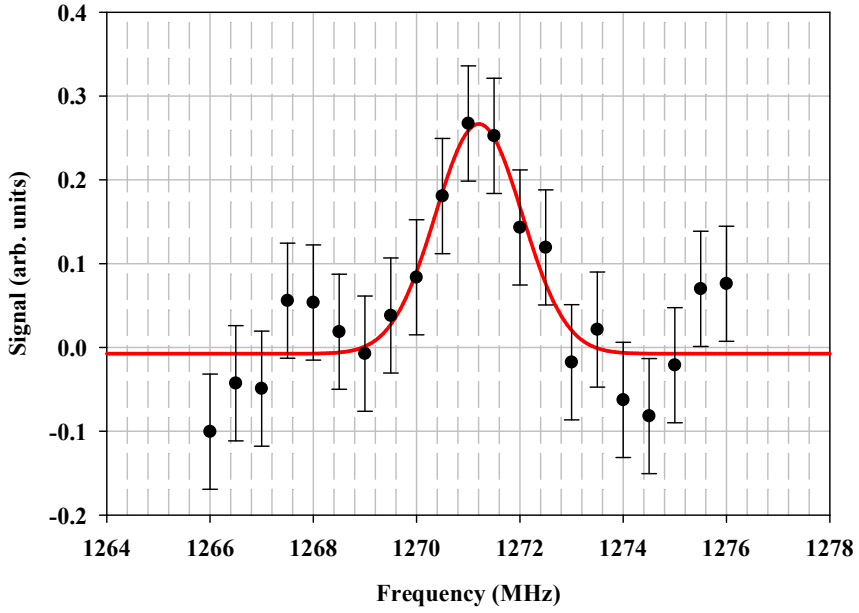


Figure B.12: $Th^{2+}$ $n$=28 $L$=10, $K$=10.5 to $L'$=11, $K'$=11.5 line shape, seen in the co-propagating direction with data from JAK5-086.

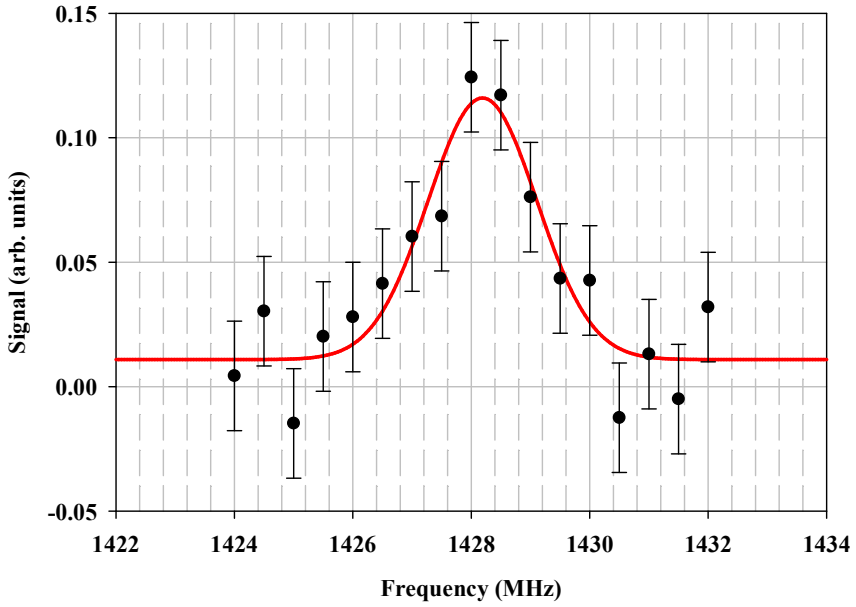


Figure B.13: $Th^{2+}$ $n$=28 $L$=10, $K$=10.5 to $L'$=11, $K'$=10.5 line shape, seen in the co-propagating direction with data from JAK7-052.

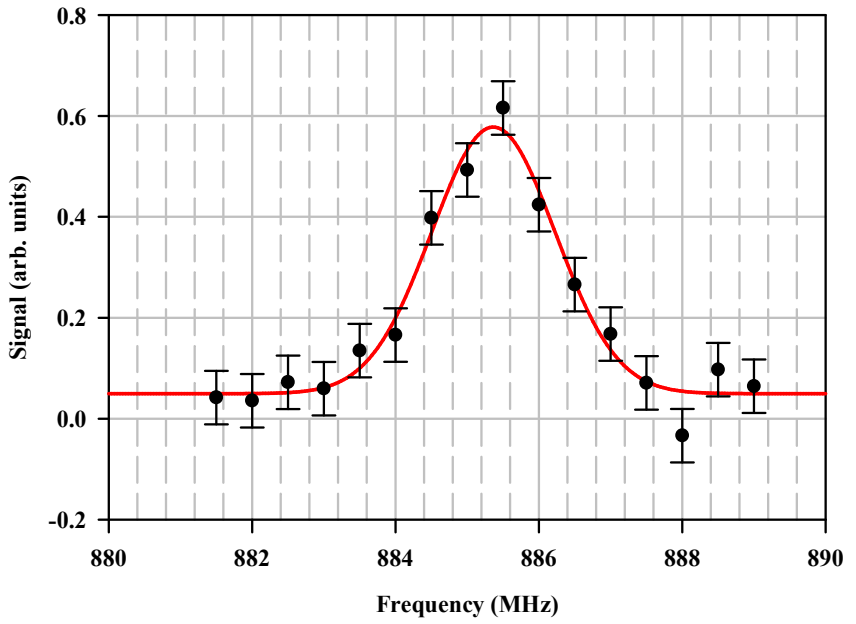


Figure B.14: $Th^{2+}$ $n$=28 $L$=10, $K$=11.5 to $L'$=11, $K'$=12.5 line shape, seen in the co-propagating direction with data from JAK7-094.

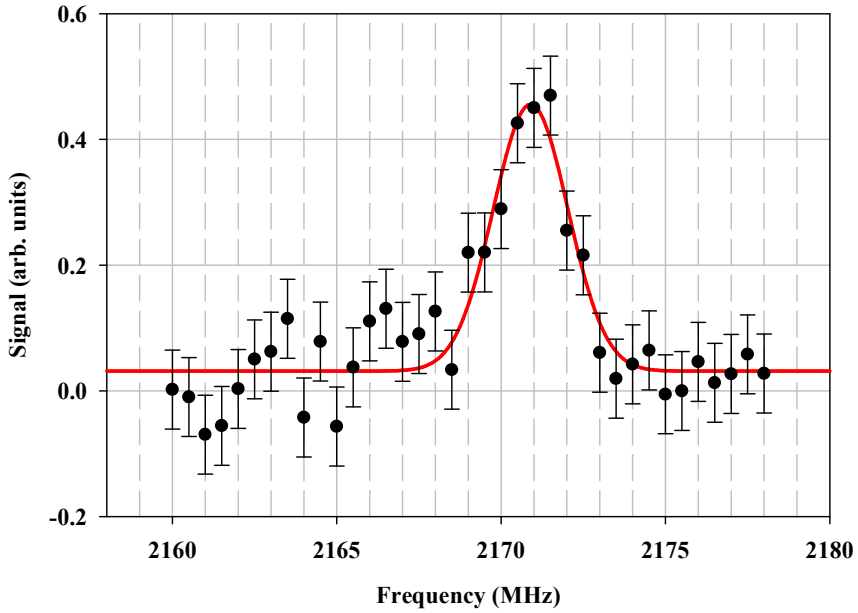


Figure B.15: $Th^{2+}$ $n$=28 $L$=10, $K$=7.5 to $L'$=12, $K'$=9.5 line shape, seen in the co-propagating direction with data from JAK6-093. The power exiting the rf region was 2.0mW.

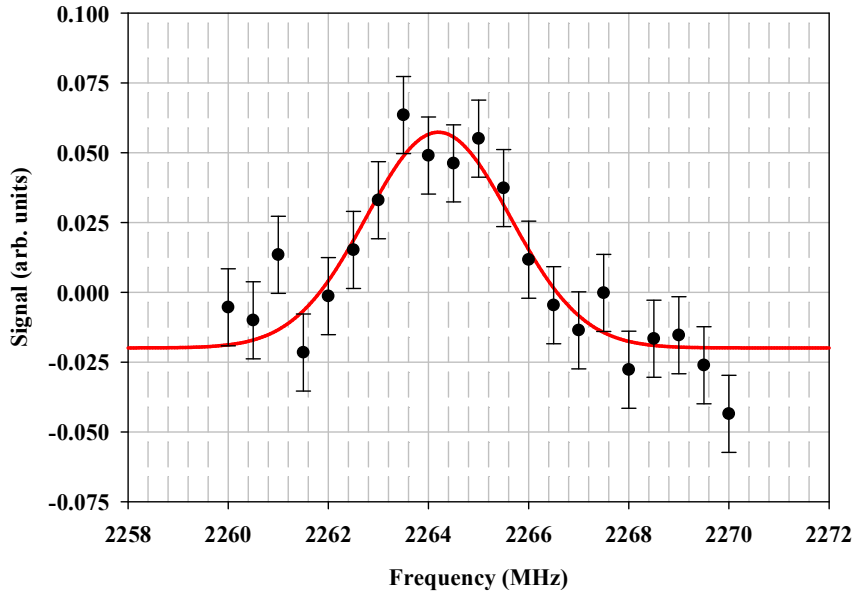


Figure B.16: $Th^{2+}$ $n$=28 $L$=10, $K$=8.5 to $L'$=12, $K'$=10.5 line shape, seen in the co-propagating direction with data from JAK5-112. The power exiting the rf region was 2.6mW.

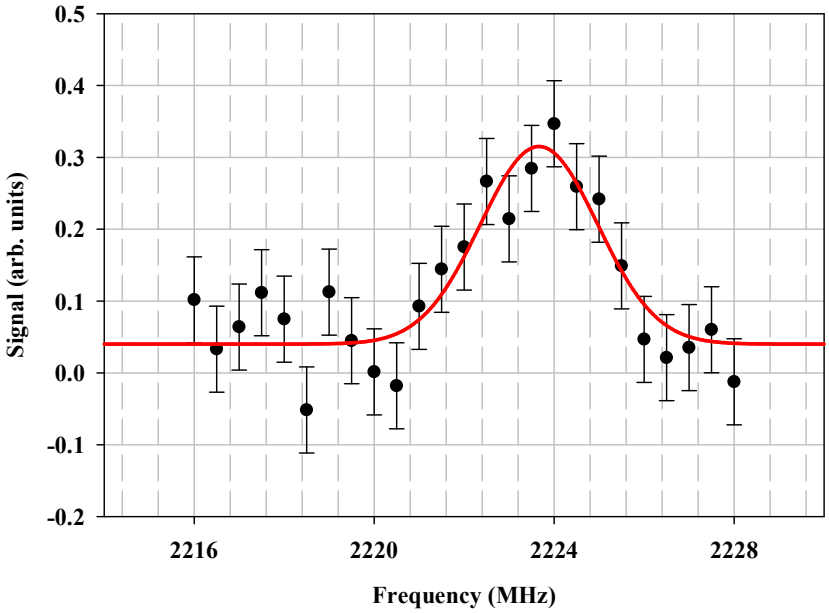


Figure B.17: $Th^{2+}$ $n$=28 $L$=10, $K$=9.5 to $L'$=12, $K'$=11.5 line shape, seen in the co-propagating direction with data from JAK7-069. The power exiting the rf region was 1.64mW

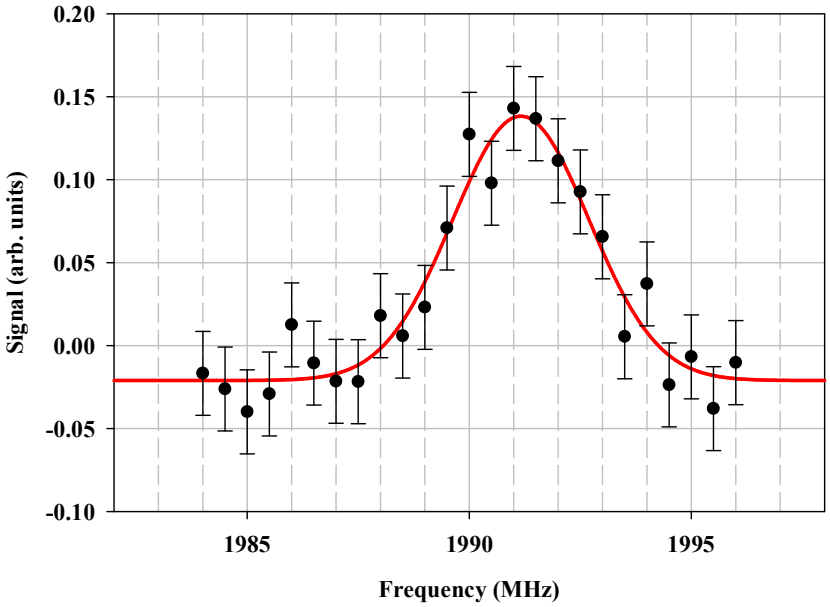


Figure B.18: $Th^{2+}$ $n$=28 $L$=10, $K$=10.5 to $L'$=12, $K'$=12.5 line shape, seen in the co-propagating direction with data from JAK5-105. The power exiting the rf region was 0.96mW

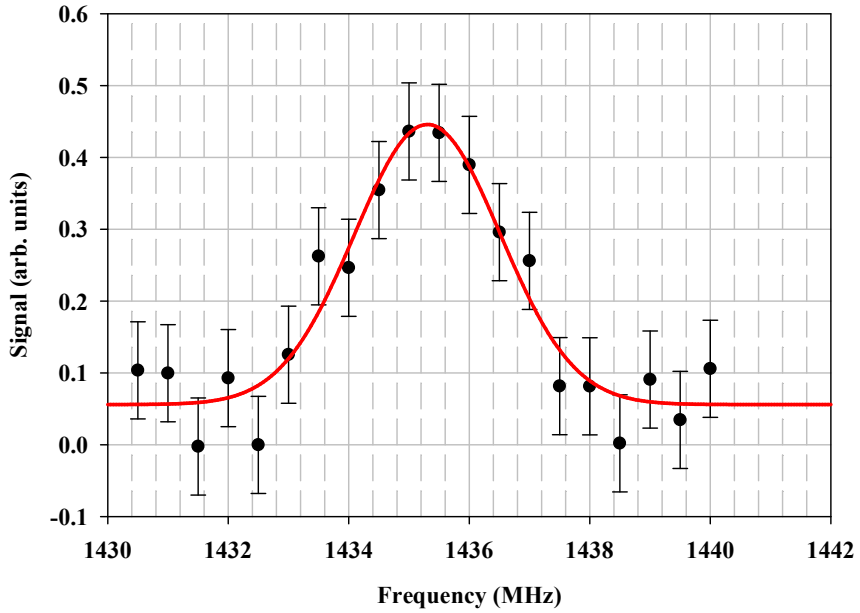


Figure B.19: $Th^{2+}$ $n$=28 $L$=10, $K$=11.5 to $L'$=12, $K'$=13.5 line shape, seen in the co-propagating direction with data from JAK7-095. The power exiting the rf region was 0.71